

Schriftenreihe der Reiner Lemoine-Stiftung



Jörg Schube

Metallization of Silicon Solar Cells with Passivating Contacts

Metallization of Silicon Solar Cells with Passivating Contacts

Dissertation
zur Erlangung des Doktorgrades
der Technischen Fakultät
der Albert-Ludwigs-Universität Freiburg im Breisgau

vorgelegt von

Jörg Schube

Fraunhofer-Institut für Solare Energiesysteme (ISE)
Freiburg im Breisgau

2020

Dekan:

Prof. Dr. Rolf Backofen

Erstgutachter:

Prof. Dr. Stefan W. Glunz

Zweitgutachter:

Prof. Dr. Frank Balle

Vorsitzender der Prüfungskommission:

Prof. Dr. Bastian E. Rapp

Beisitzer:

Prof. Dr. Roland Zengerle

Datum der Prüfung: 26. November 2020

Institut für Nachhaltige Technische Systeme INATECH

Technische Fakultät der Albert-Ludwigs-Universität Freiburg

Schriftenreihe der Reiner Lemoine-Stiftung

Jörg Schube

**Metallization of Silicon Solar Cells
with Passivating Contacts**

Shaker Verlag
Düren 2021

Bibliographic information published by the Deutsche Nationalbibliothek

The Deutsche Nationalbibliothek lists this publication in the Deutsche Nationalbibliografie; detailed bibliographic data are available in the Internet at <http://dnb.d-nb.de>.

Zugl.: Freiburg, Univ., Diss., 2020

Copyright Shaker Verlag 2021

All rights reserved. No part of this publication may be reproduced, stored in a retrieval system, or transmitted, in any form or by any means, electronic, mechanical, photocopying, recording or otherwise, without the prior permission of the publishers.

Printed in Germany.

ISBN 978-3-8440-7853-4

ISSN 2193-7575

Shaker Verlag GmbH • Am Langen Graben 15a • 52353 Düren

Phone: 0049/2421/99011-0 • Telefax: 0049/2421/99011-9

Internet: www.shaker.de • e-mail: info@shaker.de

“If the doors of perception were cleansed
everything would appear to man as it is, infinite.”

(William Blake, *The Marriage of Heaven and Hell*)

Abstract

This work develops and analyzes innovative metallization and contact formation of next-generation silicon solar cells, namely silicon heterojunction (SHJ) and Tunnel Oxide Passivating Contact (TOPCon) cells. Thereby, the focus is set on metallization with reduced silver consumption along with extremely fast and effective contact formation techniques. For this purpose, the development of new printing approaches and a deep understanding of contact formation mechanisms using advanced characterization methods are necessary.

A new printing technique with large silver saving potential, called *FlexTrail* printing, is developed. Using the same nanoparticle-based inks as for inkjet printing, it allows for the application of very narrow metal electrodes down to 10 μm width on textured substrates and down to 8 μm width on planar surfaces. This minimizes shading-related losses, hence, enabling a SHJ cell efficiency of up to 23.7%. The wet ink laydown is reduced down to below 10 mg/cell, certainly offering a significant cost saving potential compared to state-of-the-art screen printing with a typical laydown of 100 mg/cell (busbarless).

Extremely fast intense pulsed light (IPL) is evaluated towards solar cell processing. Thereby, it is demonstrated that an entire replacement of time-consuming thermal post-metallization treatments is possible. IPL-induced electrical contact formation in finger-patterned metal electrodes printed on top of a SHJ substrate is investigated. The substrate absorbs pulsed light and, thus, heat is transferred to the metal/transparent conductive oxide (TCO) interface inducing sintering of metal particles. Additionally, it is demonstrated that the lateral conductivity of metal fingers is increased by heating due to light being directly absorbed in the metal electrode. Based on the knowledge of contact formation, IPL processes are developed allowing low finger resistances of down to 3.0 Ω/cm and contact resistivities of down to 2.7 $\text{m}\Omega\cdot\text{cm}^2$.

Furthermore, the impact of IPL on the SHJ is investigated. For this purpose, an in-situ temperature measurement setup is developed enabling to characterize the

substrate temperature during millisecond-lasting IPL flashes. Peak temperatures are correlated with the SHJ passivation quality. For such contacts, an optimum peak temperature of 325°C is identified. It is tolerated by the temperature-sensitive SHJ due to the shortness of pulsed light. In comparison to thermal annealing, thus, up to 5 mV higher implied open-circuit voltages are achieved.

Using the findings of this work, busbarless IPL-processed SHJ cells are manufactured that outperform their thermally treated counterparts in terms of cell efficiency by up to 0.4%_{abs}. Thereby, curing, annealing, and light soaking is effectively combined in one single process step. IPL's efficiency advantage, high throughput potential, and compact design enable a cost of ownership saving potential of 6%_{rel} compared to state-of-the-art thermal annealing and even a cost reduction potential of 2%_{rel} on module level.

In order to make use of printed metal electrodes' full electrical potential, higher annealing temperatures are required than are compatible with the SHJ. They can be used, for example, in combination with temperature-tolerant TOPCon/TCO layer systems. Comprehensive microstructural analyses reveal that higher temperatures induce more effective particle sintering in printed electrodes. Therefore, thermal annealing is developed operating at temperatures of up to 350°C. This leads to lateral resistivities in the range of 3 $\mu\Omega\cdot\text{cm}$, comparable to those of high-temperature-processed contacts (temperatures of up to 800°C). Regarding contact formation at the metal/TCO interface, a contact formation model is presented. Thereby, the surface energy ratio of metal particles and TCO plays a crucial role. If the TCO layer's surface energy is too low, voids occur at the interface, hence, increasing the electrical contact resistivity.

Also in the case of TOPCon, IPL can replace thermal annealing. Both-sides TOPCon solar cells featuring front TCOs and screen-printed metal contacts are IPL-annealed. Thereby, high passivation quality and implied open-circuit voltages of up to 709.3 mV are obtained. This is similar to 709.4 mV as achieved in case of thermal annealing at 350°C. First results on lab-size cells reveal that IPL can achieve similar cell performance as thermal annealing. The best TOPCon cell in this work is IPL-processed and has the potential for 21.6% conversion efficiency, demonstrating the applicability of IPL for TOPCon.

Zusammenfassung

In dieser Arbeit werden innovative Metallisierungs- sowie Kontaktierungsansätze für Siliciumsolarzellen der nächsten Generation entwickelt. Diese betreffen Silicium Heterojunction (SHJ) und Tunnel Oxide Passivating Contact (TOP-Con) Solarzellen. Der Schwerpunkt der Arbeit liegt dabei auf der Metallisierung mit reduziertem Silberverbrauch und extrem schneller und effektiver Kontaktierung. Dazu sind die Entwicklung neuartiger Metalldruckverfahren und ein tiefes Verständnis der physikalischen Kontaktbildungsmechanismen erforderlich.

Ein neues Druckverfahren mit großem Silbereinsparungspotential, der sogenannte *FlexTrail*-Druck, wird vorgestellt. Damit lassen sich mittels kommerziell erhältlicher Nanopartikelintinten sehr schmale Metallelektroden mit bis zu $10\ \mu\text{m}$ Strukturbreite auf texturierten Substraten und bis zu $8\ \mu\text{m}$ Strukturbreite auf planaren Oberflächen erzielen. Indem sich dadurch metallisierungsbedingte Abschattung reduziert, werden Wirkungsgrade von SHJ Solarzellen von bis zu 23.7% ermöglicht. Gleichzeitig beträgt der Tintenauftrag weniger als $10\ \text{mg/Zelle}$, wodurch sich ein erhebliches Kosteneinsparungspotential im Vergleich zum Siebdruckverfahren mit einem typischen Auftrag von $100\ \text{mg/Zelle}$ (ohne Busbars) ergibt.

Weiter wird das Intense Pulsed Light (IPL) Verfahren für die Kontaktierung von Solarzellen entwickelt. Thermische Ofenprozesse nach der Metallisierung lassen sich damit vollständig ersetzen. Die elektrische Kontaktbildung in gedruckten Metallelektroden, verursacht durch IPL, wird untersucht. Es zeigt sich, dass das Substrat IPL absorbiert und sich erwärmt. Die Wärme wird zur Grenzfläche von Substrat und Metall übertragen, was die Kontaktbildung/Sinterung von Metallpartikeln induziert. Zusätzlich wird die laterale Leitfähigkeit von Kontaktfingern durch Erwärmung aufgrund von direkt absorbierten Lichts im Metall erhöht. Basierend auf dem Verständnis der Kontaktbildung werden IPL-Prozesse entwickelt, die niedrige Fingerwiderstände von bis zu $3.0\ \Omega/\text{cm}$ und spezifische Kontaktwiderstände von bis zu $2.7\ \text{m}\Omega\cdot\text{cm}^2$ ermöglichen.

Darüber hinaus wird der Einfluss von IPL auf die SHJ-Struktur untersucht. Zu diesem Zweck wird ein Messverfahren entwickelt, das eine Substrattemperaturmessung während der nur Millisekunden dauernden IPL-Blitze ermöglicht. Die Spitzentemperaturen werden mit der SHJ-Passivierungsqualität korreliert. Eine optimale Spitzentemperatur von 325°C wird identifiziert. Im Vergleich zum thermischen Referenzprozess erzielt IPL dadurch bis zu 5 mV höhere implizite Leerlaufspannungen.

Auf Basis der gewonnenen Erkenntnisse werden busbarlose, IPL-prozessierte SHJ-Solarzellen hergestellt, die thermisch prozessierte Zellen in Bezug auf ihren Wirkungsgrad um bis zu 0.4%_{abs} übertreffen. Dies ist nicht zuletzt auf Light Soaking Effekte zurückzuführen. Der Wirkungsgradvorteil von IPL und das hohe Durchsatzpotenzial ermöglichen eine Betriebskosteneinsparung von 6%_{rel} im Vergleich zum thermischen Prozess und sogar ein Kosteneinsparungspotenzial von 2%_{rel} auf Modulebene.

Um das volle Potential gedruckter Metallelektroden zu nutzen, sind höhere Prozesstemperaturen erforderlich als mit der SHJ-Struktur verträglich wären. Sie können z.B. in Kombination mit TOPCon eingesetzt werden. Umfassende Mikrostrukturanalysen offenbaren, dass höhere Temperaturen eine effektivere Partikelsinterung in gedruckten Elektroden induzieren. Daher wird ein thermischer Prozess, bei dem Temperaturen von bis zu 350°C erreicht werden, erarbeitet. Dies führt zu geringen lateralen spezifischen Widerständen der Kontakte von bis zu 3 $\mu\Omega\cdot\text{cm}$. Für die Kontaktbildung an der Metall/Substrat-Grenzfläche wird ein Modell entwickelt. Dabei spielt das Oberflächenenergieverhältnis von Metallpartikeln und Substratoberfläche eine tragende Rolle.

Auch im Falle von TOPCon kann IPL thermische Prozesse ersetzen. TOPCon-Solarzellen mit siebgedruckten Metallkontakten werden mittels IPL prozessiert. Dadurch werden eine hohe Passivierungsqualität und implizite Leerlaufspannungen von bis zu 709.3 mV erreicht. Erste Ergebnisse auf Zellniveau zeigen, dass sich mit IPL vergleichbare Wirkungsgrade wie mit dem thermischen Referenzprozess erreichen lassen. Die beste IPL-prozessierte TOPCon-Solarzelle in dieser Arbeit erreicht ein Wirkungsgradpotenzial von 21.6%, was die prinzipielle Anwendbarkeit von IPL für TOPCon demonstriert.

Table of contents

Abstract	I
Zusammenfassung	III
1 Introduction	9
1.1 Motivation	9
1.2 Thesis outline.....	11
2 Fundamentals of silicon solar cells	13
2.1 Semiconductor physics	13
2.1.1 Semiconductors	13
2.1.2 Doping.....	16
2.1.3 Generation and recombination	17
2.1.4 Basic solar cell operation	19
2.2 Silicon solar cells with passivating and carrier-selective contacts.....	25
2.2.1 The <i>c</i> -Si/ <i>a</i> -Si:H heterojunction.....	26
2.2.2 Tunnel oxide passivating contacts.....	29
3 Printed metal contacts	33
3.1 Fundamentals of contact formation	33
3.1.1 Sintering of metal particles.....	33
3.1.2 Metal/semiconductor contact.....	35
3.2 Printing techniques	39
3.2.1 Screen printing	40
3.2.2 Inkjet printing.....	42
3.2.3 FlexTrail printing	45
3.3 Contact formation techniques	47
3.3.1 Thermal annealing.....	47
3.3.2 Ultrasound-assisted thermal annealing.....	48
3.3.3 Intense pulsed light processing.....	49
4 Metrology	51
4.1 Photoconductance-based lifetime measurement	51

Table of contents

4.2	Microscopy	53
4.2.1	Confocal microscopy.....	54
4.2.2	Scanning electron microscopy.....	55
4.3	Four-point probe measurement.....	56
4.3.1	Determination of the finger resistance and finger resistivity.....	56
4.3.2	Determination of the contact resistivity.....	57
4.4	Simulation-based strategies to avoid measurement errors.....	61
4.4.1	Determination of the finger resistance.....	61
4.4.2	Determination of the contact resistivity.....	66
4.5	High-speed in-situ temperature measurement	68
5	Advanced printing approaches	71
5.1	Motivation	72
5.2	Sample preparation and characterization	73
5.3	Silver-coated-copper-based screen-printed contacts.....	75
5.4	Inkjet-printed nanosilver-based contacts	78
5.5	Comparison of inkjet- and FlexTrail-printed solar cells.....	82
5.6	Advanced printed metallization in one-cell mini-modules	84
5.7	Chapter summary.....	87
6	Understanding of contact formation processes	91
6.1	Thermal annealing at low and medium temperatures	92
6.1.1	Motivation	92
6.1.2	Sample preparation and characterization.....	94
6.1.3	Electrical characterization of metal contacts	97
6.1.4	Microstructural analysis of silver/indium tin oxide contacts.....	103
6.1.5	Passivation as a function of annealing temperature.....	108
6.2	Ultrasound-assisted thermal annealing	110
6.2.1	Motivation	110
6.2.2	Sample preparation and characterization.....	111
6.2.3	Microstructural analysis of metal contacts	113
6.2.4	Electrical characterization of metal contacts	115
6.2.5	Passivation of silicon heterojunction structures	116
6.3	Intense pulsed light processing.....	119
6.3.1	Motivation	119

6.3.2	Sample preparation and characterization.....	120
6.3.3	Passivation of silicon heterojunction structures	125
6.3.4	Electrical characterization of metal contacts	131
6.3.5	Contact formation induced by electromagnetic irradiation	137
6.3.6	Passivation of polycrystalline-silicon-based structures	140
6.4	Chapter summary.....	143
7	Metallization of solar cells with passivating contacts	147
7.1	Intense pulsed light processing of silicon heterojunction solar cells	148
7.1.1	Motivation	148
7.1.2	Sample preparation and characterization.....	151
7.1.3	Challenges and optimization of processing full-size solar cells ...	155
7.1.4	Entirely intense-pulsed-light-processed solar cells	163
7.1.5	Intense pulsed light processing of advanced metallization.....	168
7.2	Post-metallization annealing of cells with polysilicon-based contacts	171
7.2.1	Motivation	171
7.2.2	Sample preparation and characterization.....	172
7.2.3	Thermal and intense pulsed light annealing of solar cells	173
7.3	Chapter summary.....	176
8	Summary	179
9	Outlook	183
10	Appendix	185
	Bibliography	191
	List of symbols	211
	List of abbreviations	221
	Publications	225
	Acknowledgment	229

1 Introduction

1.1 Motivation

According to the *Intergovernmental Panel on Climate Change* (IPCC), “human-induced [climate] warming reached approximately 1°C [...] above pre-industrial levels in 2017, increasing at 0.2°C [...] per decade” [1]. It is further stated that linked to global warming there would be risks to the future existence of natural and human systems such as terrestrial and ocean ecosystems, water resources, land use, food security, and human health. These would be existential risks, not least for human beings. IPCC further shows that these risks are expected to be significantly lower for 1.5°C than for 2.0°C of global warming above preindustrial level [1]. Therefore, the *Paris agreement* of 2015 sets up a global plan to reduce global warming significantly below 2.0°C and further aims at 1.5°C . Reducing global greenhouse gas emissions is a key element of the agreement to maintain this goal. Nevertheless, the rising global energy demand needs to be satisfied and, consequently, requires the installation of renewable energy sources. Photovoltaics (PV) can play an important role to keep global warming below 2°C due to the abundance of energy the sun provides and the public acceptance of solar technology, in contrast to environmental more invasive renewables such as wind or hydro [2].

Today, PV still has to compete with fossil-fuel-fired power plants. To increase its market share and, thus, to contribute to fulfill the *Paris agreement*, further decreasing levelized cost of energy is highly desired. This is achievable by increasing solar cells’ conversion efficiency and by reducing PV production costs [3]. With about 90% of market share, PV is still dominated by silicon (Si) wafer-based PV [3]. To address an increase of conversion efficiency, solar cells with passivating and carrier-selective contacts, such as Si-heterojunction- (SHJ) and polycrystalline-Si-based (*poly*-Si) contacts, are introduced [4]. They allow to further approach the theoretical conversion efficiency limit of 29.4% for crystalline Si (*c*-Si) solar cells [4, 5]. In the following they are called *passivating contacts* in short.

In order to contribute to cost reduction of passivating contacts, both metallization and contact formation of such contacts have to be developed. Conventional printing media (pastes or inks) typically contain silver (Ag), which is the most expensive non-silicon material used in Si PV manufacturing [3]. Additionally, taking Si solar cells with passivating contacts into account, standard metallization schemes such as developed for state-of-the art cells, i.e., Aluminum Back Surface Field (Al-BSF) or Passivated Emitter and Rear Cells (PERC), cannot be adapted easily [6]. Specific process restrictions for back end processing coming along with passivating contacts require the development of novel back end techniques. This is the focus of the present work.

Due to the temperature sensitivity of SHJ structures exhibiting hydrogenated amorphous Si (a -Si:H) layers, low-temperature metallization (maximum temperatures in the range of 200°C) has to be applied. Up to now, this includes time-consuming thermal annealing accompanied by large and cost-intensive devices in order to keep an adequate throughput [7]. Furthermore, low-temperature-compatible printing media have to be utilized for metallization that lead to lower Ag consumption and ohmic losses compared to state-of-the art metallization. In this work, a very fast alternative annealing process for solar cells based on intense pulsed light (IPL) is developed offering a large process time and footprint saving potential, which is reflected in reduced cost of ownership. For an in-situ measurement of substrate temperature, which is known to be a critical parameter for solar cell performance, a high-speed measurement setup has to be developed. To additionally reduce the amount of Ag consumed by metal deposition, drop-on-demand inkjet printing of Ag nanoparticle ink is utilized. To improve printing stability and cell performance, a novel printing technique called *FlexTrail* printing is co-invented by the present author. Both inkjet and FlexTrail printing have the potential for a significant reduction of Ag consumption and cell performance gain compared to state-of-the-art screen printing.

For the purpose of decreasing resistive losses of low-temperature metallization, one cannot avoid increasing annealing temperature. This requires the use of less temperature-sensitive structures such as *poly*-Si-based tunnel oxide passivating contacts (TOPCon). These enable back end process temperatures comparable to

those occurring during state-of-the-art contact formation of, e.g., Al-BSF cells or PERC. Nevertheless, utilizing standard high-temperature metallization causes recombination losses in such contacts so that their full potential cannot be exploited [8]. Therefore, this work follows a *mid-temperature* metallization approach, which means that low-temperature metallization is combined with a thermal annealing step with process temperatures significantly above 200°C and, simultaneously, well below typical firing temperatures of 700-800°C. This avoids metal-induced depassivation of the contacts. Besides a significant resistivity reduction, choosing higher annealing temperatures also allows for the reduction of process time compared to standard low-temperature processing.

1.2 Thesis outline

Industry-related metallization approaches for Si solar cells with passivating contacts are investigated, in particular for *a*-Si:H- and *poly*-Si-based structures. All investigated metallization techniques make use of printed metal electrodes applied to substrates covered by indium tin oxide (ITO) layers. Both printing and contact formation processing are addressed, whereas Ag reduction and process time reduction are steadily considered.

Chapter 2 provides the theoretical background for Si solar cells in general and for passivating contacts in particular. The focus is set on the working principle of the *c*-Si/*a*-Si:H heterojunction and *poly*-Si-based contacts.

Chapter 3 is concerned with fundamentals of contact formation. Sintering of metal particles and the electrical nature of metal-semiconductor interfaces is presented. Furthermore, the chapter provides an overview of printing and contact formation techniques being relevant in this work against the background of passivating contacts. Thereby, the focus is set on low-temperature-compatible processing (maximum temperatures of about 200°C).

Chapter 4 presents key characterization techniques utilized in this work. Moreover, an innovative high-speed measurement setup is introduced that is utilized for measuring the sample temperature in-situ during intense pulsed light processing. Additionally, special features of the electrical characterization of

low-temperature metal contacts on top of conductive layers, such as TCO, are discussed. Based on simulations, strategies to avoid systematic errors linked to such particular structures are elaborated.

Chapter 5 provides three approaches to print metal contacts with reduced silver consumption on SHJ solar cells. These are the partial substitution of silver by copper in screen printing pastes and the reduction of the printed medium's laydown utilizing drop-on-demand inkjet printing. Furthermore, to improve printing process stability and cell performance, FlexTrail printing is introduced as a novel printing technique.

Chapter 6 focusses on the understanding of contact formation on passivating contacts. To this end, thermal annealing at low and medium temperatures, ultrasound-assisted thermal annealing, and IPL processing is investigated in detail. Comprehensive studies, e.g., of the sample-temperature-dependent passivation quality and the metal electrodes' microstructure, allow for an academic understanding of such processes. Furthermore, they enable an evaluation of their applicability on SHJ and *poly*-Si-based structures. From a technological point of view, this allows a full process development of IPL for SHJ structures. It is then extended on *poly*-Si-based passivating contacts and compared to mid-temperature thermal annealing (maximum temperatures of 350°C).

Chapter 7 provides the application of elaborated contact formation techniques on Si solar cells with passivating contacts. Entirely IPL-processed full-size SHJ cells are presented. Chances and challenges of IPL processing are discussed. Additionally, thermally annealed *poly*-Si-based solar cells are compared to their IPL-processed equivalents. It is demonstrated that both contact formation techniques are applicable on such cells.

Chapter 8 summarizes this work's findings.

Chapter 9 discusses perspectives of the developed metallization and contact formation approaches.

2 Fundamentals of silicon solar cells

In this chapter, basics for the understanding of silicon solar cell operation are provided, mainly resting upon Ref. [9, 10]. Furthermore, passivating and charge-carrier-selective contacts, namely the c-Si/a-Si:H heterojunction and poly-Si-based contacts are introduced. Thereto, appropriate literature is provided in the corresponding sections.

2.1 Semiconductor physics

2.1.1 Semiconductors

The direct conversion of light into electrical energy requires semiconductor materials. These are to be distinguished from other solids such as metals and insulators. This distinction is physically drawn by the rate of occupied electron states in the valence and conduction band as well as the band gap E_g existing between these two. The underlying concept is the quantum-mechanical band model, which describes the possible energy states of electrons in solids, taking into consideration positive atomic cores which form a periodically-repeating lattice. The wave function $\psi(\mathbf{r})$ of an electron in such a periodic potential is a solution of the time-invariant Schrödinger equation, referred to as *Bloch wave*, and has the form

$$\psi(\mathbf{r}) = u(\mathbf{r}) \cdot e^{i\mathbf{k}\mathbf{r}}, \quad (2-1)$$

where \mathbf{r} is the position vector, \mathbf{k} is the wave vector and $u(\mathbf{r})$ includes information about the periodic potential [11]. Based on Bloch waves, the probability density of electrons within the periodic lattice potential can be calculated. Instead of discrete energy states as in the case of isolated atoms (not surrounded by a periodic lattice potential), it turns out that the allowed energy states of electrons cover broad ranges. These are called *energy bands*. The gaps between them,

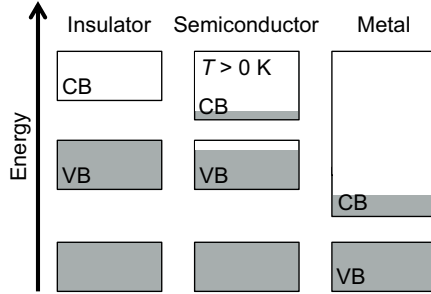


Figure 2-1 Schematic drawing of band configurations of different solids, taken from Ref. [12]. The focus is set on the valence and conduction band.

where the electron probability is zero, decrease when the electron’s distance from the atomic core increases. The highest band in terms of energy, which is entirely occupied by electrons, is called the *valence band* (VB). The next-higher energy band is called the *conduction band* (CB).

In Figure 2-1, band configurations of a metal, a semiconductor, and an insulator are drawn schematically. The metal’s CB is partially occupied by electrons. In contrast to electrons energetically located in the VB, these electrons have a non-vanishing mobility μ_n and, thus, contribute to the electrical conductivity of metals. In insulators, the CB is empty and E_g is so large that electrons are prohibited from moving to higher energy states in the CB. Therefore, the conductivity of insulators is close to zero. In the case of semiconductors, the CB is almost empty as well, even at a temperature T of 0 K. But electrons are able to overcome E_g , which is smaller as in the case of insulators. This can be achieved by thermal effects in case that $T > 0$ K and/or absorption of photons. As electrons reach the CB, they contribute to the electrical conductivity of the semiconductor. This is similar to metals. Electrons moving from the VB into the CB leave unoccupied states in the VB behind, which also have a non-zero mobility μ_p . Such states, usually, are treated as positively polarized charge carriers and are called *holes*. They also contribute to the electrical conductivity σ of a semiconductor, which is described by the equation

$$\sigma = q(n\mu_n + p\mu_p). \quad (2-2)$$

2.1 Semiconductor physics

Here, q is the elementary charge. n and p are the densities of electrons in the CB and holes in the VB, respectively. Mobilities depend on temperature and the degree of doping of the semiconductor. Doping is introduced in section 2.1.2. The electron and hole densities are calculated by the equations

$$n = \int_{E_c}^{\infty} D(E)f(E)dE, \quad (2-3)$$

$$p = \int_{-\infty}^{E_v} D(E)[1 - f(E)]dE, \quad (2-4)$$

where E is the energy, $D(E)$ is the energy-dependent density of charge carrier states and $f(E)$ is the probability distribution of electrons among the states. Furthermore, E_c is the CB's lower edge and E_v is the upper edge of the VB. By using the Fermi distribution

$$f(E) = \frac{1}{e^{\frac{E-E_F}{k_B T}} + 1}, \quad (2-5)$$

where k_B is the Boltzmann constant and E_F the Fermi energy, n and p can thus be determined as follows:

$$n = N_c e^{-\frac{E_c - E_F}{k_B T}}, \quad (2-6)$$

$$p = N_v e^{-\frac{E_F - E_v}{k_B T}}. \quad (2-7)$$

Thereby, N_c and N_v are the effective densities of states in the CB and VB, respectively. The product of n and p is called the intrinsic density n_i . It is expressed as

$$n_i^2 = n \cdot p. \quad (2-8)$$

In the case of a non-doped, so-called *intrinsic* semiconductor, $n = p$ holds. Using this together with the equations (2-6) and (2-7), E_F , which is also called *Fermi level*, can be determined to

$$E_F = \frac{1}{2}(E_v + E_c) + \frac{1}{2}k_B T \ln \frac{N_v}{N_c}. \quad (2-9)$$

In the case of silicon, it is located 0.023 eV above the center of the bandgap, assuming $m_n^* = 1.09 m_0$ and $m_p^* = 1.15 m_0$ for the effective masses of electrons and holes, respectively, using the electron rest mass m_0 . The Fermi level, especially its splitting for electrons and holes in the illuminated case, plays a crucial role for the understanding of solar cells as described in section 2.1.4.

2.1.2 Doping

One can achieve an increase of a semiconductor's conductivity by specific use of impurity atoms, which is typically understood as *doping*. *Donors* are such impurities which have one valence electron more than required for chemical bonding to the neighbor atoms in the crystal lattice. The additional electron is weakly bound to the impurity atom by Coulomb force only. It features an amount of energy, which is only slightly lower than E_c . Therefore, far less energy compared to E_g is needed to lift the electron from such an energy state into the CB than from E_v . Examples for donors in the case of Si are Phosphorus (P) and Arsenic (As).

Acceptors, in contrast, have one valence electron less than required for the chemical bonding to the neighbor atoms in the crystal lattice. An electron replacing the missing valence electron is not as strongly bound as the other valence electrons because the Coulomb force is missing in this case. Its energy is only slightly higher than E_v because the valence bond is strong compared to the missing Coulomb force. This means that electrons of the VB can easily reach such acceptor states. In other words, holes are only weakly bound to acceptors and can easily be transferred to the valence band. Typical acceptors in the case of Si are Boron (B) or Indium (In).

Shallow doping means that donors and acceptors are almost completely ionized at room temperature. n and p can be reasonably assumed as equal to the density of donors n_D and acceptors n_A , respectively.

2.1.3 Generation and recombination

The density of charge carriers increases in a semiconductor if they are generated at a rate G and it decreases if charge carriers recombine at a rate R or if there is a current density j of charge carriers out of the considered volume. In the case of electrons, this is expressed by the continuity equation as follows:

$$\frac{\partial n}{\partial t} = G(\mathbf{r}) - R(\mathbf{r}) - \text{div } j(\mathbf{r}). \quad (2-10)$$

In the dark, pairs of electrons and holes are generated in semiconductors as a consequence of thermal effects. A thermal equilibrium, expressed by $G = R$, is established if j is zero. Under illumination, electron-hole pairs can be generated by absorption of photons in addition, which carry a minimal energy $h \cdot \nu$ that is equal to E_g . Here, h is the Planck constant and ν is the frequency corresponding to the photon. Under such illumination, electrons are lifted to energy states in the CB and excess charge carriers are generated, expressed by the excess charge carrier densities Δn and Δp for electrons and holes, respectively. This is valid at least for direct semiconductors. In the case of indirect semiconductors, additionally, an impulse gap between valence and conduction band needs to be overcome by means of quantified vibrations of the lattice, which are called *phonons*. For radiation with $h \cdot \nu < E_g$, a semiconductor is transparent and G induced by photons is zero. If $h \cdot \nu > E_g$, the excess energy of generated electrons ($G > 0$) in the CB is emitted in form of phonons, which is also called *thermalization*. This is a very fast process and lasts for several 10^{-12} s only. When the charge carriers reach the lower edge of the CB due to thermalization, this state lasts for much longer, i.e., several 10^{-3} s, before they move back to the VB. This time delay is caused by the absence of possible energy states in the band gap prohibiting faster recombination. As will be discussed further below in this section, this is valid in an ideal case only. During their so-called *lifetime* in the CB, electrons

contribute to the conductivity of the semiconductor. Concerning the example of electrons, the effective lifetime τ_{eff} can be written as

$$\tau_{\text{eff}} = \frac{\Delta n}{R}. \quad (2-11)$$

The higher the recombination rate, the lower is the lifetime. There are several recombination mechanisms contributing to τ_{eff} , which are briefly introduced in the following.

Radiative recombination is the inverse process to electron-hole pair generation when a photon is absorbed. In this case, an electron moves from the CB to a free energy state in the VB (i.e., a hole) and emits the corresponding energy amount by means of a photon. Radiative recombination increases linearly with the concentration of electrons and holes. Nevertheless, it plays a subordinate role in terms of charge carrier lifetime, especially in the case of indirect semiconductors such as silicon, compared to the other recombination mechanisms.

This is different for *Auger recombination*. In this case, an electron or a hole dissipates energy, which is released by the reaction of another electron with a hole. Such a process can be understood as an inverse process to collision ionization. The dissipated kinetic energy is transferred to the lattice (thermalization). Auger recombination of electrons and holes increases with the square of n and p , respectively, which means that it becomes relevant especially in the case of heavy doping. Therefore, it is relevant in silicon solar cells.

Typically, the charge carrier lifetime in semiconductors is mainly limited by impurities or defects in the crystal lattice. Other than in the case of shallow doping, where the additional energy states are located in the vicinity of the band gap, other impurity atoms may cause trap states deep in the band gap. These states can be occupied, e.g., by electrons of the CB. From there, they can recombine with holes in the VB. This significantly reduces their lifetime in the CB because E_g can be overcome stepwise, which significantly increases recombination probability. This process is assumed to be a two-step process and, consequently, trap states in the middle of the band gap rather contribute to this kind of recombination. The theory of this mechanism is developed by

2.1 Semiconductor physics

Shockley, Read, and Hall [13]. According to their initial letters, it is called *SRH recombination*. In order to avoid this sort of recombination, high purity of the semiconductor material is to be ensured.

Many defect states or impurity atoms adsorbed by the lattice can be found at the semiconductor's surface. The energies of such states is distributed throughout the whole bandgap. In principal, the *surface recombination* can be explained by SRH recombination. Strategies to avoid this kind of recombination, namely the use of passivating contacts, are discussed in section 2.2.

The effective lifetime τ_{eff} is dependent on all of the mentioned mechanisms. For symmetrically passivated samples with a spatially uniform distribution of charge carriers the following definition of τ_{eff} is valid:

$$\frac{1}{\tau_{\text{eff}}} = \frac{1}{\tau_{\text{b,SRH}}} + \frac{1}{\tau_{\text{rad}}} + \frac{1}{\tau_{\text{Auger}}} + \frac{2 \cdot S_{\text{eff}}}{d_{\text{wafer}}}, \quad (2-12)$$

where $\tau_{\text{b,SRH}}$ is the Shockley-Read-Hall charge carrier lifetime in the bulk, τ_{rad} the radiative lifetime, τ_{Auger} the Auger lifetime, S_{eff} the effective surface recombination velocity, and d_{wafer} the thickness of the semiconductor material.

2.1.4 Basic solar cell operation

Under illumination, $G > R$ is valid in a semiconductor and, consequently, the electron and hole concentration is greater than in the dark. This means that $n \cdot p > n_i^2$. As a consequence, the Fermi level splits for electrons and holes. On the one hand, the Fermi level of electrons with the Fermi energy $E_{\text{F,c}}$ approaches the lower edge of the conduction band. The Fermi level of holes, on the other hand, with the Fermi energy $E_{\text{F,v}}$ approaches the upper edge of the valence band. According to this, under illumination n and p is to be expressed as follows:

$$n = N_{\text{c}} e^{-\frac{E_{\text{c}} - E_{\text{F,c}}}{k_{\text{B}} T}}, \quad (2-13)$$

$$p = N_{\text{v}} e^{-\frac{E_{\text{F,v}} - E_{\text{v}}}{k_{\text{B}} T}}. \quad (2-14)$$

The Fermi energies can be identified as the electrochemical potentials η_n and η_p of the charge carriers:

$$\eta_n = E_{F,c}, \quad (2-15)$$

$$\eta_p = -E_{F,v}. \quad (2-16)$$

In other words, in a semiconductor incident radiation is converted into electrochemical energy, which is the sum of η_n and η_p . In order to operate an electrical load, a solar cell needs to provide electrical energy. Understanding the transformation from electrochemical into electrical energy in a solar cell requires a closer look at charge currents, which is provided in the following paragraphs.

The relevant forces acting on charge carriers in solar cells are the gradients of their chemical potentials and the electrical potential ϕ . The former induces a so-called *diffusion current* and the latter a *drift current*. Both forces can be summarized by the gradient of the electrochemical potential inducing a net electron and hole current density j_n and j_p , respectively. The corresponding equations in one dimension are as follows:

$$j_n = +qD_n \frac{\partial n}{\partial x} - q\mu_n n \frac{\partial \phi}{\partial x} = \mu_n n \frac{\partial \eta_n}{\partial x}, \quad (2-17)$$

$$j_p = -qD_p \frac{\partial p}{\partial x} - q\mu_p p \frac{\partial \phi}{\partial x} = \mu_p p \frac{\partial \eta_p}{\partial x}. \quad (2-18)$$

Thereby, diffusion parameters for electrons and holes D_n and D_p are introduced, respectively. In a semiconductor, the total net current density is the sum of j_n and j_p .

A device sufficient to convert radiative into electrochemical energy and then into electrical energy, needs to induce a directed current of charge carriers so that a voltage between two terminals is established. For this purpose, according to the equations (2-17) and (2-18), a gradient of the electrochemical potential between the two terminals is required under illumination. An example for an inadequate structure is provided in Figure 2-2 (a). The band diagram of a *n*-type semiconductor under illumination and open-circuit conditions is depicted. The

2.1 Semiconductor physics

Fermi levels for electrons and holes are splitted due to illumination. At the terminals on the left and the right side, a large surface recombination is assumed and, therefore, the Fermi energies of electrons and holes join there. In practice, the terminals are realized by metal contacts applied to the cell. The difference of the Fermi energies of the left ($E_{F,l}$) and the right ($E_{F,r}$) terminal (or the difference of the electrochemical potentials, which is the same) of this device is zero, which means that the net charge current of electrons and holes between the terminals is zero and no voltage is produced. At both terminals, the hole current to the terminals is completely compensated by the electron current. Despite the gradient of $E_{F,v}$ is much greater than the gradient of $E_{F,c}$, the currents of electrons and holes are compensated because μ_n is greater than μ_p in the n -type semiconductor.

In order to generate a voltage between the terminals and to provide electrical energy, the Fermi levels are to be pinned close to the conduction band at one terminal and close to the valence band at the other terminal. This can be achieved by using a pn junction, as it is depicted in an open-circuit state and under illumination in Figure 2-2 (b). The difference of the Fermi energies on the left and the right terminal results in the open-circuit voltage V_{OC} of the device, which is

$$V_{OC} = \frac{1}{q} \int_{left}^{right} \frac{\partial E_{F,c}}{\partial x} dx = -\frac{1}{q} \int_{left}^{right} \frac{\partial E_{F,v}}{\partial x} dx. \quad (2-19)$$

In general, this is not the same as $E_{F,c} - E_{F,v}$, i.e., the difference of the Fermi levels in the device away from the terminals divided by the unit charge. The latter expression leads to the definition of the implied open-circuit voltage iV_{OC} . It is the maximum open-circuit voltage, which can be realized by a certain device. It is defined as follows:

$$iV_{OC} = (E_{F,c} - E_{F,v})/q. \quad (2-20)$$

Passivating contacts can reach voltages close to iV_{OC} , as will be discussed in section 2.2.

2 Fundamentals of silicon solar cells

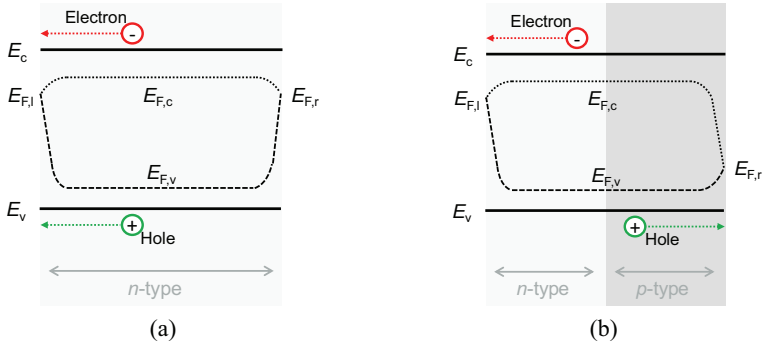


Figure 2-2 Band diagram of a *n*-type semiconductor under illumination and open-circuit conditions in (a). In (b), the band diagram of a *pn* junction under illumination and open-circuit conditions is displayed. Images are redrawn from Ref. [9].

A *pn* junction as depicted in Figure 2-2 (b) is the essential part of a solar cell because it enables the utilization of electrical energy. To describe its current density-voltage (j - V) characteristics, in principal, it can be assumed as a diode with a shallow emitter and a comparatively thick base/absorber, which is doped opposite to the emitter. (In the case of Si PV, a wafer is the base material.) The simplest description of its j - V characteristics is the equation of an ideal diode

$$j = j_0 \left(e^{\frac{qV}{k_B T}} - 1 \right) - j_{ph} \quad (2-21)$$

with the saturation current density j_0 and the photo-generated current density j_{ph} . The latter current density is negative by definition because it is orientated in reverse direction so that the solar cell is charged in forward direction ($V > 0$). Both, the j - V characteristics in the dark and the illuminated case are depicted in Figure 2-3. In the short-circuit state, when $V = 0$, the short-circuit current density j_{sc} is

$$j_{sc} = -j_{ph}. \quad (2-22)$$

This parameter reflects how efficiently an illuminated semiconductor converts incident photons into charge carriers. It is limited by the incident radiative spectrum and E_g . The maximum j_{sc} of silicon solar cells is determined to be 43.3 mA/cm² [5].

2.1 Semiconductor physics

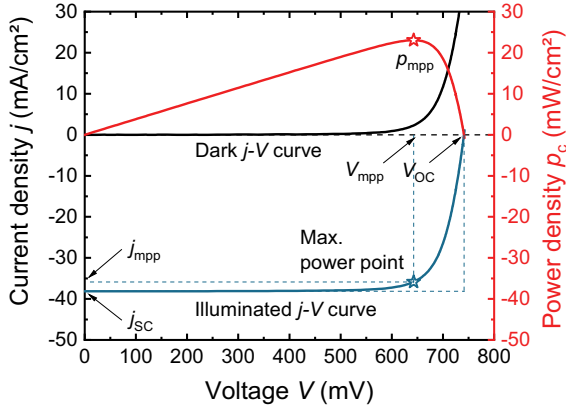


Figure 2-3 Dark (black) and illuminated (blue) j - V curve and power density p_c (red) are depicted.

Furthermore, from equation (2-21), a simple expression for the open-circuit voltage V_{OC} can be derived which is the device's voltage in case that $j = 0$:

$$V_{OC} = \frac{k_B T}{q} \ln \left(\frac{j_{ph}}{j_0} + 1 \right) \approx \frac{k_B T}{q} \ln \left(\frac{j_{ph}}{j_0} \right), \text{ for } j_{ph} \gg j_0. \quad (2-23)$$

In order to achieve a high V_{OC} , it is necessary that j_0 is very small. In other words, the recombination in the cell is to be minimized so that its voltage maximizes.

Even V_{OC} and j_{sc} are important parameters to describe solar cells, both $j = 0$ and $V = 0$, are no relevant cases for practical solar cell operation. In practice, one aims for the maximum power density p_{mpp} , which is reached at the maximum power point (see Figure 2-3), where the voltage and the current density is V_{mpp} and j_{mpp} , respectively.

These parameters lead to another important cell parameter, namely the fill factor FF . It is calculated as follows:

$$FF = \frac{V_{mpp} j_{mpp}}{V_{OC} j_{sc}}. \quad (2-24)$$

2 Fundamentals of silicon solar cells

It is a measure for the *squareness* of a j - V curve. The shape of the j - V curve and, therefore, the value of FF is determined by the series resistance R_s , the shunt resistance R_p , and also recombination losses.

An ideal fill factor FF_0 , which is free from ohmic and recombination losses in the space-charge region, can be calculated by the equation

$$FF_0 = \frac{V_{OC} - \ln(v_{OC} + 0.72)}{v_{OC} + 1} \quad (2-25)$$

with a normalized voltage $v_{OC} = V_{OC} / \left(\frac{n_x k_B T}{q} \right)$, where n_x is an ideality factor with a value close to one [14].

Another important variety of the fill factor is the pseudo fill factor pFF , which can be obtained experimentally, e.g., by means of the *Suns* V_{OC} method. Detailed information can be found in Ref. [15]. The pFF is free of series resistance losses but not free of recombination losses. Together with the FF it allows to determine the series resistance losses in the cell.

The most prominent solar cell parameter is the conversion efficiency η , which is calculated as follows

$$\eta = \frac{V_{OC} j_{SC} FF}{P_{in}} = \frac{P_{out}}{P_{in}}, \quad (2-26)$$

where P_{out} and P_{in} is the output and the input power of the device, respectively.

As described above, the one-diode-model is a simple but powerful tool to describe a solar cell's j - V characteristics. However, to draw a more holistic picture of a solar cell, which means to pay respect to its recombination in the space charge region (j_{02}), the shunt resistance (R_p), and its series resistance R_s , one has to switch to the two-diode model:

$$j = j_{01} \left(e^{\frac{q(V-jR_s)}{n_1 k_B T}} - 1 \right) + j_{02} \left(e^{\frac{q(V-jR_s)}{n_2 k_B T}} - 1 \right) + \frac{V - jR_s}{R_p} - j_{sc}. \quad (2-27)$$

Here, j_{01} is the saturation current density. n_1 and n_2 are the so-called *ideality factors*, which can be assumed to be equal to one and two, respectively.

2.2 Silicon solar cells with passivating and carrier-selective contacts

State-of-the-art homojunction solar cells such as Al-BSF cells and PERC are limited in terms of their efficiency because they exhibit recombination-active direct metal/silicon contacts [4]. At these interfaces, numerous electrically active states in the silicon bandgap exist, causing surface recombination that limits the overall device performance. The ongoing development towards thinner wafers even increases the significance of surface recombination [16]. There are two principally different approaches, which are often utilized together, to address this issue: the reduction of surface states and the reduction of free charge carriers at the surface [16]. The former is often referred to as *chemical passivation* scheme, which seeks to saturate dangling bonds, e.g., by means of hydrogen. The latter can be obtained by means of a built-in field, repelling charge carriers of a distinct polarity to move to the surface. Technologically, such a *field-effect passivation* can be realized, e.g., by an appropriate doping profile below the silicon surface or as a consequence of electrical charges in an overlying insulator. Typically, both methods are combined in order to achieve high cell performance. Nevertheless, industrial Al-BSF and PERC cells are limited in terms of their conversion efficiency in the range of 20% and 23-24%, respectively [3, 17].

To further reduce surface recombination and to approach the theoretical efficiency limit of 29.4% for Si solar cells, passivating contacts are developed [5]. A general review of this topic is provided in Ref. [4]. Passivating contacts make use of passivating thin films between the metal electrodes and the Si base. In addition to preventing direct contact of metal electrodes and Si, they ensure pronounced charge carrier selectivity (i.e., minority carrier mirror) and sufficient conductivity for majority carriers at the same time [18]. As a consequence, the density of minority carriers at the contacts is low, which results in very little recombination. This work makes use of two different kinds of passivating and

charge-carrier-selective contacts, namely the *c-Si/a-Si:H* heterojunction, referred to as SHJ in this work, and a *poly-Si*-based approach, namely tunnel oxide passivating contacts (TOPCon). These are the objectives of the following sections 2.2.1 and 2.2.2, respectively.

2.2.1 The *c-Si/a-Si:H* heterojunction

SHJ contacts have first been successfully applied to solar cells by *Sanyo/Panasonic* in the nineties [19]. Such devices are of great interest even to this day because of their high efficiency potential as well as the lean production process. Furthermore, only low-temperature ($T \leq 200^\circ\text{C}$) process steps are required during fabrication. A review of such contacts is provided in Ref. [20]. Varying device architectures basing on the SHJ are discussed in Ref. [21].

A both-sides-contacted (BSC) and bifacial structure with a rear emitter is depicted in Figure 2-4 (a). It is based on an alkaline textured *n*-type *c-Si* absorber. High efficiencies can be reached also by the use of *p*-type material [23]. Yet, *n*-type material with its lower sensitivity towards impurities and higher minority charge carrier lifetime potential is typically used to exploit the full performance of SHJ-based passivating contacts. Both sides of the absorber are covered by 10-20 nm thin stacks of non-doped and doped hydrogenated

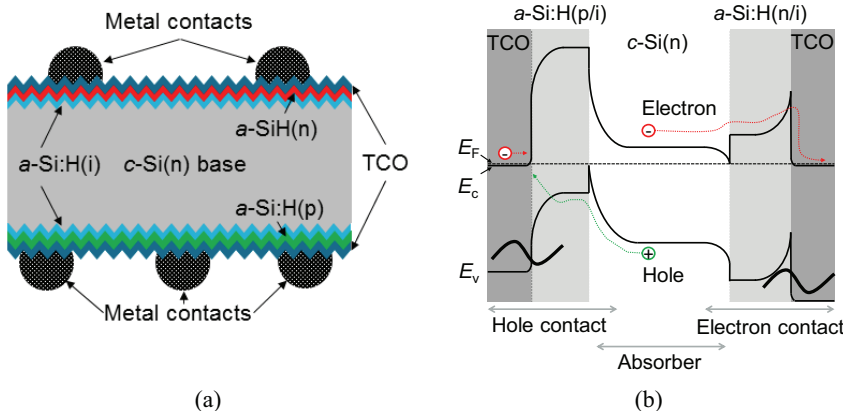


Figure 2-4 Schematic drawing of a both-sides-contacted bifacial silicon heterojunction solar cell structure, which is utilized in this work (a). In (b), the corresponding band structure in the dark is presented, redrawn from Ref. [22].

amorphous Si layers (a -Si:H(i) and a -Si:H(p) or a -Si:H(n), respectively) forming the hole- and electron-collecting contacts. The layers are deposited by means of plasma-enhanced chemical vapor deposition (PECVD). Doping is typically performed in-situ. The intrinsic layers featuring low defect density ensure chemical passivation of the c -Si/ a -Si:H interface. They need to be thick enough to guarantee passivation and thin enough in order to ensure current transport from the absorber into the doped a -Si:H layers. The latter layers are required in order to form the c -Si/ a -Si:H heterojunction, which is responsible for the SHJ's strong charge carrier selectivity. Furthermore, they transport charge carriers towards adjacent transparent conductive oxide (TCO) layers. A high hydrogen content in the layer stack is known to improve passivation quality [24]. Hydrogen effuses at temperatures significantly above 200°C. Therefore, such contacts are known as temperature-sensitive [25]. Typically, 100 nm thick indium tin oxide (ITO) layers are used as TCO layers, which are applied by means of physical vapor deposition, also known as *sputtering*. These layers ensure lateral charge carrier transport to the metal contacts. Moreover, they act as anti-reflection coatings (ARC). Sputtering of TCO layers leads to damage in the a -Si:H layers, which can be cured by means of a thermal treatment subsequently, referred to as *annealing* [26]. Typically, before annealing, metal contacts are formed, e.g., by means of a printing step (see section 3.2) on both sides of the device.

A schematic drawing of a SHJ band diagram (dark state, open-circuit condition) is depicted in Figure 2-4 (b). At this point, it has to be noted that the abundance of defect states in the a -Si:H layers are responsible for less effective doping compared to c -Si. Therefore, the Fermi levels remain further away from the corresponding majority carrying band edges. The different band gaps E_g and work functions ξ of c -Si ($E_g = 1.1$ eV, $\xi = 4.1$ eV) and a -Si ($E_g = 1.7$ eV, $\xi = 3.9$ eV) are responsible for the hetero gaps at the c -Si/ a -Si:H interfaces. They enhance carrier selectivity of such devices by acting as mirrors for electrons in the direction of the hole contact and vice versa. However, there are potential barriers for electrons moving into the electron contact and holes moving into the hole contact caused by band bending in the c -Si absorber and lower doping efficiency in the a -Si:H layers. According to literature, it is

improbable that these barriers are overcome by direct tunneling but rather by means of thermal transport [4, 27]. Potential barriers also occur at the a -Si:H/TCO interfaces. Typical TCO layers can be described as highly/degenerately doped high-bandgap n -type semiconductors [28]. They exhibit much higher charge carrier densities compared to the a -Si:H stacks, which induce strong band bending in the electron and hole contacts. Because of the metal-like nature of the TCO layers, the TCO/ a -Si:H contacts can be approximated as Schottky contacts, which are discussed in section 3.1.2. The interplay of a -Si:H and TCO layers and working conditions for the whole device derived from that are analyzed in detail in Ref. [29]. Besides the Schottky barriers, there are also hetero barriers at the TCO/ a -Si:H contact interfaces. This is not an issue at the electron contact. However, the valence band offset at the TCO/ a -Si:H(p) contact requires band-to-band tunneling [30].

The schematic cross-section of a SHJ solar cell depicted in Figure 2-4 (a) exhibits a rear emitter. Rear emitters allow for the use of less conductive and more transparent TCO layers on the front due to the combined lateral conductivity of TCO and bulk [31]. Furthermore, emitter optimization such as layer thickening or higher doping can be performed on the rear more extensively without reducing device performance [32]. Such devices enable efficiencies up to 25.1% and especially benefit from very high V_{OC} [33]. A main shortcoming of this structure is the parasitic absorption in the a -Si:H and TCO layers [34]. This is addressed, e.g., by the more complex interdigitated back contact (IBC) design, which holds the record efficiency of 26.7% for Si-based solar cells [35]. Other approaches keep the BSC structure and reduce parasitic absorption by diluting the a -Si:H layers with carbon or oxygen [36, 37]. Moreover, the doped a -Si:H layers are replaced by micro- or nanocrystalline silicon. The latter also improves the contact to the TCO layer [38]. Work is conducted on novel TCO layers as well providing both higher conductivity and transparency compared to ITO, such as zirconium-doped indium oxide [39].

Nevertheless, back end processing of SHJ cells is challenging because of the temperature sensitivity of a -Si:H layers, especially when it comes to industry-related processes [7]. However, metallization has improved over the years and lately, an efficiency of 24.6% of a full-size SHJ solar cell exhibiting state-of-

the-art screen-printed metallization is announced [40]. Chances and challenges for metallization of SHJ cells are discussed in the following of this work, for example, in chapter 3.

2.2.2 Tunnel oxide passivating contacts

Passivating contacts based on polycrystalline silicon offer not only higher doping efficiency compared to the *c*-Si/*a*-Si:H heterojunction but also higher temperature tolerance. A detailed review on this topic is provided in Ref. [41, 42]. The technology of *poly*-Si emitters and semi-insulating *poly*-Si is originally developed for bipolar junction transistors. A review on such devices is given in Ref. [43]. Based on these approaches, tunnel oxide passivating contacts (TOPCon) are developed [44]. Recently, an efficiency of up to 26.0% is achieved by means of TOPCon applied on the rear side of a *p*-type both-sides-contacted cell [45]. Such cells exhibit diffused emitters on the front side. Therefore, their architecture is called *hybrid*. Very high efficiencies are also achieved using hybrid *n*-type cells [46]. Using a *p*-type IBC architecture, a cell holds the record efficiency for *poly*-Si-based solar cells which is 26.1% [45, 47].

A monofacial BSC cell architecture exhibiting TOPCon on both sides, which is

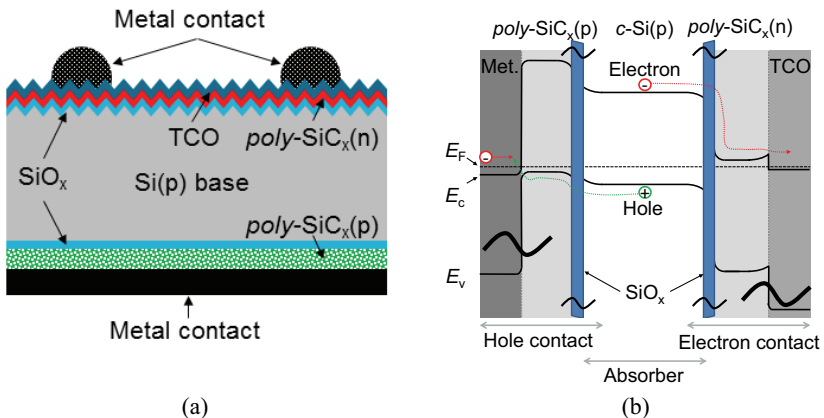


Figure 2-5 Schematic drawing of a both-sides-contacted monofacial solar cell structure featuring TOPCon layer systems on both sides, which is utilized in this work in (a). In (b), the corresponding band structure in the dark and under open-circuit conditions is presented, redrawn from Ref. [18].

utilized in this work, is sketched in Figure 2-5 (a). Similar structures are also investigated in Ref. [48–50]. This architecture has the advantage of high V_{OC} potential because a homojunction is avoided. In order to minimize j_{SC} losses, especially the front TOPCon layer system needs to be thin. A p -type absorber is sandwiched between p - (rear) and n -type (front) TOPCon layers. On the front, TOPCon consists of a thin (15 nm) and highly doped $poly\text{-SiC}_x$ (carbonized $poly\text{-Si}$) layer and an ultra-thin (1-2 nm) silicon oxide (SiO_x) in this case. The $poly\text{-SiC}_x$ layer can be fabricated by means of PECVD or low-pressure chemical vapor deposition (LPCVD) of $a\text{-Si}$, which is subsequently crystallized by means of high-temperature annealing (800°C-1050°C). It is shown that hydrogenation improves the passivation quality of such layers [51]. The alloy of these layers with carbon is optional. Adding carbon tunes the bandgap of the material and its morphology resulting in a heterojunction at the $c\text{-Si}/\text{SiO}_x/poly\text{-SiC}_x$ contact, as displayed in Figure 2-5 (b). (Please note that non-carbonized $poly\text{-Si}$ forms a heterojunction with $c\text{-Si}$, too.) Furthermore, blistering of the layers during annealing is less pronounced when carbon is added to the matrix [18].

Doping of these layers can either be performed in- or ex-situ. During high-temperature annealing, dopants diffuse partially into the $c\text{-Si}$ absorber. This results in a shallow doping profile, repelling charge carriers and, hence, increasing passivation quality. Obviously, this diffusion process is to be tuned in order to avoid increasing Auger recombination [52]. High doping of the $poly\text{-SiC}_x$ layers increases the passivation quality of the contact. The reason is stronger band bending in the absorber material, as shown for the SHJ in Ref. [53].

The SiO_x layer is generated before fabrication of the $poly\text{-Si}$ -based layers, e.g., thermally, wet-chemically or by means of UV/ O_3 (ultraviolet/ozone) growth [54, 55]. It is used to passivate the $c\text{-Si}$ surface [56]. Furthermore, it acts as a semi-permeable membrane for charge carriers. Electrons pass into the electron-collecting contact whereas holes are repelled and vice versa at the hole-collecting contact. Together with the formation of a $c\text{-Si}/poly\text{-SiC}_x$ heterojunction, this ensures a high level of carrier-selectivity.

The current transport mechanism through SiO_x layers can be governed by quantum mechanical tunneling, local current paths in the oxide (pinhole model),

or a combination of both. The oxide tunneling model fits for *poly*-Si emitters having a thin wet-chemically-grown interfacial oxide [57]. Furthermore, this theory describes the temperature dependence of TOPCon structures [58]. However, amongst others, it fails to describe the experimental findings provided in Ref. [59]. Here, efficient *poly*-Si contacts featuring interfacial oxide layers, which are too thick to enable an efficient tunneling transport, are presented. Their findings, however, are sufficiently described by the pinhole model, which is solely based on current transport through local disruptions in the oxide [60]. In general, one can discriminate two extreme cases: tunneling is dominant for oxides thinner than 1.5 nm and pinhole transport in oxides thicker than 2 nm [52]. In practice, both transport paths can coexist.

The process route necessary to fabricate TOPCon solar cells is very similar to state-of-the-art PV processing. Therefore, it has the potential to be easily integrated into industrial production. This is shown, e.g., by taking the example of a bifacial *n*-type hybrid cell architecture [61]. It has the advantage of a highly transparent front side but, in contrast to the both-sides TOPCon architecture as sketched in Figure 2-5 (a), still features a homojunction limiting passivation quality. Furthermore, the high temperature tolerance of TOPCon allows for high-temperature firing-through metallization in combination with silicon nitride (SiN_x) or aluminum oxide (AlO_x) layers [51]. Unfortunately, fired metal contacts can damage even thick TOPCon layers [8, 62]. The metal pastes (see section 3.2.1) etch through the dielectric layers and consume parts of the *poly*-Si-based layer. Inverted pyramids are formed, which can penetrate such a layer. Therefore, the contact can be depassivated resulting in reduced cell performance. Using thick *poly*-Si layers curbs this issue. Yet, it is accompanied by higher parasitic absorption in these thick layers as well as longer deposition time.

Another approach to circumvent depassivation is the use of low-temperature metallization. Such metallization is free from inorganic binders (glass frit), which may deteriorate the TOPCon layer system (see section 3.2.1). Before low-temperature metallization, a TCO layer instead of a SiN_x or AlO_x layer has to be deposited for the purpose of lateral charge carrier transport and ARC on top of TOPCon. This is realized on the cell's front depicted in Figure 2-5 (a).

(On the rear, a full-area contact is realized, which could be replaced by a TCO/low-temperature metallization stack as well.) Indeed, sputtering of TCO damages the TOPCon layer. However, passivation can be restored by subsequent curing. Furthermore, hydrogenated TCO layers are reported to further improve passivation quality of TOPCon [63]. The low-temperature metallization on top of TOPCon can be annealed at significantly higher temperatures compared to SHJ cells in order to reduce ohmic losses of the metal electrodes. Yet, at temperatures significantly above 300°C, the TCO/TOPCon contact tends to degenerate, presumably due to interfacial oxides [64]. This is further discussed in section 6.3.6.

3 Printed metal contacts

This chapter deals with printed metal electrodes fabricated for silicon solar cells with passivating contacts. The aim is twofold: providing fundamental theory of contact formation and giving an overview over metallization techniques utilized in this work, which have the potential to be applied on industrial production. The former includes both the lateral electrical contact in the metal electrode and the electrical contact at the metal/semiconductor interface. The latter takes into account both metal application (printing) techniques and contact formation techniques (annealing). Thereby, the focus is set on low-temperature metallization schemes instead of high-temperature-processed/fired contacts.

3.1 Fundamentals of contact formation

3.1.1 Sintering of metal particles

As described in detail in section 3.2, printing media as utilized for the realization of metal contacts exhibit metal particles of micro- and/or nanosize and are embedded in an organic matrix. Using such small particles lowers the required annealing temperature down to 200°C and even below for the formation of a cohesive and electrically conductive structure of these particles. Thereby, the relevant process is sintering. Sintering is defined as joining of material (powder) at temperatures below the material's specific bulk melting temperature. A review over joining of Ag nanomaterials at low temperatures is provided in Ref. [65]. Melting of Ag takes place at $T = 961^\circ\text{C}$ [66]. However, the melting temperature decreases for sub-micrometer-sized particles compared to the corresponding bulk material, which is called *melting point depression* [67]. Although in general, sintering takes place without melting, melting point depression can contribute to a reduced sintering temperature [65].

Before annealing, micro- and/or nanoscale metal particles of printing media are coated by stabilizer shells. Typically, these are of organic nature and prohibit the particles from undesired spontaneous sintering with one another. Furthermore, they electrically isolate the metal particles from each other. In order to obtain electrical conductivity amongst the particles, the capping layers have to be removed, which can be achieved by temperature increase [68, 69]. The required minimum temperature is dependent on the specific stabilizer shell material. Once the bare metal particles are in direct contact with each other, the printed structure already exhibits (low) electrical conductivity. To further increase conductivity, the inter-particle contact has to be promoted by means of sintering. By definition, this is material transport driven by excess free energy due to broken bonds at the particles' surfaces, which is called *surface energy* [70]. Therefore, a prerequisite for sintering is that the sintering partners are in range of the atomic forces of their counterpart, requiring the removal of stabilizer shells from the particles. In a system of micro- and/or nanosized particles, the total amount of surface energy is very high because of the high surface-to-volume ratio of every particle. As a consequence, a high affinity of the particle system exists to reduce this free energy. Therefore, sintering necks are formed (*necking*) between adjacent particles, reducing the total surface area and the total surface energy of the system.

A back-driving force to this process is provided by grain boundary growth in the neck region where the particles are joined. The energy balance between necking and grain growth steers the final shape of the sintered particles [71]. To further evolve sintering and, consequently, densification of the whole structure, temperature has to be further increased. Please note that the necessary temperatures remain well below the melting temperature of the bulk material if the particles are small. The printed contacts, which are presented in this work, typically require temperatures in the range of 200°C.

By means of sintering, the electrical conductivity amongst metal particles significantly increases [72]. A sintering model relating densification and conductivity can be found in Ref. [71]. However, sintering of metal particles in printed metal contacts does not only include inter-particle contact formation. Metal particles also sinter with the surface layer of the substrate on which they

3.1 Fundamentals of contact formation

are applied. If this is a semiconductor, the resulting metal-semiconductor contact exhibits special electrical properties, which are described in the following section 3.1.2.

3.1.2 Metal/semiconductor contact

When metal is in direct contact with a semiconductor, an asymmetric electrical conduction between these two materials is observed [73]. William Schottky has explained this phenomenon by band bending at the contact interface leading to a barrier for charge carriers. In honor of his work, metal/semiconductor contacts are also called *Schottky contacts* [74, 75]. The theory has further been expanded by Bardeen, Cowley, and Sze [11, 76, 77]. Taking the example of a SHJ solar cell, Schottky contacts can occur at the *a*-Si:H(p or n)/TCO and at the TCO/metal contact interface (compare section 2.2.1). The lowest possible contact resistivity ρ_c at such contacts is desired in order to reduce series resistance losses of the device. ρ_c is defined as

$$\rho_c = \left(\frac{\partial j}{\partial V} \right)_{V \rightarrow 0}^{-1}. \quad (3-1)$$

The physical nature of Schottky contacts and the dependence of ρ_c from the

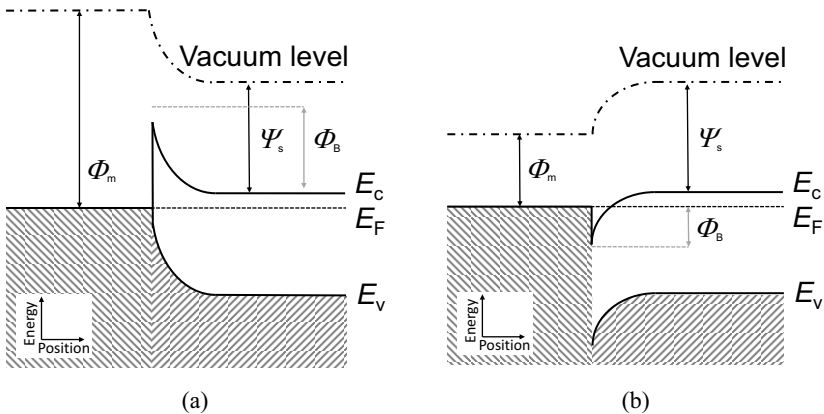


Figure 3-1 Band configuration of metal/semiconductor contacts with a high work function metal ($\phi_m > \psi_s$) (a) and a low work function metal ($\phi_m < \psi_s$) (b). The pictures are adapted from Ref. [78].

contact configuration is briefly introduced in the following.

The Fermi energies of metals and semiconductors being in direct contact are on the same level under steady-state conditions. Because of the lower charge carrier concentration in the semiconductor, its conduction and valence bands are bent to balance the difference between electron affinity Ψ_s of the semiconductor and work function of the metal ϕ_m . The former describes the energy per unity charge required to lift an electron from the semiconductor's conduction band to the vacuum energy level. The latter describes the energy per unity charge required to lift an electron from the metal's Fermi level to the vacuum energy level. The Schottky barrier ϕ_B , which is formed at the contact interface, can be determined by means of the difference of Ψ_s and ϕ_m as follows:

$$\Phi_B = \Phi_m - \Psi_s \text{ for } n\text{-type semiconductors,} \quad (3-2)$$

$$\Phi_B = E_g - (\Phi_m - \Psi_s) \text{ for } p\text{-type semiconductors.} \quad (3-3)$$

In Figure 3-1, two band configurations of metal/semiconductor (*n*-type) contacts are depicted exemplarily. In (a), a metal with $\phi_m > \Psi_s$ is chosen. Consequently, the bands in the semiconductor are bent upwards in the contact region, resulting in a potential barrier ϕ_B for majority charge carriers (here: electrons) and a non-ohmic behavior of the contact. This configuration is called a *rectifying contact*. Such a contact can be found, e.g., at the *a*-Si:H(*n*)/TCO contact, assuming a metal-like behavior of the TCO (see section 2.2.1). In (b), $\phi_m < \Psi_s$ is chosen so that the bands in the semiconductor are bent downwards in the contact region. Consequently, electrons are accumulated at the contact (*accumulating contact*). Nevertheless, a potential barrier ϕ_B is present also in this configuration. It can be diminished by high doping of the semiconductor, which shifts E_F closer towards E_c . In the case that ϕ_B approaches zero, the contact exhibits ohmic behavior. This is the case, e.g., for typical ITO/metal contacts because ITO is an extremely high (*degenerately*) doped *n*-type semiconductor [28]. For lowly doped ITO layers, the band configuration is more closely comparable to the one depicted in Figure 3-1 (b).

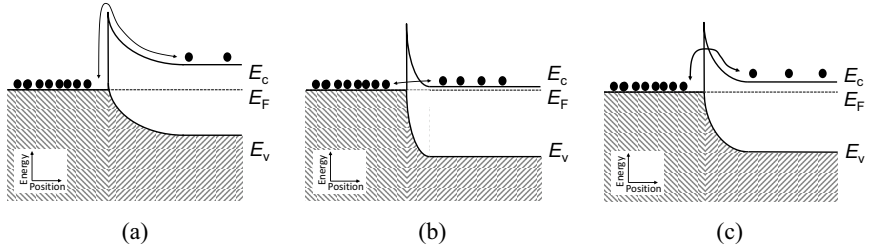


Figure 3-2 Illustrations of current flow mechanisms over Schottky barriers, namely thermionic emission (a), field emission (b), and thermionic field emission (c). The pictures are adapted from Ref. [79].

Actually, the height of such potential barriers is decreased by an effect called *image force lowering* [78]. A charge carrier in the semiconductor induces a charge carrier configuration in the metal as if an image charge of opposite polarity (referring to the charge carrier in the semiconductor) would be present in the metal. Such an *image charge carrier* would be exactly the same distance away from the metal/semiconductor interface as the charge carrier in the semiconductor. The resulting electrical field superimposes the electrical field induced by the Schottky barrier in a way that ϕ_B is reduced by $\Delta\phi_B$. Please note that even considering image force lowering, the dependence of ϕ_B on Ψ_s is not as strong as expected from theory in real metal/semiconductor contacts. One explanation for this are interface states at these contacts [76].

An overview over the current flow mechanisms of majority charge carriers in Schottky contacts is provided in Ref. [79]. Figure 3-2 illustrates three mechanisms for different band configurations, which are: *thermionic emission* (TE, Figure 3-2 (a)), *field emission* (FE, Figure 3-2 (b)), and *thermionic field emission* (TFE, Figure 3-2 (c)). Which mechanism is dominant in a specific Schottky contact configuration depends on the doping concentration N_D of the semiconductor. For lowly doped material ($N_D < 10^{17} \text{ cm}^{-3}$), TE is dominant. Charge carriers overcome the (comparatively wide) potential barrier by thermal activation, provided that their energy is higher than the barrier height. For highly doped material ($N_D > 10^{19} \text{ cm}^{-3}$), field emission is dominant. The Schottky barrier becomes so narrow for highly doped semiconductors that charge carriers can tunnel through the barrier. For intermediate doping concen-

3 Printed metal contacts

trations ($10^{17} \text{ cm}^{-3} \leq N_D \leq 10^{19} \text{ cm}^{-3}$), the potential barrier is slightly thicker compared to high doping so that charge carriers can tunnel through the barrier with a reduced probability. Moreover, charge carriers of sufficient energy can overcome the barrier also by means of TE. This means that a combination of both mentioned mechanisms takes place (TFE).

The formulas describing ρ_c at the contact interface for the three mechanisms are provided in the following:

$$\rho_c = \rho_1 \cdot \exp\left(\frac{q(\Phi_B - \Delta\Phi_B)}{k_B T}\right) \text{ for TE,} \quad (3-4)$$

$$\rho_c = \rho_1 \cdot C_1 \cdot \exp\left(\frac{q(\Phi_B - \Delta\Phi_B)}{E_{00}}\right) \text{ for FE,} \quad (3-5)$$

$$\rho_c = \rho_1 \cdot C_2 \cdot \exp\left(\frac{q(\Phi_B - \Delta\Phi_B)}{E_0}\right) \text{ for TFE,} \quad (3-6)$$

where C_1 and C_2 are functions of N_D , T and Φ_B . E_{00} characterizes the tunnel process and is a function of N_D . E_0 is a function of E_{00} and T . For more details, the reader is referred to Ref. [79]. ρ_1 is given by

$$\rho_1 = \frac{k_B}{q \cdot A^* \cdot T}. \quad (3-7)$$

A^* is the Richardson constant here. It becomes obvious that ρ_c depends mainly on Φ_B , N_D , and T . In short: the higher N_D and the lower Φ_B as well as T , the lower is ρ_c . Typically, the contact quality of a real device is tunable only by N_D . Simulations of ρ_c as a function of N_D for varying Φ_B can be found in Ref. [80].

Please note that ρ_c at the contact interface of printed metallization and semiconductor exhibits values which are orders of magnitude higher than expected from theory [81]. This is caused both by impurities at the metal/semiconductor contact interface and the fact that, typically, printed metallization electrically contacts only a small fraction of the semiconductor surface, which it covers [82].

3.2 Printing techniques

The metal electrodes of a silicon solar cell are typically divided into so-called *fingers* and *busbars*. Together, they form a *contact grid*. In the case of full-size SHJ solar cells, a five-busbar grid layout can be seen as standard today [3]. Fingers are responsible for extracting photogenerated charge carriers out of the cell and into the busbars. Busbars collect charge carriers from the fingers as well as generated charge carriers from the cell area nearby the busbar. They enable interconnection of cells in order to form a module, which can operate an electric load. Today, multi-busbar and even busbarless grid designs receive more and more attention [3]. In the case of busbarless cells, thin copper wires typically adopt the role of busbars, which are coated with an alloy and, e.g., laminated onto the cell by means of a special foil. Most prominent in this field is the Smart Wire Interconnection Technology (SWCT) [83]. A comparison of a five-busbar and a busbarless layout is provided in Figure 3-3.

In industry, metal electrodes are usually fabricated by means of state-of-the-art flatbed screen printing [3, 85]. Please note that a variety of other methods for the fabrication of such contacts is available. In the case of lab-type high-efficiency cells, typically, photolithographic processes are utilized in order to produce high-performance metal contacts. However, the great number of process steps and material waste prohibit this technique's application in industry [86]. Probably most prominent besides screen printing is electrochemical

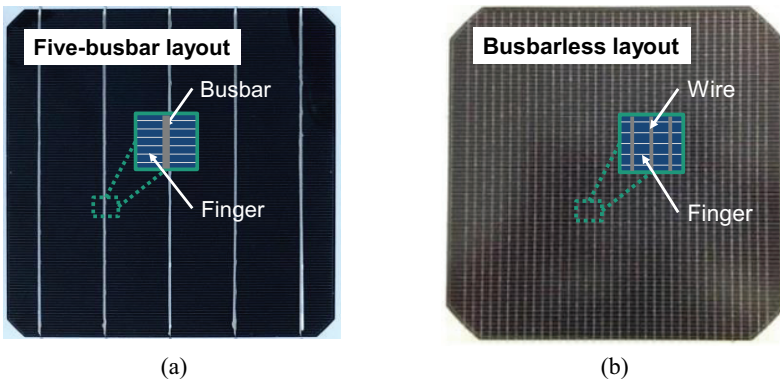


Figure 3-3 Comparison of front grid designs. A five-busbar layout is depicted in (a) and a busbarless layout is depicted in (b). The picture in (b) is adapted from Ref. [84].

processing in order to fabricate metal electrodes. Regarding SHJ metallization, lots of work has been conducted on plated metal contacts in the last years [87–89]. Moreover, in the field of printing technique, other promising approaches besides screen printing exist as, for example, dispensing and rotary printing [90, 91]. An example of dispensed metal contacts that allow for similar SHJ cell performance as screen-printed ones are presented in Ref. [92]. Nevertheless, screen printing is dominating PV production because of its great cost efficiency and reliability. Moreover, it is still improving performance today [3, 91].

Because of its claim to industry-relevance, this work uses flatbed screen printing (termed *screen printing* in the following) as the benchmark. It is contrasted with a printing technique, that is state of the art in printed electronics industry today, namely drop-on-demand inkjet printing (termed *inkjet printing* in the following) [93]. Furthermore, a novel printing technique, called *FlexTrail* printing, is introduced, which is developed with the support of the present author [94, 95]. The following sections are concerned with these three printing techniques.

3.2.1 Screen printing

In this work, a semi-automatic screen printing tool from *Ekra* is used to print test structures. For the purpose of full-size solar cell metallization, a full-automatic screen printing machine from *Asys* is utilized. Figure 3-4 (a) depicts a sketch of a screen printing assembly. A screen with a stencil acts as the printing plate. It consists of a mesh, which is clamped in a frame. For PV application, the mesh typically exhibits metal wires. In this work, meshes with a fineness of 360 wires per inch of fabric length are utilized. The calandered wires are 16 μm thick. The spaces between them are either covered by a light-treated photopol-

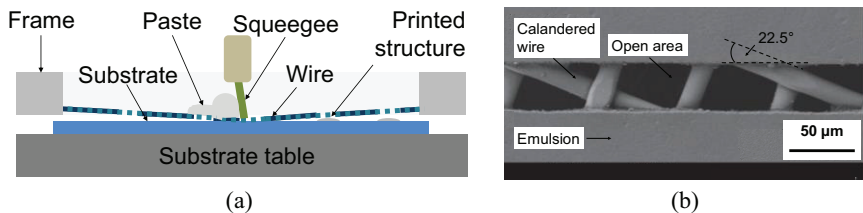


Figure 3-4 Sketch of a flatbed screen printing assembly (a), redrawn from Ref. [85]. A SEM image of a screen, adapted from Ref. [96], is depicted in (b).

mer-based emulsion or are open, according to the printing layout. Through the openings, a metal-containing printing medium (here: paste) is applied onto the substrate (for example, a Si wafer) by means of a movable squeegee. Please note that the screen is not in contact with the substrate (snap-off distance between screen and substrate) except for the position where the squeegee presses the mesh onto the substrate. Behind the squeegee, the mesh is lifted and the printed paste remains on the substrate (i.e., lift-off). The squeegee speed has an impact on the paste laydown. The screen and the substrate stand still during printing.

The metal fibers are typically positioned at an angle of 22.5° referring to the openings' edges (see Figure 3-4 (b)). Lately, so-called *knotless* screens with an angle of 0° receive more and more interest. Due to the absence of knots in the open areas, finger interruptions become less likely. In order to further develop printing quality and stability at the same time, a slightly larger angle of 22.6° is identified as an optimum by means of simulations [97]. Much work is also done on the optimization of the emulsion, particularly in the region of the screen openings, in order to improve the paste transfer to the substrate [98].

High-viscous metal-containing printing media, so-called *pastes*, consist of 60-95%_{wt} (percentage referring to the paste's weight) conductive material, e.g., silver. Solar cells covered by ITO layers also allow for the application of other metals such as copper (Cu) because such layers act as a diffusion barrier [99]. The metal particles' sizes typically range from about 100 nm to several micrometers. Their shape is either spherical or flake-like. Moreover, metal pastes exhibit binders and solvents, which are together called the *paste vehicle*. Its purpose is to ensure both stability (storage) and printability of the paste. In addition, high-temperature pastes developed to etch through dielectric ARC layers contain glass frit [100]. For metallization of SHJ solar cells, special low-temperature-compatible pastes (without glass frit) have to be used. The shape and the size of metal particles are to be tuned in a way so that low sintering temperatures are enabled (see section 3.1). The sintering affinity of such metal particles requires cappings of them to stabilize the paste [69]. The binders polymerize during annealing in order to achieve a sufficient mechanical finger/substrate contact as well as a mechanically stable finger [101]. Thereby, the conductivity of the metal electrode should be as high as possible. In fact, the

demand of low-temperature processing usually results in higher ohmic losses in the metal electrodes. Typically, the conductivity of low-temperature contacts is about two to three times lower compared to their high-temperature-processed counterparts [102].

Flatbed screen printing is state of the art in industry since many years not least because of its high level of reliability. Printing quality is steadily improving and record screen-printed fingers of only 19 μm width are already reported [103]. Furthermore, its throughput potential is still improving. Today, a speed of 4000 wafers per hour can be realized in industry [91].

A shortcoming of screen printing is that screen and wafer stand still during printing limiting throughput. Moreover, it is not a contactless printing technique. This is an issue in the case of extremely thin substrates and inhomogeneous substrate thickness, which might lead to breakage. Furthermore, the inhomogeneous height of screen-printed metal electrodes reduces the efficient use of metal paste. Since metal paste is the most critical and expensive non-silicon material in PV production, this is of particular interest [3]. According to the *International Technology Roadmap for Photovoltaic*, on average 200 mg of Ag paste is consumed for metallization of one SHJ solar cell (including busbarless and busbar-exhibiting cells) [3]. The paste consumption is expected to be halved within the next ten years.

3.2.2 Inkjet printing

A contactless printing technique, which allows for very efficient and flexible material usage, is inkjet printing. A review on this topic can be found in Ref. [93]. Inkjet printing has many applications. In this work, a direct printing of metal electrodes is performed. For this purpose, a *LP50* device from *PIXDRO* is utilized. A *Dimatix DMC* printhead is implemented that enables very small droplet volumes of down to 1 pl. There is no other printhead available on the market that allows smaller drop volumes. In general, small droplets enable high precision printing of extremely narrow structures.

3.2 Printing techniques

Figure 3-5 (a) depicts a sketch of a corresponding inkjet setup exhibiting one nozzle. The printing medium (here: ink) enters a small channel in the printhead with a piezoelectric transducer from an ink reservoir, realized, for example, by a cartridge. The transducer is controlled with pulsed voltage (see add-in window in Figure 3-5 (a)), which is converted into a mechanical pressure wave applied to the ink. This causes the ejection of small droplets out of the nozzle and onto the substrate, which is also called *jetting*. The printhead is heatable in order to modify the viscosity of the ink in the printhead and, therefore, the whole printing process. Tuning the waveform of the pulse is required to achieve stable droplets of sufficient size. If the kinetic energy of a droplet is too small, it cannot overcome the ink's surface tension in the printhead and it is sucked back. If the kinetic energy of the droplet is at its optimum, it is ejected with a small tail that is sucked into the droplet before it hits the substrate. If the kinetic energy is too large, the tail separates from the droplet after ejection and forms a so-called *satellite droplet*. It may influence the printing image in an undesired way, for example, by deviation of the main droplet [93].

To further reduce wetting-related effects or the width of the printed structures, the substrate can be heated by means of a heatable substrate table. This causes the exhaust of inks' solvents directly after landing on the substrate and, hence, before spreading. Thus, direct printing of silver fingers exhibiting a width of $18\ \mu\text{m}$ is possible [104]. Please note that the printing performance and size of the printed image is not only dependent on the droplet size, energy, and sub-

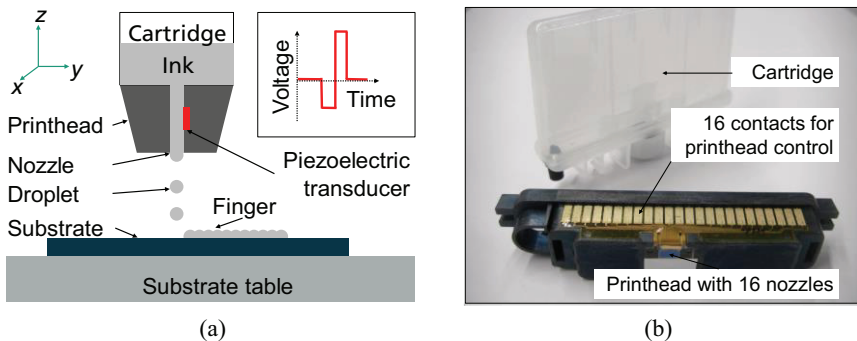


Figure 3-5 Sketch of a one-nozzle inkjet printing setup (a). In (b) a photograph of a *Dimatix DMC* setup is shown exhibiting 16 nozzles.

strate temperature but also on the surface tension and energy of the ink and the substrate surface, respectively [105].

The substrate is moved under the printhead in y -direction (see Figure 3-5 (a)) so that a line is printed consisting of multiple connected droplets. The droplets' distance is defined by the adjustable resolution in the corresponding dimension. The same printing step (also called *pass*) can be repeated at the same position so that one line consisting of more than one printed layer is fabricated. Typically, a higher number of passes increases the height and also the width of the printed image. To print another line next to the first one, the printhead is moved in x -direction (see Figure 3-5 (a)). The printhead is also moveable in z -direction so that substrates of varying thickness can be processed. The distance between substrate surface and printhead is chosen to be 100 μm in this work. Such a small distance improves both printing quality and reproducibility. The *DMC* printhead exhibits 16 nozzles positioned in line each with an opening width of 10 μm (see Figure 3-5 (b)). For improved process control at the expense of process time, only one nozzle is operated at one time in this work.

In contrast to screen printing pastes, the printing media for inkjet printing, called *inks*, exhibit a much lower viscosity of typically 5-20 $\text{mPa}\cdot\text{s}$ [93]. The viscosity should be independent of the shear rate to achieve proper jetting. Basically, metal inks consist of up to 50%_{wt} metal particles as well as solvents or water [105]. As a rule of thumb, the diameter of metal particles should not exceed one tenth of the nozzle opening in order to avoid clogging of nozzles [93]. This requires using nanosized, spherical metal particles (diameter of 50-150 nm). They are prevented from agglomeration by polymer cappings. The particles are dissolved in a solvent. The solvent must evaporate very quickly after jetting of the droplet on the substrate to prevent undesired spreading. On the other hand, it must not evaporate too quickly because then the ink would already dry out at the nozzle and block it. Moreover, it can lead to foaming of the ink.

Inkjet printing is already state of the art in printed electronics industry, which means that industrial equipment with a large throughput potential is available. It is also used in PV fabrication not only for metallization but also for structuring. Unlike screen printing, the printing template is digital. This allows for a high

flexibility in terms of layout design and short-term adaptations. The large number of printheads for all kinds of applications (e.g., doping, mask and etch, metallization) increases the flexibility even more. An overview over different printheads and applications can be found in Ref. [93]. However, the printing process can be sophisticated and it is dependent on a large number of parameters. Printing, especially of particle-based inks, is not always reliable.

3.2.3 FlexTrail printing

FlexTrail printing is developed which can be operated using commercially available (metal) inks for inkjet printing [94, 95]. A sketch of the FlexTrail printing setup used in this work is depicted in Figure 3-6 (a).

A small ink reservoir is positioned on top of a hollow glass capillary. Atmospheric pressure from 10 mbar up to 10 bar is applied on the ink in the reservoir so that it is pressed into the capillary. The capillary is bent at its lower end and tapered. Figure 3-6 (b) depicts a capillary's opening with an inner diameter of $6\ \mu\text{m}$ at its lower end. If the opening of the capillary is in contact with the substrate and ink escapes the capillary while being moved relatively to the substrate, ink is wetting the substrate continuously. Please note, that the thin capillary is extremely flexible so that the substrate is not damaged. The force of the capillary applied to the substrate is neglectable (i.e., quasi-contactless printing process). To this date, the FlexTrail printing process is not fully

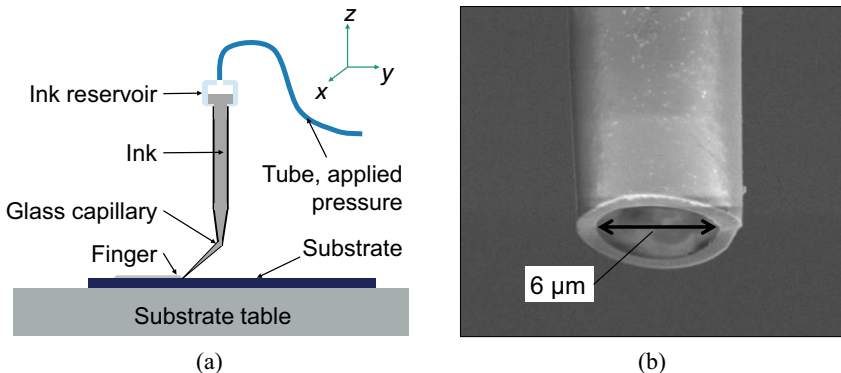


Figure 3-6 Sketch of a one-capillary FlexTrail printing assembly (a). In (b) a SEM image of a capillary's lower end is shown.

understood and requires further research. Certainly, the ink/capillary/substrate interaction during printing, the dimensions of the capillary, and the surface properties of ink (wetting), capillary, and substrate play an integral role.

Although a detailed analysis of the FlexTrail printing process is still to be conducted, it becomes obvious that FlexTrail printing is to be differentiated from inkjet printing because there is no dynamic jetting process influencing the ink's rheology. Furthermore, the potential viscosity range of the printing medium is wider and deposition of printing media is smooth compared to jetting. FlexTrail is also to be differentiated from dispensing because a direct contact of the capillary with the substrate is required for printing. Therefore, no form stability of the printing medium is needed for deposition allowing a wider viscosity range of the medium in the case of FlexTrail. That is why FlexTrail printing is to be seen as a different and completely new printing technique.

Due to its simplicity, FlexTrail printing ensures a significant process stability increase compared to inkjet printing. Like inkjet printing, it requires a digital template and, therefore, allows for a high flexibility, not only in terms of layout and applications but also in terms of ink rheology. Experimentally, it is verified that not only metal inks for inkjet printing are printable but also selected screen printing pastes, for example, with a comparatively low viscosity. The fact that, in contrast with inkjet, the printing medium is in contact with glass only, allows for printing of, e.g., corrosive or other sensitive materials. FlexTrail printing is expected to offer at least the same throughput potential as inkjet printing. Concepts for printing parallelization by arranging many capillaries next to each other already exist.

In this work, a one-capillary setup is utilized. Structures with an extremely small width of down to 10 μm can be achieved with FlexTrail printing [94]. Unfortunately, these structures are not only narrow but also very flat in terms of finger height h_f , which is a shortcoming for direct metallization of Si solar cells. However, there is promising potential to fix this issue by adapting the printed inks (or pastes) or by modifying the capillary diameter, surface properties, and shape.

3.3 Contact formation techniques

Directly after printing, metal contacts do not exhibit the required mechanical (stability and adhesion to the substrate) and electrical properties (low lateral resistance and contact resistivity). In order to achieve these properties, state-of-the-art solar cells undergo a high-temperature contact firing process after printing [106, 107]. As described in section 2.2, firing is prohibited by the sensitivity of the passivating contacts under investigation. Therefore, low-temperature processing is required. Typically, this is realized by simple thermal annealing at temperatures of about 200°C using an oven [102]. It is investigated in this work whether the effect of thermal annealing on electrical contact formation can be improved by means of an ultrasonic pretreatment of the samples in addition to thermal annealing. Furthermore, an alternative contact formation technique, namely intense pulsed light (IPL), is analyzed.

3.3.1 Thermal annealing

After printing of low-temperature pastes or inks, the printed samples can be thermally annealed, e.g., by means of a hotplate (lab-scale) or a conveyor furnace (industry-related scale). In this work, the latter is performed by means of a machine from *Essemtec*. Thereby, convection heating induces evaporation of remaining solvents in the metal electrodes, electrical contact formation (sintering), and mechanical contact formation (polymerization of binders). Critical process parameters are the annealing temperature $T_{\text{annealing}}$ and time $t_{\text{annealing}}$. Temperature is typically chosen to be 200°C in this work in the case of SHJ solar cells. Annealing times from about 10 min up to 30 min, depending on the printing medium, are typical in industry. In this work, $t_{\text{annealing}} = 30$ min is chosen because it is recommended by paste manufacturers in order to achieve high electrical and mechanical performance of the printed structures.

The main advantage of such thermal annealing is its simplicity. However, even a shorter industrial process is time-consuming and is accompanied by large and cost-intensive devices in order to keep an adequate throughput. To achieve a gross throughput of 4700 wafers per hour (wafers exhibiting 156 mm edge length), corresponding devices consume more than 100 m² of floor space (two-

lines processing). This has an impact on costs, as is discussed in section 7.1.1. Therefore, an annealing time and footprint reduction is highly desired.

3.3.2 Ultrasound-assisted thermal annealing

Low-temperature-processed metal contacts are less conductive after low-temperature annealing compared to fired contacts. As is shown in section 6.1.4, this originates in the microstructure of such contacts. Their electrical performance suffers from high porosity, which is also reported in Ref. [72]. In the present work, it is investigated whether such porosity can be reduced by means of an ultrasonic pretreatment performed directly before thermal annealing. For this purpose, an ultrasonic device *HiS VARIO B 4800* from *Herrmann Ultrashall* is used. Ultrasound is typically applied on welding of similar or dissimilar materials [108, 109]. This device is designed for welding of non-ferrous metals.

Sketches of the experimental setup are depicted in Figure 3-7. Ultrasound produced by a generator is coupled into the metal contact by a sonotrode placed on its top. The sonotrode has a planar (non-textured) surface in order to reduce damage of the metal finger. The longitudinal oscillations applied parallel to the substrate level with a frequency of 20 kHz are coupled into the finger either along or perpendicular to the finger's orientation. Please note that ultrasonic oscillations applied perpendicular to the substrate level would cause damage of the substrate. The maximum applied displacement amplitude is 25 μm .

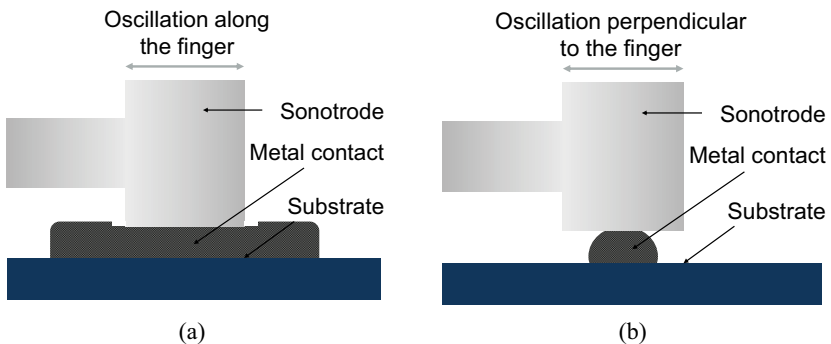


Figure 3-7 Sketches of experimental setup. In (a), ultrasound couples into the metal along and in (b) perpendicular to the finger. Finger and sonotrode are in contact.

3.3.3 Intense pulsed light processing

An alternative annealing process is very fast intense pulsed light (IPL) processing. This technique provides energy in form of millisecond-lasting pulsed electromagnetic radiation impinging on the specimen. The target's characteristic absorption leads to heating and, therefore, curing and contact formation. IPL mostly consists of visible light being absorbed by silicon solar cells and causing multiple electrons moving from the valence band into available conduction band states (compare section 2.1.3). Electrons with energies greater than the bandgap release their excess energy by thermalization leading to heating of the solar cell. However, not only Si but also most metal nanoparticles strongly absorb such radiation. The reasons are strong resonance bands in the visible part of the electromagnetic spectrum [110]. Although highly concentrated dispersions like metal pastes or inks exhibit a more bulk-metal-like optical behavior, printed metal contacts absorb strongly in the visible wavelength range [111]. As in the case of thermal annealing, rapid heating of metal contacts due to IPL induces evaporation of solvents in the metal contacts, electrical contact formation (sintering), and mechanical contact formation (polymerization), simultaneously.

IPL is also addressed as photonic curing or photonic (flash) sintering [112, 113]. It is already successfully employed to sinter silver-, copper-, or nickel-based electrodes of printed electronics (e.g., electric devices on flexible substrates, wearable electronics, displays) on top of temperature-sensitive substrates (e.g., based on polyethylene terephthalate) [114]. Roll-to-roll IPL devices with a large throughput potential and moderate footprint are available today [115, 116]. An overview over IPL as well as related techniques, such as ultraviolet-, infrared-, and laser-sintering, is given in Ref. [114]. A review over the application of IPL in PV manufacturing is provided in Ref. [117]. Especially in the field of metallization, IPL is already used to sinter copper-based electrodes on Si wafers and on metal-compound-based heterojunction structures [118, 119]. However, no solar cell results are reported so far. Furthermore, no successful integration of IPL into the fabrication of SHJ or TOPCon cells is reported to the author's knowledge up to now.

3 Printed metal contacts

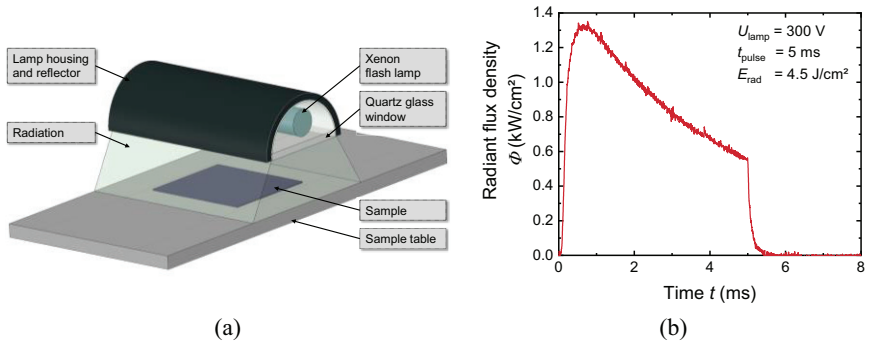


Figure 3-8 Sketch of a lab-scale IPL device (a). In (b), the shape of a pulse expressed by the radiant flux density Φ received by a sample as a function of time t is shown. It is measured using a thin molybdenum bolometer. Both images are redrawn from Ref. [120].

A schematic drawing of the lab-scale IPL device utilized in this work, namely the *PulseForge 1300* from *NovaCentrix*, is depicted in Figure 3-8 (a). It mainly consists of a water-cooled Xenon flash lamp integrated into a housing with a reflector on its inside. A quartz-glass window protects the lamp from pollution during processing. The sample is placed on a table 10 mm underneath the glass window so that homogenous irradiation is ensured. The sample table is made out of aluminum with a matt surface. A sufficiently dimensioned power supply provides the lamp with tunable high voltage by means of a capacitor array. A trigger signal induces the capacitors to apply voltage on the lamp, which then emits pulsed light. The conversion of electrical to radiant energy is at least 30%, which is about one order of magnitude more compared to corresponding laser applications [116]. The duration of the light pulse is the pulse time t_{pulse} . It can be tuned from 0.1-100 ms. The lamp voltage U_{lamp} starts at a maximum voltage and decreases exponentially during the pulse because of the discharge characteristic of the capacitors. Because U_{lamp} determines the radiant flux density of the lamp, the light pulse, i.e., the radiant flux density received by a sample Φ resolved over time t , is shaped accordingly (see Figure 3-8 (b)). According to the tool manufacturer, a maximum radiant exposure of the samples E_{rad} of 100 J/cm² and a maximum radiant flux density of 35 kW/cm² can be achieved. The number of applied pulses is freely selectable, which is not the case for the pulse frequency f_{pulse} (i.e., the reciprocal of the time between pulses). The time required to charge the capacitors according to U_{lamp} limits f_{pulse} .

4 Metrology

The impact of contact formation processing on passivating contacts is analyzed by means of photoconductance-based lifetime measurements. Moreover, this chapter deals with key characterization methods utilized to evaluate the metallization of passivating contacts. Printed metal contacts are analyzed both by microscopy and four-point probe measurements. In the case that metal contacts are electrically characterized on top of conductive layers, such as transparent conductive oxide layers, strategies to avoid systematic measurement errors are required. These are developed based on simulations in this chapter.

4.1 Photoconductance-based lifetime measurement

To determine the influence of contact formation processing on passivation quality, the knowledge of corresponding samples' iV_{OC} is crucial. It is obtained by timely resolved measuring of the excess-charge-carrier-induced photoconductance followed by deriving the effective charge carrier lifetime τ_{eff} . For this purpose, the *WCT-120* setup from *Sinton Instruments* is utilized in this work.

The following description of the measurement principle, by taking the example of a *p*-type sample, is mainly based on Ref. [121]. Assuming that there is no external current applied to the sample, the continuity equation (2-10) reads as

$$\frac{\partial n}{\partial t} = G - R. \quad (4-1)$$

Using this together with equation (2-11) leads to the expression

$$\tau_{eff}(\Delta n) = \frac{\Delta n}{G - \partial \Delta n / \partial t}. \quad (4-2)$$

Based on this equation, there are two basic approaches to measure the excess carriers in semiconductors. The first makes use of the steady-state mode, where $G \gg \partial\Delta n/\partial t$ holds, so that

$$\tau_{\text{eff}}(\Delta n) = \frac{\Delta n}{G}. \quad (4-3)$$

In practice, the condition for G is fulfilled by illuminating the sample by means of a flash of light with the duration t_{flash} , which is much greater than τ_{eff} . The second approach makes use of the transient mode, where $G \ll \partial\Delta n/\partial t$ holds. This leads to

$$\tau_{\text{eff}}(\Delta n) = -\frac{\Delta n}{\partial\Delta n/\partial t}. \quad (4-4)$$

In practice, the illumination of the sample is chosen so that $t_{\text{flash}} \ll \tau_{\text{eff}}$. Independent of which mode is chosen, Δn needs to be determined. This is achieved by measuring the time- (transient mode) or illumination-dependent (steady-state mode) conductivity of the sample, which is related to Δn . To this end, the *WCT-120* makes use of an inductor that is part of a radio-frequency circuit producing a voltage proportional to the sample's conductivity. Under illumination, electron-hole pairs are generated, which increase the sample's conductivity according to

$$\Delta\sigma = q \cdot d_{\text{wafer}}(\mu_n + \mu_p)\Delta n, \quad (4-5)$$

where d_{wafer} is the wafer thickness. By means of a sufficient calibration in terms of σ , Δn can be extracted from $\Delta\sigma$. In the case of the steady-state mode, the photogeneration rate is to be determined in addition. Typically, this is performed by using a photodetector, e.g., a calibrated solar cell. It is used to measure the incident flux of photons N_{ph} . Thereby, G can be calculated as follows:

$$G = \frac{N_{\text{ph}} \cdot f_{\text{abs}}}{d_{\text{wafer}}}. \quad (4-6)$$

The absorption fraction f_{abs} includes information about the absorption characteristics of the sample in relation to the photodetector.

Since the transient mode, which is also known as the *photoconductance decay method*, requires the measurement of the samples' time-dependent conductivity only, it is quite robust and typically preferred over the steady-state mode. However, it is recommended to be used for long carrier lifetimes only, because the measurement of short lifetimes is limited by the speed of electronics for recoding the photoconductance decay and by the slope of the light pulse's cut-off ramp [122]. Since most of the samples measured in this work exhibit $\tau_{\text{eff}} > 1$ ms, the transient mode is mainly used.

Illuminating the sample during lifetime measurement induces a splitting of its quasi-Fermi levels (see section 2.1.4). The corresponding iV_{OC} is given by the pn product at the junction. It is determined using the information about Δn contained by the $\Delta\sigma$ measurement together with the following equation [123]:

$$iV_{\text{OC}} = \frac{k_{\text{B}}T}{q} \cdot \ln \left[\left(\frac{\Delta n(n_{\text{A}} + \Delta p)}{n_{\text{i}}^2} \right) + 1 \right]. \quad (4-7)$$

It is assumed that the excess charge carrier density is distributed homogeneously across the whole sample. In this work, iV_{OC} is determined at an illumination of 1000 W/m^2 .

4.2 Microscopy

High demands are placed on printed metal contacts in terms of their shape and microstructure. This holds especially for the front side of solar cells but also for the rear of bifacial cells. The contact fingers should be narrow in order to ensure that as many incident photons as possible generate charge carriers in the solar cell. Therefore, a critical parameter is the shading finger width w_{f} , which characterizes the width of the metal finger including all of its parts that contribute to the shading of the cell. In contrast to w_{f} , the finger's height h_{f} and cross-sectional area A_{f} need to be large in order to achieve sufficient conductivity,

hence, keeping ohmic losses as low as possible. Both requirements are fulfilled for high values of the aspect ratio AR , which is defined as follows:

$$AR = \frac{h_f}{w_f}. \quad (4-8)$$

In order to characterize metal contacts regarding the mentioned parameters, optical and confocal microscopy is utilized in this work. Yet, not only the finger geometry (and the material it exists of) determines its electrical characteristics, but also its microstructure. Porous contacts, for example, are less conductive than solid fingers of the same material. Information about the contacts' microstructure is obtained by means of scanning electron microscopy (SEM).

4.2.1 Confocal microscopy

The principle of confocal microscopy has been invented by M. Minsky in 1957. The present work makes use of confocal laser scanning microscopy (CLSM) [124]. The tool's name is *LEXT* from *Olympus*. Figure 4-1 depicts schematic drawings of a typical CLSM setup. A collimated laser beam hits a semi-transparent mirror and is reflected to the direction of the specimen, where it is focused by means of a lens (here it is called the *lower lens*). (The *Olympus LEXT* tool allows for both using a laser beam at a wavelength λ of 405 nm and white light.) Light reflected by the specimen passes the lower lens again, but in

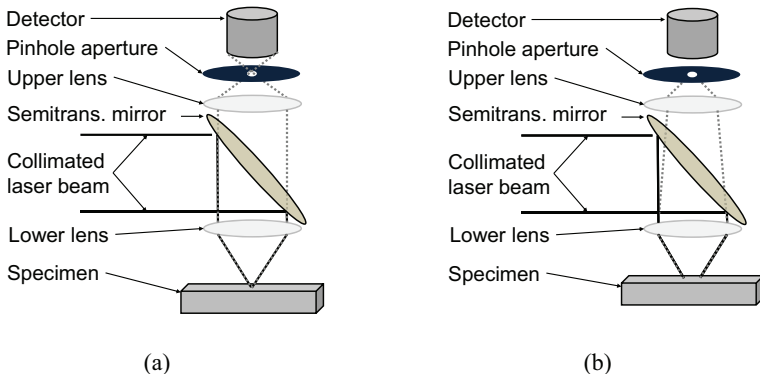


Figure 4-1 Schematic drawings of a CLSM setup. In (a) incoming and reflected light are confocal, which is not the case in (b). Both images are redrawn from Ref. [124].

the opposite direction than the incident light. In case that the lens' focus level is exactly on the specimen's surface, incoming and reflected light are confocal (Figure 4-1 (a)). In a next step, the reflected light passes through the semi-transparent mirror and is focused by a second lens, the *upper lens*, next to the pinhole aperture. It passes through the pinhole and is detected by a photomultiplier. If the CLSM focus level does not equal the specimen's surface level, the reflected light is not confocal with the incoming light and is, therefore, not focused by the upper lens next to the pinhole. Consequently, it fails to pass through the pinhole (Figure 4-1 (b)) and is not detected by the photomultiplier.

The focus point can be shifted by a scanning unit in a flat plane parallel to the specimen's upper surface (not shown in Figure 4-1). Further, the surface's topography can be scanned by shifting the whole optics up- and downwards. The three-dimensional information about samples' surfaces is used in this work to characterize the geometry of (printed) contact fingers. The CLSM images are automatically analyzed by means of the tools *Spotlob* [125] and *FineUp* [126].

4.2.2 Scanning electron microscopy

To investigate contact fingers' microstructure, SEM is utilized, which allows for the analysis of sub-micrometer-sized structures. This work makes use of the *Hitachi SU-70* device. The working principle of a SEM is briefly introduced in the following according to Ref. [127]. A tungsten hairpin filament emits thermionic electrons, which can then be accelerated up to energies of 0.1-30 keV. In this work, an electron energy of 5 keV is used. When the electrons reach their target energy, the electron beam is focused on the specimen's surface by means of electromagnetic lenses. The electron beam interacts with the specimen within a certain volume underneath the surface. Thereby, the electrons undergo one or, more likely, several elastic scattering processes in the volume so that their trajectory changes once or several times. As a result, some of these electrons are backscattered in a way that they leave the specimen again. Some of the beam electrons undergo inelastic scattering processes as well. They interact with loosely bound outer shell electrons of the specimen atoms, which receive enough kinetic energy in order to be ejected from the atom and out of the specimen. They are called *secondary electrons*. The backscattered and second-

ary electrons constitute the most often used signals for SEM. They are collected by means of an appropriate detector. Note that the detected signal includes information of a certain volume of the specimen and not only of its surface. The signal depends on the energy of the beam electrons and the material characteristics of the specimen. In order to achieve a very smooth sample surface and, consequently, an improved SEM image quality, regions of interest are typically prepared by Argon ion beam polishing before SEM [128].

To form a SEM image, the beam scans over a defined region of interest. The pixels' differences in contrast are caused by the varying extend of the corresponding signal strength.

4.3 Four-point probe measurement

Key electrical parameters of solar cells' metal contacts are the finger resistance r_f , i.e., the resistance alongside the finger within a defined distance, and the contact resistivity ρ_c at the finger/semiconductor interface. Both are obtained by means of four-point probe measurements. Thereby, two probes are used to enter small measurement currents. Two extra contacts are utilized to conduct voltage measurements. If the voltmeter exhibits high impedance, the voltage drops at the sensors and the sensor/specimen interfaces are neglectable. Thus, it is possible to measure small resistance values correctly.

4.3.1 Determination of the finger resistance and finger resistivity

To measure the resistance alongside the finger, a configuration as depicted in

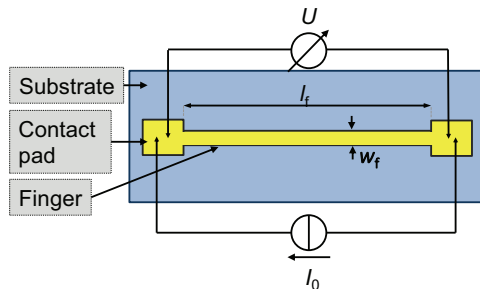


Figure 4-2 Four-point probe measurement configuration used to determine r_f .

4.3 Four-point probe measurement

Figure 4-2 is used. Electrical current I_0 is applied by the two outer probes and the voltage drop along the finger U is measured by the two inner probes. All four probes are positioned on highly conductive contact pads, which are assumed to be equipotential surfaces. The finger between the pads has the length l_f and exhibits the absolute finger resistance R_f . The length-independent finger resistance r_f is calculated as follows:

$$r_f = \frac{U}{I_0 \cdot l_f} = \frac{R_f}{l_f}. \quad (4-9)$$

Obviously, r_f still depends on the finger's profile. If A_f is known, the entirely geometry-independent finger resistivity ρ_f can be determined as follows [112]:

$$\rho_f = r_f \cdot A_f. \quad (4-10)$$

ρ_f is used in this work in the case that metal contacts of very different shapes are compared to each other. Yet, mostly r_f is preferred over ρ_f because it is less prone to errors caused by the determination of A_f . Furthermore, r_f indicated together with w_f enables a rather intuitively estimation of whether a metal contact fits the requirements of a certain solar cell design.

4.3.2 Determination of the contact resistivity

The contact resistivity ρ_c at a metal/semiconductor contact is conveniently determined by means of the transfer length method (TLM) [129, 130]. William Shockley introduced the corresponding theory for the first time [131]. Later, the application of TLM on silicon solar cells with screen-printed metal contacts has been considered, too, which is discussed in Ref. [132].

The following explanation of the measurement principle mainly follows Ref. [112]. Figure 4-3 shows a typical TLM sample layout: the resistance between contact fingers 1 and 2, namely R_{TLM} , is measured by means of the probe configuration depicted on the left side. Using this setup, the applied current has to overcome two times the contact resistance at the metal/semiconductor contact R_c and one time the resistance of the layer(-system) between the contacts R_{layer} . In this work, a one-dimensional TLM approach can be utilized because the

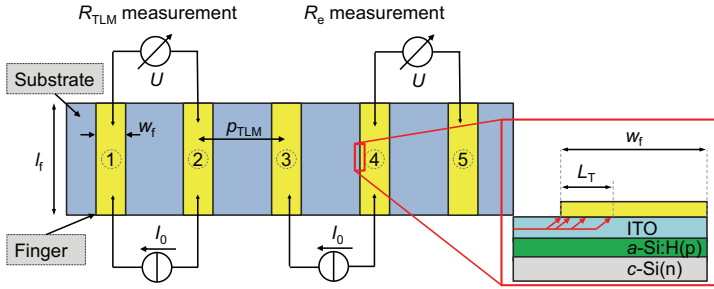


Figure 4-3 TLM sample layout and explanatory sketch of the transfer length L_T , adapted from Ref. [134].

current-carrying layer underneath the contact, i.e., an ITO layer, is very thin (≤ 100 nm). Furthermore, current flow through the bulk is prohibited by a rectifying pn junction. Without a pn junction, currents through the bulk would have to be taken into account as well. Corresponding two- and three-dimensional TLM theory is elaborated in Ref. [133]. R_{layer} can be expressed by the sheet resistance of the relevant layer underneath the contact R_{SH} and the sample geometry. The measured resistance R_{TLM} is equal to

$$R_{\text{TLM}} = 2 \cdot R_c + R_{\text{layer}} = 2 \cdot R_c + R_{\text{SH}} \frac{p_{\text{TLM}}}{l_f}, \quad (4-11)$$

where p_{TLM} is the distance between contacts and l_f the length of a contact (see

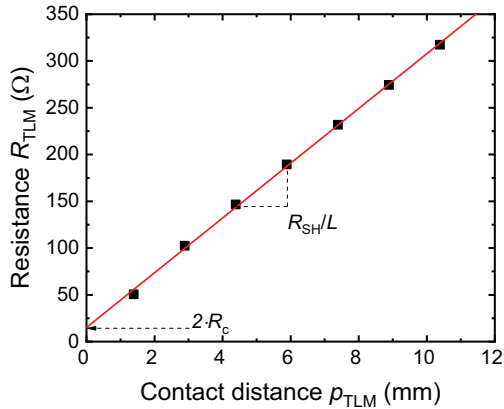


Figure 4-4 R_{TLM} plotted as a function of p_{TLM} .

4.3 Four-point probe measurement

Figure 4-3). l_f is equal to the width of the sample L . The finger ends are flush with the longer sample edges. If p_{TLM} is varied, e.g., by measuring from finger 1 to 2, from 1 to 3 and so on, R_{TLM} can be plotted as a function of p_{TLM} (see Figure 4-4). Here, the y -axis intercept of a linear fit is equal to two times the contact resistance R_c . The sheet resistance R_{SH} can be extracted from the slope of the fit.

Still, R_c is dependent on the area contacted by the metal electrode. To compare varying metal contacts, eventually measured using varying sample geometries, a geometry-independent parameter, namely the contact resistivity ρ_c , is required. To this end, it seems reasonable to simply weight R_c with the contacted area $l_f \cdot w_f$, which means to assume that the applied current enters the contact homogeneously. Unfortunately, this is not the case for real contacts because the current flows inhomogeneously in and out of them. This effect is called *current crowding* [135]. The spatial distribution of the voltage U under the contact in combination with an applied current I_0 is expressed as follows:

$$U(x) = \frac{I_0 \sqrt{R_{\text{sk}} \cdot \rho_c}}{L} \frac{\cosh[(w_f - x)/L_T]}{\sinh(w_f/L_T)}. \quad (4-12)$$

$x = 0$ is defined as the edge of the finger, where I_0 exhibits its highest value compared to all other positions underneath the contact. In general, the sheet resistance under the contact is not necessarily equal to the sheet resistance in the non-metallized area because of possible interactions of the metallization with the underlying layer(s). Therefore, a sheet resistance under the contact R_{sk} is introduced. The distance underneath the finger within which the applied current I_0 drops from its initial value, i.e., at the finger's edge, to $1/e$ is called the *transfer length* L_T (see Figure 4-3). It is defined as follows:

$$L_T = \sqrt{\rho_c / R_{\text{sk}}}. \quad (4-13)$$

Measuring the voltage from contact 1 to 2 (see Figure 4-3) at $x = 0$ leads to the contact *front* resistance, which is typically identified as the contact resistance R_c . It is expressed as

$$R_c = \frac{U(x)}{I_0} = \frac{\sqrt{R_{\text{sk}} \cdot \rho_c}}{l_f} \coth(w_f/L_T) = \frac{\rho_c}{L_T l_f} \coth(w_f/L_T). \quad (4-14)$$

This expression can be simplified for the two extreme cases, namely for $w_f \leq 0.5 L_T$, where $\coth(w_f/L_T) \approx L_T/w_f$. In this case, R_c can be expressed as

$$R_c \approx \frac{\rho_c}{w_f l_f}. \quad (4-15)$$

The second case is $w_f \geq 1.5 L_T$, where $\coth(w_f/L_T) \approx 1$. This leads to

$$R_c \approx \frac{\rho_c}{L_T l_f}. \quad (4-16)$$

Still, the extraction of ρ_c requires an additional measurement: when the current sensors are shifted so that current is applied, e.g., between finger 3 and 4, and the voltage sensors are placed on the fingers 4 and 5 (see the probe configuration depicted on the right side in Figure 4-3), the voltage at $x = w_f$ is measured. The resistance occurring there is called the end resistance R_e and is expressed as follows:

$$R_e = \frac{V}{I_0} = \frac{\sqrt{R_{sk} \cdot \rho_c}}{l_f} \frac{1}{\sinh(w_f/L_T)} = \frac{\rho_c}{L_T l_f} \frac{1}{\sinh(w_f/L_T)}. \quad (4-17)$$

When both R_c and R_e are measured, L_T can be extracted from dividing R_c by R_e :

$$\frac{R_c}{R_e} = \cosh\left(\frac{w_f}{L_T}\right). \quad (4-18)$$

Once L_T is obtained, ρ_c can be calculated using the equations (4-17) and (4-18) as follows:

$$\rho_c = R_c \cdot L_T \cdot l_f \cdot \tanh\left(\frac{w_f}{L_T}\right). \quad (4-19)$$

Please note that the TLM is applicable if the contact fingers' resistance is very small. In the case of printed and fired silver-based contacts this is valid but not necessarily in the case of their low-temperature equivalents. How this influences the contact resistance R_c and how to adapt the specimen design in order to be able to determine R_c and ρ_c correctly is discussed in the following section 4.4.

4.4 Simulation-based strategies to avoid measurement errors

Electrical characterization of a contact finger on top of a conductive layer is challenging because of possible parasitic measurement currents through such a layer. Moreover, other metal structures on top of the conductive layer and in vicinity of the finger may influence the measurement. In the case of r_f determination, both can easily be prevented by transferring the measurement to parallel processed samples, where the conductive layer is replaced by an insulating one. For example, a conductive ITO layer can be replaced by a dielectric silicon nitride (SiN_x) layer. Yet, some metallization techniques, as, for example, inkjet printing, are significantly influenced by the surface properties of the substrate. Especially its wetting behavior determines the interplay of the applied metal and the surface and, therefore, printability [93]. This may require r_f determination on the originally intended conductive layer and strategies to avoid systematic measurement errors are needed.

Errors may also occur in the case of ρ_c determination at the metal/conductive layer contact. In fact, the sample's layout on which the TLM is conducted can have a significant influence on the performed measurements. Both electrical and geometrical characteristics of layer and metal are, thus, to be considered carefully. Based on *Quokka 3* simulations, a benchmark for a robust test structure design is identified in the following [136]. Three different low-temperature metallizations are considered, which are to be characterized in terms of r_f and ρ_c on top of an ITO-coated SHJ sample. Three-dimensional views of the addressed sample layouts are depicted in Figure 4-5.

4.4.1 Determination of the finger resistance

In the following, it is consecutively investigated how the $a\text{-Si(p)}$ layer, the ITO layer, and an adjacent finger influence the measurement of a particular finger's resistance. Especially, the resistance R_{12} between contact pad 1 and 2 (see Figure 4-5(a)) is examined. The pads can be treated as equipotential surfaces and, therefore, are electrically neglectable. The distance between the pads, or the finger length l_f , is defined to be 1 cm. w_f is chosen to be 50 μm . Three different kinds of metallization are considered: a screen-printed low-temperature silver-

based finger ($\rho_f = 5 \mu\Omega \cdot \text{cm}$, $h_f = 20 \mu\text{m}$), a screen-printed low-temperature copper-based contact ($\rho_f = 15 \mu\Omega \cdot \text{cm}$, $h_f = 20 \mu\text{m}$), and an inkjet-printed low-temperature silver-based contact ($\rho_f = 5 \mu\Omega \cdot \text{cm}$, $h_f = 1 \mu\text{m}$). The metal's sheet resistances $R_{\text{SH,metal}}$ is calculated as follows:

$$R_{\text{SH,metal}} = g \cdot \frac{\rho_f}{h_f}, \tag{4-20}$$

where g is a geometry factor. It is chosen to be 1.3 in the case of screen-printed contacts taking into account that such fingers' profiles are typically not rectangular but rather hoof-shaped. Since a typical inkjet-printed contact is flat, $g = 1$ is valid. $R_{\text{SH,metal}}$ and w_f together with the metal/ITO contact resistivity ρ_c , which is chosen to be $4 \text{ m}\Omega \cdot \text{cm}^2$, serve as metallization-specific input parameters for the simulations.

The other input parameters are the ITO layer thickness, which is 100 nm, and the ITO sheet resistance $R_{\text{SH,ITO}} = 100 \Omega/\text{sq}$, which is a typical value [28]. The $a\text{-Si(p)}$ layer thickness is 10 nm. $a\text{-Si(p)}$ layers typically exhibit high resistivities $\rho_{a\text{-Si(p)}}$ [137]. It is chosen to be $1 \cdot 10^5 \Omega \cdot \text{cm}$ in this work. All input parameters are also provided in Table 4-1. Because of the rectifying pn junction, the measurement current is prohibited to flow through the bulk. Therefore, it is neglected.

The results of the simulations are plotted in Figure 4-6. On the y -axis, the ratio

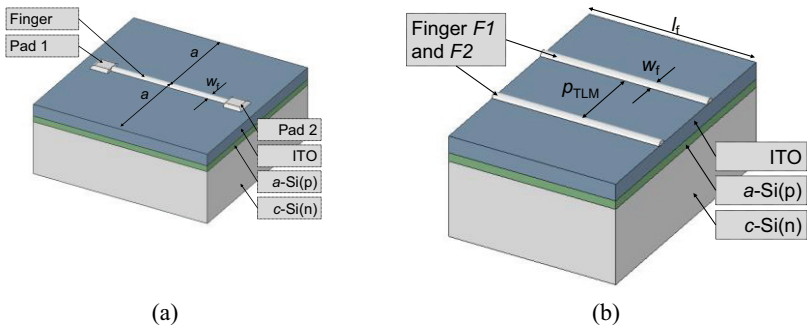


Figure 4-5 Sample structures based on which simulations are performed. In (a) the configuration used to determine the finger resistance is depicted, in (b) the configuration used to determine the contact resistivity is displayed.

4.4 Simulation-based strategies to avoid measurement errors

of the simulated resistance R_{12} (possibly affected by parallel current flow through underlying layer) and the actual absolute finger resistance R_f (unaffected by parallel current flow through underlying layer) is entered. In case that it equals one, the corresponding simulated configuration would allow for a correct determination of r_f . For $R_{12}/R_f < 1$, r_f would be underestimated and vice versa.

Table 4-1 Summary of input parameters for Quokka 3 simulations.

Input parameter	Value
l_f (cm)	1
w_f (μm)	50
h_f (μm)	20 / 20 / 1 (Ag / Cu / inkjet-printed Ag)
ρ_f ($\mu\Omega\cdot\text{cm}$)	5 / 15 / 5 (Ag / Cu / inkjet-printed Ag)
$R_{\text{SH,metal}}$ (m Ω /sq)	3 / 10 / 50 (Ag / Cu / inkjet-printed Ag)
$R_{\text{SH,ITO}}$ (Ω /sq)	100
ρ_c (m $\Omega\cdot\text{cm}^2$)	4
$\rho_{a\text{-Si(p)}}$ ($\Omega\cdot\text{cm}$)	$1\cdot 10^5$

In Figure 4-6 (a), $\rho_{a\text{-Si(p)}}$ is varied from almost zero to 1 m $\Omega\cdot\text{cm}$. It is obvious that for all three considered metal contacts R_{12}/R_f approaches 1 for $\rho_{a\text{-Si(p)}} > 0.6$ m $\Omega\cdot\text{cm}$. For lower values of $\rho_{a\text{-Si(p)}}$, r_f would be underestimated. The reason is the parallel operation of the finger's, the ITO layers', and the $a\text{-Si(p)}$ layer's resistance. Yet, typical $a\text{-Si(p)}$ layers exhibit $\rho_{a\text{-Si(p)}} > 1\cdot 10^5$ $\Omega\cdot\text{cm}$. It follows that their influence on the determination of r_f is neglectable.

In Figure 4-6 (b), the TCO sheet resistance $R_{SH,TCO}$ is varied from 25 to 1000 Ω/sq . To evaluate the impact of an ITO layer exhibiting $R_{SH,ITO} = 100 \Omega/sq$ on r_f determination, the x -axis is interrupted at this value. Systematic errors of 1% and 2% in the case of screen-printed silver- and copper-based fingers, respectively, are identified for $R_{SH,TCO} = R_{SH,ITO} = 100 \Omega/sq$. In the case of the inkjet-printed silver finger, the error is 9%. Yet, these values are increasing as $R_{SH,TCO}$ decreases. For example, taking a high mobility TCO like zirconium-doped indium oxide (IO:Zr) into account exhibiting a sheet resistance $R_{SH,IO:Zr} = 25 \Omega/sq$, the systematic error is 2%, 8% and 29%, respectively [39].

To avoid such errors, a correction of the r_f determination is certainly needed. If the electrical and geometrical characteristics of the TCO layer and the geometry of the metal contact are well-known, a simulation-based correction can be conducted: R_{12} can be simulated as a function of the metal's sheet resistance $R_{SH,metal}$. The simulated R_{12} value that equals the measured R_{12} value is to be associated with the corresponding value of $R_{SH,metal}$. From this, one can easily

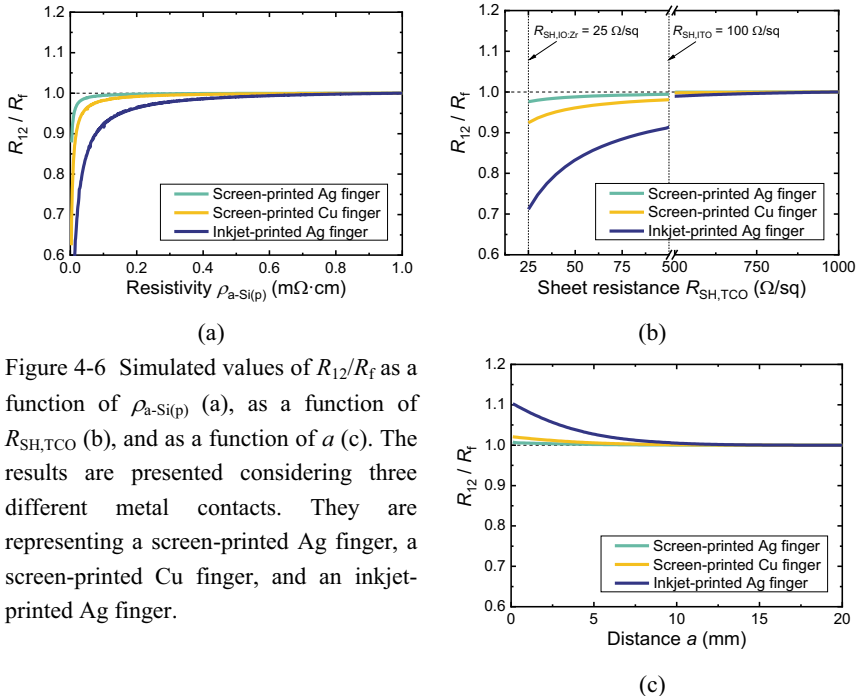


Figure 4-6 Simulated values of R_{12}/R_f as a function of $\rho_{a-Si(p)}$ (a), as a function of $R_{SH,TCO}$ (b), and as a function of a (c). The results are presented considering three different metal contacts. They are representing a screen-printed Ag finger, a screen-printed Cu finger, and an inkjet-printed Ag finger.

4.4 Simulation-based strategies to avoid measurement errors

count back to ρ_f and r_f using equation (4-20) and (4-10), respectively. A simpler and more practical method to correct the measured resistance R_{12} is to assume a parallel circuit of R_f and R_{ITO} , which is the resistance of the ITO layer underneath the finger. Then, r_f can be easily obtained from the measured resistance R_{12} , if R_{ITO} is known. This correction method is chosen in this work if necessary.

In Figure 4-6 (c), the width of the sample expressed by the distance a between finger and sample edge is varied (compare Figure 4-5 (a)). At all distances for which $R_{12}/R_f \approx 1$ holds, an additional metal contact can be placed on the ITO layer without electrically influencing the measurement of R_{12} . At all distances for which $R_{12}/R_f > 1$ holds, a parallel circuit of R_f , R_{ITO} , and the resistance of an additional metal contact, if present there, would be measured from pad 1 to 2. Considering the screen-printed silver- and copper-based contacts, a distance between two equal contacts is to be chosen to at least 1 mm and 5 mm, respectively, to ensure a systematic error of r_f of less than 1%. In the case of inkjet-printed silver-based contacts, the systematic r_f error is less than 1% for a distance of 10 mm. In this work, a distance of 14 mm is chosen in all cases (see also the guideline for test structure designs provided in Table 4-2).

Table 4-2 Guideline for test structure designs suitable for the determination of the finger resistance r_f on a transparent conductive oxide exhibiting a sheet resistance of 100 Ω/sq . The values in brackets are valid for a TCO exhibiting 25 Ω/sq .

	Screen-printed Ag	Screen-printed Cu	Inkjet-printed Ag
Systematic r_f error due to TCO	1% (2%)	2% (8%)	9% (29%)
Recommended contact distance	≥ 1 mm	≥ 5 mm	≥ 10 mm

Please note that if many fingers are measured in parallel such as, for example, in the case of a measurement from busbar to busbar of a full-size five-busbar SHJ solar cell exhibiting a finger number of 100, the ITO layer's influence vanishes. The reason is that in such case the ITO resistance R_{ITO} underneath each finger

from busbar to busbar is $2 \text{ k}\Omega$ (assuming $R_{\text{SH,ITO}} = 100 \text{ }\Omega/\text{sq}$), which is usually orders of magnitude higher than R_f .

4.4.2 Determination of the contact resistivity

In order to extract a benchmark for a robust TLM sample layout, *Quokka 3* simulations are performed using the structure depicted in Figure 4-5 (b). The same input parameters as mentioned in section 4.4.1 are used (see Table 4-1). Again, the three different kinds of metallization introduced there are considered. The y -axis in Figure 4-7 are entered by the ratio of the simulated resistance R_{12} from finger 1 to 2 with the actual resistance R_{TLM} . If $R_{12}/R_{\text{TLM}} > 1$, R_{TLM} is overestimated, if $R_{12}/R_{\text{TLM}} \approx 1$, R_{TLM} can be determined correctly.

In Figure 4-7 (a), the contact length l_f is chosen to be 10 mm and the finger width w_f is $50 \text{ }\mu\text{m}$. The contact distance p_{TLM} is varied from 1 mm to 10 mm . Even for small distances, the simulated resistance R_{12} is significantly higher than

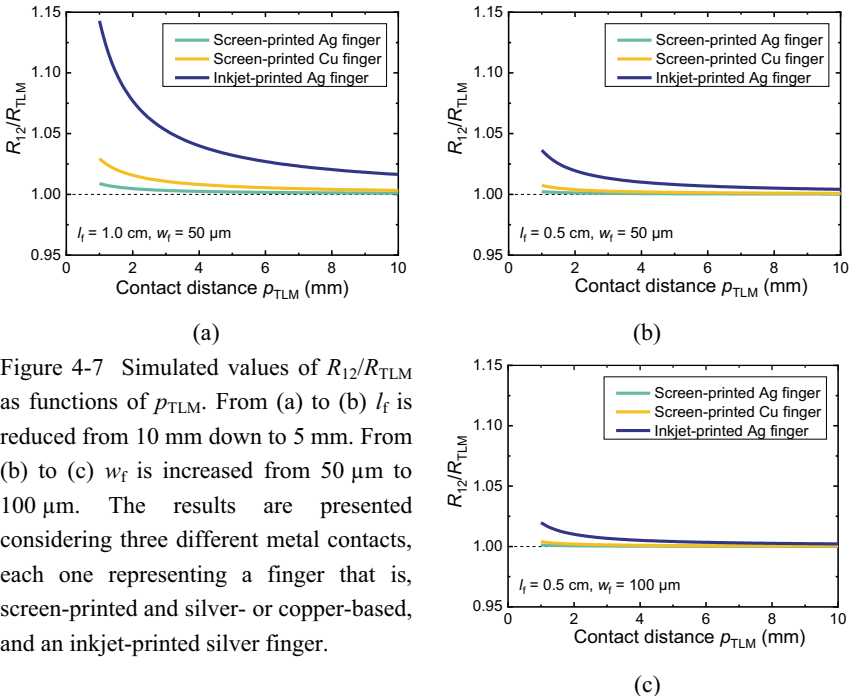


Figure 4-7 Simulated values of R_{12}/R_{TLM} as functions of p_{TLM} . From (a) to (b) l_f is reduced from 10 mm down to 5 mm . From (b) to (c) w_f is increased from $50 \text{ }\mu\text{m}$ to $100 \text{ }\mu\text{m}$. The results are presented considering three different metal contacts, each one representing a finger that is, screen-printed and silver- or copper-based, and an inkjet-printed silver finger.

4.4 Simulation-based strategies to avoid measurement errors

R_{TLM} . At $p_{TLM} = 1$ mm, this would cause a systematic error of 1% and 3% in the case of screen-printed silver- and copper-based contacts, respectively. In the case of the inkjet-printed contact, R_{TLM} is overestimated by 14%. The reason for this is the distribution of electrical field lines. TLM theory typically assumes that $r_f \approx 0$ (see section 4.3.2). The fingers can, thus, be seen as equipotential surfaces. As a consequence, the field lines are distributed homogeneously between the fingers (see Figure 4-8 (a)). If $r_f \approx 0$ is not valid, as especially in the case of the considered inkjet-printed metallization, the density of the electrical field lines decreases from the middle of the sample to the outer edges, assuming that the fingers are contacted in the middle for measurements (see Figure 4-8 (b)). Therefore, the effective electrically active ITO area between the contacts decreases, which leads to an overestimation of $R_{SH,ITO}$ and, according to equation (4-11), of R_{TLM} as well. Additionally, if $r_f \approx 0$ is not valid, R_{TLM} includes R_f , too, which also contributes to an overestimation of R_{TLM} . The former effect can be reduced by decreasing l_f to 5 mm as can be seen in Figure 4-7 (b). The latter effect can be reduced by decreasing R_f , e.g., by increasing w_f to 100 μm , as can be seen in Figure 4-7 (c).

In practice, there are limits to increase w_f and decrease l_f : if w_f is too large, TLM is not applicable any more since R_c tends to zero and, hence, cannot be measured correctly anymore [112]. If l_f is too small, handling of the samples becomes rather difficult. Furthermore, from Figure 4-7 (a)-(c) one can deduce that large contact distances would result in more reliable measurements. Yet, in practice, p_{TLM} cannot be chosen too large, because R_{ITO} would dominate R_{TLM} in such

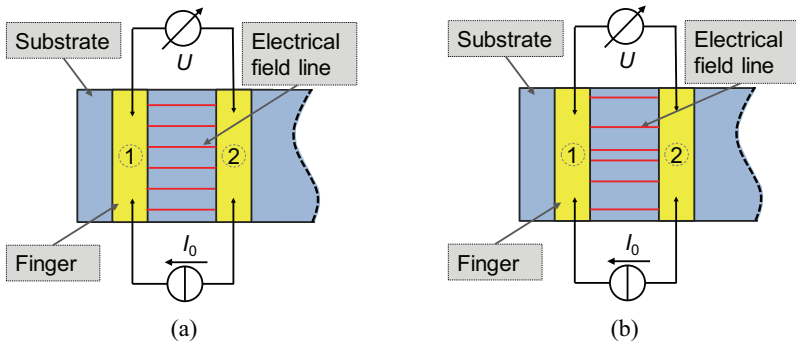


Figure 4-8 Electrical field lines between two fingers with $r_f \approx 0$ (a) and $r_f > 0$ (b) during R_{TLM} measurements.

case. As a consequence, signal-to-noise ratio would decrease. In this work, TLM samples of 4 mm width are used, exhibiting eight to ten fingers of 100 μm set finger width. The contact distance between adjacent fingers is 1.5 mm.

4.5 High-speed in-situ temperature measurement

To gain a deep understanding of contact formation processing and its impact on SHJ precursors, the knowledge of the sample temperature T_{sample} resolved over time during processing is crucial. For in-situ temperature measurements during IPL processing, the main challenge is the short pulse time t_{pulse} of down to 1 ms. Thus, a measurement rate of more than 10 kHz is required to ensure a sufficient resolution in time. In order to characterize the temperature of thin copper films during IPL processing, a measurement setup exhibiting a thermocouple with a response time of 1 ms is presented in Ref. [138]. However, such a thermocouple would be too slow to characterize the progress in temperature of the samples induced by the IPL processes developed in this work. Moreover, it cannot be applied to SHJ samples without significantly influencing the thermal system and, therefore, temperature. Thus, a thermographic measurement setup is developed to characterize T_{sample} during IPL processing. Since it is a contactless measurement, the measurement system's influence on the specimen is minimized. This has already been utilized, e.g., for the characterization of the wafer temperature during fast firing processes (process time of about one minute), as described in Ref. [107].

A second challenge for in-situ temperature measurements during IPL is that there is only limited space available in the IPL device's process chamber. To overcome both challenges (high speed and limited space), the pyrometer¹ *Metis H318* from *Sensortherm* is utilized, which is small and enables fast and spot-size (diameter of about 2 mm) in-situ temperature measurements during IPL processing of SHJ cells. The measurement rate is up to 20 kHz.

¹ Infrared cameras cannot meet such a high demand on speed. This prohibits temperature measurements during IPL processing resolved over space.

4.5 High-speed in-situ temperature measurement

Thermographic temperature sensing makes use of thermal radiation, emitted spontaneously by a body at a finite temperature [139]. The specific radiation M_λ of a so-called *black body* is described by Planck's law, namely:

$$M_\lambda = \frac{2\pi hc^2}{\lambda^5} \left(\frac{1}{e^{hc/\lambda k_B T} - 1} \right), \quad (4-21)$$

where λ is the wavelength, h is the Planck constant, c the velocity of light, k_B the Boltzmann constant and T the absolute temperature. The probability of a black body's surface to emit radiation of a certain wavelength, its emissivity ε , is equal to its absorption probability α at the same wavelength. This is known as *Kirchhoff's law*:

$$\alpha = \varepsilon = 1. \quad (4-22)$$

Real bodies are called *grey bodies* and their emissivity is less than one. Please note that ε depends on T , λ , and the angle γ under which thermal radiation is emitted. For thermographic measurements, the exact knowledge of ε in the specific measurement scenario is fundamentally important. It is determined by means of careful calibration [140]. Once ε is identified correctly, thermographic measurements ensure accurate recording of even fast temperature changes because of very short response times. The calibration procedure of the pyrometer performed in this work is explained in appendix A.

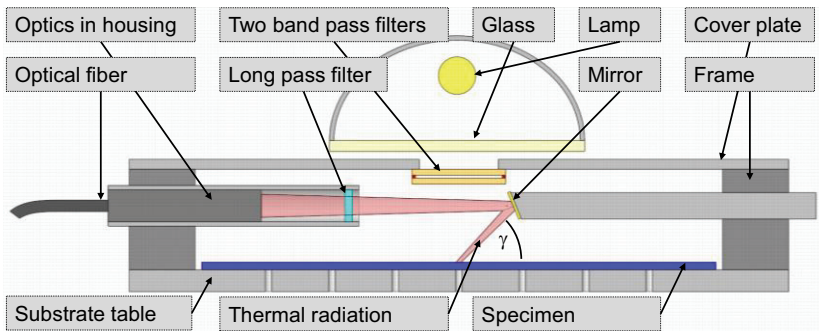


Figure 4-9 Thermographic measurement setup used to characterize T_{sample} in-situ during IPL processing. The sensor box connected with the optics by the optical fiber is not displayed. It is placed outside the IPL tool.

Figure 4-9 depicts the measurement setup utilized in the present work. Basically, a pyrometer, or radiometer, consists of a lens system and a detector [141]. The *Metis H318* uses an indium gallium arsenide (InGaAs) photodiode as a detector. Its current-voltage characteristics, when directed onto the specimen, is measured and converted into T_{sample} . Thermal radiation of wavelengths from 1.7 to 2.1 μm are detected. This allows for measuring temperatures from 120-520°C according to the tool manufacturer. Due to the shortage of space in the IPL process chamber, the thermal radiation emitted by the sample surface under an angle γ is directed to the pyrometer optics by means of a gold mirror. The objective exhibits a diameter of 12 mm and is connected with the sensor box by means of an optical fiber. Such a configuration is beneficial because of the lack of space in the IPL process chamber. Furthermore, the sensor box can be placed in a way that it is not irradiated during IPL processing and, thus, not heated up, which could influence the measurement. Before radiation enters the optics, it passes a long-pass filter. It ensures that no intense pulsed light of wavelengths below 1 μm hits the sensor and causes it to be damaged. The frame, on which all components are mounted, consists of aluminum with a glass-beaded surface. Steel cover plates are used to vary the size of the irradiated sample area and to avoid thermal radiation of the surroundings to influence the temperature measurements. A two-filter stack (band pass filters) located between sample and flash lamp is used to prevent thermal radiation of the lamp to reach the sensor. Both filters are thermally decoupled from each other by means of an about 3 mm wide air gap in order to prevent the detector from being influenced by the filters' thermal radiation. Both, thermal radiation of the lamp and the filters would artificially influence the temperature measurements. However, the Xenon flash passes the filters. Since the transmission of the Xenon flash through the filters is less than 100%, a correction of each temperature measurement is required. The correction procedure is described in detail in appendix A.

5 Advanced printing approaches

The present chapter is motivated by a reduction of the amount of silver consumed in printing of low-temperature metal contacts. In a first attempt, state-of-the-art screen printing is retained but silver in the printed paste is partially replaced by copper. Second, silver particles continue to be the base material but the printing technique changes to inkjet printing. However, such printing of metal particle-based inks is challenging in terms of process stability. To tackle this, thirdly, FlexTrail printing is utilized. All three approaches are evaluated on full-size silicon heterojunction solar cells towards characteristic solar cell parameters.

Selected cells are further processed into one-cell mini-modules. Still, the focus is set on reducing silver consumption by considering advanced module technology, i.e., NICE (New Industrial Solar Cell Encapsulation) and SWCT (Smartwire Connection Technology).

The sections 5.1-5.5 are based on Ref. [94, 95] which are published by the present author who is the main author of these publications as well.² The NICE modules also contributed to the results presented in Ref. [142].

² Jörg Schube is the main author of both mentioned publications. He has designed the corresponding experiments, performed and optimized the inkjet and FlexTrail printing processes, took the SEM pictures, coordinated and supervised all remaining process steps, and did the analyses. Mike Jahn is the inventor of FlexTrail printing. Moreover, he contributed to FlexTrail printing process development for SHJ solar cells.

5.1 Motivation

Today SHJ solar cell metallization typically consumes 200 mg silver per cell on average (including cells with and without busbars), which is the most expensive non-silicon material used in PV production [3]. Therefore, metallization schemes with a reduced silver consumption are highly desired. This chapter aims for both silver-reducing and industry-relevant metallization techniques for SHJ solar cells that additionally ensure high cell performance. Please note that even today optimized screen printing enables a paste laydown of down to 60 mg per SHJ cell [143]. This is contributed to the ongoing progress of screen printing in terms of finger width reduction but also to metal grid layouts that abandon busbars used together with innovative interconnection such as SWCT. Therefore, screen-printed busbarless SHJ cells allow for record efficiencies of up to 24.6%, especially due to less shading and also less ohmic losses [40].

A promising attempt for further silver reduction in screen printing, which could be easily integrated into current mass production, is to replace pastes' pure silver particles by silver-coated-copper-based ones. Lately, work is performed on the development of such pastes [144]. Silver coatings prevent the copper particles from oxidation and, therefore, ensure a high conductivity of the printed structures as well as simple handling (e.g., ambient instead of inert atmosphere). An optimum silver content of silver-coated copper pastes of only 37% is reported in Ref. [144].

A second approach to reduce silver consumption makes use of the well-known inkjet printing technique. However, inkjet-printed fingers exhibit a much lower A_f than screen-printed ones and, therefore, an increased r_f . In order to still keep ohmic losses of solar cells at a tolerable level, l_f needs to be reduced. Finger length is reduced if the number of busbars per cell is increased. However, such an approach would increase undesired silver consumption again. To avoid that, a busbarless grid layout and interconnection by means of multiple copper wires is a promising alternative (e.g., SWCT). Hence, the use of inks based on nanoscale silver particles enables a significant decrease in wet ink laydown (wet ink applied to the substrate) even down to below 10 mg per cell (busbarless) [104].

5.2 Sample preparation and characterization

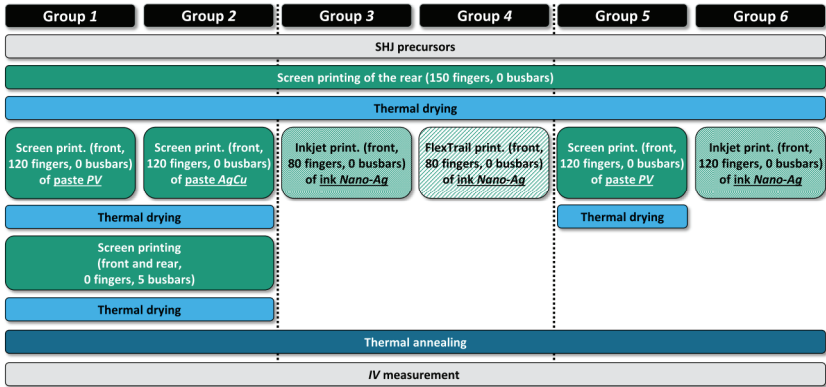


Figure 5-1 Sketch of experimental process flow utilized to investigate advanced printing techniques applied to SHJ samples. The picture is adapted from Ref. [94, 95].

A known issue, which arises along with inkjet printing of nanoparticles, is unreliable jetting behavior [93]. This often restricts the printing process window and the jetting stability. *FlexTrail* printing is developed at Fraunhofer ISE (see section 3.2.3) to overcome this challenge. With the same nanoparticle ink as used for inkjet printing, the process stability enhances significantly and the finger geometry as well as the cell performance improves.

5.2 Sample preparation and characterization

In order to investigate advanced printing techniques for SHJ solar cells, an experiment as displayed in Figure 5-1 is conducted. SHJ precursors from an external manufacturer with 156.8 mm edge length (area of 244.3 cm²) and a thickness of 160 μm are utilized. They exhibit an alkaline textured *n*-type Czochralski-grown (Cz) Si base substrate with a resistivity ρ_{base} of 1.3 Ω·cm, in- and extrinsic (*p*- and *n*-type on the rear and front side, respectively) hydrogenated *a*-Si:H layers, and ITO layers on both sides. More details about the sample structure are provided in section 2.2.1.

On the rear side of all cells, contact grids with 150 fingers and a set finger width $w_{\text{f,set}} = 50 \mu\text{m}$ are screen-printed utilizing a commercially available low-

temperature silver-based paste. Then, they are dried at a temperature of 200°C for 1 min.

On the group 1 samples' front sides, 120 fingers with $w_{f,set} = 40 \mu\text{m}$ are screen-printed using a commercially available silver-based paste *PV* designed for PV application and dried afterwards (200°C for 1 min). In group 2, a screen printing paste *AgCu* is utilized, which is based on silver-coated copper particles and commercially available as well. According to the paste manufacturer, paste *AgCu* contains about 30% less silver than paste *PV* (referring to the pastes' masses). More details about the pastes are provided in appendix B. After printing and drying of the rear and front fingers, group 1 and 2 samples receive five silver-based busbars on both sides by means of screen printing.

The front sides of group 3 cells obtain grids exhibiting 80 fingers, which is identified as an optimum number with respect to the busbarless layout using a *Gridmaster*- and *Pitchmaster*-based tool [145, 146]. Front grids are printed by means of inkjet printing utilizing a commercially available Ag nanoparticle ink. It is labelled *Nano-Ag* in the following (see appendix B for further information). The number of passes per finger n_{pass} varies from one to five. During printing, the cells and the printhead are kept at a constant set temperature of 60°C (cells) and 50°C (printhead) for the purpose of reduced finger width and printing process stability. In group 4, SHJ cells' front sides are metallized by means of FlexTrail printing (80 fingers) at a constant substrate temperature of 60°C using the same ink *Nano-Ag*. Since inkjet and FlexTrail printing is performed on lab-type equipment, the number of fabricated samples of group 3 and 4 is rather small (two to three samples per group). In order to determine the wet ink laydown, one cell is FlexTrail-printed at a set substrate temperature of 25°C, which reduces evaporation of solvents. The sample is weighted before and after printing by means of a high-precision weighing tool (corresponding process steps not displayed in Figure 5-1).

Cells of group 5 and 6 are provided with screen-printed front grids exhibiting $w_{f,set} = 40 \mu\text{m}$ and inkjet-printed grids with $n_{pass} = 1$, respectively. Inkjet printing is performed as described above (compare group 3). For comparison reasons, the finger number of the screen- and inkjet-printed grids is 120 in both cases.

5.3 Silver-coated-copper-based screen-printed contacts

After all printing steps are completed, the SHJ cells are annealed at a temperature of 200°C for 30 min using a conveyor belt furnace. Finally, *IV*-measurements at standard testing conditions against a black background are conducted [147]. The busbarless cells are measured by means of a PCB^{TOUCH} system from *Pasan* exhibiting 30 wires for current and five for voltage measurements, which are excluded with respect to shading during calibration procedure [148]. In the case of extremely thin and flat metal contacts, a potential *FF* overestimation is to be respected in such measurements as discussed in detail in Ref. [149]. An analytical calculation of the *FF* and corresponding η overestimation is provided in section 5.4. Moreover, selected grids are analyzed by means of confocal microscopy and SEM. Other samples are analyzed regarding finger geometry, r_f , and ρ_c (not shown in Figure 5-1).

Two cells of group 1 and 2 (one printed with paste *PV* and one with paste *AgCu*) are used for further processing into bifacial New Industrial Solar Cell Encapsulation (NICE) one-cell mini-modules [150, 151]. Such modules do not exhibit ethylene-vinyl acetate (EVA) foils and soldered interconnections. Copper interconnectors (width of about 1.5 mm) instead of standard silver-coated-copper-based ones are glued on the cells' busbars. On the module edges, a seal tape is applied. Finally, solar glass planes (both sides are provided with ARCs) are pressed on both sides. All these manual steps are conducted externally.

Moreover, selected cells of group 3 and 4 serve as basis for monofacial SWCT one-cell mini-modules (in each case one inkjet sample with n_{pass} varied from one to five, one sample without a front grid, and one FlexTrail-printed sample). They exhibit glasses with ARCs on the front and backsheets at the rear. 18 copper wires (round, width of 250 μm) coated with an alloy, which melts at low temperatures for the purpose of contact formation, are laminated using a thermoplastic polyolefin (TPO) foil on both sides of the cells. All process steps are conducted externally and manually as well.

5.3 Silver-coated-copper-based screen-printed contacts

In a first step, screen printing of a paste based on silver-coated copper particles is investigated. In Figure 5-2 (a), a SEM picture showing such particles' cross-

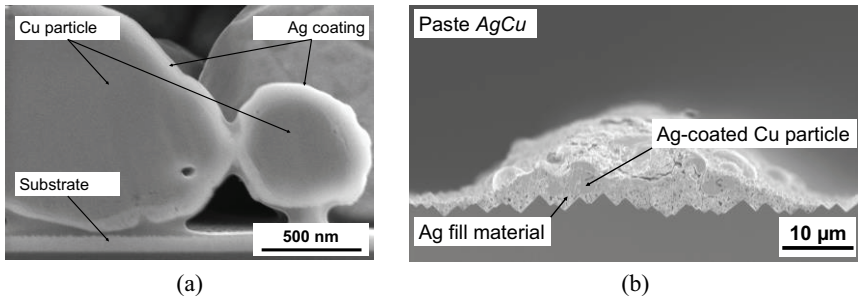


Figure 5-2 Cross-sectional view of a silver-coated copper particle in (a).³ In (b) a cross-section of a finger screen-printed by means of paste *AgCu* is depicted. (b) is redrawn from Ref. [120].

sections is presented. Here, copper is prevented from oxidation by means of a thin silver coating, which can be produced, e.g., electrochemically. Such a coating enables metallization processing even without the use of inert conditions simplifying back end processing. Between the large silver-coated copper particles (diameters of about 5 μm), small silver particles (diameters of 0.1–1.0 μm) act as fill material (see Figure 5-2 (b)). They enhance inter-particle contacts in the metal electrode and, therefore, its conductivity.

The mean SHJ cell performance (five busbar layout) achieved with paste *AgCu* (samples of group 2) is compared to that obtained by using paste *PV* (samples of group 1). Table 5-1 presents corresponding *IV*-related data. The V_{OC} values of both groups of cells are on a similar level (734.9 ± 0.8 mV and 733.4 ± 0.5 mV for paste *PV* and *AgCu* front grids, respectively). Because the ITO layer prohibits the paste from interaction with the SHJ wafer (e.g., copper inter-diffusion), no metallization-induced degradation of the cells is detected [99].

However, the difference in mean FF of 0.8%_{abs} is significant. It indicates that the front grids printed by means of paste *AgCu* cause even less series resistance

³ Please note that the silver-coated copper particle depicted in Figure 5-2 (a) does not correspond to paste *AgCu* but to a similar paste based on such particles. The reason is that the manufacturer of paste *AgCu* forbids to publish detailed views of this paste.

5.3 Silver-coated-copper-based screen-printed contacts

losses than the paste-*Ag*-based grids. The high amount of silver fill material of paste *AgCu* pays off here because it ensures a pronounced inter-particle contact on microstructural level and, therefore, a low finger resistance. In fact, r_f is $2.1 \pm 0.1 \Omega/\text{cm}$ and $2.8 \pm 0.3 \Omega/\text{cm}$ in the case of paste *AgCu* and paste *PV*, respectively (typical values for low-temperature pastes). Please note that the lower r_f of paste *AgCu* compared to paste *PV* is also contributed to the slightly higher A_f of paste *AgCu* ($A_f = 398.7 \pm 22.0 \mu\text{m}^2$) compared to paste *PV* ($A_f = 380.4 \pm 22.1 \mu\text{m}^2$). Nevertheless, ρ_f of paste *AgCu* is $8.4 \pm 0.6 \mu\Omega \cdot \text{cm}$ and, therefore, $2.3 \mu\Omega \cdot \text{cm}$ lower compared to paste *PV* ($\rho_f = 10.7 \pm 1.3 \mu\Omega \cdot \text{cm}$). For the calculation of ρ_f , the reader is referred to equation (4-10). The contact resistivity of both pastes at the ITO/metal contact interface does not differ significantly. It is below $5 \text{ m}\Omega \cdot \text{cm}^2$ in both cases.

Table 5-1 *IV*-related data of SHJ solar cells (6 samples per group) exhibiting five busbars (group 1 and 2 samples, see Figure 5-1). The front fingers are screen-printed either by means of paste *PV* or *AgCu*. Mean values and corresponding standard deviations are presented.

Paste	V_{oc} (mV)	j_{sc} (mA/cm ²)	<i>FF</i> (%)	η (%)
<i>PV</i>	734.9 ± 0.8	37.3 ± 0.1	78.8 ± 0.5	21.6 ± 0.1
<i>AgCu</i>	733.4 ± 0.5	37.0 ± 0.1	79.6 ± 0.1	21.6 ± 0.1

Due to the higher w_f of paste *AgCu* fingers ($w_f = 59.7 \pm 3.4 \mu\text{m}$) compared to the paste *PV* fingers ($w_f = 49.4 \pm 1.3 \mu\text{m}$), the j_{sc} of cells with a paste *AgCu* front grid ($j_{\text{sc}} = 37.0 \pm 0.1 \text{ mA}/\text{cm}^2$) is slightly reduced compared to the j_{sc} of those exhibiting a paste *PV* front grid ($j_{\text{sc}} = 37.3 \pm 0.1 \text{ mA}/\text{cm}^2$).

Regarding η , the differences in *FF* and j_{sc} of the two groups of cells are levelled out and both achieve a mean η of $21.6 \pm 0.1\%$. However, according to the pastes' specifications, paste *AgCu* contains 30% less silver (referring to the paste's mass) compared to paste *PV*. Actually, in this experiment the silver saving potential of paste *AgCu* is not exploited because it is compensated by the 30% higher wet paste laydown during printing. This is $45.6 \pm 0.9 \text{ mg}$ per front

grid and 63.2 ± 0.5 mg per front grid in the case of paste *PV* and *AgCu*, respectively. A lower paste laydown of paste *AgCu* is expected from a screen printing process optimization, e.g., squeegee speed or lift-off (see section 3.2.1).

5.4 Inkjet-printed nanosilver-based contacts

Inkjet printing is known for its significant silver saving potential compared to screen printing. A particularly low wet ink laydown is achievable if n_{pass} is low. In this section, the correlation between SHJ solar cell performance and n_{pass} is investigated.

Figure 5-3 depicts *IV*-related data of busbarless cells as a function of n_{pass} . The variation of n_{pass} is conducted on front grids exhibiting 80 fingers (samples of group 3). Cells without a front grid ($n_{\text{pass}} = 0$) are considered as well.

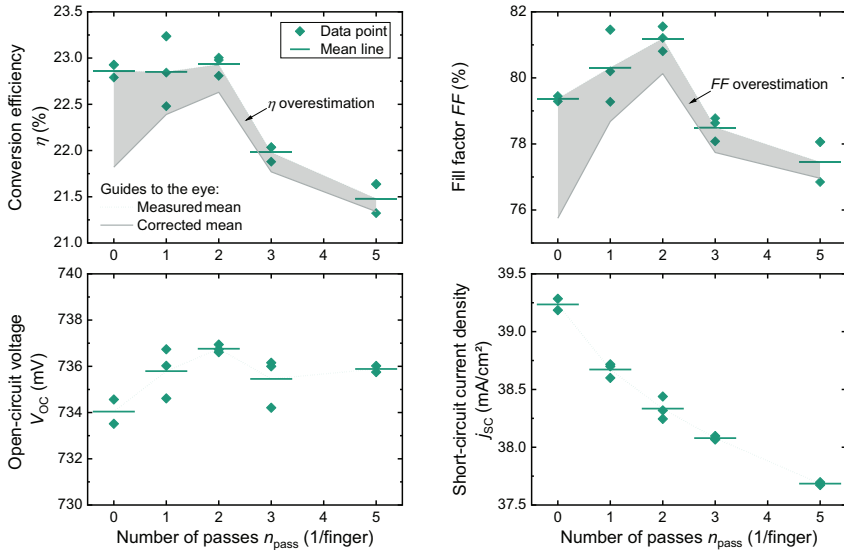


Figure 5-3 *IV*-related data of busbarless SHJ solar cells with inkjet-printed front grids, exhibiting 80 fingers, plotted versus n_{pass} , redrawn from Ref. [94, 95]. Samples with $n_{\text{pass}} = 4$ are not fabricated. The connecting lines of the measured mean values (green, dotted) and the connecting lines of the corrected mean values (grey, solid) are displayed as guides to the eye. The correction of FF and η is explained further below in the present section.

5.4 Inkjet-printed nanosilver-based contacts

The solar cells' V_{OC} values are mainly independent of n_{pass} . This is quite different with the j_{SC} : the more passes the lower is the j_{SC} because the finger width w_f of fingers with $n_{pass} = 1$ ($w_f = 75.0 \pm 1.4 \mu\text{m}$) is smaller than of fingers with $n_{pass} = 5$ ($w_f = 80.8 \pm 6.0 \mu\text{m}$).⁴ Additionally, fingers printed with one pass only do not cover the pyramid tips of the SHJ cells' alkaline texture as much as those fabricated with five passes. This results in an additional j_{SC} gain of the corresponding solar cells (also see add-in window in Figure 5-5 (a)). In fact, comparing the achieved j_{SC} values of the cell group featuring $n_{pass} = 1$ to the one featuring $n_{pass} = 0$ and taking the measured finger width into account, an effective optical finger width for the group with $n_{pass} = 1$ of only 40% of the actually printed width is determined. In contrast, the effective finger width of the fingers featuring $n_{pass} = 5$ is close to 100% as it covers entirely all pyramid tips (also compare Figure 5-9).

Nevertheless, η reaches its mean maximum for $n_{pass} = 2$ instead of $n_{pass} = 1$, namely 23.0%. In order to explain this, one has to take the FF data into account. A maximum mean FF of 81.2% is achieved in the case of a grid exhibiting $n_{pass} = 2$. The reduced mean FF of solar cells with grids featuring $n_{pass} = 0$ or $n_{pass} = 1$ (2.1%_{abs} and 0.9%_{abs} reduction, respectively) can be explained by higher series resistance losses due to reduced A_f or $A_f = 0$. However, for $n_{pass} > 2$, FF strongly decreases as well. This can be attributed to the PCB^{TOUCH} measurement setup: the front metal grids with $n_{pass} > 2$ are higher than those featuring $n_{pass} \leq 2$. Therefore, the PCB^{TOUCH} front wires contact the metal fingers only (Figure 5-4 (a)), while for flatter grids the wires also contact the ITO layer besides the fingers (see sketch in Figure 5-4 (b)) resulting in lower series resistance and thus higher FF . This interpretation is supported by a comparison of IV -related data of solar cells with inkjet- and screen-printed front grids (samples of group 5 and 6) exhibiting the same number of fingers (IV -related data provided in Table 5-2). Although the finger resistance of a screen-printed

⁴ Please note that the presented values of w_f are rather high because the printing process is optimized regarding process stability at the expense of w_f in the present work. Narrower fingers printed with particle-based inks are already reported, e.g., in Ref. [104].

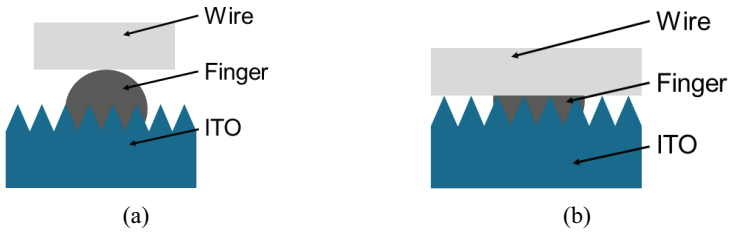


Figure 5-4 Wire contact configuration in the case of a finger exceeding the substrate texture in terms of its height (a) and in the case of a finger, which does not exceed the texture in terms of its height (b).

finger is at least one order of magnitude smaller than the finger resistance of an inkjet-printed one exhibiting $n_{\text{pass}} = 1$, the mean FF of cells with such inkjet-printed front grids is higher than the one of cells with a screen-printed front grid. Due to the FF advantage and a j_{sc} gain of 0.8 mA/cm^2 , the cell with the highest efficiency in this experiment features an inkjet-printed front grid reaching $\eta = 23.3\%$.

Table 5-2 Mean IV -related data (corrected values are noted in brackets) of busbarless SHJ solar cells (five samples per group) with inkjet- or screen-printed front grids exhibiting 120 fingers (group 5 and 6 in Figure 5-1). The rear sides of both groups of cells are screen-printed. Errors represent the standard deviations.

Printing technique	n_{pass} (1/finger)	V_{OC} (mV)	j_{sc} (mA/cm ²)	FF (%)	η (%)
<i>Inkjet printing</i>	1	733.6 ± 1.1	38.6 ± 0.1	81.7 ± 0.2 (80.4)	23.1 ± 0.1 (22.7)
<i>Screen printing</i>	-	736.5 ± 1.0	37.9 ± 0.1	80.1 ± 0.5	22.4 ± 0.2

Taking into account the SEM images presented in Figure 5-5, the behavior of FF as a function of n_{pass} can be explained as follows: the inkjet-printed finger with $n_{\text{pass}} = 1$ (see Figure 5-5 (a)) is mainly located in the valleys of the alkaline textured cell surface in a way that an interconnecting wire contacts the metal

5.4 Inkjet-printed nanosilver-based contacts

finger and the ITO layer besides the finger as well. The screen-printed finger (Figure 5-5 (b)), on the other hand, is significantly higher and, therefore, lifts the contacting wire above the ITO layer, which allows electrical contact formation at the wire-finger crossings only. Please note that in SWCT modules, the wires are laminated on the cell by means of a foil. It is assumed that, thereby, wires also contact the substrate in the case of screen-printed metallization.

Regarding PCB^{TOUCH} measurements, it is important to note that FF and, therefore, η is artificially increased proportionally to r_f , or more precisely the effective resistance $r_{f,eff}$ taking into account conductivity of the underlying ITO layer. The reason is the 2 mm wide gap between adjacent current and voltage wires, for high r_f inducing a non-neglectable voltage drop between current and voltage probe. This voltage drop is added to the cells' V_{mpp} increasing the FF artificially. This effect is discussed in detail in Ref. [149].

The FF of cells featuring inkjet-printed front grids is overestimated in the present work as well. Here the overestimation is analytically determined at the maximum power point, assuming $R_{SH,ITO} = 60 \Omega/sq$ and $r_f = 250 \Omega/cm$ ($n_{pass} = 1$). The use of a grid exhibiting 120 fingers results in a calculated voltage drop of 10.2 mV between the adjacent current and voltage sensors of the PCB^{TOUCH} unit (distance of 2 mm). In other words: the current measurement is associated with a too high voltage value. Therefore, FF is overestimated by 1.3%_{abs} and η by 0.4%_{abs} (see corresponding corrections in brackets in Table

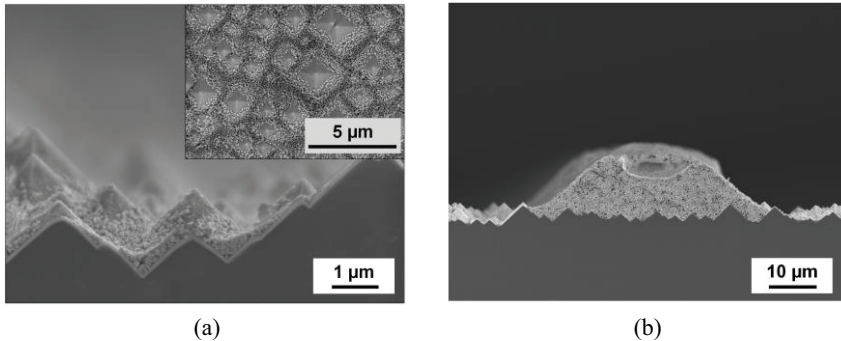


Figure 5-5 SEM images of an inkjet-printed one-pass finger's (a) and a screen-printed finger's (b) cross-section (paste PV) at different magnifications, redrawn from Ref. [94, 95]. The add-in window in (a) depicts the top-view of the same inkjet-printed finger.

5-2). For higher values of n_{pass} , as presented in Figure 5-3 (note that the finger number is 80 here), r_f is decreasing and, therefore, the FF overestimation decreases as well (see grey, solid lines in Figure 5-3). On the other hand, the overestimation is significantly increasing as no grid is printed on the front ($n_{\text{pass}} = 0$). In this case, the current transport to the wires is completely performed by the ITO layer and 3.6%_{abs} and 1.0%_{abs} FF and η overestimation are calculated, respectively. If the distance of adjacent current and voltage probes was reduced to 1 mm, the FF overestimation would be smaller than 1%_{rel} in all cases relevant in this work.

5.5 Comparison of inkjet- and FlexTrail-printed solar cells

The previous section 5.4 shows that even higher performance of busbarless SHJ cells is achieved if inkjet printing is used for (front) metallization instead of screen printing. However, inkjet printing of particle-based inks is sophisticated and sometimes not reliable. Therefore, FlexTrail printing is introduced (for more details, the reader is kindly referred to section 3.2.3).

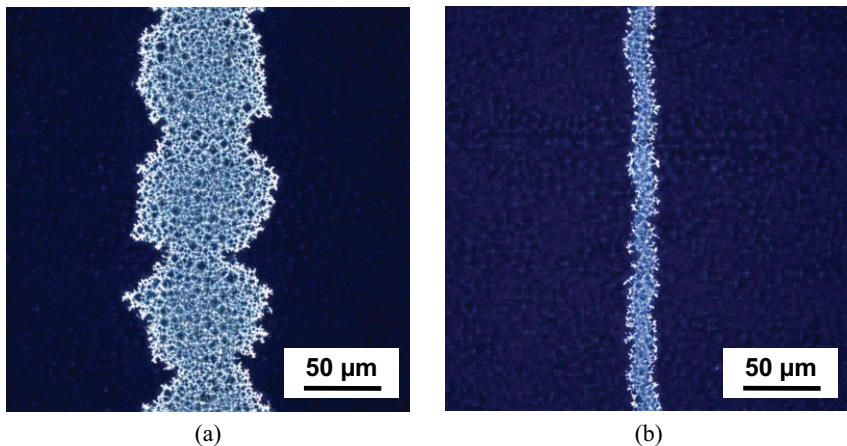


Figure 5-6 Microscopy images depicting the top view of an inkjet-printed finger ($n_{\text{pass}} = 1$) featuring a mean $w_f = 75.0 \pm 1.3 \mu\text{m}$ and a finger printed by means of FlexTrail (b) featuring a mean $w_f = 15.9 \pm 0.9 \mu\text{m}$ on top of alkaline textured SHJ solar cells. Both fingers are printed using the same ink *Nano-Ag*. h_f is in the range of 200 nm. The images are redrawn from Ref. [94, 95].

5.5 Comparison of inkjet- and FlexTrail-printed solar cells

In Figure 5-6, an inkjet-printed finger ($n_{\text{pass}} = 1$) is compared to a finger fabricated by means of FlexTrail printing (samples of group 3 and 4, respectively), whereby the same ink *Nano-Ag* is utilized. The comparison shows that for FlexTrail-printed fingers, the edges are significantly more homogenous and the finger appears more compact. The mean finger width is significantly reduced from $75.0 \pm 1.3 \mu\text{m}$ (inkjet) down to $15.9 \pm 0.9 \mu\text{m}$ (FlexTrail). These values are achieved on alkaline textured SHJ solar cells covered by ITO layers (see description of the sample structure in section 5.2 and section 2.2.1).⁵ On cell level, this results in a mean gain in j_{SC} of 0.5 mA/cm^2 . Thereby, the maximum efficiency increases from 23.2% by $0.5\%_{\text{abs}}$ up to 23.7% (both *FF* and η uncorrected/as-measured). Table 5-3 presents corresponding cells with the highest efficiencies, printed by means of inkjet and FlexTrail.

Table 5-3 *IV*-related data of busbarless SHJ solar cells, each one with the highest η , printed by means of inkjet and FlexTrail (front grids exhibiting 80 fingers). Corrections are shown within brackets.

Printing technique	n_{pass} (1/finger)	V_{OC} (mV)	j_{SC} (mA/cm ²)	<i>FF</i> (%)	η (%)
<i>Inkjet printing</i>	1	736.7	38.7	81.5 (79.9)	23.2 (22.7)
<i>FlexTrail printing</i>	-	737.4	39.2	82.1 (80.5)	23.7 (23.2)

The FlexTrail printing process is very stable and simple to handle compared to inkjet printing (e.g., no jetting instability, less parameters to be tuned). It offers a large process window in the case of the ink *Nano-Ag* and interruptions of the printed lines are very unlikely. Furthermore, it offers the opportunity to enhance

⁵ FlexTrail printing already achieves minimal finger widths of $10 \mu\text{m}$ and $8 \mu\text{m}$ on textured and planar ITO-coated surfaces, respectively.

the ink's silver content compared to inkjet and, thereby, higher aspect ratios of metal fingers can be expected. Work aiming at further process optimization and parallelization is in progress.

These results demonstrate that SHJ solar cells featuring FlexTrail-printed grids outperform inkjet-printed ones. Thereby, printing process stability is significantly improved. Proof of this fact is that more cells can be printed with FlexTrail without process interruptions (e.g., due to finger interruptions or missing fingers) compared to inkjet printing using the same ink. Thereby, FlexTrail reduces wet ink laydown to below 5 mg per front grid exhibiting 80 fingers. This demonstrates both the silver reduction potential of FlexTrail printing and, simultaneously, the performance potential of busbarless SHJ solar cells with FlexTrail-printed contact grids. In the following section 5.6, the performance of resource-effective fabricated mini-modules consisting of such cells is analyzed.

5.6 Advanced printed metallization in one-cell mini-modules

To evaluate the potential of SHJ solar cells featuring screen-, inkjet-, or FlexTrail-printed front grids as presented in the preceding sections, selected cells are further processed into one-cell mini-modules. Cell-to-module losses (CTM), e.g., of the FF , are calculated by means of the equation

$$CTM_{FF} = \frac{FF_{\text{module}}}{FF_{\text{cell}}} \cdot 100\% - 100\%. \quad (5-1)$$

Figure 5-7 presents the obtained CTM results. Both NICE modules exhibit a high maximum power P_{mpp} in the range of 4.8 W and efficiencies of up to 20.1% (see Figure 5-7 (a)). Their V_{OC} values appear to be not affected by module fabrication. Furthermore, there is only little relative FF loss (1.0%_{rel} and 1.1%_{rel} loss for paste PV and $AgCu$ front grids, respectively), which demonstrates the high quality of the NICE pressing contacts. (A comprehensive analysis of the modules' R_s can be found in Ref. [142].) A photo of an exemplary NICE module is depicted in Figure 5-8.

5.6 Advanced printed metallization in one-cell mini-modules

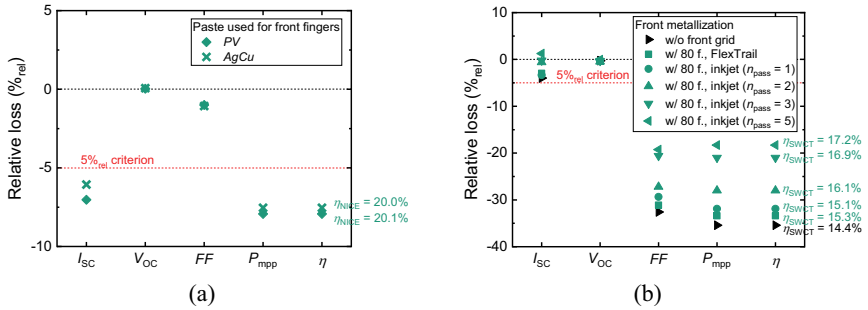


Figure 5-7 Relative CTM losses of NICE (a) and SWCT one-cell mini-modules (b), which are based on cells with screen-, inkjet-, and FlexTrail-printed front grids. The relative losses of I_{SC} , V_{OC} , FF , P_{mpp} , and η are depicted. Each data point represents one one-cell mini-module. The red-dotted lines mark the 5%_{rel} criterion for module power, which is defined as the target.

The main CTM loss in the case of NICE is contributed to the short-circuit current I_{SC} (7.0%_{rel} and 6.1%_{rel} loss for paste *AgCu* and *Ag* front grids, respectively) mainly driven by the absence of an EVA. This causes significant losses due to reflections at the air-glass interface in the module. Furthermore, the shape and size of the copper interconnectors are not fully optimized in terms of optics (e.g., no texture). In this work, a loss of less than 5%_{rel} is targeted following the international electrotechnical commission standard, which is only barely failed (7.5%_{rel} and 7.9%_{rel} P_{mpp} and also η loss for paste *AgCu* and *Ag* front grids, respectively) [152]. Based on simulations, it is stated in Ref. [142] that module efficiency would be increased by 0.6%_{abs} if an EVA was utilized. This simple add-on would allow for passing the 5%_{rel} criterion for both paste *PV* and *AgCu* NICE modules.

I_{SC} losses are not an issue in the case of the SWCT modules presented in Figure 5-7 (b). This is attributed both to the presence of a TPO foil as well as the small wire size and beneficial (here: round) wire geometry [143]. One can see from the data that module fabrication does not affect V_{OC} , too.

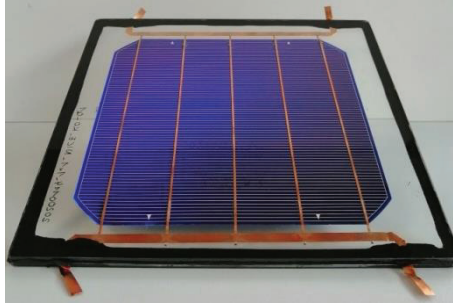


Figure 5-8 Photo of a NICE one-cell mini-module existing of one SHJ solar cell with an edge length of 156.8 mm.

However, the FF loss of all presented modules is large with more than 19%_{rel.}. All modules thus fail the 5%_{rel.} criterion. A large FF loss has actually been expected because the IV -measurements are performed using a configuration exhibiting 30 current wires on the front, but the modules exhibit 18 wires (per side) only. As a consequence, the distance between wires and, therefore, l_f is increased by a factor of 1.7 in the case of the modules. This significantly increases R_s -related losses because inkjet- and FlexTrail-printed metal contacts exhibit high values of r_f . Although CTM_{FF} losses are decreased when n_{pass} is increased, which corresponds to a reduction of r_f , they remain rather high. A FF increase of about 20%_{rel.} (inkjet, five passes) to 25%_{rel.} (FlexTrail and inkjet, one pass) is expected if the wire number increased from 18 to 30. (This estimation assumes that a R_s reduction of $1 \Omega \cdot \text{cm}^2$ induces a FF increase of 4.6%_{abs.} [153].) This would reduce CTM_{FF} to about 5% and 10% in the case of inkjet with $n_{pass} = 5$ and in the case of both FlexTrail and inkjet featuring $n_{pass} = 1$, respectively.

Moreover, it is assumed, that the electrical contact between wire interconnectors and cell is not ideally formed in these SWCT modules, which may also contribute to the high CTM_{FF} loss. The alloy covering the copper wires is optimized for contacting silver fingers of a typical height [154]. As mentioned above, the inkjet- and FlexTrail-printed grids are very flat ($h_f < 1 \mu\text{m}$) and cover the pyramid tips of the alkaline texture only partially. Certainly, this increases contact resistivity at the wire/cell interface. The fact that FF loss decreases

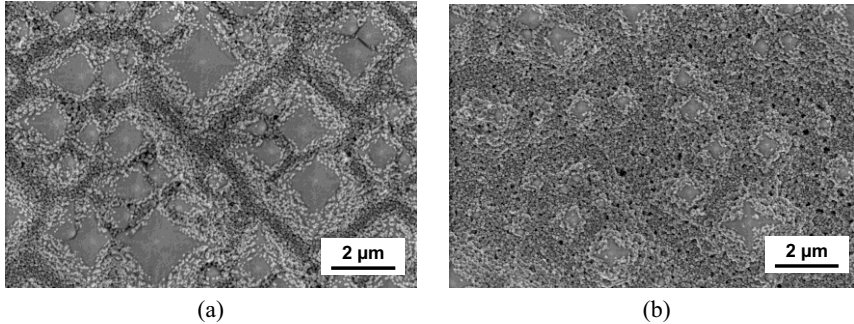


Figure 5-9 Comparison of fingers with $n_{\text{pass}} = 1$ (a) and $n_{\text{pass}} = 5$ (b). The SEM pictures display the fingers in the top view.

when n_{pass} increases supports this interpretation (see Figure 5-7 (b)). The higher fingers printed with $n_{\text{pass}} = 5$ allow an improved wire/metal finger contact in contrast with fingers exhibiting $n_{\text{pass}} = 1$ because the former metal fingers entirely cover the alkaline textured surface of the substrate, which the latter do not (see comparison of a finger featuring $n_{\text{pass}} = 1$ and $n_{\text{pass}} = 5$ in Figure 5-9 (a) and (b), respectively). To this date, this hypothesis cannot be further tested because the modules are fabricated externally and have not been sent back to the present author. This prohibits the necessary microstructure analyses that could further confirm this assertion.

It is assumed that SWCT mini-modules based on inkjet- and FlexTrail-printed SHJ solar cells exhibiting 30 wires per side would lead to a significant module performance increase (and decrease in CTM loss).

5.7 Chapter summary

In this chapter, three approaches aiming at silver reduction in SHJ solar cell metallization are investigated. Furthermore, the performance of corresponding cells is analyzed on mini-module level as well.

In a first attempt, a conventional and solely silver-based paste for screen printing is replaced by a paste exhibiting silver-coated copper particles. The pastes are commercially available. The comparison of both pastes is conducted on the front of SHJ solar cells (five-busbar layout). It reveals that equal conver-

sion efficiencies are achievable. However, the silver reduction potential of 30% (referring to the paste's weight) of the paste $AgCu$ is not fully exploited in this study because the substitution of silver by copper is compensated by higher paste laydown during printing. This issue needs to be addressed either by optimization of the screen printing process and/or by a further reduction of the silver amount in the paste. On module level (one-cell NICE mini-modules), both pastes exhibit a similar high performance as well (η of 20.0% to 20.1%). The use of an EVA could even increase η by 0.6%_{abs} and would allow the modules to pass the 5% criterion, according to simulations presented in Ref. [142]. The NICE technology offers an additional resource saving potential compared to standard module technologies, e.g., by means of the use of pure copper ribbons instead of silver-coated ones.

Inkjet printing using silver-nanoparticle-based inks allows for a silver reduction down to below 10 mg/busbarless SHJ solar cell. It is demonstrated in a second step that even with very low values of n_{pass} , high η can be achieved. Thereby, FF benefits from the current extraction both at the metal contact and at the ITO layer contact besides the metal electrode. However, it is to be noted that the specific wire configuration of the PCB^{TOUCH} device is accompanied by an artificially enhanced FF and, hence, η scaling with increasing r_f . In the present work, this issue is addressed by an analytical correction of the measurements at the maximum power point. Even after correction, inkjet-printed solar cells outperform comparable screen-printed ones, significantly.

Inkjet printing of particle-based inks is known for sophisticated process tuning and its unreliability in terms of jetting behavior. However, it can be replaced by FlexTrail printing using the same inks for inkjet printing. Thereby, FlexTrail allows for an enhanced printing process stability, extremely narrow fingers ($w_f = 15.9 \pm 0.9 \mu\text{m}$ on cell level with the potential of a further reduction down to 10 μm on textured substrates), and high cell performance (maximum of $\eta = 23.7\%$, as-measured). Thereby, FlexTrail reduces wet ink laydown to below 5 mg per front grid exhibiting 80 fingers (busbarless). Until now, only flat fingers (h_f of about 200 nm) are FlexTrail-printed. However, in terms of h_f , FlexTrail printing offers large room for improvements, e.g., by means of

increasing the silver load of the ink or by tuning the shape and/or size of the glass capillary.

SHJ solar cells exhibiting inkjet- and FlexTrail-printed front grids offer high performance and a large silver saving potential. Unfortunately, on module level (one-cell SWCT mini-modules) they cannot realize their full potential in this work. This is partially attributed to an inappropriate number of contacting wires (18 instead of 30 wires) used for module manufacturing. Moreover, the electrical wire/cell contact is assumed to be insufficient in the case of too flat fingers (due to insufficient coverage of the alkaline texture).

6 Understanding of contact formation processes

This chapter provides an understanding of innovative contact formation and its impact on the electrical performance of printed metal electrodes and passivating contacts. The investigated contact formation techniques are thermal annealing at low ($180^{\circ}\text{C} \leq T \leq 220^{\circ}\text{C}$) and medium ($250^{\circ}\text{C} \leq T \leq 350^{\circ}\text{C}$) temperatures, intense pulsed light processing, and ultrasound-assisted thermal low-temperature annealing. The metal contacts' electrical performance is characterized both in terms of the lateral resistivity and the contact resistivity at the metal/indium tin oxide contact interface. Additional microstructure analysis allows for an understanding of surface-energy-driven effects in the contacts, which constitute their electrical properties. Since the considered contact formation processes are developed for application on passivating contacts, their impact on passivation quality of silicon heterojunction and tunnel oxide passivating contacts is evaluated. For the first time, the temperature of such specimens is measured in-situ during intense pulsed light processing in the millisecond range and correlated with the implied open-circuit voltage.

The sections 6.1 and 6.3 are partly based on Ref. [155] and Ref. [120, 156], respectively. These are written and published by the author of this thesis.⁶

⁶ Jörg Schube is the main author of all three mentioned publications. He designed the corresponding experiments, performed process steps such as annealing, printing, and characterization, took the SEM pictures, coordinated and supervised all remaining

6.1 Thermal annealing at low and medium temperatures

6.1.1 Motivation

One of the major challenges of Si-based passivating contacts are restrictions for metallization and contact formation in terms of thermal budget [7]. For instance, the silicon heterojunction structure allows for maximum process temperatures in the range of 200°C only (compare section 3.3.1). Considering screen printing, thus, low-temperature-compatible metal pastes instead of state-of-the-art firing-through pastes, typically fired at temperatures in the range of 700-800°C, have to be utilized. These low temperature pastes exhibit comparatively high finger resistivities ρ_f in the range of 5.5-10.0 $\mu\Omega\cdot\text{cm}$ after low-temperature annealing ($T \approx 200^\circ\text{C}$) [20, 159]. Such values are more than two times higher than those typical for fired contacts.

In order to estimate a solar cell's potential conversion efficiency change $\Delta\eta_{\text{sim}}$ from lower ρ_f , simulations are performed by means of a *Gridmaster*- and *Pitchmaster*-based tool being adapted for bifacial solar cells with passivating contacts [145, 146]. Typical input parameters of a 156 mm x 156 mm-sized solar cell exhibiting a V_{OC} potential of 730 mV serve as starting basis. For the front and rear irradiance, typical values of 1000 W/m² and 100 W/m², respectively, are chosen. The electrodes on both sides of the cell are assumed to exhibit five busbars and fingers with w_f of 50 μm , 40 μm , or 30 μm as well as finger cross-sectional areas of 333 μm^2 , 213 μm^2 , or 120 μm^2 , respectively. The finger pitch on both sides of the cell is optimized for each simulated data point. Shadow losses due to the fingers and busbars are taken into account, too. The finger/substrate surface contact resistivity ρ_c is chosen to be 5 m Ωcm^2 . ρ_f is varied from 3 $\mu\Omega\cdot\text{cm}$ to 10 $\mu\Omega\cdot\text{cm}$.

process steps, and did the analyses. In Ref. [120, 155], Leonard Tutsch developed the ITO deposition processes, performed sputtering and corresponding characterization. Maximilian Weil developed the IPL processes presented in Ref. [156]. His work has been supervised by Jörg Schube and is published in form of his master thesis [157]. In Ref. [120], the TOPCon precursors are manufactured by Angelika Harter who has been supervised by Jana-Isabelle Polzin. Her work is published as her master thesis [158].

6.1 Thermal annealing at low and medium temperatures

The simulation-based results are depicted in Figure 6-1. They reveal a potential cell efficiency gain of about 0.5%_{abs} in the case of $w_f = 50 \mu\text{m}$ as a consequence of the metal electrodes' resistivity reduction (and corresponding finger pitch adaptation in order to get the optimum for each value of ρ_f). An even stronger sensitivity on the efficiency gain regarding ρ_f is expected in the case of cost-optimized contact grids with reduced finger numbers. The sensitivity on $\Delta\eta_{\text{sim}}$ is also increasing if w_f is decreased, as displayed in Figure 6-1. For $w_f = 30 \mu\text{m}$, $\Delta\eta_{\text{sim}}$ increases to even 0.9%_{abs} when ρ_f is decreased from $10 \mu\Omega\cdot\text{cm}$ down to $3 \mu\Omega\cdot\text{cm}$. Both reduced finger number and decreased w_f correspond to the ongoing trend of silver reduction [3]. These simulations demonstrate the significant η potential of cells featuring metal contacts with low ρ_f , which highly motivates the development of such contacts.

In order to obtain the full electrical performance of low-temperature screen printing pastes, they can be annealed at temperatures significantly above 200°C. Therefore, this study considers three commercially available silver-based pastes that are annealed not only at low temperatures (180-220°C) but also at medium temperatures (250-350°C).

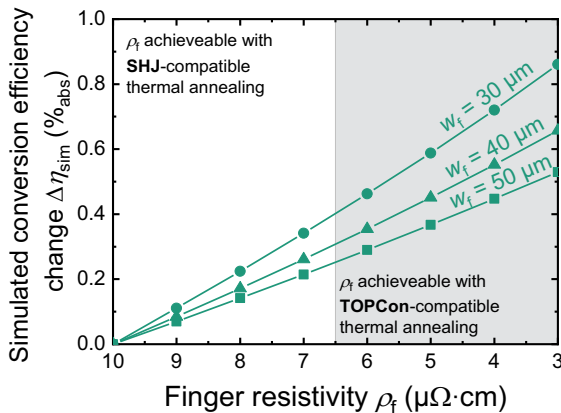


Figure 6-1 Simulated conversion efficiency change $\Delta\eta_{\text{sim}}$ as a function of the finger resistivity ρ_f considering varying finger widths w_f , redrawn from Ref. [155]. Each data point represents a cell (five-busbar layout) featuring an optimized quantity of fingers on both sides of the cell (V_{OC} potential in the range of 730 mV). The distinction of ρ_f achievable with SHJ- and TOPCon-compatible annealing processes is drawn by the experimental results presented in section 6.1.3.

Since passivating contacts, such as SHJ and TOPCon, require a TCO layer if metallization is performed based on low-temperature pastes (see section 2.2), it is useful to develop metallization and TCO simultaneously. For this purpose, three different ITO layers are considered in this study exhibiting three different charge carrier concentrations N_c . The electrical contact at the metal/ITO interface in terms of ρ_c and its dependence on N_c is investigated as well. Moreover, an ITO layer surface pretreatment based on atmospheric air plasma, that is performed directly before the printing step, is considered and its potential in terms of ρ_c is analyzed. SEM-based microstructural analysis of the metal/ITO interfaces allows for a model approach for metal/ITO contact formation. For the ITO layers' optical properties, which complete this study, the reader is referred to Ref. [64].

The applicability of the considered thermal annealing processes on SHJ and TOPCon is evaluated, too. Due to their temperature-sensitivity, SHJ structures are expected to be incompatible with thermal annealing at medium temperatures (250-350°C). Therefore, TOPCon structures, which are more tolerant towards higher process temperatures, are considered in addition. Polysilicon-based passivating contacts are typically metallized using high-temperature pastes [8, 51, 160]. However, such back end processing is often accompanied by metal spiking that significantly harms passivation quality (also compare section 2.2.2). This issue can be solved by low- and mid-temperature metallization approaches as developed in this work.

6.1.2 Sample preparation and characterization

The process flow used for the investigation of low- and medium-temperature thermal annealing is sketched in Figure 6-2. The experiment is divided into four groups. Alkaline textured 156 mm x 156 mm-sized *n*-type Cz-grown Si wafers serve as input material for samples of group 1 and 2. An 80 nm thin insulating silicon nitride (SiN_x) layer is deposited single-sided on the group 1 wafers. All group 2 wafers are coated single-sided with a 10 nm thick layer of *a*-Si:H(p) in order to form a *pn* junction. On top of the *a*-Si:H(p) layer, 80 nm thick ITO layers are deposited. The flow of oxygen during DC magnetron sputtering is varied so that three different ITO layers, labelled *ITO 1*, 2, and 3, are fabricated.

6.1 Thermal annealing at low and medium temperatures

ITO 1 is sputtered at 0.8 sccm, *ITO 2* at 2.0 sccm, and *ITO 3* at 6.0 sccm oxygen gas flow. Further details with regard to the ITO layers are provided in Ref. [64]. Subsequently, all wafers of group 1 and 2 are laser-cut, each one into sixteen 39 mm x 39 mm-sized samples. Then, they are screen-printed (single-sided, on top of the SiN_x and ITO layer, respectively) using two different printing layouts and dried at 100°C for 10 min subsequently. Since group 1 and 2 address the investigations of ρ_f and ρ_c , respectively, the printing layout applied to group 1 is optimized for the determination of ρ_f and the layout applied to group 2 samples is optimized for the determination of ρ_c (compare section 4.3.2). Three different silver pastes are utilized: paste *PV* is a standard low-temperature paste for PV application, which serves as the reference here, paste *PE* is originally developed for printed electronics applications, and paste *NP* is a nanoparticle-based paste, which is developed for printed electronics applications, too. Appendix B provides further information about the pastes.

In a next step, six different thermal annealing processes are performed using a hotplate, namely 30 min of annealing at 180°C, 200°C, and 220°C (referred to as the *low-temperature approach*) as well as 15 min of annealing at 250°C, 300°C, and 350°C (referred to as the *mid-temperature approach*). In group 1, R_f is measured by means of the four-point probe method (see section 4.3.1) before and also after one certain annealing process. Thereby, the insulating dielectric SiN_x layer restricts the current flow to the fingers only. From the mean values of R_f and the finger geometry data obtained by means of confocal microscopy, ρ_f is calculated using the equations (4-9) and (4-10). In group 2, ρ_c at the silver/ITO interface is obtained after annealing by means of four-point probe measurements and analyzed according to the transfer length method (see section 4.3.2). Thereby, the *pn* junction of the samples restricts the lateral measurement current to the ITO layer. Additionally, SEM and energy dispersive X-ray spectroscopy (EDX) analyses of ion beam-polished printed metal electrodes are performed for structural and chemical investigations [127]. All screen printing pastes are analyzed by means of simultaneous thermogravimetric-differential scanning calorimetry (TG-DSC) in order to characterize chemical reactions in the pastes (not shown in Figure 6-2) [161, 162]. In crucibles, about 50 mg of each paste is dried at 100°C for 10 min first. Then, the mass and the temperature of the filled

6 Understanding of contact formation processes

crucibles as well as of an empty one, which serves as the reference, are measured simultaneously during heating up to 1000°C at a rate of 3°C/min.

The samples of group 3 are utilized for the measurement of the charge carrier density N_c of the three ITO layers (*ITO 1 to 3*, see above in this section). Therefore, planar glass plates serve as substrates in order to facilitate Hall measurements on the deposited ITO layers [163]. Such measurements are conducted on each sample before and after thermal annealing. The six annealing processes are performed by using another sample for each process.

The influence of the thermal low- and mid-temperature annealings on non-metallized SHJ samples' passivation quality is investigated in group 4. SHJ precursors from an external manufacturer with 156.8 mm edge length and a thickness $d_{\text{wafer}} = 180 \mu\text{m}$ are utilized. The precursors exhibit an alkaline textured *n*-type Cz-grown Si base substrate with a resistivity ρ_{base} of 2.0 $\Omega\cdot\text{cm}$, in- and extrinsic (*p*- and *n*-type on the rear and front side, respectively) hydrogenated *a*-Si:H layers, and ITO layers on both sides. More details about these samples as well as a sketch of their layer composition can be found in section 2.2.1. The precursors are laser-cut into 39 mm x 39 mm-sized samples. Then, the impact of thermal annealing on the passivation quality of the samples is

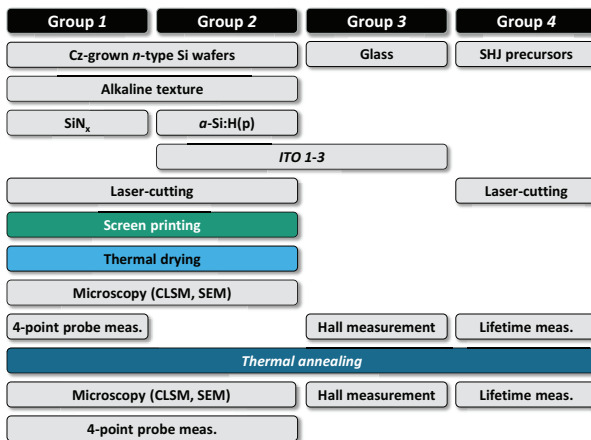


Figure 6-2 Sketch of experimental process flow used for the investigation of low- and mid-temperature thermal annealing. Redrawn from Ref. [155].

6.1 Thermal annealing at low and medium temperatures

studied by means of photoconductance-based lifetime measurements before and after annealing. It is quantified by the iV_{OC} before ($iV_{OC,before}$) and after ($iV_{OC,after}$) each annealing process at an illumination of 1000 W/m^2 . Based on that, the iV_{OC} change ΔiV_{OC} is calculated according to the equation

$$\Delta iV_{OC} = iV_{OC,after} - iV_{OC,before}. \quad (6-1)$$

Negative values indicate a loss and positive values a gain of passivation quality compared to the initial state.

6.1.3 Electrical characterization of metal contacts

In a first step, the finger resistivity ρ_f of printed metal contacts as a function of annealing temperature $T_{annealing}$ is investigated (samples of group *I*). Corresponding data is presented in Figure 6-3. With typical low-temperature annealing at 200°C conducted for 30 min, ρ_f values of $6.5\text{-}9.4 \mu\Omega\cdot\text{cm}$ are achieved using pastes *PV*, *PE*, and *NP*. This corresponds to values presented in Ref. [164], which are achieved with paste *PV* as well. This data is also displayed in Figure 6-3 in form of black asterisks. When annealing temperature is decreased to $T_{annealing} = 180^\circ\text{C}$, ρ_f increases. In contrast to this, ρ_f strongly benefits from

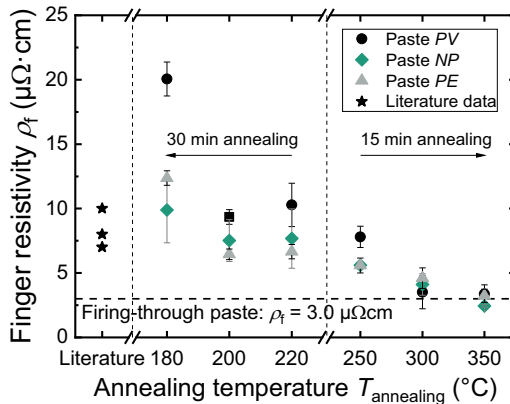


Figure 6-3 ρ_f as a function of $T_{annealing}$, redrawn from Ref. [155]. Additionally, a typical value of a high-temperature firing-through paste and data from literature corresponding to paste *PV* (black asterisks) are presented [164]. Errors are calculated by means of Gaussian error propagation.

6 Understanding of contact formation processes

increasing $T_{\text{annealing}}$. As a consequence, using $T_{\text{annealing}} = 350^{\circ}\text{C}$ finger resistivities of 2.4-3.5 $\mu\Omega\cdot\text{cm}$ are reached. These values are in the range of those of typical silver-based firing-through pastes after a standard high-temperature firing step performed at 700-800 $^{\circ}\text{C}$.

In order to explain such low ρ_f values, TG-DSC data is considered by taking the example of paste *PV*. Chemical reactions during heating can be interpreted based on the paste's datasheet, which is disclosed by the corresponding manufacturer. Nevertheless, it is commonly known that high-temperature firing-through pastes do not only consist of conductive material (e.g., silver) and the organic paste vehicle but of inorganic binders such as glass frit as well (see section 3.2.1). Inorganic binders are used for thermally activated etching of, e.g., SiN_x -based ARC layers during fast-firing processes [134]. Since the low-temperature pastes utilized in this work are not designed for etching such layers, these pastes abandon inorganic binders. This corresponds to the datasheet and is also supported by SEM images presented in Figure 6-4. Figure 6-4 (a) shows a sample covered by an *ITO 2* layer in the top view. The entire area was covered by a paste-*PV*-based finger (annealed at 200 $^{\circ}\text{C}$, 30 min), which has been etched-back using diluted (35%) HNO_3 . Figure 6-4 (b) shows a similar sample in the top view covered by a non-metallized *ITO 2* layer. The two surfaces appear equally and no impact of the low-temperature paste on the ITO layer, e.g., due

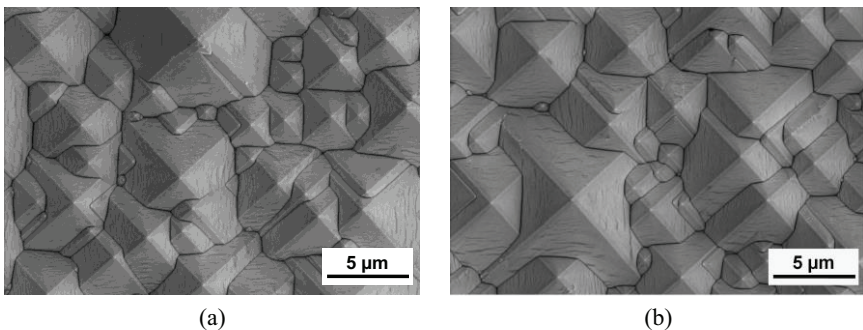


Figure 6-4 SEM images of samples coated with *ITO 2* layers (top view), redrawn from Ref. [155]. The entire surface of the sample shown in (a) was covered by a paste-*PV*-based finger (annealed at 200 $^{\circ}\text{C}$ for 30 min), which is etched-back before SEM analysis is performed. The surface of the sample in (b) was not covered by a metal finger before SEM.

6.1 Thermal annealing at low and medium temperatures

to etching or imprints, is visible. (The depicted images are representatives for the entire wafer surfaces under investigation.) This is also valid for samples that undergo annealing operated at $T_{\text{annealing}} = 350^\circ\text{C}$ (not shown here). Based on this, it is assumed, that metal spiking through passivating layers is not an issue occurring in combination with such pastes.

The TG-DSC data is shown in Figure 6-5. In this graph, two distinctive drops of the paste's mass during heating, marked with (I) and (II), are visible. Drop (I) is caused by the evaporation of solvents, which remained in the paste after the previous drying step. Drop (II) is caused by burning of binders and is correlated with a very distinct exothermic peak of the DSC signal occurring at $T = 284^\circ\text{C}$. The fact that paste *PV* contains silver and organic binders only at this temperature (note that solvents are already evaporated at drop (I)) supports this interpretation. As a consequence, the silver/silver inter-particle contacts in the bulk of the paste improve and ρ_f drops significantly. Moreover, it is conspicuous that the DSC signal is at a positive level for $57^\circ\text{C} < T < 961^\circ\text{C}$. ($T = 961^\circ\text{C}$ is the melting temperature of silver causing a drop of the DSC signal [66].) This can be explained by densification and sintering processes in the paste: when the silver particles are densified and sintered together, surface energy is set free (compare section 3.1.1), which contributes to an exothermic DSC signal within the mentioned temperature range. A SEM-based microstructure analysis

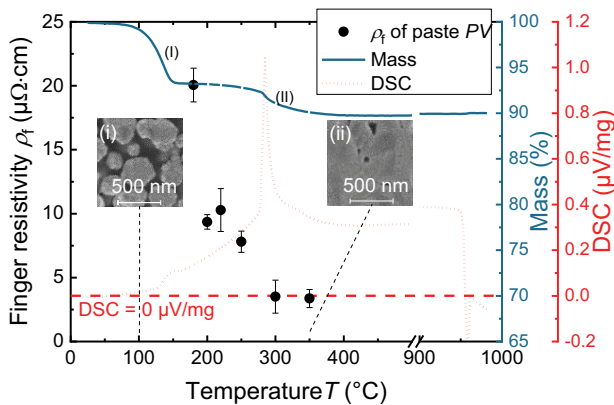


Figure 6-5 TG-DSC data corresponding to paste *PV* as a function of $T_{\text{annealing}}$, redrawn from Ref. [155]. ρ_f is taken from Figure 6-3.

6 Understanding of contact formation processes

supports this interpretation. In the case of $T_{\text{annealing}} = 350^\circ\text{C}$ (add-in window marked with (ii) in Figure 6-5), the silver particles are significantly more densified and sintered together compared to after drying at 100°C (add-in window marked with (i) in Figure 6-5). The effect of densification and sintering during the increase of temperature is also correlated with a decreasing finger resistivity, as can be derived from Figure 6-5 as well.

To briefly sum up the results obtained so far: the low ρ_f achieved especially with $T_{\text{annealing}} \geq 300^\circ\text{C}$ originates from both burnt-out organic binders and pronounced sintering and densification of silver particles. This happens for temperatures significantly below the melting temperature of silver of 961°C , indicated by a drop of the DSC signal.

In the following, the ρ_c data is discussed (samples of group 2), which is presented in Figure 6-6. The combinations of paste *PV* and *PE* with *ITO 1* and *2* layers

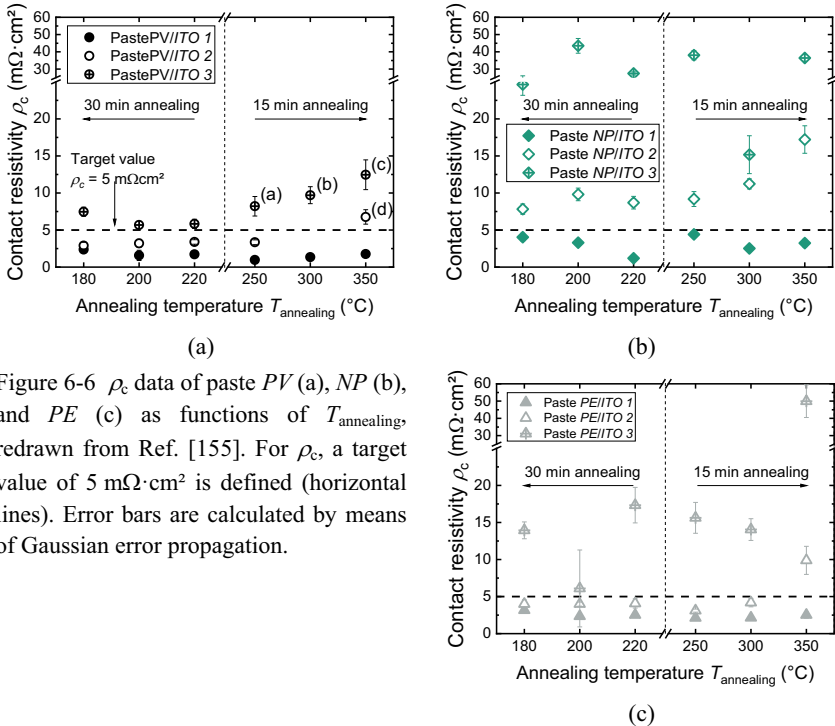


Figure 6-6 ρ_c data of paste *PV* (a), *NP* (b), and *PE* (c) as functions of $T_{\text{annealing}}$, redrawn from Ref. [155]. For ρ_c , a target value of $5 \text{ m}\Omega\cdot\text{cm}^2$ is defined (horizontal lines). Error bars are calculated by means of Gaussian error propagation.

6.1 Thermal annealing at low and medium temperatures

achieve contact resistivities below the defined target value of $5 \text{ m}\Omega\cdot\text{cm}^2$ in the case of $T_{\text{annealing}} \leq 300^\circ\text{C}$. Paste *PV* achieves $\rho_c < 5 \text{ m}\Omega\cdot\text{cm}^2$ on *ITO 1* only. Apart from this, there are two specific observations from Figure 6-6, which are to be discussed in the following:

1. $\rho_{c,\text{ITO1}} < \rho_{c,\text{ITO2}} < \rho_{c,\text{ITO3}}$ is valid for all three pastes under investigation and for all considered annealing processes.
2. For $T_{\text{annealing}} \geq 250^\circ\text{C}$, ρ_c increases if $T_{\text{annealing}}$ is further increased. This trend is less significant in the case of *ITO 1*. However, in the case of *ITO 2* and *3*, this effect becomes severely pronounced. An exception to this is the combination of paste *NP* and *ITO 3*.

Observation 1 can be explained by taking the example of paste *PV*. To this end, ρ_c is plotted as a function of N_e in Figure 6-7. N_e is determined by means of hall measurements of group 3 samples. Since *ITO 1* is sputtered at the lowest oxygen gas flow, it exhibits the highest N_e values compared to the other ITO layers. *ITO 3*, on the other hand, is sputtered at the highest oxygen gas flow and, therefore, reaches the lowest N_e values of the three ITO layers. *ITO 2* exhibits intermediate N_e values because it is sputtered at an intermediate oxygen gas flow. From the

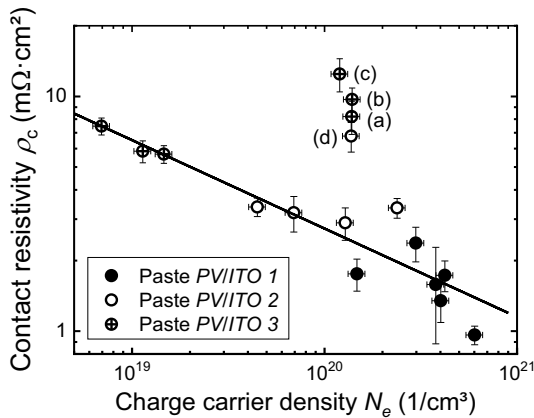


Figure 6-7 ρ_c of the paste *PV*/ITO contact as a function of N_e featured by the three different ITO layers, redrawn from Ref. [155]. The ρ_c data is taken from Figure 6-6. A relative error of N_e of 10% is assumed. The linear fit (black solid line) does not include the data points (a)-(d). The reason for this is explained in section 6.1.4.

fitted line in Figure 6-7, one can see that ρ_c is decreasing when the charge carrier density N_c in the ITO layers increases. The well-known metal/semiconductor junction theory (see section 3.1.2) can explain this observation: higher values of N_c in the ITO layer, which is a (degenerate) semiconductor, correspond to a thinner potential barrier at the silver/ITO interface. Therefore, tunneling of charge carriers through the potential barrier becomes more probable resulting in a decrease of ρ_c . This is valid for the two current transport mechanisms thermionic field emission and field emission. In fact, both seem to be the relevant mechanisms in the case of the present study because $6 \cdot 10^{19} \text{ 1/cm}^3 < N_{e,\text{ITO}1-3} < 7 \cdot 10^{20} \text{ 1/cm}^3$. In other words: the reason why $\rho_{c,\text{ITO}1} < \rho_{c,\text{ITO}2} < \rho_{c,\text{ITO}3}$ holds, is that $N_{e,\text{ITO}1} > N_{e,\text{ITO}2} > N_{e,\text{ITO}3}$.

Certainly, the high N_c of *ITO 1* can be adverse in terms of optical performance due to considerable parasitic absorption in the longer wavelength range (see corresponding data in Ref. [64]). Although E_g is increased here, the absorption induced by free charge carriers would limit j_{SC} if *ITO 1* was implemented on the front side of a solar cell. Therefore, *ITO 2* may be preferred over *ITO 1* when optical performance is considered in addition, despite the fact that *ITO 1* achieves the lowest ρ_c values. For more details, the reader is kindly referred to Ref. [64] as well as to section 7.2.

At this point, there are two aspects to be noted: first, the absolute values of ρ_c at the silver paste/ITO contacts cannot completely be explained by Schottky's metal/semiconductor contact theory because there is a huge discrepancy between measured and calculated data. Second, the data points (a)-(c) (measured on the *ITO 3* layer), and (d) (measured on the *ITO 2* layer), which are marked in Figure 6-7, do not fit the above-mentioned relationship of ρ_c and N_c . From Figure 6-6 (a), one can see that these values are achieved for $T_{\text{annealing}} \geq 250^\circ\text{C}$. Here an additional effect has to be taken into account. (Therefore, they are not included by the linear fit in Figure 6-7.) This has already been indicated by observation 2 and will be discussed in detail in the following section 6.1.4.

6.1.4 Microstructural analysis of silver/indium tin oxide contacts

In Figure 6-8, SEM images of sample cross-sections are presented in order to gain an insight in microstructural effects that constitute printed metal contacts' ρ_f and ρ_c . On each picture, one can see a textured silicon substrate (bottom) covered by an ITO 2 layer (bright film on top of the silicon pyramids) and silver particles belonging to the contact finger, which is printed on top. The left column (Figure 6-8 (a), (c), and (e)) shows the three pastes after annealing operating at $T_{\text{annealing}} = 200^\circ\text{C}$ and the right column (Figure 6-8 (b), (d), and (f)) after annealing using $T_{\text{annealing}} = 350^\circ\text{C}$. Comparing the left with the right column, it becomes obvious that the silver particles are significantly more densified and sintered together after annealing using $T_{\text{annealing}} = 350^\circ\text{C}$ than after annealing using $T_{\text{annealing}} = 200^\circ\text{C}$. As already mentioned in section 6.1.3, pronounced sintering and densification are the cause of low ρ_f values (see Figure 6-3 and Figure 6-5 as well).

Furthermore, focusing on the silver/ITO interface, cavities (Figure 6-8 (b)) and even gaps (Figure 6-8 (d) and (f)) are visible in the right column of Figure 6-8 but not in the left column (Figure 6-8 (a), (c), and (e)). Moreover, in Figure 6-8 (f), structures appearing as *bridges* between silver and ITO layer are visible. The EDX analysis reveals that these bridges mostly consist of carbon, which is assumed to be the main element of the organic binders.⁷ By means of a punctual EDX measurement of the silicon substrate (not shown here), a carbon contamination, for example, due to sample preparation, is excluded. This strengthens the interpretation that the bridges consist of organic binders and do not contribute to current transport. The small silicon and silver peaks of the EDX signal might originate from silver and silicon in the bridge or, due to scattering effects during measurement, from the silicon substrate underneath and the silver finger above. Nevertheless, because of the silver peaks, a contribution of these bridge-like structures to the electrical silver/ITO contact cannot be excluded completely.

⁷ Paste *PE* contains different organic binders than paste *PV*, which burn out at temperatures above 350°C , unlike the binders of paste *PV* (compare Figure 6-5).

6 Understanding of contact formation processes

With respect to the mentioned cavities and gaps, it seems as if at temperatures higher than 200°C the Ag particles rather tended to sinter together with each

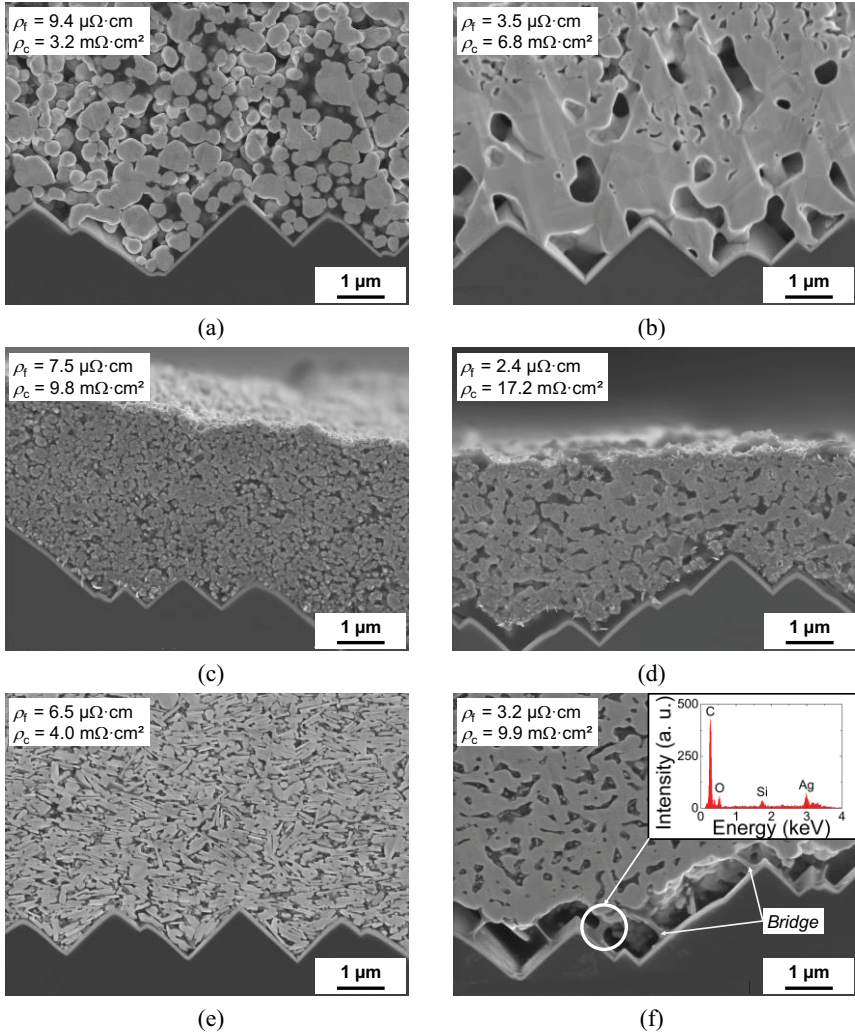


Figure 6-8 SEM images of sample cross-sections after thermal annealing at 200°C, 30 min (left column) and after thermal annealing at 350°C, 15 min (right column) redrawn from Ref. [155]. (a) and (b) show paste *PV*, (c) and (d) show paste *NP*, and (e) and (f) show paste *PE*. All contacts are printed on samples coated with *ITO* 2 layers (bright films on top of the pyramids). Additionally, EDX data is presented in (f). ρ_f and ρ_c are taken from Figure 6-3 and Figure 6-6, respectively.

6.1 Thermal annealing at low and medium temperatures

other than to sinter with the ITO layers. As a reason for this, the higher surface energy reported for silver particles $E_{\text{surface,Ag}}$ of 1.1-1.3 J/m² compared to the one of ITO layers $E_{\text{surface,ITO}}$ of 0.03-0.05 J/m², according to literature, is suggested [66, 165–168]. The surface energies of the materials utilized in this work may slightly differ from those reported in literature. Still, for silver particles and ITO layers, a surface energy discrepancy in the range of two orders of magnitude can be assumed. Therefore, silver/silver inter-particle sintering is energetically more favorable than silver/ITO sintering because it lowers the overall surface energy significantly more.

Taking into account the findings in the preceding paragraphs, the increase of ρ_c at annealing temperatures higher than 220°C and up to 350°C (observation 2 in section 6.1.3) is suggested to be interpreted as follows: at lower temperatures (180-220°C), silver particles and ITO layer are predominantly in contact, which causes low ρ_c . However, annealing temperatures in the range of 250°C to 350°C lead to more pronounced sintering of silver particles than temperatures in the range of 180-220°C. At the silver/ITO interface, due to the surface energy discrepancy of the two different materials in the range of two orders of magnitude, silver particles rather tend to sinter together with adjacent particles than with the ITO layer. Consequently, voids are formed at the silver/ITO interface reducing the ITO area touched by metal (see Figure 6-8 (b), (d), and (f)). Since ρ_c is calculated by means of a measured constant w_B , this induces the determination of an increased ρ_c after annealing operating at temperatures of 250°C to 350°C. This effect seems to be less crucial in the case of the *ITO 1* layer exhibiting high N_c because of the very low overall level of the ρ_c values. Nevertheless, it is assumed to cause the data points (a)-(d) in Figure 6-7 not to follow the fitted line while the other data points do, which is indicated by observation 2 in section 6.1.3.

To further strengthen this contact formation model and the significance of the surface energy in particular, paste *PV* is screen-printed on samples that exhibit an evaporated 100 nm thin Ag layer instead of an *ITO 2* layer. This is motivated by the assumption that Ag particles and evaporated Ag layers exhibit a similar

6 Understanding of contact formation processes

amount of surface energy per surface area. Therefore, it is expected that the microstructural effects leading to voids at the interface are strongly reduced.

After printing and drying (100°C, 10 min), the samples are annealed at 350°C for 15 min. Figure 6-9 (a) shows a cross-sectional view of a corresponding specimen exhibiting an Ag layer. It is compared to a sample exhibiting an *ITO 2* layer (Figure 6-9 (b)). At the Ag particle/Ag layer contact interface (Figure 6-9 (a)), the number of voids is similar to the number of voids at the Ag particle/*ITO 2* layer interface (Figure 6-9 (b)) but their size is decreased significantly. As a consequence, the Ag particle/Ag layer contact is increased. In order to quantify this increase, based on the SEM images, the lengths of the visible regions where metal electrode and substrate surface are in direct contact are measured utilizing a conventional image evaluation tool. The sum of the diameters visible at the cross-sectional area is divided by the total length of the substrate surface's cut edge, which is clearly visible in the sample's cross-sectional view. This fraction is increased by a factor of two for a sample exhibiting an Ag coating instead of an *ITO 2* coating. This increase in contacted area can be explained by a vanishing discrepancy of surface energies.

Nevertheless, some voids appear at the Ag particle/Ag layer interface. It is assumed that the surface-to-volume ratio, which is higher for Ag particles than for the Ag layer, still causes a higher affinity towards inter-particle sintering than towards particle-substrate sintering. Another possible reason for such voids

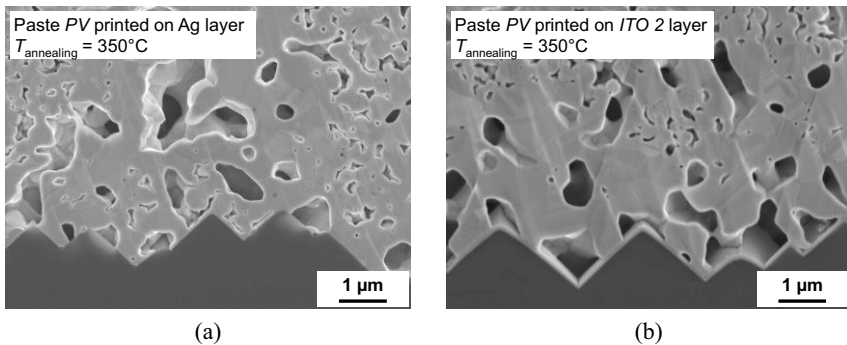


Figure 6-9 SEM images of sample cross-sections recorded after thermal annealing at 350°C for 15 min. In (a), paste *PV* is printed on top of an evaporated Ag layer. In (b), paste *PV* is printed on top of an *ITO 2* layer (taken from Figure 6-8 (b)).

6.1 Thermal annealing at low and medium temperatures

might be evaporation of solvents and polymerization processes of binders during annealing leaving cavities behind.

In order to further strengthen the author's argument, samples covered by *ITO 2* layers are pretreated by means of atmospheric pressure air plasma directly before the screen printing step. After printing and drying (100°C, 10 min), the samples are annealed at 350°C for 15 min. The name of the plasma tool is *Arcospot* manufactured by *Arcotec*. This simple, low-cost, and high-speed technique offers a broad range of application possibilities, e.g., biomedical application, deposition of coatings, and surface modifications [169]. It is also used to increase the wetting behavior of ITO layers as reported in Ref. [170].

The plasma is generated in air by means of high voltage applied to two electrodes. It is driven onto the target surface from a distance of 15 mm using a steady-state air flow (applied pressure of 6 bar). Since the plasma spot size of the utilized device is in the range of 15 mm, scanning across the whole sample is necessary in order to process the whole specimen. The scanning speed is chosen to be 50 mm/s.⁸ Plasma causes a cleaning of the ITO surface in terms of decreasing its carbon concentration. Moreover, it increases the oxygen concentration on the surface, which is related to the formation of new polar oxygen-based groups. The generation of such groups increases the ITO layer's surface energy [171].

In Figure 6-10, cross-sectional views of samples with and without plasma pretreatment ((Figure 6-10 (a) and (b), respectively) of the ITO layers performed before screen printing are depicted. As a result of the pretreatment, the direct Ag/ITO contact increases by 52% (same calculation as provided in this section above). This results in a significant ρ_c reduction of 1.9 m Ω ·cm², or a reduction of 25%_{rel.} Thereby, it is shown that there is a correlation between the fraction of the ITO layer touched by metal and ρ_c of this interface. Further, it is found that

⁸ The plasma pretreatment is not optimized with regard to throughput. Certainly, the process could be conducted at higher speeds by means of only little adaptations.

6 Understanding of contact formation processes

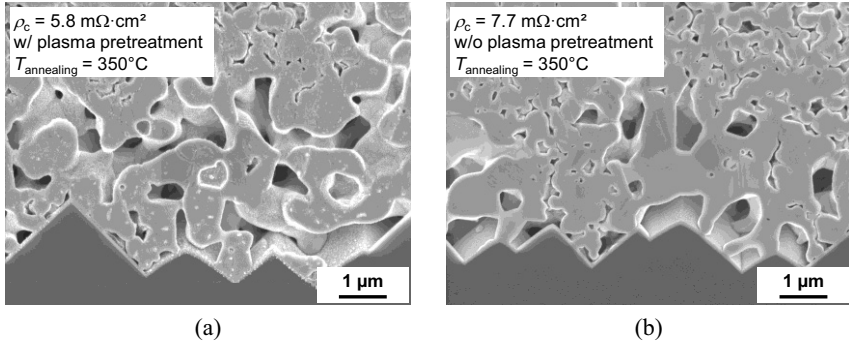


Figure 6-10 SEM images of sample cross-sections after thermal annealing at 350°C for 15 min. In (a) paste *PV* is printed on top of a plasma-pretreated *ITO 2* layer. In (b) paste *PV* is printed on top of an *ITO 2* layer without pretreatment.

this effect occurs for low-temperature annealing at $T_{\text{annealing}} = 200^\circ\text{C}$ as well. Thereby, ρ_c at the paste *PV*/*ITO 2* contact is decreased by $1.8 \text{ m}\Omega\cdot\text{cm}^2$, or 30%_{rel.}

The investigations conducted on Ag particle/Ag layer interfaces and on Ag particle/plasma-pretreated ITO interfaces support the contact formation model introduced above. Furthermore, it is shown that a plasma pretreatment allows for low ρ_f and ρ_c at $T_{\text{annealing}} = 350^\circ\text{C}$, simultaneously. In the following section 6.1.5, the influence of the thermal low- and mid-temperature annealing processes and the plasma pretreatment on passivating contacts is investigated.

6.1.5 Passivation as a function of annealing temperature

The impact of thermal annealing on non-metallized SHJ samples in terms of iV_{OC} is depicted in Figure 6-11 (samples of group 4). The data refers to an initial iV_{OC} of $724.0 \pm 3.1 \text{ mV}$. In general, SHJ structures' passivation benefits from moderate annealing after ITO deposition because sputtering damages in the thin amorphous silicon layers are cured [26]. This is the case for $T_{\text{annealing}} = 200^\circ\text{C}$ and an annealing time of 30 min. Thereby, iV_{OC} slightly increases by $1.9 \pm 1.4 \text{ mV}$ compared to the initial state. iV_{OC} does not change significantly owing to annealing at $T_{\text{annealing}} = 180^\circ\text{C}$. Obviously, such annealing is not strong enough for curing.

6.1 Thermal annealing at low and medium temperatures

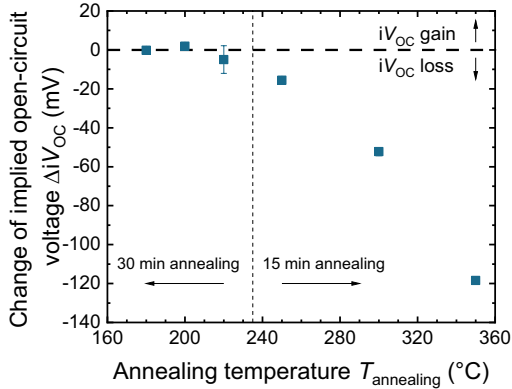


Figure 6-11 ΔiV_{OC} (iV_{OC} gain if greater than zero, loss if smaller than zero) as a function of $T_{\text{annealing}}$. Error bars represent the standard deviations. The initial iV_{OC} of these samples is 724.0 ± 3.1 mV.

For $T_{\text{annealing}} \geq 200^\circ\text{C}$, there is a trend towards decreasing iV_{OC} values, which becomes even pronounced for $T_{\text{annealing}} > 220^\circ\text{C}$. It leads, for example, to $\Delta iV_{\text{OC}} = -118.5 \pm 1.4$ mV after annealing at 350°C for 15 min. The main reason for the degradation of SHJ structures at temperatures above 220°C is hydrogen effusion out of the $a\text{-Si:H}$ layers (compare section 2.2.1) inducing defects at the $c\text{-Si}/a\text{-Si:H}$ interface. From Figure 6-11 it becomes obvious that SHJ structures are compatible in terms of passivation quality/ iV_{OC} with thermal low-temperature annealing ($T_{\text{annealing}}$ of $180\text{-}220^\circ\text{C}$, $t_{\text{annealing}} = 30$ min) and incompatible with mid-temperature annealing ($T_{\text{annealing}}$ of $250\text{-}350^\circ\text{C}$, $t_{\text{annealing}} = 15$ min).

Furthermore, the impact of atmospheric air plasma treatment on non-metallized SHJ samples is determined. The plasma process is described in section 6.1.4. The mean iV_{OC} of plasma-treated samples does not deviate significantly from the initial mean iV_{OC} . Therefore, plasma pretreatment is compatible to SHJ structures.

To get the full electrical performance of low-temperature screen printing pastes, one has to switch to mid-temperature annealing and, therefore, to less temperature-sensitive passivating contacts such as *poly*-Si-based ones. In Ref. [63], promising iV_{OC} values significantly above 720 mV of TOPCon lifetime samples after mid-temperature annealing are reported. It demonstrates a great potential

of such contacts to be combined with the mid-temperature metallization scheme developed in this work. The dependence of TOPCon passivation quality on annealing is investigated in detail in section 6.3.6 of this work.

6.2 Ultrasound-assisted thermal annealing

6.2.1 Motivation

The previous section 6.1 shows that in terms of ρ_f , printed metal contacts cannot exploit their full potential if thermal annealing is conducted at low temperatures of 180-220°C. SEM-based microstructural analysis reveals that metal particles are not sintered sufficiently at such conditions. This is identified as a main reason for the higher ρ_f compared to mid-temperature thermal annealing.

In order to obtain more compact and effectively sintered metal electrodes, even after annealing at low temperatures, and therefore lower ρ_f , ultrasonic oscillations are investigated as a pretreatment performed directly before the thermal annealing step. More precisely, oscillations are coupled into metal electrodes causing vibrations of each metal particle in the printed finger. The metal particles, thus, are expected to rearrange and move closer together in such a way that voids between them vanish. In order to achieve this, ultrasonic welding equipment *HiS VARIO B 4800* from *Herrmann Ultraschall* is utilized. For more details about this technique, the reader is kindly referred to section 3.3.2 as well as the literature suggested there.

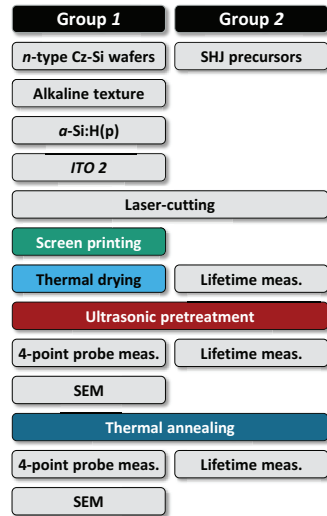


Figure 6-12 Experimental process flow utilized for the investigation of ultrasound as a pretreatment of metal electrodes before thermal low-temperature annealing.

6.2.2 Sample preparation and characterization

Ultrasonic oscillations used as pretreatment of printed metal contacts are investigated by means of the experimental process flow sketched in Figure 6-12. The experiment is divided into two groups. In group 1, the same type of samples as in group 2 of the experiment presented in section 6.1.2 are used (see Figure 6-2). Indeed, solely samples exhibiting *ITO* 2 layers on one side (sputtered at 2.0 sccm oxygen gas flow) are fabricated. Then the samples are screen-printed by means of paste *PV* (see appendix B and description of this paste in section 6.1.2) on the ITO-coated side and dried by means of a conveyor furnace (100°C, 10 min). The set finger width according to the printing layout is $w_{f,set} = 50 \mu\text{m}$.

Table 6-1 Parameter settings corresponding to the conducted three different ultrasonic pretreatments.

Ultrasonic process	Frequency f_{ultra} (kHz)	Displacement amplitude A_{ultra} (μm)	Time t_{ultra} (s)	Energy E_{ultra} (J)	Power P_{ultra} (W)
<i>U-low</i>	20	18	1	25	50
<i>U-mid</i>	20	18	2	50	50
<i>U-high</i>	20	25	2	100	100

In a next step, the ultrasonic pretreatment is performed externally at three different settings, namely *U-low*, *U-mid*, and *U-high* differing in applied energy. The corresponding parameter settings are presented in Table 6-1. The processes are time-controlled. Oscillations are each applied both perpendicular to the metal electrodes and along the electrodes with the sonotrode touching them (see sketches in Figure 3-7). Relevant parameters are the ultrasound frequency f_{ultra} , the displacement amplitude of the oscillations A_{ultra} , the application time t_{ultra} , the energy input into the sample E_{ultra} , and the corresponding input power P_{ultra} . After the conduction of the ultrasonic treatments, the samples are investigated by means of SEM. Furthermore, determination of r_f is performed by means of a

four-point probe setup. Due to the parasitic measurement current through the ITO layer, r_f is corrected assuming a parallel circuit of the ITO resistance underneath the contact and r_f (for more details see section 4.4.1). Please note that, due to the deformation of the fingers as a result of ultrasonic treatment, a reliable determination of the finger geometry and ρ_f is not possible. This becomes obvious even from the SEM pictures presented in Figure 6-13. After annealing at 200°C for 30 min using a hotplate, the samples are investigated using four-point probe sensing in order to extract r_f and SEM again.⁹

By means of group 2 samples, the impact of ultrasonic treatments on the passivation quality of the SHJ structure is investigated. SHJ precursors from an external manufacturer with 156.8 mm edge length and a thickness $d_{\text{wafer}} = 160 \mu\text{m}$ are utilized as precursors. They exhibit an alkaline textured n -type Cz-grown Si base substrate with a resistivity ρ_{base} of $1.3 \Omega \cdot \text{cm}$, in- and extrinsic (p - and n -type on the rear and front side, respectively) hydrogenated a -Si:H layers, and ITO layers on both sides. For more details about the sample structure, the reader is kindly referred to section 2.2.1. The precursors are laser-cut into 69 mm x 78 mm-sized samples. In a next step, photoconductance-based lifetime measurements are performed. Furthermore, in order to extract spatially resolved information about the samples' charge carrier lifetime, photoluminescence (PL) imaging is conducted on the samples [172]. Subsequently, the samples are ultrasound-treated on the front side (a -Si:H(n) side) using the same settings as mentioned above and re-measured in terms of lifetime afterwards. Then, thermal annealing (200°C, 30 min) is performed by means of a hotplate. Subsequently, lifetime measurements are conducted again. Subsequently, ΔiV_{OC} is calculated according to equation (6-1).

⁹ In terms of a complete electrical characterization of ultrasound-pretreated and annealed metal electrodes, one would possibly await the investigation of ultrasound's impact on ρ_c in addition to the investigation of r_f . However, the small size of the metal electrode/sonotrode contact and the very inhomogeneous finger shape of ultrasound-pretreated contact fingers (see SEM images in Figure 6-13) prohibit a reliable application of the transfer length method to the samples.

6.2.3 Microstructural analysis of metal contacts

The impact of ultrasonic oscillations on printed metal electrode's microstructure is investigated by means of SEM (samples of group 1). Figure 6-13 (a) and (b) provide overviews of fingers, which are treated by ultrasound operating with oscillations that are directed perpendicular to and along the fingers, respectively. Due to the mechanical metal electrode/sonotrode contact, the fingers are apparently pressed together resulting in a decrease of the finger height h_f . Moreover, significant abrasion as a consequence of the oscillation perpendicular to the finger is observed. After such an ultrasonic treatment, the finger is widely spread across the adjacent substrate surface area. Certainly, this would cause a significant shading-related j_{sc} loss when applied to a solar cell. This issue is tackled by an ultrasonic treatment operating with oscillations along the finger instead, as can be derived from Figure 6-13 (b). In this case, the finger is not broadened due to abrasions. Accordingly, no corresponding shading-related losses would be expected on solar cell level.

From Figure 6-13 (c) and (e), one can see that ultrasonic treatment and subsequent thermal low-temperature annealing significantly densify and sinter metal particles together, especially at the finger's top but also at its bottom. Comparing these SEM images to Figure 6-8 (a), showing a comparable finger in terms of printed paste (paste PV) and thermal annealing (200°C, 30 min) but without a pretreatment, reveals that the ultrasonic treatment enhances sintering and densification processes. In fact, the metal particle connections visible in Figure 6-13 (c) and (e) are rather similar to those obtained after thermal annealing at 350°C (compare Figure 6-8 (b)).

In order to understand whether this effect arises from ultrasound application alone or rather from the mechanical pressure of the sonotrode that occurs when it touches the metal electrode, SEM images of an additional sample are taken. Here, the metal electrode is touched by the sonotrode while no oscillations are applied (Figure 6-13 (d) and (f)). Due to the similarity of the microstructures in Figure 6-13 (c)/(e) and Figure 6-13 (d)/(f), it is assumed that the mechanical pressure exerted by the sonotrode is a significant driver of the metal particles' densification.

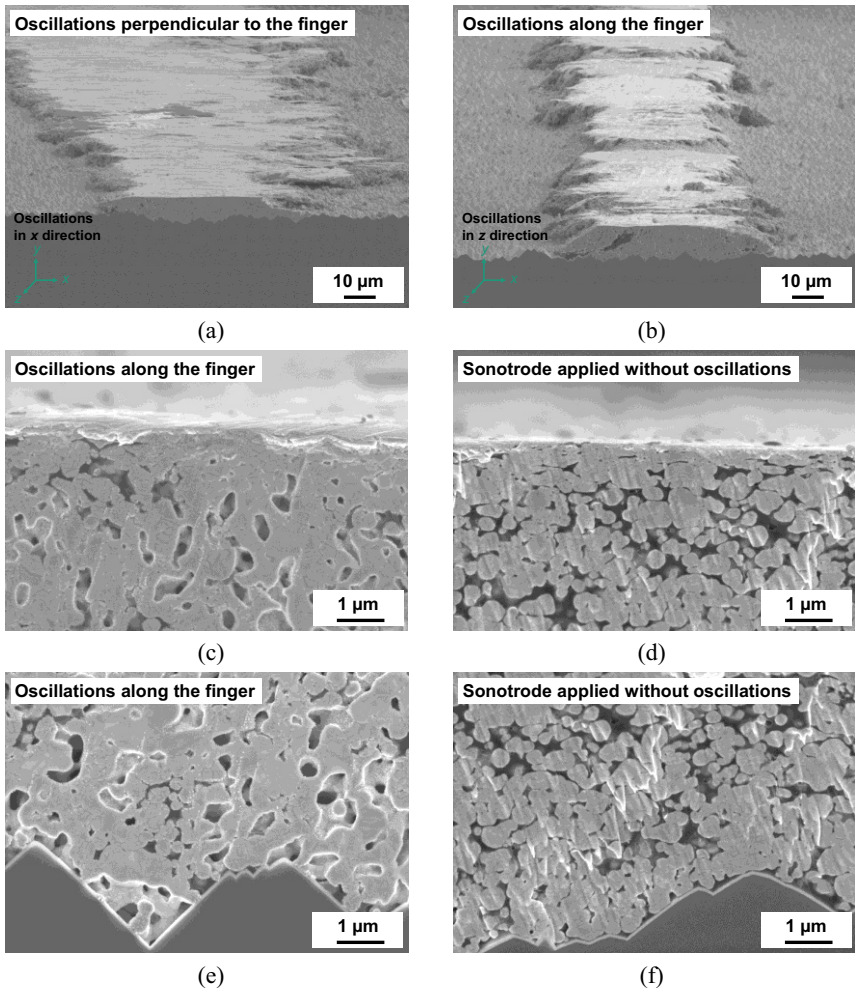


Figure 6-13 SEM images of sample cross-sections taken after thermal annealing at 200°C, 30 min. In (a), ultrasonic oscillations are directed perpendicular to the finger, in (b), (c), and (e), ultrasound is applied along the fingers (ultrasound application operated at *U-mid*). The images (d) and (f) show fingers, which are touched by the sonotrode as all other fingers but without the application of ultrasound. In (c) and (d) the tops of fingers are presented, whereas (e) and (f) show the corresponding bottoms of the same fingers.

However, the structures in Figure 6-13 (c)/(e) appear slightly more densified, which indicates that an oscillation-induced densification exists. Therefore, the enhanced inter-particle contacts certainly originate from both mechanical pressure and ultrasonic treatments. Their impact on the metal fingers' electrical performance is investigated in the following section 6.2.4.

6.2.4 Electrical characterization of metal contacts

In the following, the impact of ultrasonic treatments on r_f of printed metal electrodes is investigated (samples of group 1). Figure 6-14 depicts r_f as a function of the three ultrasonic pretreatments. All samples are thermally annealed (200°C, 30 min) after the corresponding preprocesses.

Without the use of ultrasound, r_f of 1.3 Ω/cm is obtained (black, dashed line). By means of *U-low* and *U-mid*, slightly lower r_f values of 1.2 Ω/cm are achieved. Since the relative errors are in the range of 1%, the reduction is significant. The r_f reduction of 8%_{rel} is caused by enhanced particle sintering and densification (compare Figure 6-13 and the discussion in the preceding section).

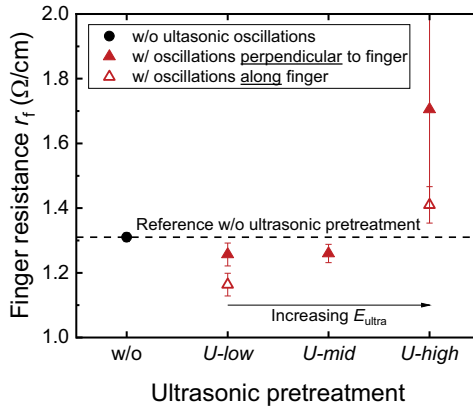


Figure 6-14 r_f as a function of the conducted ultrasonic pretreatments. All samples are thermally annealed at 200°C for 30 min after ultrasonic pretreatments. $w_{f,\text{set}}$ is chosen to be 50 μm . Mean values and corresponding standard deviations, represented by the error bars, are shown. Because the samples being processed using *U-mid* (ultrasound applied along the fingers) broke after processing, a corresponding data point is missing.

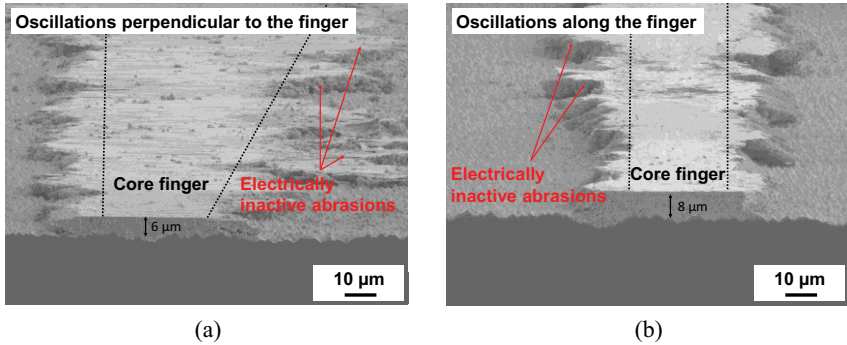


Figure 6-15 SEM images of fingers, which are pretreated using *U-high* and then annealed at 200°C for 30 min. In (a) oscillations are directed perpendicular to the finger and in (b) oscillations are directed along the finger.

After *U-high*, r_f exhibits a higher value than the reference. From the SEM pictures depicted in Figure 6-15, it is obvious that the fingers are extremely crushed by the sonotrode during the application of *U-high*. It seems as if the position of the sonotrode was not sufficiently adjusted to the samples' surfaces during such processing. Consequently, the fingers are flat (h_f of $6\text{--}8\ \mu\text{m}$) resulting in a reduced cross-sectional area of the metal electrodes. Furthermore, at the sides of both fingers, abraded metal is visible disconnected from the bulk finger and, obviously, not contributing to the overall lateral conductivity of the finger (see markings in Figure 6-15). This further reduces the electrically relevant fingers' cross-sectional areas.

Considering all three ultrasonic settings, it is further obvious that ultrasound applied perpendicularly to the fingers leads to higher r_f values than ultrasound applied along the fingers. This is assumed to originate from larger amounts of electrically inactive parts, as ultrasound is applied perpendicularly instead of along the fingers (see Figure 6-15 as well as Figure 6-13 (a) and (b)). In general, the higher abrasion caused by ultrasound applied perpendicularly to the finger leads to higher r_f .

6.2.5 Passivation of silicon heterojunction structures

In order to evaluate the impact of ultrasonic processing on SHJ structures, PL images prior to and after processing are compared to each other (samples of

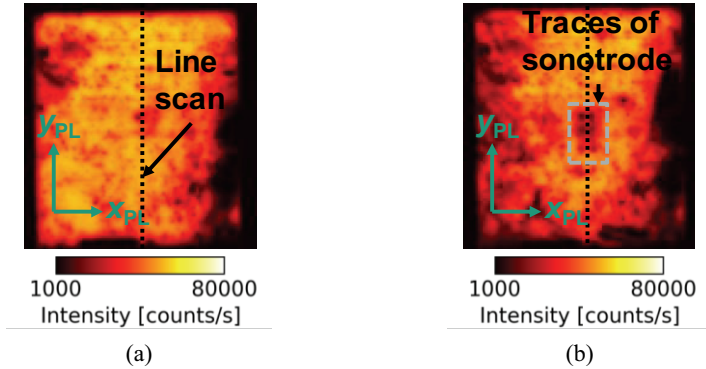


Figure 6-16 Photoluminescence images of the same sample recorded at an illumination of 1000 W/m^2 before (a) and after (b) ultrasonic preprocessing operating at *U-high* (both without thermal annealing).

group 2). In Figure 6-16, such a comparison is displayed by taking the example of *U-high*. The same sample appears slightly darker after ultrasonic treatment, which is reflected by a $18\%_{\text{rel}}$ lower mean overall PL intensity compared to the initial state. This indicates a loss of passivation quality as a result of the ultrasonic treatment. Furthermore, traces of the mechanical sample/sonotrode contact are visible in Figure 6-16 (b). The corresponding dark regions in the middle of the PL image indicate a particularly high loss of passivation quality in this area.

Line scans of the PL intensity are performed according to the black, dashed lines in y_{PL} -direction displayed in Figure 6-16 (a) and (b), respectively. The corresponding results are depicted in Figure 6-17. The PL intensity loss across the sample is marked grey here. It is low except for in the region adjacent to position $y_{\text{PL}} = 0.5$. This is the position where sample and sonotrode are in mechanical contact. Here, the photoluminescence intensity \mathcal{I}_{PL} is significantly reduced, which underlines that ultrasonic preprocessing at *U-high* is not damage-free. The thin passivating layers, obviously, suffer from ultrasonic oscillations along the whole sample. In particular, where ultrasound is coupled into the sample (mechanical sonotrode/sample contact), passivation quality degrades.

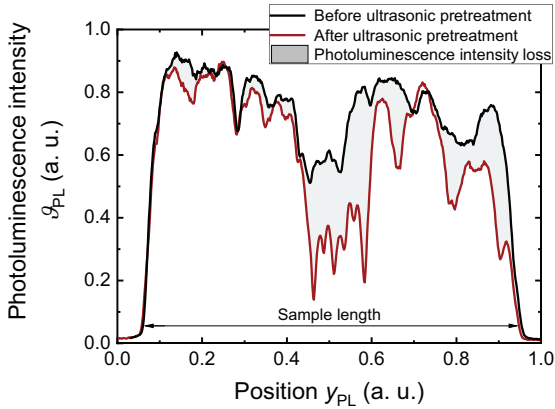


Figure 6-17 Line scans in terms of I_{PL} as a function of y_{PL} across the samples (see corresponding markings (black, dashed lines) in Figure 6-16).

The other two ultrasonic preprocessings *U-low* and *U-mid* also cause significant damage to the SHJ samples, as can be deduced from the ΔiV_{OC} data presented in Figure 6-18. Actually, no proportional decrease of iV_{OC} as a consequence of increasing E_{ultra} is determinable.

Directly after the ultrasonic pretreatments, all samples' iV_{OC} values are reduced

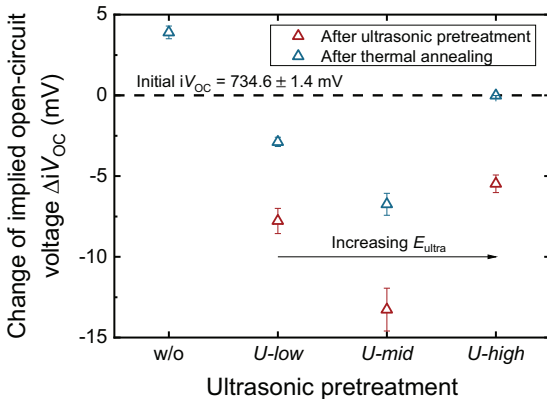


Figure 6-18 ΔiV_{OC} (iV_{OC} gain if greater than zero, loss if smaller than zero) as a function of the ultrasonic treatments. The error of ΔiV_{OC} is estimated to be 10%. The data points represented by the brown symbols are taken after ultrasonic treatments, the data points represented by blue symbols are taken after additional thermal annealing.

6.3 Intense pulsed light processing

by more than 5 mV (see brown triangles in Figure 6-18). The ultrasound-induced damages can be cured to a certain amount by means of thermal annealing at 200°C conducted for 30 min. However, an iV_{OC} gain of 3.9 ± 0.4 mV, such as in the case of the reference process without ultrasonic preprocessing, is not reached (see blue triangles in Figure 6-18).

Please note that for the non-metallized samples considered here, a direct contact of sonotrode and sample surface cannot be avoided during the application of oscillations. If the samples exhibited metal electrodes and the sonotrode's position were perfectly aligned, a mechanical contact of sonotrode and SHJ substrate could be avoided. Thereby, the main reason for passivation quality loss could be eliminated (i.e. mechanical sonotrode/sample contact) because the sonotrode would touch the tops of the metal contacts only. However, this would require very sensitive alignment even considering a full-size solar cell.

6.3 Intense pulsed light processing

6.3.1 Motivation

In the previous sections 6.1 and 6.2, thermal contact formation processes applicable to SHJ and TOPCon structures are investigated that enable high electrical performance of printed metal electrodes. However, thermal annealing continues to be a time-consuming and, therefore, expensive process. A possible alternative is intense pulsed light (IPL), promising to be faster due to pulse times in the range of milliseconds and, in consequence, more cost-effective.

IPL's potential to substitute thermal steps in back end processing of SHJ solar cells is investigated in the following. A comprehensive process development aiming at damage-free annealing of SHJ solar cells and low-resistive metal electrodes is presented. Moreover, the temperature of SHJ substrates is measured in-situ during IPL processing. To the author's knowledge, it is the first time that the time-resolved sample temperature is recorded during millisecond-lasting IPL pulses using a pyrometer. The in-situ-measured temperature enables a correlation of substrate temperature and IPL-induced gains and losses in passivation quality of SHJ structures. Further, IPL's impact on metal electrodes

is investigated in terms of electrical contact formation. For this purpose, the optical properties of both substrates and metal contacts are considered as well.

In a next step, the understanding of IPL processing of SHJ-based samples is transferred to IPL post-metallization annealing of TOPCon. Since these structures are more tolerant towards thermal budget during IPL than the silicon heterojunction, printed metal contacts can exploit their full potential regarding electrical performance here.

6.3.2 Sample preparation and characterization

In the first part of the experiment, IPL processes suitable for the metallization of SHJ samples are developed. Figure 6-19 depicts the corresponding process flow. In group 1 and 3 SHJ precursors from an external manufacturer with 156.8 mm edge length and a thickness $d_{\text{wafer}} = 160 \mu\text{m}$ are utilized as starting material. The precursors exhibit an alkaline textured n -type Cz-grown Si base substrate with a resistivity ρ_{base} of $1.3 \Omega \cdot \text{cm}$, intrinsic and doped (p - and n -type on the rear and front, respectively) hydrogenated a -Si:H layers, and ITO layers on both sides. More details as well as a sketch of the samples' architecture can be found in section 2.2.1. The precursors are laser-cut into 78 mm x 69 mm-sized samples.

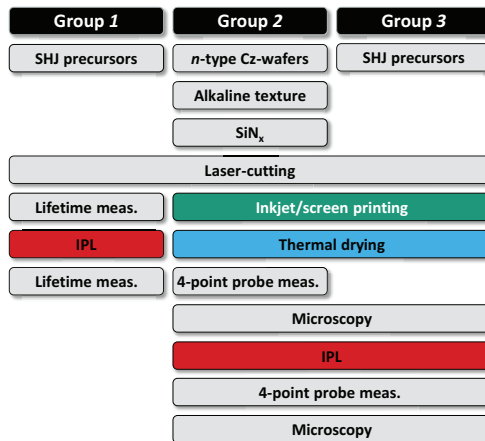


Figure 6-19 Experimental process flow used for the investigation of IPL's potential in SHJ back end processing.

6.3 Intense pulsed light processing

In group 1, the samples' iV_{OC} is determined by means of photoconductance-based lifetime measurements. Then, varying IPL processes are applied in such a way that the front side (n -type a -Si:H side) of each sample is exposed to the irradiation. In a next step, the samples' iV_{OC} is determined by means of photoconductance-based lifetime measurements again. The mean difference of the implied open-circuit voltage ΔiV_{OC} for each process is calculated by using equation (6-1). Thereby, the variation of IPL settings focuses on three parameters: these are the lamp voltage U_{lamp} , which is correlated with the intensity of the lamp's emitted radiation, the duration of the pulsed light t_{pulse} , and the pulse number n_{pulse} applied at a constant frequency f_{pulse} , i.e., the reciprocal of the time between light pulses. More than 50 parameter combinations within defined parameter ranges are selected by means of a design of experiment creator [173]. Thereby, U_{lamp} is varied from 400 to 700 V, t_{pulse} is varied from 0.5 to 8 ms, n_{pulse} is varied from one to three, and f_{pulse} is kept constant at 0.1 Hz. Thermal annealing at 200°C for 30 min is performed as well, as it is the reference process in this whole work. The corresponding ΔiV_{OC} data are experimentally obtained by means of equation (6-1). Subsequently, the other ΔiV_{OC} values are calculated by means of metamodeling [174].

In order to understand the dependence of passivation quality on different IPL processes, selected ΔiV_{OC} data are correlated with in-situ temperature measurements conducted on non-metallized SHJ samples processed in parallel (not shown in Figure 6-19). For details about the temperature measurement setup, the reader is kindly referred to section 4.5 and appendix A.

Settings with a high ΔiV_{OC} potential are selected for processing the samples of group 2 and 3. Samples of both groups are printed using a silver nanoparticle ink, labelled ink *Nano-Ag* (also utilized in chapter 5) as well as two silver-based screen printing pastes *PV* and *PE*, and one paste based on silver-coated copper particles, paste *AgCu*. For more details about the three printing media see appendix B. All pastes and the ink are commercially available. During inkjet printing, the samples are kept at a constant temperature of 60°C and the print-head at a temperature of 50°C in order to achieve both printing stability and optimized finger width. The screen-printed samples undergo a drying step

performed at 100°C for 10 min using a conveyor furnace. In group 2, the printed patterns are dumbbell-shaped structures used for r_f determination (see Figure 4-2). They exhibit a set finger width $w_{f,set}$ of 50 μm in the case of screen printing and ten layers ($n_{pass} = 10$) in the case of inkjet printing. As these samples target on r_f , alkaline textured Cz-Si samples (laser-cut into 78 mm x 69 mm-sized samples as well) coated with an insulating SiN_x layer are used as substrates instead of SHJ precursors. The insulating layer restricts the current flow to the printed patterns without a parasitic flow through underlying layers, such as TCO, during four-point probe measurements. In group 3, in contrast, TLM-compatible structures with an equal distance of 1.5 mm on SHJ solar cells suitable for the determination of ρ_c at the metal/ITO contact are printed (eight contacts exhibiting $w_{f,set} = 100 \mu\text{m}$, see section 4.3.2). All samples are characterized by means of confocal microscopy and SEM after printing. On the group 2 samples, four-point probe measurements are conducted in order to determine r_f . Then, the IPL settings with a high ΔV_{OC} potential are applied to the samples (metallization facing flash lamp). A thermal annealing step performed at 200°C for 30 min is used as the reference process in both groups (not shown in Figure 6-19). Subsequently, four-point probe measurements in order to determine r_f (group 2) and ρ_c (group 3) as well as confocal microscopy and SEM (group 2 and 3) are performed.

In a next experiment, the focus is set on an understanding of how radiative energy enables metal electrodes to form an electrical contact. First, the wavelength-dependent emission spectrum of the Xenon flash lamp, which is received by a sample within t_{pulse} , is measured using an ultraviolet-visible spectrometer. Second, the transmittance T_i and reflectance R_i of square-shaped metal pads exhibiting an area of 9 cm^2 are measured utilizing an ultraviolet-visible-near-infrared spectrometer (*PerkinElmer Lambda 900*). One metal pad is screen-printed on a planar glass substrate using paste *AgCu*. Directly after printing, it is dried at 100°C for 10 min for handling reasons. Moreover, a silver pad evaporated on a second planar glass substrate as well as a non-metallized SHJ sample are used to measure T_i and R_i .

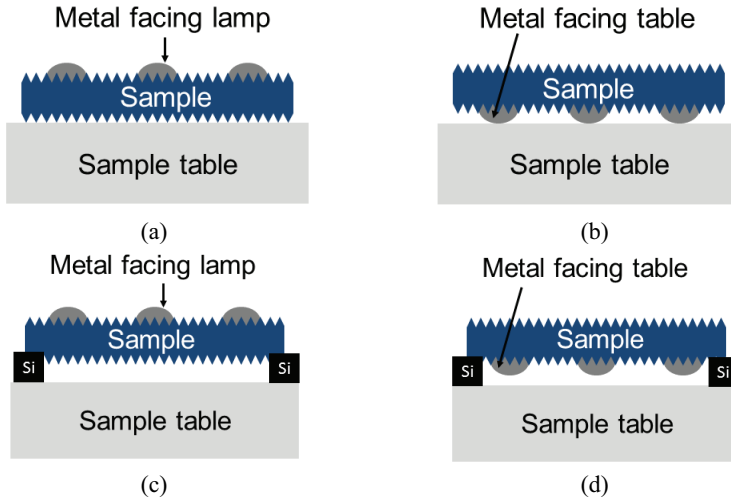


Figure 6-20 IPL processing of metallized test sample with varying orientations: metallization facing lamp ((a) and (c)) or the sample table ((b) and (d)). Some samples are lifted 2 mm above the sample table by means of Si cuboids ((c) and (d)).

Then, it is further differentiated in which way IPL induces electrical contact formation in terms of r_f and ρ_c . To this end, spare samples of group 2 and 3 (see Figure 6-19), exhibiting screen-printed paste-*AgCu*-based metal contacts in a dried state (100°C, 10 min), are utilized. One half of the samples is IPL-treated with the metal contacts facing the lamp (see Figure 6-20 (a)) and the other half of the samples with the metal contacts facing the sample table (see Figure 6-20 (b)). Additionally, to minimize the cooling effect by the sample table, the same processes are conducted on samples lifted 2 mm above the sample table by means of two small Si cuboids (see Figure 6-20 (c) and (d)) with the dimension of 30 mm x 2 mm x 2 mm (length x width x height). These are positioned at the samples' longer edges. All samples receive the same IPL process in terms of parameter settings, namely *IPL-all* (see Table 6-2 or appendix B for more details). r_f and ρ_c is determined afterwards.

In a next experiment, IPL processing is extended to also include solar cells exhibiting tunnel oxide passivating contacts, which can withstand higher temperatures than the SHJ. To this end, symmetrical TOPCon lifetime samples,

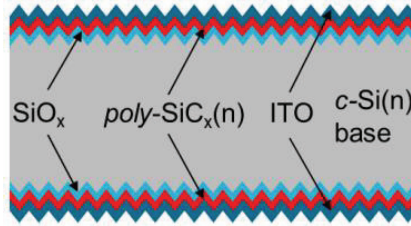


Figure 6-21 Sketch of a symmetrical TOPCon lifetime sample. Picture adapted from Ref. [120].

as sketched in Figure 6-21, are utilized. The base material are 160 μm thick alkaline textured n -type Cz-grown Si wafers ($\rho_{\text{base}} = 1.0 \Omega \cdot \text{cm}$). On both sides, n -type TOPCon layers featuring 1.2 nm thick tunnel oxides (SiO_x) and 15 nm thick poly-SiC_x layers are deposited. Then, the samples are laser-cut into square samples with 39 mm edge length and ITO layers are deposited via DC magnetron sputtering on both sides. Here, the low-invasive ITO dual layer sputter process developed for the application on ultra-thin poly-Si -based passivating contacts is utilized (first introduced in Ref. [63]). Before and after ITO deposition, photoconductance-based lifetime measurements are conducted in order to extract iV_{OC} . Then, some of the samples are IPL-processed on one side using four different settings, namely *IPL-all*, *IPL-PV*, *IPL-TOP1* and *IPL-TOP2* (see Table 6-2 for more details). These are evolutions of the processes developed for SHJ samples in the sections 6.3.3 and 6.3.4. Each process is conducted on a separate group of samples.

Table 6-2 IPL processes applied to TOPCon samples. Also compare Table 6-3.

IPL process	Description	U_{lamp} (V)	t_{pulse} (ms)	n_{pulse}	f_{pulse} (Hz)
<i>IPL-all</i>	Standard for SHJ	550	1	3	0.1
<i>IPL-PV</i>	Developed for paste PV	550	2	3	0.1
<i>IPL-TOP1</i>	Evolution for TOPCon	550	2	3	0.5
<i>IPL-TOP2</i>	Evolution for TOPCon	550	2	6	0.5

6.3 Intense pulsed light processing

After the application of these IPL annealings, the samples are characterized by means of photoconductance-based lifetime measurements again. In order to classify the IPL processes with regard to their impact on the passivation quality on TOPCon samples, thermal annealing is considered for comparison reasons. Lifetime samples as described above are thermally annealed for 10 min at 200°C, 300°C, and 350°C as well as for 3 min at 350°C instead of using IPL. These are lifetime-measured before and after annealing as well.

In a final step, all TOPCon lifetime samples are provided with 1 μm thick silver-based contact pads on both sides in order to extract the sum of the contact resistivities $\rho_{\text{c,stack}}$ occurring at the interfaces of the *c*-Si/SiO_x/poly-SiC_x/ITO/silver stack from vertical *IV*-measurements through the sample. In a preceding step, the samples are cut into square samples with 5 mm edge length.

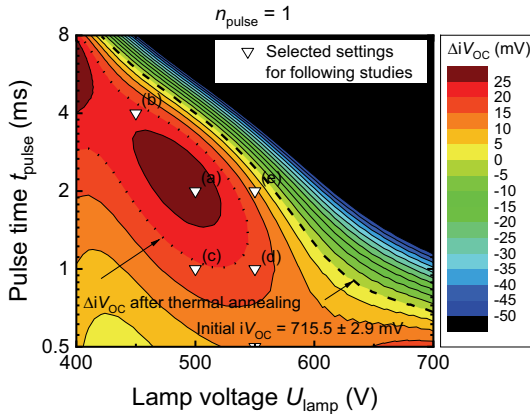
6.3.3 Passivation of silicon heterojunction structures

In the first part of the IPL process development, a SHJ-compatible IPL process window is identified taking into account the temperature-sensitivity of the *a*-Si:H layers. The influence of numerous IPL processes on passivation quality is quantified by the ΔiV_{OC} referring to non-metallized test samples with a mean initial iV_{OC} value of 715.5 ± 2.9 mV (group 1 in Figure 6-19). On the one hand, negative ΔiV_{OC} values indicate a degradation of the SHJ structures' passivation or even a destruction of the samples. Positive values, on the other hand, indicate that passivation is improved due to the conducted annealing process.

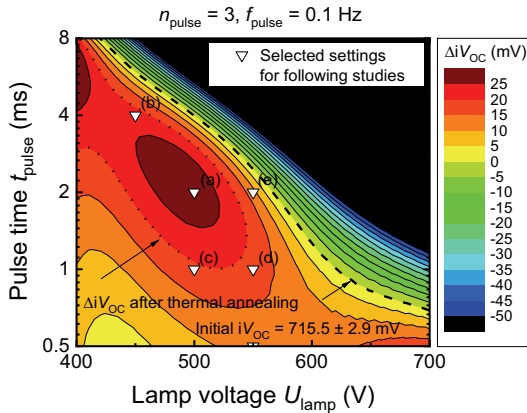
In Figure 6-22, ΔiV_{OC} is plotted as a function of U_{lamp} and t_{pulse} using $n_{\text{pulse}} = 1$ (Figure 6-22 (a)) and $n_{\text{pulse}} = 3$ (Figure 6-22 (b)). The regions drawn in black indicate that either the samples' iV_{OC} is drastically reduced ($\Delta iV_{\text{OC}} < -50$ mV) or the samples are even physically cracked during IPL processing as a result of thermally induced stress. Optima regarding passivation quality are identified within the dark-red regions. At the marked point (a) in Figure 6-22 (a), a mean ΔiV_{OC} gain of 25.9 ± 2.3 mV is determined. By means of thermal annealing (reference process), a mean ΔiV_{OC} gain of only 20.4 ± 2.2 mV is obtained.

6 Understanding of contact formation processes

In general, SHJ structures benefit from annealing (typically $T \approx 200^\circ\text{C}$) after ITO deposition due to curing of sputtering damage [26]. Nevertheless, the data in Figure 6-22 (a) reveal that passivation quality additionally benefits from IPL processing, which results in a 5.5 mV higher iV_{OC} compared to thermal annealing. This additional gain can be explained by light soaking (LS) effects, as



(a)



(b)

Figure 6-22 IPL-induced iV_{OC} gain, if ΔiV_{OC} is greater than zero, or loss, if ΔiV_{OC} is smaller than zero, as a function of t_{pulse} and U_{lamp} . In (a) and (b) n_{pulse} is equal to one and three, respectively. The relative error is 0.5%. Data points (a)-(e) mark settings selected for subsequent parts of the experiment. The initial mean iV_{OC} serving as the reference point determined before IPL is 715 ± 2.9 mV. (a) is redrawn from Ref. [156].

discussed in Ref. [175, 176]. In these publications, it is demonstrated that LS occurs even if annealing effects (curing) are suppressed by keeping the samples close to room temperature. Thus, LS is assumed to exist based on fundamentally different physical mechanisms compared to thermal curing. It is suggested that LS is caused by an inverse *Staebler-Wronski-effect*, which requires the presence of doped *a*-Si layers [177]. In such case, the Fermi-level at the *c*-Si/*a*-Si:H heterojunction is moved close to the conduction (*a*-Si:H(n)) or the valence band (*a*-Si:H(p)) so that defect and recombination kinetics are positively affected. Healing of defects is obtained due to the energy released by the recombination of excess carriers, which are generated by photon absorption (e.g., due to IPL) or biasing of the device. It is further shown that SHJ cells' V_{OC} and also FF benefit from irradiation with wavelengths λ greater than that of blue light, resulting in a η gain 0.3%_{abs} [175]. Since IPL utilizes a broad emission spectrum with a peak in the green wavelength range (compare Figure 6-29 (a)), LS is assumed to lead to the additional gain in iV_{OC} in Figure 6-22. It is shown in section 7.1 that the described LS effect is also reflected in high values for V_{OC} and FF of IPL-processed SHJ cells fabricated as part of this work.

Four SHJ-compatible processes (a)-(d) are selected for the application on metallized test samples. Paste PV even requires setting (e), as shown in section 6.3.4, which unfortunately is of limited SHJ compatibility. According to Figure 6-22 (a), ΔiV_{OC} at setting (e) results in a gain of 10.0 ± 3.2 mV. Nevertheless, it is used as a base parameter set in combination with more temperature-tolerant structures such as TOPCon (see section 6.3.6).

A variation of the pulse number n_{pulse} reveals that the application of three pulses instead of one has no significant impact on ΔiV_{OC} considering settings (a)-(e) (Figure 6-22 (b)). However, greater pulse numbers than three would damage the SHJ samples (not shown here). Lower pulse numbers are assumed to be adverse for electrical contact formation of printed metal structures. In fact, the investigations conducted in section 6.1 regarding thermal annealing reveal that the higher the energy input, the lower is r_f . This is also valid, to a certain extent, for ρ_c , too. In order to avoid both damage of the SHJ structure due to too high thermal

6 Understanding of contact formation processes

budget and high resistances of the metal electrodes due to too low energy input, $n_{\text{pulse}} = 3$ is selected in the following.

Using the measurement setup introduced in section 4.5 (see appendix A as well), the temperature profiles of non-metallized SHJ samples are measured in-situ during IPL processing at selected settings. In Figure 6-23, the temperature profiles of SHJ samples are displayed, which are measured during four varying IPL processes. These correspond to the settings *IPL-all*, *IPL-PV*, *IPL-PE*, and *IPL-AgCu/IPL-NanoAg* listed in Table 6-3 but differing in n_{pulse} ($n_{\text{pulse}} = 1$). The measurements are corrected to obtain the temperature $T_{m,\text{corr}}$ as explained in appendix A. Calculated peak temperatures $T_{\text{peak,c}}$ are obtained using the equation

$$T_{\text{peak,c}} = T_{\text{room}} + \frac{E_{\text{rad}}}{c_{\text{Si}} \cdot m_{\text{sample}}}, \quad (6-2)$$

where T_{room} is the room temperature, c_{Si} is the specific heat capacity of silicon, and m_{sample} is the mass of the sample's part below the area irradiated by means

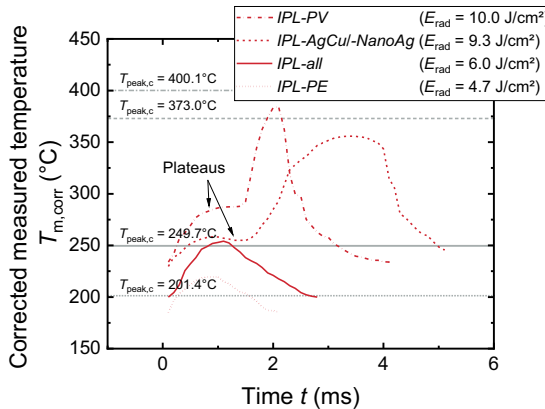


Figure 6-23 Temperature profiles (average of three measurements) as functions of time t measured during IPL processing of non-metallized SHJ samples. The curves are corrected according to the procedure presented in appendix A. They begin and end at the lower edge of the pyrometer's measurement range dependent on the correction (see appendix A as well). Additionally, corresponding calculated peak temperatures $T_{\text{peak,c}}$ are displayed (horizontal lines). The relative error of the temperature measurements is assumed to be 5% (for explanation see appendix A).

6.3 Intense pulsed light processing

of IPL with E_{rad} . The radiant exposure E_{rad} is experimentally obtained by means of a bolometer. The absorption of the sample is assumed to be 100%.

One can see from Figure 6-23 that for *IPL-all*, the measured and corrected peak temperature $T_{\text{peak,m,corr}}$ and the calculated peak temperature $T_{\text{peak,c}}$ are very similar. For *IPL-PE*, $T_{\text{peak,m,corr}}$ exceeds $T_{\text{peak,c}}$, presumably due to the fact that the lower edge of the temperature measurement range is reached in this case. Moreover, infrared radiation from the surroundings might artificially affect the measurement at this comparably low temperature. For *IPL-PV* and *IPL-AgCu-NanoAg*, $T_{\text{peak,m,corr}}$ tends to remain below $T_{\text{peak,c}}$. Since the latter settings exhibit $t_{\text{pulse}} > 1$ ms, cooling effects might become relevant during these longer pulses due to air convection at the sample's upper side and also by cooling induced by the sample table. These effects are not regarded in equation (6-2), possibly explaining the difference of $T_{\text{peak,m,corr}}$ and $T_{\text{peak,c}}$. Another possible explanation is provided in the following paragraph.

After the end of a pulse, the measured and corrected temperature $T_{\text{m,corr}}$ decreases below the measurement-setup-specific minimum measureable temperature within one to two milliseconds. However, in the heating section it is conspicuous that for *IPL-PV* and *IPL-AgCu-NanoAg* the temperature profiles exhibit

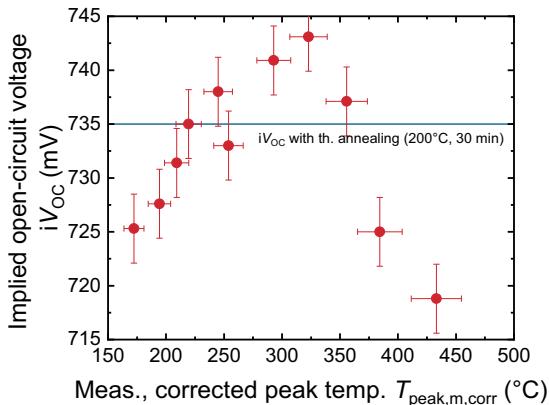


Figure 6-24 Implied open-circuit voltage iV_{OC} of non-metallized SHJ samples (data taken from Figure 6-22 (a)) as a function of the measured and corrected peak temperature $T_{\text{peak,m,corr}}$ (average of three measurements) obtained for varying IPL processes. The relative error of the temperature measurements is assumed to be 5% (see appendix A).

plateaus at $T_{m,corr}$ in the range of 250 to 275°C. With parallel processed samples glued to the sample table and, thereby, holding the specimens in position, it is excluded that this effect is caused by movements of the samples during processing, such as bending or jumping. Another interpretation is thus preferred: it is assumed that a process in the sample is triggered at 250 to 275°C absorbing latent heat and, thereby, causing the characteristic plateaus in the heating sections during the application of *IPL-PV* and *IPL-AgCu/-NanoAg*. Such a processes could be hydrogen effusion out of the *a*-Si:H layers reaching its peak at about 250°C according to Ref. [178].¹⁰ Moreover, the absorption of latent heat could be an alternative, or an additional, explanation for the difference of $T_{peak,m,corr}$ and $T_{peak,c}$ in the case of *IPL-PV* and *IPL-AgCu/-NanoAg*: $T_{peak,m,corr}$ is lower than $T_{peak,c}$ because equation (6-2) assumes that E_{rad} is completely converted into temperature increase, whereas E_{rad} is partially consumed for hydrogen effusion.

Furthermore, please note that the coincidence of the temperature plateau of $T_{m,corr}$ and the temperature of the maximum hydrogen effusion rate out of *a*-Si:H indicates a high accuracy of the developed in-situ temperature measurement method, under the assumption that such effusion causes the plateaus in $T_{m,corr}$.

In Figure 6-24, iV_{OC} is plotted as a function of $T_{peak,m,corr}$. First, it becomes obvious, that during IPL in the millisecond range, SHJ samples can withstand significantly higher temperatures than 200°C, which is commonly used for thermal annealing. The highest iV_{OC} of 743.1 ± 3.2 mV is achieved for $T_{peak,m} = 322.9^\circ\text{C}$. This corresponds to the setting marked with (a) in Figure 6-22 (a). Please note that light soaking effects have to be taken into account here as well in order to explain the high iV_{OC} (see above in the present section). The rapid IPL process allows for such high temperatures in the SHJ samples without harming passivation quality. This peak temperature would significantly deterio-

¹⁰ It cannot be excluded that other processes such as, e.g., crystallization of the temperature-sensitive layers (*a*-Si:H or ITO) play an additional role here. However, from measurements of the Xenon flash lamp's radiant flux density it can be excluded that the plateaus are caused by inhomogeneity of intense pulsed light.

6.3 Intense pulsed light processing

rate iV_{OC} if typical annealing times in the range of minutes were used, as it is the case for thermal annealing (compare Figure 6-11). Interestingly, the IPL process with $t_{pulse} = 1$ ms and $T_{peak,m,corr} = 219.5^{\circ}C$ achieves a similar iV_{OC} value (including light soaking effects in the case of IPL) as the thermal reference process performed at $200^{\circ}C$ for 30 min (horizontal line). This suggests that the short process time of milliseconds is compensated by higher peak temperatures in the case of IPL to reach similar values of iV_{OC} . For $T_{peak,m,corr} > 322.9^{\circ}C$, a critical temperature is exceeded and SHJ samples degrade. This is the reason why, e.g., the setting marked with (e) in Figure 6-22 (a) (labelled *IPL-PV* in section 6.3.4) is of limited SHJ-compatibility. The other selected settings (a)-(d) (see Figure 6-22 (a)), in contrast, lead to $T_{peak,m,corr} < 322.9^{\circ}C$ and, thus, are SHJ-compatible.

Based on the determination of $T_{peak,m,corr}$, one can generally conclude with regard to Figure 6-22 (a): iV_{OC} is reduced in the top right and bottom left corner of the graph because $T_{peak,m,corr}$ exceeds or remains far below $322.9^{\circ}C$, respectively. Optima in terms of iV_{OC} can be found along an imaginary line from the top left to the bottom right corner of the graph because $T_{peak,m,corr}$ being in the range of $300-330^{\circ}C$ for the corresponding IPL settings, which is identified as the IPL-specific SHJ-related optimum temperature range.

6.3.4 Electrical characterization of metal contacts

After the identification of SHJ-compatible IPL settings in the previous section, their potential of electrical contact formation is investigated in the following by considering four different types of metallization (samples of group 2 and 3).

First, the suitability of $n_{pulse} = 3$, which is selected above, is evaluated by taking the example of paste *PE* and the setting marked with (a) in Figure 6-22 (a). r_f is measured after drying ($n_{pulse} = 0$) and consecutively after the application of n_{pulse} increasing from one to five. Figure 6-25 confirms the correlation of higher energy input, in terms of increasing n_{pulse} , lowering r_f . Obviously, the paste *PE*-based metal contacts exhibit a low r_f already after drying. However, a significant r_f reduction is achieved as a consequence of the application of one IPL pulse. For $1 < n_{pulse} < 5$, r_f decreases only little.

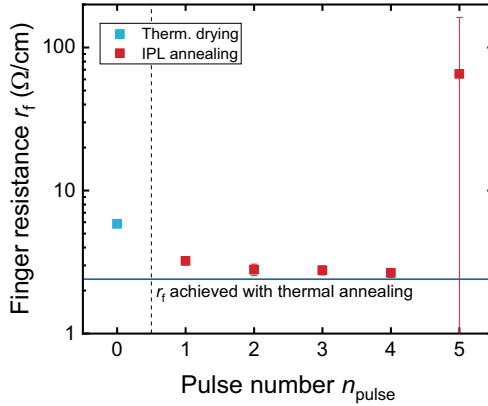


Figure 6-25 Mean r_f values of fingers printed using paste *PE* as a function of n_{pulse} utilizing the IPL process marked with (a) in Figure 6-22. The error bars represent corresponding standard deviations. The horizontal blue line marks r_f achieved with thermal annealing. The graph is redrawn from Ref. [156].

Conspicuous is the very strong increase of r_f in the case of $n_{\text{pulse}} > 4$. Here, at least partly, fingers are cracked and detached from the substrate leading to an increase of r_f . In this experiment, not more than six pulses are applied because at $n_{\text{pulse}} = 6$ the fingers are already completely destroyed. Therefore, r_f measurements cannot be performed anymore. Despite the findings of Figure 6-25

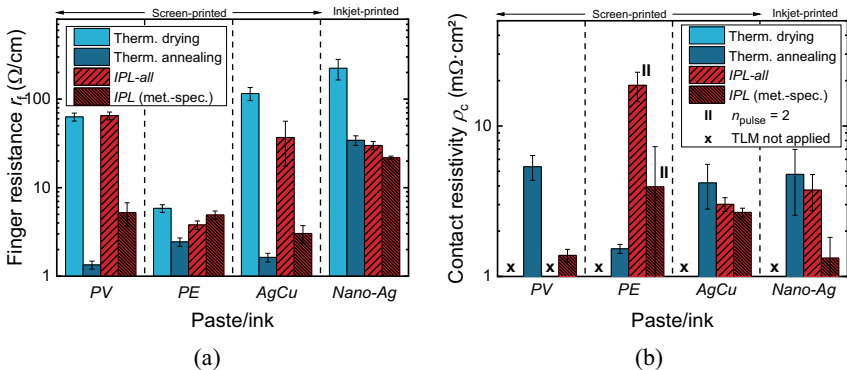


Figure 6-26 Mean r_f (a) and ρ_c (b) data versus the three pastes and the ink. Graphs are redrawn from Ref. [156]. TLM is applied to planar SHJ substrates in the case of ink *Nano-Ag* in order to avoid that the substrates' texture distorts the ρ_c determination if the fingers did not entirely cover the pyramid tips. Error bars represent the standard deviation in the case of r_f . The ρ_c errors are calculated by Gaussian error propagation.

6.3 Intense pulsed light processing

suggest $n_{\text{pulse}} = 4$, in the following n_{pulse} is set equal to a more conservative value of $n_{\text{pulse}} = 3$ in order to minimize the probability of finger detachments.

Table 6-3 IPL processes and corresponding settings as well as ΔiV_{OC} data of SHJ samples (relative error of 0.5%) taken from Figure 6-22 (b). *IPL-AgCu* and *IPL-NanoAg* are of the same parameter set. f_{pulse} is 0.1 Hz for all settings. The corresponding settings marked in Figure 6-22 (b) are noted in brackets besides the ΔiV_{OC} data.

Setting	Applied to paste/ink	ΔiV_{OC} (mV)	U_{lamp} (V)	t_{pulse} (ms)	n_{pulse}
<i>IPL-all</i>	<i>PV, PE, AgCu,</i> <i>Nano-Ag</i>	18.1 (d)	550	1	3
<i>IPL-PV</i>	<i>PV</i>	10.6 (e)	550	2	3
<i>IPL-PE</i>	<i>PE</i>	19.5 (c)	500	1	3
<i>IPL-AgCu/</i> <i>IPL-NanoAg</i>	<i>AgCu, Nano-Ag</i>	22.0 (b)	450	4	3

In a subsequent experiment, a metallization-related IPL process development is conducted. Figure 6-26 sums up core results.¹¹ r_f and ρ_c data are presented versus the three printed pastes and the ink. Thermal drying, thermal annealing, an IPL process labelled *IPL-all*, and various metallization-specific IPL processes (*IPL-PV*, *IPL-PE*, *IPL-AgCu*, and *IPL-NanoAg*) are considered. The IPL processes, their application possibility, and the corresponding IPL settings are listed in Table 6-3. Please note that in the case of the inkjet-printed metallization (ink *Nano-Ag*) and its thin-layer deposition, TLM is performed on planar SHJ substrates in order to avoid insufficient metal covering of pyramid tips due to the alkaline texture prohibiting TLM measurements. These substrates are comparable to their textured equivalents in terms of their architecture. Furthermore, the ITO deposition conditions for textured and planar samples are equal. Therefore, they resemble one another regarding electrical properties. Moreover,

¹¹ Actually, all processes (a)-(e) are applied to all considered kinds of metallization and evaluated. For the sake of clarity, only selected and relevant results are presented in the following.

TLM is not applied if the printed structures are not conductive enough, e.g., directly after drying (compare TLM theory provided in section 4.3.2).

Paste *PV* has the potential for very low finger resistances. Thus, a r_f reduction from $63.1 \pm 6.5 \Omega/\text{cm}$ down to $1.3 \pm 0.1 \Omega/\text{cm}$ is achieved by means of thermal annealing. However, after the application of *IPL-all* r_f remains principally unchanged with $r_f = 65.0 \pm 6.6 \Omega/\text{cm}$ compared to the dried state. Obviously, this particular IPL process is not suitable for the application to paste *PV*. However, the (limited SHJ-compatible) process *IPL-PV* causes a significant reduction of r_f down to $5.2 \pm 1.5 \Omega/\text{cm}$. This low value is explainable when the metal finger's microstructure is considered, which is depicted in Figure 6-27. After the application of *IPL-PV*, numerous pronounced sintering necks connecting the silver particles are visible both at the top (Figure 6-27 (a)) and at the bottom of the finger (Figure 6-27 (b)). These enhance the finger's electrical conductivity (compare the findings of section 6.1). Because during IPL processing, radiation hits the finger's top first, one could expect that sintering is more pronounced at this position than at the finger's bottom. Yet, this is not observed from the comparison of Figure 6-27 (a) and Figure 6-27 (b). The reason for sintering to occur very homogenously across the whole finger height is assumed to be that heat is not only generated in the metal contact itself as a result of absorbed impinging radiation. Heat is also generated in the substrate, which is exposed to radiation where it is not covered by the metal finger. The transferred heat from the finger and the substrate causes homogenous sintering in the entire metal finger (also compare section 6.3.5).

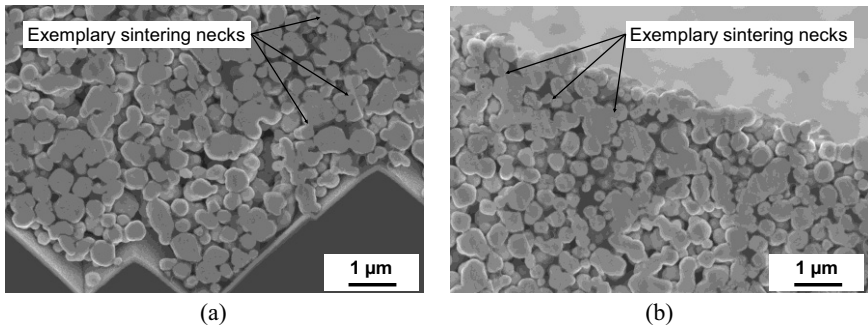


Figure 6-27 SEM images of fingers' cross-sections existing of paste *PV*. In (a) the bottom of an *IPL-PV*-processed finger is depicted. (b) depicts the same finger's top.

6.3 Intense pulsed light processing

Not only the SEM images in Figure 6-27 but also the ρ_c data in Figure 6-26 indicates that Ag particle/ITO sintering is performed sufficiently by IPL processing. In fact, the ρ_c of the paste *PV*/ITO contact processed using *IPL-PV* is $1.4 \pm 0.1 \text{ m}\Omega\text{-cm}^2$ and, therefore, even lower than ρ_c of $5.4 \pm 1.0 \text{ m}\Omega\text{-cm}^2$ after thermal annealing. However, *IPL-PV* harms the passivation quality of SHJ structures and, thus, is not considered as contact formation processing of SHJ solar cells in section 7.1. Yet, the promising electrical performance achieved with metal contacts processed by means of *IPL-PV* suggests the application to more temperature-tolerant TOPCon structures. Indeed, in section 6.3.6 *IPL-PV* is successfully utilized for the development of a TOPCon-specific IPL process.

Paste *PE* exhibits a comparatively low r_f of $5.8 \pm 0.6 \text{ }\Omega\text{/cm}$ already after the thermal drying step. This can be explained by the microstructure of this paste (see Figure 6-28 (a)). The Ag particles are flake-shaped instead of spherical. Therefore, the inter-particle contact is pronounced, even after drying, which results in a low finger resistance. The pastes *PV* and *AgCu* as well as the ink *Nano-Ag* are based on spherical particles. Therefore, their r_f is comparatively higher after drying. Consequently, both with *IPL-all* and *IPL-PE*, only a small reduction of r_f down to $3.8 \pm 0.4 \text{ }\Omega\text{/cm}$ and $4.9 \pm 0.5 \text{ }\Omega\text{/cm}$, respectively, is achieved at all. These values are only slightly higher than the r_f values achieved by means of thermal annealing, which is $2.4 \pm 2.7 \text{ }\Omega\text{/cm}$.

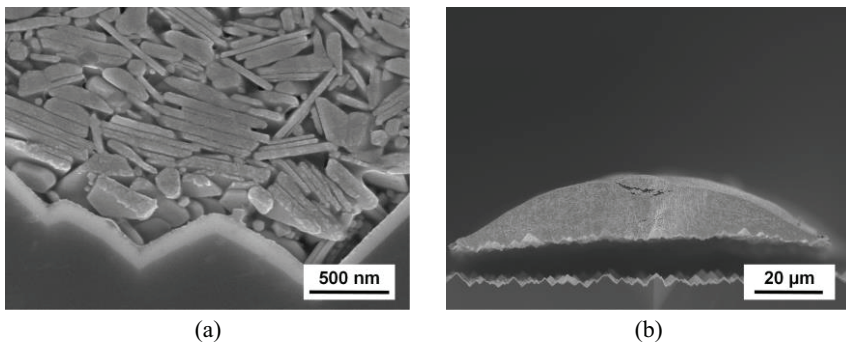


Figure 6-28 SEM images of fingers' cross-sections fabricated by means of paste *PE*. In (a) flake-shaped particles in a dried state are depicted. A finger (printed with a $100 \text{ }\mu\text{m}$ wide screen opening) detached from the substrate after application of *IPL-all* is presented in (b). Both images are redrawn from Ref.[156].

However, the ρ_c data corresponding to the two IPL processes (*IPL-all* and *IPL-PE*) reveal that challenges occur at the paste *PE*/ITO contact. The SEM image depicted in Figure 6-28 (b) shows that the metal contacts are detached from the substrate due to IPL processing. It is assumed that during the measurements necessary to apply the transfer length method, the contact fingers are selectively touched onto the substrate, which results in a measurable (high) contact resistance. The reason for the fingers to detach from the substrate could be very rapid outgassing of paste *PE*'s solvents during IPL processing. They seem to be strongly dissipated at the finger/substrate interface causing the fingers to be blown-off from the substrate. A similar observation is described in Ref. [116].

In the case of paste *AgCu*, both *IPL-all* and *IPL-AgCu* show a significant r_f reduction compared to thermal drying ($r_f = 115.7 \pm 19.5 \Omega/\text{cm}$). By means of *IPL-AgCu*, $r_f = 3.0 \pm 0.7 \Omega/\text{cm}$ and $\rho_c = 2.7 \pm 0.2 \text{ m}\Omega\cdot\text{cm}^2$ are achieved. In comparison, a lower $r_f = 1.6 \pm 0.2 \Omega/\text{cm}$ but a higher $\rho_c = 4.2 \pm 1.4 \text{ m}\Omega\cdot\text{cm}^2$ is obtained with the thermal reference process. As in the case of paste *PV*, even lower ρ_c values are achieved by means of IPL compared to thermal annealing. Ablation of the fingers is not observed here. Therefore, paste *AgCu* combined with the developed IPL processes appears to be very promising for integration in back end processing of SHJ solar cells.

In the case of the inkjet-printed ink *Nano-Ag*, the application of both IPL processes (*IPL-all* and *IPL-Nano-Ag*) results in a significant reduction of r_f compared to thermal drying ($r_f = 222.9 \pm 58.4 \Omega/\text{cm}$). Using *IPL-all* and *IPL-NanoAg*, r_f values of $30.0 \pm 3.3 \Omega/\text{cm}$ and $21.8 \pm 0.9 \Omega/\text{cm}$ are reached, respectively. Both r_f and ρ_c values are lower after both IPL processes compared to thermal annealing. This reference process achieves $r_f = 34.2 \pm 4.3 \Omega/\text{cm}$ and $\rho_c = 4.8 \pm 2.2 \text{ m}\Omega\cdot\text{cm}^2$ on planar samples. ρ_c values after *IPL-all* and *IPL-NanoAg* are $3.8 \pm 1.0 \text{ m}\Omega\cdot\text{cm}^2$ and $1.3 \pm 0.5 \text{ m}\Omega\cdot\text{cm}^2$, respectively. Due to the larger effectively contacted surface area of alkaline textured substrates compared to planar ones, an even lower ρ_c would be expected on typically textured SHJ wafers. The r_f values of the inkjet-printed structures are higher compared to the screen-printed ones due to their much smaller cross-sections A_f . Nevertheless, as already demonstrated in section 5.4, these r_f values are sufficient for the

fabrication of busbarless SHJ solar cells, which tolerate higher finger resistances. No issues regarding the mechanical and electrical contact at the ink *Nano-Ag/ITO* interface are observed. Therefore, combined with the developed IPL processes, this ink is a promising candidate to be integrated into SHJ solar cell back end processing.

6.3.5 Contact formation induced by electromagnetic irradiation

The normalized spectral flux density Φ_λ of the radiation emitted in the case of *IPL-all* (here: $n_{\text{pulse}} = 1$) integrated over the whole pulse time is presented in Figure 6-29 (a). The corresponding time-resolved radiant flux density Φ can be found in Figure 3-8 (b). The pulse's spectrum ranges from 300 to 900 nm. It is slightly different compared to a typical Xenon flash lamp spectrum, which can be found in Ref. [117]. The deep ultraviolet (UV) radiation of the Xenon flash lamp is blocked by the quartz glass window, which is coated with an UV-blocking layer. The maximum values of Φ_λ are found in the range of 480 to 540 nm. The global maximum of Φ_λ is identified at 492 nm. Strong peaks in the infrared wavelength range, which are typical for Xenon flash lamps, are damped by the water surrounding the lamp for cooling reasons (see IPL setup presented in section 3.3.3).

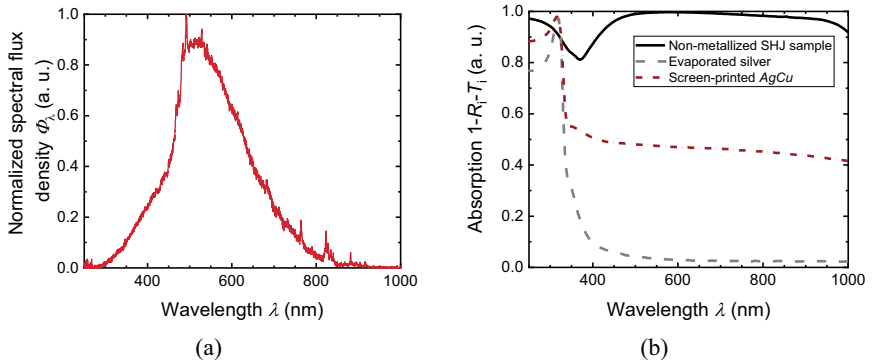


Figure 6-29 Normalized spectral flux density Φ_λ of IPL integrated over t_{pulse} depicted in (a). Absorption characteristics, determined by $1-R_t-T_i$, of a non-metallized SHJ sample as well as an evaporated silver pad and a screen-printed and thermally dried pad based on paste *AgCu* on glass are depicted in (b). Both graphs are redrawn from Ref. [120].

6 Understanding of contact formation processes

Figure 6-29 (b) depicts the absorption characteristics of a SHJ precursor expressed as $1-R_i-T_i$ and of two different metal pads deposited on glass. T_i of all samples is close to zero in the selected wavelength range of 250-1000 nm and is, thus, not plotted in addition. Obviously, the SHJ wafer strongly absorbs in the visible wavelength range, where Φ_λ of IPL has its peak (see Figure 6-29 (a)). Considering contact formation of metal contacts on SHJ wafers during IPL processing, this suggests that the wafer is heated up as a consequence of the absorbed radiative energy. Then, heat is transferred to the metal contacts inducing contact formation.

This scenario would be complete, if the printed metal contacts did not absorb any radiative energy themselves. Yet, the $1-R_i-T_i$ data, in particular these of the *AgCu*-based metal pad, suggest that metal contacts are heated also by absorbing IPL themselves. Integration of Φ_λ multiplied with $1-R_i-T_i$ of highly reflective evaporated silver from 250-1000 nm reveals that 5% of IPL's emitted radiative energy is absorbed. However, the screen-printed paste *AgCu* absorbs 48% of IPL's emitted radiative energy. Considering contact formation of metallization deposited on SHJ cells, this suggests an additional heating mechanism by direct

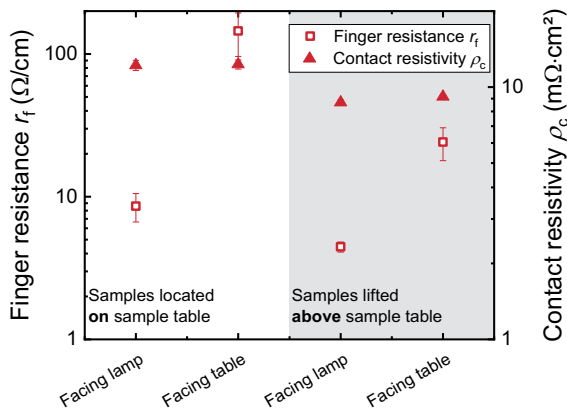


Figure 6-30 Mean finger resistance r_f and mean contact resistivity ρ_c of test samples oriented in two different ways (facing lamp or table). The results shown on the left half of the diagram (white background) are obtained with samples, which are in contact with the sample table, those on the right half (grey background) are obtained with samples that are lifted above the sample table. Error bars are calculated using the standard deviation. The graph is redrawn from Ref. [120].

6.3 Intense pulsed light processing

absorption of the metal finger in conjunction with the heat transferred by the Si wafer. This extra amount of absorbed energy has an impact on contact formation in terms of r_f and ρ_c , as will be shown further below.

Please note that the $1-R_i-T_i$ results are valid for rather flat metal pads only. In the case of solar cells, the metal contacts exhibit the shape of contact fingers. It is known that the fingers' sides partially reflect incoming radiation onto the substrate [179]. Therefore, the amount of absorbed radiative energy in the metal during IPL might be reduced in this case compared to flat metal pads.

Based on metallized test samples, it is verified that absorption of IPL in metal contacts has an impact on contact formation. This is achieved by comparing IPL-processed samples exhibiting metal patterns that face the lamp during processing to samples exhibiting metal patterns that face the sample table (see sketches in Figure 6-20). In the former case, radiative energy is absorbed by the SHJ wafer and additionally by the metal contacts. In the latter case, IPL is absorbed by the SHJ wafer only. In the first instance, this comparison is conducted on samples placed directly on the sample table (significant thermal coupling). From Figure 6-30, one can deduce that the contact resistivity ρ_c is not affected by the metallization's orientation during IPL processing. In both cases it is $12 \text{ m}\Omega \cdot \text{cm}^2$. The finger resistance r_f , in contrast, is 17 times higher if the fingers face the sample table instead of the lamp during IPL processing. However, one could argue here that this difference in r_f is caused by cooling of the metallization only because it is in direct contact with the substrate table if the sample is oriented accordingly. Therefore, the experiment is repeated with another batch of samples, which are lifted 2 mm above the substrate table. Due to the air gap, the samples and the substrate table are thermally decoupled, hence, increasing the heating induced by IPL. Compared to samples directly located on the sample table, this causes a reduced ρ_c down to $9 \text{ m}\Omega \cdot \text{cm}^2$. Still, ρ_c is not affected by the orientation of the sample during IPL processing. However, the difference of the r_f values is significant although it is reduced. If the metallization faces the sample table, still, r_f is five times higher as if the metallization faces the lamp.

These findings are interpreted as follows: radiative energy is not only absorbed by the SHJ wafer but also by the metallization itself when it faces the lamp during IPL processing. This amount of energy absorbed by the metal contact induces a significant finger resistance reduction. The contact resistivity at the metal/ITO contact, in contrast, is hardly affected by the orientation of the sample. In both cases, the metal/ITO contact is formed by transferred heat. Unlike in the case of r_f , it makes no difference in the case of ρ_c whether this heat is absorbed by the SHJ wafer and then transferred to the metal or absorbed in the metal itself.

6.3.6 Passivation of polycrystalline-silicon-based structures

Within IPL process development addressing low-temperature substrates, an obvious observation is made: the IPL tool is capable to release radiant energy to such a degree that SHJ solar cells' passivation provided by the a -Si:H layers is deteriorated. Furthermore, considering paste PV , it is shown that corresponding settings, e.g., $IPL-PV$, can reach an improved electrical performance compared to SHJ-compatible processes, such as $IPL-all$. This, certainly, suggests to extend IPL processing to passivating contacts that can withstand significantly higher process temperatures than the a -Si:H-based approach. Therefore, in the following, the influence of different annealing processes on TOPCon structures exhibiting $poly$ -SiC_x layers is investigated based on symmetrical lifetime samples (see sketch in Figure 6-21). The corresponding results are depicted in Figure 6-31 (a). Thermal annealing is also considered in order to identify a benchmark for IPL in terms of iV_{OC} .

After laser-cutting, the samples exhibit a mean iV_{OC} of 722.6 ± 3.7 mV. ITO deposition results in a significant iV_{OC} reduction down to 651.2 ± 5.5 mV due to sputter-induced damage in the $poly$ -SiC_x layers and/or at the tunnel oxide interface. In contrast to SHJ structures, thermal annealing in the range of 200°C is not sufficient to cure TOPCon structures effectively. Higher temperatures are required. Both with 300°C and 350°C ($t_{annealing}$ of 3 min and 10 min), iV_{OC} is restored to values greater than 700 mV (also compare Ref. [64]).

6.3 Intense pulsed light processing

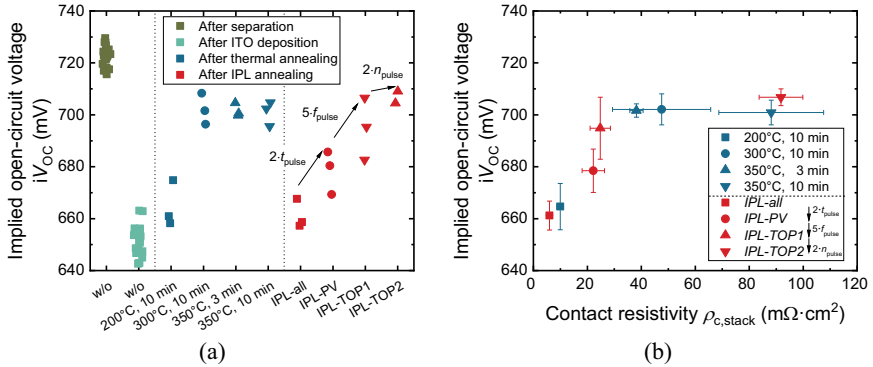


Figure 6-31 iV_{OC} of symmetrical TOPCon lifetime samples after separation, ITO deposition, and varying thermal and IPL annealing steps in (a). Each annealing step is conducted on a different specimen group, each one formed by three samples. In (b), the mean iV_{OC} (data taken from (a)) is plotted as a function of the mean contact resistivity $\rho_{c,stack}$ of the whole c -Si/SiO₂/poly-Si(n)/ITO/silver stack. (A sketch of the sample architecture can be found in Figure 6-21.) Error bars are determined using the standard deviation. Both graphs are redrawn from Ref. [120].

IPL-all proves to cure SHJ samples effectively (see section 6.3.3). Obviously, the thermal budgets of *IPL-all* and also *IPL-PV* (two times t_{pulse} compared to *IPL-all*) are not sufficient to cure sputtering damages of the TOPCon layers. Yet, with *IPL-TOP1* (fivefold f_{pulse} compared to *IPL-all* and *IPL-PV*), iV_{OC} values above 700 mV are achieved and using *IPL-TOP2* (fivefold f_{pulse} and double n_{pulse} compared to *IPL-all* and *IPL-PV*), a maximum iV_{OC} of 709.3 mV is obtained. This is comparable to those values achieved with thermal annealing (iV_{OC} of 709.4 mV). The reason is that from *IPL-all* to *IPL-TOP2*, gradually total radiant energy is increased (also see Table 6-2 for more details), which results in higher temperatures of the samples. More precisely, from measurements of SHJ samples (see section 6.3.3) it is known that the temperature is increased from 250°C to up to 380°C ($n_{pulse} = 1$) when *IPL-all* is replaced by *IPL-PV*. Please note that the absolute temperature values may slightly differ for TOPCon samples. As from *IPL-PV* to *IPL-TOP1* f_{pulse} is increased, the off-time of the lamp between pulses is decreased. It is assumed that the samples do not

completely cool down to room temperature between two pulses, which may result in higher peak temperatures within pulse two and three.¹² From *IPL-TOP1* to *IPL-TOP2* n_{pulse} is doubled, which leads to a longer total irradiation time. As expected from the data achieved with thermal annealing, higher thermal budget than achievable with *IPL-all* used for SHJ is required to cure the TOPCon layers.

It is known from literature that TOPCon/ITO layer stacks require careful consideration of thermal budget owing to interactions at the *poly-SiC_x/ITO* contact [63]. Therefore, $\rho_{\text{c,stack}}$ (contact resistivity of the *c-Si/SiO_x/poly-SiC_x(n)/ITO/silver* stack) is considered in this work as well. In Figure 6-31 (b), iV_{OC} is depicted as a function of ρ_{c} . For all considered annealing processes, $\rho_{\text{c,stack}}$ remains well below $100 \text{ m}\Omega\cdot\text{cm}^2$, which is defined as the target value here. It is assumed that $\rho_{\text{c,stack}}$ is dominated by the contact resistivity at the TOPCon/ITO contact interface [63]. In the case of thermal annealing, $\rho_{\text{c,stack}}$ increases if annealing temperature is increased from 200°C to 350°C provided the same process time. This effect is likely due to the formation of an interfacial oxide caused by oxygen effusion from the ITO [180]. Annealing at 200°C for 10 min achieves the lowest $\rho_{\text{c,stack}} = 9.9 \pm 1.2 \text{ m}\Omega\cdot\text{cm}^2$. Yet, iV_{OC} is not restored sufficiently. Mean iV_{OC} values above 700 mV are reached for annealing at 300°C and 350°C . However, $\rho_{\text{c,stack}}$ is increased to $47.5 \pm 18.2 \text{ m}\Omega\cdot\text{cm}^2$ and $88.1 \pm 19.4 \text{ m}\Omega\cdot\text{cm}^2$, respectively, when the annealing time is 10 min. A reduction of $t_{\text{annealing}}$ from 10 min down to 3 min at a temperature of 350°C leads to a similar $\rho_{\text{c,stack}}$ as achieved with thermal annealing at 300°C for 10 min, namely $38.2 \pm 2.4 \text{ m}\Omega\cdot\text{cm}^2$. Due to the gradual increase in total radiant energy (and, therefore, sample temperature) in the case of IPL, $\rho_{\text{c,stack}}$ increases from *IPL-all* to *IPL-TOP2*. However, using *IPL-all*, *IPL-PV*, or *IPL-TOP1*, $\rho_{\text{c,stack}}$ remains well below $30 \text{ m}\Omega\cdot\text{cm}^2$ ($6.0 \pm 0.6 \text{ m}\Omega\cdot\text{cm}^2$, $22.2 \pm 4.2 \text{ m}\Omega\cdot\text{cm}^2$, and

¹² This cannot be verified using the temperature measurement introduced in section 4.5 because f_{pulse} is too high leading to heating of the setup during application of *IPL-TOP1* and *IPL-TOP2*. This artificially influences the temperature measurement.

$24.8 \pm 3.8 \text{ m}\Omega \cdot \text{cm}^2$, respectively). Simultaneously, *IPL-TOP1* reaches a mean iV_{OC} of $694.9 \pm 11.9 \text{ mV}$ whereas *IPL-all* and *IPL-PV* are insufficient to restore iV_{OC} . Doubling n_{pulse} (*IPL-TOP2*) leads to a mean iV_{OC} of $706.8 \pm 3.2 \text{ mV}$ but also a significant increase of $\rho_{c,\text{stack}}$ of up to $91.7 \pm 8.1 \text{ m}\Omega \cdot \text{cm}^2$. Still, by using *IPL-TOP2* the trade-off of high passivation quality and low resistive losses is sufficiently controlled. Therefore, it is integrated into TOPCon solar cell processing. Corresponding results are provided in section 7.2.

6.4 Chapter summary

Contact formation by means of thermal annealing at low ($180\text{-}220^\circ\text{C}$) and medium ($250\text{-}350^\circ\text{C}$) temperatures is investigated in section 6.1. Using $T_{\text{annealing}} = 350^\circ\text{C}$, finger resistivity is reduced from $6.5\text{-}9.4 \mu\Omega \cdot \text{cm}$ (low-temperature annealing) down to $2.4\text{-}3.5 \mu\Omega \cdot \text{cm}$, which is comparable to typical values of fired contacts in the range of $3 \mu\Omega \cdot \text{cm}$. The reasons are both burning of binders in the pastes and more effective sintering and densification of metal particles compared to low-temperature annealing. However, applied to SHJ cells, the pastes would not be able to utilize their full potential with regard to electrical performance because the *a*-Si:H layers restrict process temperatures to about 200°C only. To make use of higher process temperatures and lower ρ_f , one can switch to more temperature-tolerant passivating contacts such as TOPCon.

Furthermore, the silver/ITO contact is investigated in detail. Contact resistivities in the range of $1.0\text{-}2.5 \text{ m}\Omega \cdot \text{cm}^2$ are achieved after mid- and low-temperature annealing using an ITO layer exhibiting a high charge carrier density N_c (*ITO I*). ρ_c decreases when N_c of the ITO layer increases. Furthermore, it is conspicuous that ρ_c tends to increase as a result of mid-temperature annealing. A contact formation model approach is suggested, which may explain this by a surface-energy-driven microstructural effect at the silver/ITO interface. It is shown that the ρ_c increase occurring at medium annealing temperatures can be prohibited by an increase of ITO surface energy, e.g., due to an air plasma pretreatment of the sample surface. Thus, mid-temperature annealing, if combined with air plasma pretreatment, simultaneously allows for both low ρ_f and low ρ_c .

For temperature-sensitive passivating contacts such as SHJ, still a low-temperature metallization scheme is required that does not harm passivation quality. Although metal pastes cannot exploit their full potential in terms of ρ_f in such case, it is possible to achieve a gain of their electrical performance in terms of ρ_c . This can be done also by means of air plasma pretreatment which allows for a ρ_c reduction of 30%.

In order to increase the conductivity of low-temperature-annealed metal electrodes, ultrasound as a pretreatment performed directly before the thermal annealing step is investigated in section 6.2. Microstructural analysis reveals that the ultrasonic treatments cause pronounced densification and sintering of metal particles. However, this effect originates also from mechanical pressure occurring at the metal electrode/sonotrode contact area and not only from ultrasonic oscillations alone. Furthermore, ultrasonic treatments cause significant damage of the metal electrodes in form of abrasions. Thereby, the electrically active cross-sectional area of the electrodes is reduced. As a consequence, only a little electrical performance gain in terms of r_f can be achieved using ultrasonic treatments.

Moreover, ultrasonic treatments cause degradation of the passivating thin layers of the SHJ, especially in the region where ultrasound is coupled into the specimen. Presumably, this effect could be circumvented by careful alignment of the sonotrode to the sample position reducing mechanical contact to the SHJ substrate. In this work, no such ultrasonic setup is available. Therefore, this technique is not considered for the application on solar cells in the following. However, the effect of densification of metal electrodes and the corresponding increase in conductivity could be used for less sensitive samples as utilized in this work, for example, in printed electronics.

In section 6.3, the application possibility of IPL for passivating contacts is characterized providing the potential to substitute time-consuming thermal annealing steps. With regard to SHJ samples, a mean ΔiV_{OC} gain of 25.9 ± 2.3 mV is measured after IPL processing. Besides from curing of sputter damages, the SHJ benefits from light soaking effects induced by IPL. This additional effect results in a 5.5 mV higher iV_{OC} compared to thermal annealing.

This is expected to be reflected in SHJ solar cells' V_{OC} and pFF (hence FF). Corresponding results are provided in section 7.1. The ΔiV_{OC} data is correlated with in-situ temperature measurements of non-metallized SHJ samples during IPL processing. An optimum IPL-induced peak temperature in terms of iV_{OC} of about 325°C is identified.

Moreover, a low mean finger resistance r_f of $3.0 \pm 0.7 \Omega/\text{cm}$ and contact resistivity ρ_c of $2.7 \pm 0.2 \text{ m}\Omega\cdot\text{cm}^2$ is achieved by means of IPL processing using a commercially available silver-coated-copper-based paste. Due to the pulse time in the millisecond range, IPL allows for a significant reduction of the post-metallization annealing time from several minutes down to milliseconds. Its cost saving potential, considering pulse times of several milliseconds and low footprint simultaneously combined with a silver-coated copper paste, constitutes a promising low-cost alternative to conventional thermal processing (also see section 7.1.1).

In a final step, the IPL process development is expanded towards TOPCon structures. Based on symmetrical lifetime samples, it is shown that comparable iV_{OC} values of up to 709.4 mV can be achieved both with thermal mid-temperature annealing and IPL processing. Thereby, the sum of the contact resistivities of the interfaces occurring at the TOPCon/ITO layer system remains well below $100 \text{ m}\Omega\cdot\text{cm}^2$. Compared to SHJ samples, a higher thermal budget is necessary in order to cure sputter-induced damage in the TOPCon layers.

Besides the IPL process developments for SHJ and TOPCon structures, insights in the contact formation mechanisms induced by IPL processing are provided. It is shown that IPL is not only absorbed by SHJ precursors but also directly by screen-printed metal contacts. This extra amount of absorbed energy significantly increases the electrical conductivity of the contacts. The electrical metal/ITO contact, in contrast, is mainly formed by means of transferred heat generated by absorbed radiation in the substrate. As a consequence, sintering of metal particles is homogeneous across the whole finger height as can be deduced from SEM-based microstructure analyses.

7 Metallization of solar cells with passivating contacts

The preceding chapters present innovative printing techniques and novel contact formation approaches for silicon solar cells with passivating contacts based on amorphous and polycrystalline silicon layers. This chapter deals with the integration of these methods into back end processing of such cells. Intense pulsed light is applied to full-size silicon heterojunction solar cells. It is capable to substitute both post-metallization thermal drying and annealing. This is shown for screen-printed as well as for inkjet- and FlexTrail-printed contacts. Due to its speed, IPL enables a cost saving potential, even more if combined with resource-saving metallization such as FlexTrail. The full electrical potential of low-temperature screen-printed contacts is exploited, as they are combined with tunnel oxide passivating contacts. Both thermal mid-temperature annealing and IPL processing adapted to such contacts are applied to TOPCon cells. Thereby, the trade-off between low contact resistivity at the TOPCon/ITO interface and high-quality surface passivation is balanced. This chapter is based on Ref. [120, 156]. Both are published by the present author, who is the main author of these publications as well.¹³

¹³ Jörg Schube is the main author of these two publications. He designed the experiments, took the SEM pictures, performed inkjet and FlexTrail printing, coordinated and supervised all other process steps, and did the analyses. In Ref. [120], Leonard Tutsch developed and fabricated the ITO layers. In Ref. [156], Maximilian Weil developed the IPL processes under supervision of Jörg Schube. His work is published as his master

7.1 Intense pulsed light processing of silicon heterojunction solar cells

7.1.1 Motivation

Section 6.3 reveals the great potential of IPL application in SHJ back end processing. It demonstrates that such passivating contacts particularly benefit from IPL, for example, due to light soaking effects in terms of iV_{OC} . Therefore, higher V_{OC} and also FF values are expected for IPL-processed SHJ solar cells compared to their thermally treated counterparts. The work presented in this section mainly deals with the process integration of IPL. The previously investigated processes (see section 6.3) are transferred to the fabrication of busbarless full-size SHJ cells. The busbarless grid layout is motivated both by its resource saving potential and its greater tolerance towards higher r_f compared to a typical five-busbar layout. Moreover, inkjet and FlexTrail printing (see chapter 5) are combined with IPL processing.

In a first step, challenges of IPL processing and further process development potential regarding cell performance and process speed are elaborated. The acquired knowledge is implemented in form of a further optimized IPL process, which is then applied to full-size SHJ solar cells. Moreover, an IPL drying process is introduced. Thereby, it is demonstrated that IPL can fully replace thermal process steps within the SHJ back end sequence, even with increasing cell performance.

Due to advantages in speed, footprint, and also conversion efficiency, IPL promises to be more cost effective than standard thermal annealing. In fact, cost of ownership (COO) calculations using the $SCost$ model indicate a significant cost saving potential for IPL [181]. Figure 7-1 depicts corresponding results. These are based on data sets, which are discussed in detail with notable tool manufacturers.

thesis [157]. In Ref. [120], the TOPCon precursors are manufactured by Angelika Harter, supervised by Jana-Isabelle Polzin. Her work is published as her master thesis, too [158].

7.1 Intense pulsed light processing of silicon heterojunction solar cells

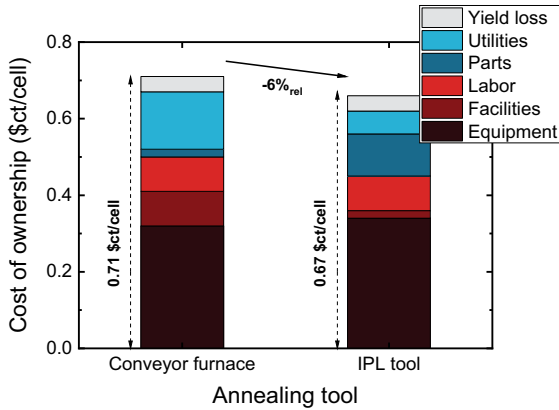


Figure 7-1 Comparison of the cost of ownership of intense pulsed light and thermal annealing in back end processing of full-size silicon heterojunction solar cells. The calculations are based on the *SCost* model.

For thermal annealing (reference process), a conveyor furnace allowing a gross throughput of 4800 wafers per hour (wph) is assumed. An industry-related IPL device operated with an optimized IPL process would allow for a gross throughput of 5400 wph according to a tool manufacturer. This higher throughput is originated in parallel processing of two lines and a high velocity of the transport system, which is enabled by the speed of the IPL process. Thereby, IPL potentially reduces the consumption of required floor space (including equipment, working, and handling space) by more than 50%. According to first estimates in cooperation with equipment manufacturers, today the capital expenditures (CAPEX) of such an IPL tool would be 10-20% higher than of a state-of-the-art conveyor furnace. However, it would already include a sophisticated automation (that contains, e.g., a flipping unit, loop, and/or buffer unit), which is assumed to account for about one third of the total IPL setup price.

Despite the higher CAPEX of IPL, it allows for a significant COO reduction by 6%_{rel} from 0.71 \$/cell down to 0.67 \$/cell compared to thermal reference processing. In both cases, the same uptime (98.5%) and yield loss (0.05%) is assumed. Due to its lower electricity consumption, IPL enables a reduction in utility costs from 0.15 \$/cell down to 0.06 \$/cell. The costs related to spare

parts are higher in the case of IPL because of the Xenon flash lamps, which are assumed to be exchanged every ten million pulses. Labor costs related to operation as well as maintenance and support are assumed to be on a similar level for both annealing tools. In terms of facilities, IPL benefits from the more than 50% lower footprint. Therefore, in this assessment, it accounts for 0.02 \$ct/cell only instead of 0.09 \$ct/cell as in the case of thermal annealing. It has already been mentioned that the IPL equipment costs would be probably higher when first introduced compared to those of a conveyor furnace. One can extract from Figure 7-1 that IPL's cost saving potential could even be increased if its CAPEX decreased. This would certainly be the case if its implementation increased and, hence, scaling effects drove costs down.

The cost calculations so far reveal a saving potential of IPL, which is mainly driven by the reduction of utilities' and facilities' costs. However, IPL additionally allows for a mean η gain of up to 0.4%_{abs} (see section 7.1.4) compared to thermal annealing. This is the dominant factor with regard to SHJ module costs, allowing a cost reduction of 0.43 \$ct/Wp (or a reduction by 4.3 million dollars for a fab with 1 GWp annual production). This corresponds to a cost reduction potential of 2%_{rel} compared to thermal annealing even on module level. The results demonstrate the significant cost reduction potential at an increased cell performance of IPL if integrated into SHJ mass production.

The SHJ cells under investigation are metallized using commercially available pastes for screen printing, both silver- and silver-coated-copper-based ones. There is no need to specially modify them for IPL application, which underlines the high compatibility of IPL with state-of-the-art metallization. However, IPL can be combined with advanced printing techniques offering a large silver saving potential compared to screen printing as well. (Please note that the use of screen printing pastes based on silver-coated copper also offers a significant silver saving potential.) This is demonstrated by the examples of both inkjet and FlexTrail printing. The combination of IPL with these innovative printing techniques offers an additional cost saving potential because inkjet and Flex-Trail printing consumes only very little silver (see section 5.5).

7.1.2 Sample preparation and characterization

In a first experiment, IPL processes developed in section 6.3, namely *IPL-all* and *IPL-AgCu* (for more details about IPL processes see appendix B), are applied to the front side of SHJ solar cells by taking the example of paste *AgCu* (for more details about pastes see appendix B). Chances, such as process optimization, and challenges, such as processing of full-size samples, of IPL process integration are identified. The corresponding process flow is depicted in Figure 7-2 (a).

SHJ precursors from an external manufacturer with 156.8 mm edge length and a thickness $d_{\text{wafer}} = 160 \mu\text{m}$ are utilized as basis. The precursors exhibit an alkaline textured n -type Cz-grown Si base substrate with a resistivity ρ_{base} of $1.3 \Omega \cdot \text{cm}$, intrinsic and doped (p - and n -type on the rear and front, respectively) hydrogenated α -Si:H layers, and ITO layers on both sides. Further details about the sample structure as well as a sketch of the sample layout is provided in section 2.2.1. In order to concentrate on the front side metallization only, silver-based rear grids exhibiting 150 fingers ($w_{\text{f,set}} = 50 \mu\text{m}$) are screen-printed on samples of group 1, 2 and 3 and thermally dried (200°C , 1 min). Then, group 2 and 3 samples are thermally annealed at 200°C for 30 min in a conveyor furnace in order to achieve a rear grid state that is stable towards the following process steps: group 1-3 cells' front sides are screen-printed by means of paste *AgCu* ($w_{\text{f,set}} = 40 \mu\text{m}$) and dried (200°C , 1 min). Then, samples of group 1 undergo a thermal annealing step performed at 200°C for 30 min in a conveyor furnace (reference process). Group 2 and 3 samples are processed using *IPL-all* and *IPL-AgCu*, respectively, on the front. All solar cells are *IV*-measured at standard testing conditions (STC) by means of PCB^{TOUCH} [147, 148]. The setup exhibits 30 wires for current and five wires for voltage measurements.

As explained in section 7.1.3, the application of *IPL-AgCu* affects the full-size SHJ cells' performance in an unexpected manner. The underlying effect is investigated separately on non-metallized samples of group 4. Again, *IPL-AgCu* is applied to the samples' front sides. Some of them are processed on a sample table featuring a vacuum suction. Thereby, thermal coupling of sample and sample table is ensured. All other samples are processed without vacuum

7 Metallization of solar cells with passivating contacts

suction. Before and after IPL processing, all group 4 samples are measured in terms of their lifetime.

In the second experiment sketched in Figure 7-2 (b), the influence of different drying processes, or rather the question whether a drying process is required at all, before IPL annealing of the front side metallization is evaluated. The same SHJ precursor material as described above in the present section is employed. All process steps performed in group 1-3 (see Figure 7-2 (a)) up to and including front screen printing are conducted on the samples of group 5-8 as well. Subsequently, group 5 samples are thermally dried (200°C, 1 min) and annealed

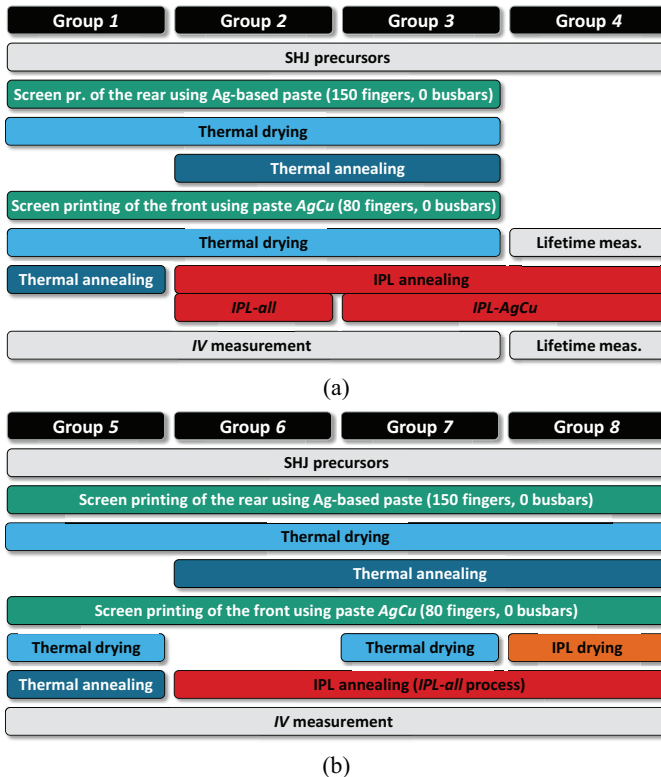


Figure 7-2 Experimental process flows. The experiment sketched in (a) aims for the identification of changes and challenges of IPL process integration. The experiment sketched in (b) investigates the impact of drying processes conducted before IPL annealing or rather the question if drying is necessary at all. The picture in (b) is adapted from Ref. [120].

7.1 Intense pulsed light processing of silicon heterojunction solar cells

at 200°C for 30 min. This group is defined as the reference group in this part of the experiment. Group 6 samples are not dried after front side screen printing, group 7 samples are thermally dried (200°C, 1 min), and group 8 samples are dried by means of IPL. Then, on the samples' front sides of group 6-8 the *IPL-all* annealing process is conducted. Finally, all cells are *IV*-measured using PCB^{Touch} (30 wires for current and five for voltage measurements).

In the third experiment, SHJ solar cells are manufactured which are IPL-dried and -annealed on both sides. In addition to paste *AgCu*, IPL is applied to a silver-based paste *Ag* as well. The corresponding process flow is depicted in Figure 7-3 (a). The experiment is divided into four groups, of which the groups 10-12 are subdivided, e.g., into group 10_{Ag} and 10_{AgCu} . Again, the same SHJ precursors as described above are utilized as starting material but this time differing in base resistivity $\rho_{base} = 1.0 \Omega \cdot \text{cm}$ and thickness $d_{wafer} = 140 \mu\text{m}$. All precursors are provided with a screen-printed rear grid exhibiting 150 fingers and $w_{f,set} = 50 \mu\text{m}$. In group 9_{PV^*} and group $10_{Ag}-12_{Ag}$, two different commercial silver-based pastes *PV** and *Ag* are screen-printed. *PV** is an evolutionary paste of paste *PV* and acts as the reference medium here. (For more details about pastes, please see appendix B.) In group $10_{AgCu}-12_{AgCu}$, paste *AgCu* is utilized. Pastes for the rear sides are utilized for the front grids as well exhibiting 80 fingers with $w_{f,set} = 40 \mu\text{m}$.

After screen printing of the rear and front grids, the samples of the groups 9-11 undergo thermal drying conducted at 200°C for 1 min. Group 12 is dried by means of IPL (both-sided). After printing and drying, the cells of group 9 and 10 are thermally annealed at 200°C for 30 min. These serve as reference cells. The groups 11 and 12 are IPL-processed on both sides, each one starting with the front. The conducted IPL process is related to *IPL-all* but f_{pulse} is doubled and, therefore, the process time is halved. This optimized process is called *IPL-opt* (see appendix B for more details). After *IV*-measurements using the PCB^{TOUCH} setup (see description above in this section), selected cells of the two groups 9 and 10 are investigated by means of confocal microscopy and SEM on the front.

7 Metallization of solar cells with passivating contacts

In the fourth experiment, IPL is combined with inkjet- and FlexTrail-printed front grids (see process flow in Figure 7-3 (b)). The same precursor material as used for cells of the groups 9-12 is employed. After screen printing of the rear (silver-based paste, 150 fingers, $w_{f, \text{set}} = 50 \mu\text{m}$) and drying (200°C , 1 min), the samples of group 15 and 16 are thermally annealed (200°C , 30 min) in order to achieve a rear grid state that is stable towards the subsequent process steps. All cells are equipped with front grids (80 fingers, 1 pass) by means of inkjet (group 13 and 15, substrate and printhead temperature of 60°C and 50°C , respectively)

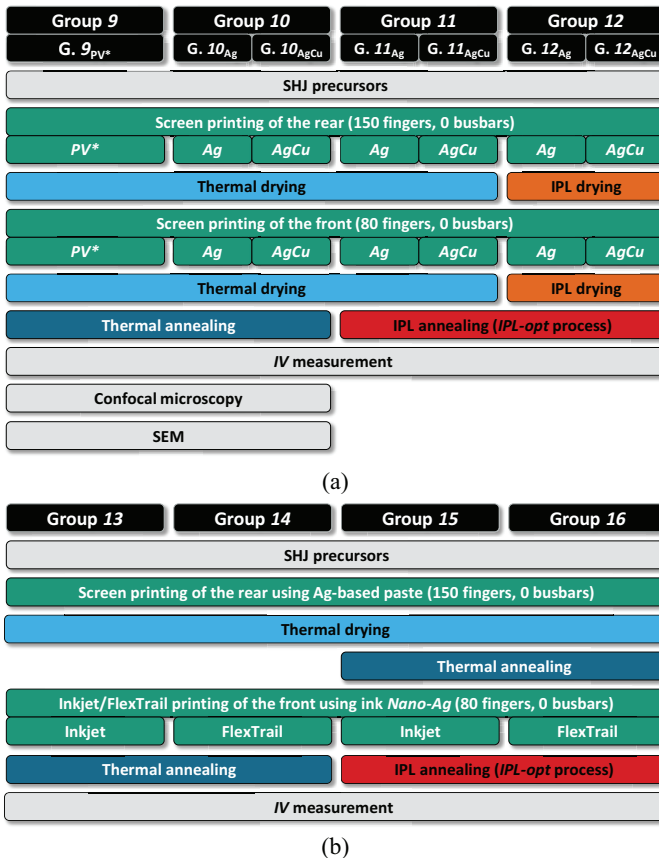


Figure 7-3 Experimental process flows. In (a) optimized IPL processing (drying and annealing) is applied to both sides of SHJ solar cells with screen-printed contact grids. (a) is adapted from Ref. [120]. In (b) IPL is combined with inkjet- and FlexTrail-printed grids applied on SHJ solar cells' front sides.

7.1 Intense pulsed light processing of silicon heterojunction solar cells

or FlexTrail (group 14 and 16, substrate temperature of 25°C). Then, thermal annealing (200°C, 30 min, without a prior drying step) is conducted on the front of cells of group 13 and 14 (reference groups) and *IPL-opt* is performed on the front of the cells of group 15 and 16. Finally, all cells are characterized in terms of *IV*-related parameters using PCB^{TOUCH}.

7.1.3 Challenges and optimization of processing full-size solar cells

The following section is threefold. First, challenges for IPL processing of full-size solar cells using a lab-type tool are discussed. They are specific for the tool utilized in this work (see section 3.3.3). Second, a general challenge occurring in the process integration of certain IPL processes into full-size SHJ solar cells is presented. Thirdly, a process optimized in terms of process speed and SHJ solar cell performance is presented.

Challenges for intense pulsed light processing of full-size solar cells

In a first step, challenges related to the specific design of the lab-type IPL tool, which is utilized in this work, are discussed. This is the spot size irradiated by IPL, which is smaller than the area of a full-size solar cell. To cope with this issue, each wafer is divided into two equal parts by means of a shutter, which are flashed separately (see Figure 7-4 (a)). Still, two subsequently applied light pulses are necessary in order to irradiate each half of the cell area homogenous-

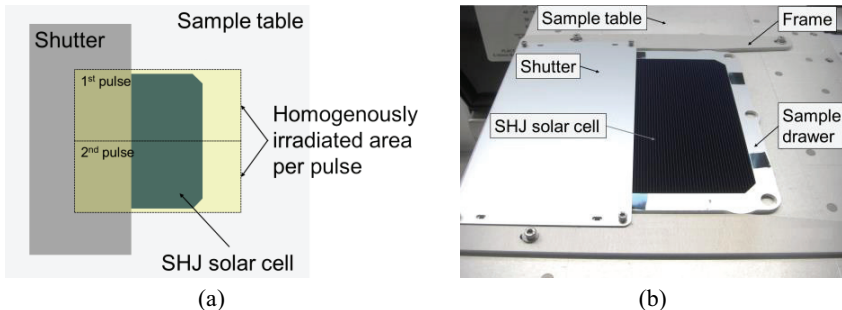


Figure 7-4 IPL setup utilized to process full-size solar cells. (a) shows a schematic drawing including markings where IPL homogeneously irradiates the solar cell. Two light pulses are required to process one half of a cell. (b) displays a photo of the actual (lab-type) setup.

ly. The homogeneity is checked by means of a foil named *UVSCALE* from *Fujifilm* [182]. Its color turns from white to blue when irradiated at a certain amount of E_{rad} . The higher E_{rad} to which the foil is exposed the darker appears the blue color. Using such a foil, the pitch between two light pulses can be adjusted in a way that transition areas due to overlapping of adjacent pulses vanish (i.e., homogenous irradiation). Photographs of the irradiated foil are displayed in Figure 7-5.

The actual sample table in the IPL tool exhibits an optional frame and a sample drawer in order to ensure that the sample position is fixed during processing (see Figure 7-4 (b)). Moreover, the sample drawer simplifies handling. This is useful, especially when the sample has to be rotated by 180° (on sample table level) in order to process both halves of the sample.

Challenges of intense pulsed light process integration

In a second step, IPL process integration is investigated. This part of the section deals with first busbarless full-size IPL-annealed (front side application) SHJ solar cells exhibiting paste-*AgCu*-based front electrodes. Corresponding *IV*-related data are provided in Figure 7-6. The mean j_{SC} of all cells is $37.8 \pm 0.1 \text{ mA/cm}^2$. Since there is no significant difference regarding j_{SC} between the individual groups 1-3, it is not further discussed in the following.

Large pitch



Optimal pitch



Small pitch



Figure 7-5 Adjustment of the pitch between two light pulses by means of a special foil that changes its color from white to blue when irradiated at a certain amount of E_{rad} . The blue tone is dependent on E_{rad} .

7.1 Intense pulsed light processing of silicon heterojunction solar cells

However, the annealing processes significantly affect η of these cells. The cells annealed by the thermal reference process (samples of group 1) reach a mean η of $22.2 \pm 0.1\%$. Remarkably, they are outperformed by the *IPL-all*-annealed SHJ cells by even $0.3\%_{\text{abs}}$. From Figure 7-6, it is obvious that this significant performance gain induced by *IPL-all* is originated in a mean V_{OC} and a mean *FF* gain of 1.7 mV and $0.7\%_{\text{abs}}$, respectively. Such an increased V_{OC} and *FF* is expected from IPL-induced LS effects, occurring in the SHJ (discussed in detail in section 6.3.3). Moreover, the mean R_s of *IPL-all*-processed SHJ solar cells is reduced by $0.1 \Omega \cdot \text{cm}^2$ compared to thermally annealed cells explaining the *FF* difference in addition to light soaking. An explanation for the R_s reduction is the about $20 \Omega/\text{sq}$ lower $R_{\text{SH,ITO}}$ of such cells compared to their thermally processed

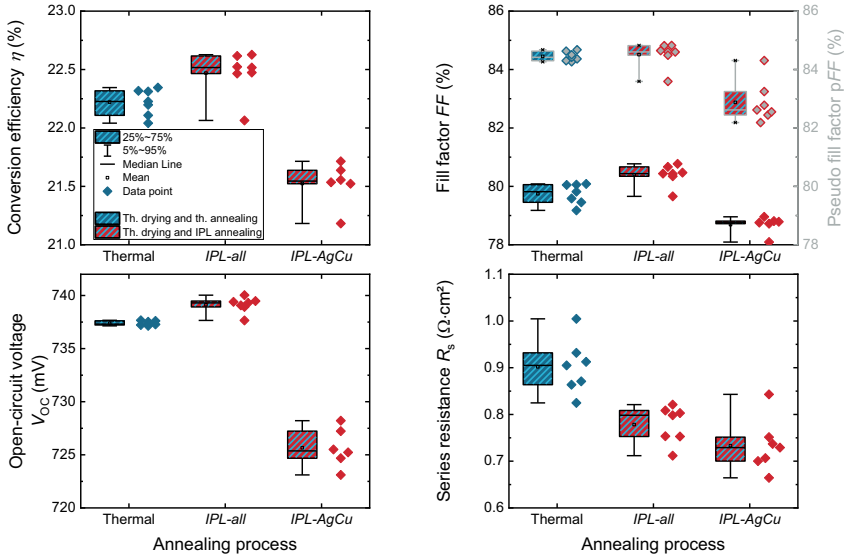


Figure 7-6 *IV*-related data of busbarless full-size SHJ solar cells exhibiting front grids based on paste *AgCu* (six to seven cells per group). The processes *IPL-all* ($U_{\text{lamp}} = 550 \text{ V}$, $t_{\text{pulse}} = 1 \text{ ms}$, $n_{\text{pulse}} = 3$, $f_{\text{pulse}} = 0.1 \text{ Hz}$, $E_{\text{rad}} = 6.0 \text{ J/cm}^2/\text{pulse}$) and *IPL-AgCu* ($U_{\text{lamp}} = 450 \text{ V}$, $t_{\text{pulse}} = 4 \text{ ms}$, $n_{\text{pulse}} = 3$, $f_{\text{pulse}} = 0.1 \text{ Hz}$, $E_{\text{rad}} = 9.3 \text{ J/cm}^2/\text{pulse}$) are integrated into back end processing of these cells. Thermal annealing at 200°C for 30 min acts as the reference process. The mean j_{SC} of all cells is $37.8 \pm 0.1 \text{ mA/cm}^2$ and does not vary significantly for the three groups (not shown). This graph is adapted from Ref. [120].

counterparts (based on analytical calculations). These data again demonstrate both the compatibility and the benefits of SHJ processing using *IPL*.

However, the use of *IPL-AgCu* causes a significant η loss of 0.7%_{abs} compared to the thermally treated solar cells. From Figure 7-6, one can see that this is caused both by *FF* and V_{OC} losses of 1.1%_{abs} and 11.7 mV, respectively. The former is not a result of increased ohmic losses, as indicated by the constant R_s for both groups. *IPL-AgCu* even results in the lowest mean R_s of 0.7 $\Omega \cdot \text{cm}^2$ achieved in this experiment. The fact that this mean value is even lower by 0.1 $\Omega \cdot \text{cm}^2$ compared to the one obtained by *IPL-all* is in accordance with the data presented in section 6.3.4. Here, both lower r_f and ρ_c are achieved by means of *IPL-AgCu* rather than with *IPL-all*.

The reason for the *FF* and V_{OC} degradation of *IPL-AgCu*-processed SHJ solar cells is rather originated in a loss in passivation quality. This is indicated partly by a V_{OC} loss (here: $V_{OC} = 725.7 \pm 1.8$ mV) but also by a *pFF* loss of 1.8%_{abs} compared to thermal annealing, indicating recombination in the space charge region. However, this contradicts the results of the *IPL* process development presented in section 6.3.3. Here, an iV_{OC} gain of 5.5 mV is reported compared to thermal annealing. In order to understand why passivation quality benefits from *IPL-AgCu* in the process development (section 6.3.3) but suffers from the same process within the process integration (present section), the differences of the specimens in both experiments have to be considered, i.e., the metallization and the sample size. The impact of both is investigated in the following.

In order to find out if the metallization of *IPL-AgCu*-processed SHJ cells causes the solar cells' degradation, photoluminescence (PL) imaging is conducted on metallized and on non-metallized SHJ samples [172]. After *IPL-AgCu* is performed, metallized and non-metallized samples both degrade to a similar amount, as can be deduced from the comparison of Figure 7-7 (a) and (b). Both samples exhibit regions where the photoluminescence intensity is very low, which indicates low access charge carrier lifetimes (colored in (dark) red). Please note that the specific pattern existing of four such regions is a consequence of *IPL* application to full-size samples at each quarter of the wafer (see description above in the present section). The similarity of both photolumines-

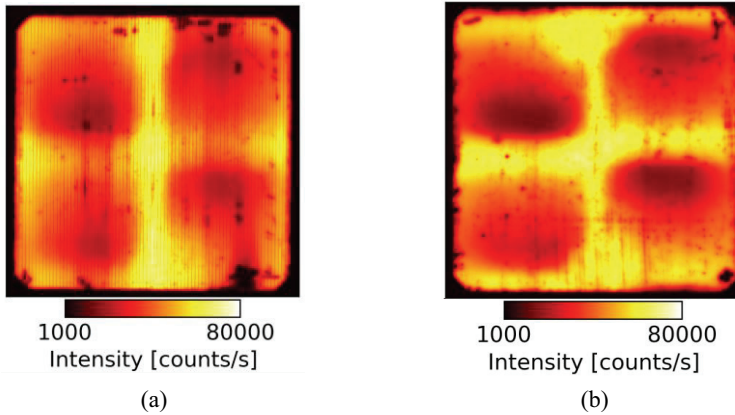


Figure 7-7 Photoluminescence measurements of a busbarless SHJ cell exhibiting a front metal grid (a) and of a non-metallized SHJ precursor (b) both annealed using *IPL-AgCu*.

cence data in Figure 7-7 (a) and (b) indicates that metallization is not responsible for the degradation of *IPL-AgCu*-processed SHJ solar cells. This finding is further strengthened by SEM-based microstructure analyses of the samples: neither in the non-metallized regions besides the metal electrodes nor underneath the metal electrodes (access given by etching of the metal) metal-induced damage can be identified (pictures not displayed in this work).

Another significant difference of the samples, which do not degrade (used in process development) after *IPL-AgCu*, and the degraded samples (used in process integration) is their size. It is commonly known that full-size samples placed on a hot plate operated, e.g., at 200°C tend to exhibit a bow. This is caused by differences in the thermal expansions within the material stack of which a solar cell consists. This causes a bending-up of the sample's edges. In Figure 7-8 (b), a photograph of such a scenario is depicted. The edges of a full-size SHJ precursor with an edge length of 156.8 mm are bent upwards when the sample is placed on a hot plate operated at 200°C. This is not the case, e.g., for a smaller 78 mm x 69 mm-sized sample as, for example, used in the IPL process development in this work (see Figure 7-8 (a)). The bow of heated full-size SHJ precursors is assumed to be the reason for the degradation of *IPL-AgCu*-processed samples, as will be explained in the following paragraphs.

SHJ samples are heated up strongly during absorbing irradiation as a result of the *IPL-AgCu* process (see section 6.3.3). This causes a bow of full-size samples, which are, therefore, thermally decoupled from the substrate table (high thermal mass) at the edges (given the bow is oriented as depicted in Figure 7-8 (b)). Only the middle of such a sample touches the substrate table, significantly reducing the cooling effect by the table. This is not the case for smaller samples, which, e.g., are of a size of 78 mm x 69 mm (enhanced thermal coupling). As a consequence, the full-size samples get hotter than the smaller ones. If a critical temperature, defined by the α -Si:H layers, is exceeded ($T > 200^\circ\text{C}$), the SHJ degrades. Please note that during processing using *IPL-all* the samples are expected to form a bow as well. However, because of the lower E_{rad} per pulse and, thus, lower substrate temperatures in this case, a bow does not lead to reduced passivation quality.

In Figure 7-7, it is further conspicuous that passivation quality is especially reduced in the middle of the sample quarters. The fact that less degradation is observed in the middle of the sample can be explained by the cooling effect of the sample table touching the sample at this position. Moreover, a heat transfer in the sample towards its non-irradiated half can be assumed, also leading to a lower temperatures in the middle of the sample (compare Figure 7-4).

The hypothesis that a bow of the samples causes degradation is tested based on non-metallized full-size SHJ precursors. Some of them are *IPL-AgCu*-processed on a sample table featuring a vacuum suction inducing a down force on the

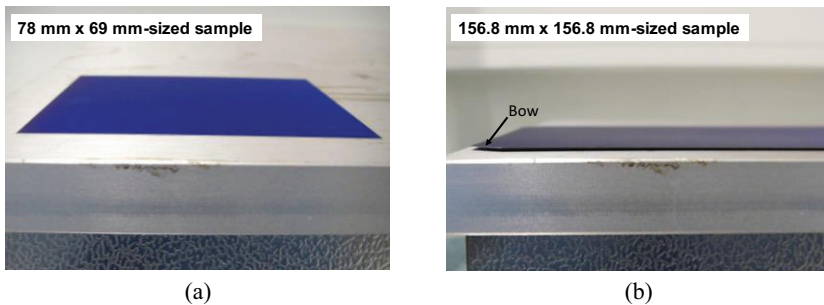


Figure 7-8 Photography of a 78 mm x 69 mm-sized non-metallized SHJ test sample (a) and of a 156.8 mm x 156.8 mm-sized SHJ precursor (b). Both samples are placed on a hotplate operated at a temperature of 200°C .

7.1 Intense pulsed light processing of silicon heterojunction solar cells

samples. The latter counteracts the bending of the sample edges (bow) and ensures a sufficient thermal coupling during IPL processing. The enhanced cooling is expected to prevent or mitigate the lifetime degradation. The other specimens are processed on the same sample table but without the use of the vacuum suction. These samples are expected to degrade during the application of *IPL-AgCu*.

The photoluminescence measurements presented in Figure 7-9 confirm the hypothesis that a bow causes degradation in the case of *IPL-AgCu*. A sample that is processed without vacuum exhibits significant degradation (see Figure 7-9 (a)).¹⁴ This is quantified by means of photoconductance-based lifetime

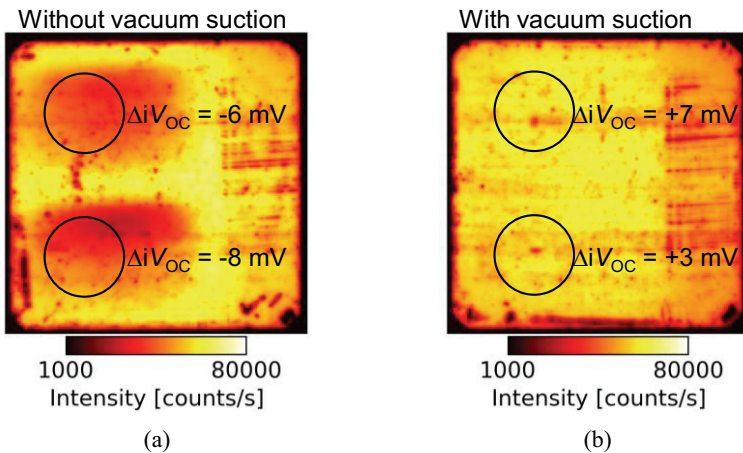


Figure 7-9 Photoluminescence measurements of two non-metallized SHJ samples. Both samples are annealed using *IPL-AgCu*. The sample in (a) is IPL-processed without vacuum suction. The sample in (b) is IPL-processed using the same sample table but the vacuum suction is switched-on (pronounced thermal coupling). The ΔiV_{OC} data is determined by means of photoconductance-based lifetime measurements.

¹⁴ Please note that the specific degradation pattern in Figure 7-9 (a) looks different than in Figure 7-7. The reason is that the setup with the vacuum prohibits the use of the shutter. Therefore, only two light pulses are applied instead of four to process the sample. Hence, only two regions exhibiting strong degradation are visible. Furthermore, a small stripe at the right side visible for both samples appears darker due to resulting insufficient irradiation.

measurements in terms of their iV_{OC} . Within the marked regions, iV_{OC} is reduced by 6 to 8 mV. By means of the vacuum suction, such degradation can be avoided as displayed in Figure 7-9 (b). Within the critical regions, an iV_{OC} gain with regard to the initial state of up to 7 mV is achieved by means of *IPL-AgCu*. In addition, the iV_{OC} results achieved with *IPL-AgCu* (presented in section 6.3.3) are reproduced by means of parallel processed 78 mm x 69 mm-sized non-metallized SHJ samples.

These investigations demonstrate that the process *IPL-all* can be integrated into back end processing of full-size SHJ solar cells without any adaptations of the process or the IPL setup (see Figure 7-6). This is different in the case of *IPL-AgCu*. In order to avoid strong degradation in terms of passivation quality of the SHJ samples, bending of the sample edges during IPL processing needs to be suppressed. This can be achieved, e.g., by means of a vacuum suction integrated into the sample chuck. However, the lab-type IPL tool used in this work does not allow proper operation of the vacuum suction and full-size solar cells simultaneously. Therefore, the focus is set on the process *IPL-all* rather than the metallization-specific processes, e.g., *IPL-AgCu*, in the following.¹⁵

Intense pulsed light process optimization

In a third step, *IPL-all* is optimized in terms of process speed and solar cell performance. The parameter set used for *IPL-all* (see Table 6-3) is utilized as a start but f_{pulse} is doubled from 0.1 to 0.2 Hz. This leads to reduced process time and a slight mean η gain of 0.2%_{abs} in the case of SHJ cells. The corresponding new process is labelled *IPL-opt*. *IV*-related data comparing *IPL-all* to *IPL-opt* is provided in Table 7-1. Here, some samples similar to those of group $1I_{Ag}$ are used and IPL processing is performed on the front only. Their rear is thermally annealed in a preceding step (200°C, 30 min). Whereas j_{SC} (mean j_{SC} of 38.0 ± 0.1 mA/cm²) is not affected by the change from *IPL-all* to *IPL-opt*, V_{OC}

¹⁵ Degradation of full-size SHJ solar cells occurs not only in the case of *IPL-AgCu* but also in case of *IPL-PV* and *IPL-NanoAg*. The reason is assumed to be the same.

7.1 Intense pulsed light processing of silicon heterojunction solar cells

and FF are increased by 1.6 mV and 0.4%_{abs}, respectively, which explains the corresponding η gain of 0.2%_{abs}. The higher V_{OC} after *IPL-opt* indicates an improved passivation quality compared to *IPL-all*. The FF increase is not caused by a R_s reduction since R_s is $0.7 \Omega \cdot \text{cm}^2$ for both processes. In fact, it is originated in a pFF increase of 0.6%_{abs}, indicating a higher charge carrier lifetime at the maximum power point compared to *IPL-all*. The improvement in the passivation quality is correlated with higher peak temperatures of the samples during the second and third pulses for *IPL-opt*. Compared to *IPL-all* the process time is reduced, leaving shorter time periods for cooling. Therefore, the samples are heated up to higher peak temperatures. As a consequence, passivation quality is improved. In the following of this work, both processes *IPL-all* and *IPL-opt* are used.

Table 7-1 Comparison of *IPL-all* to *IPL-opt* (without vacuum) by taking the example of SHJ solar cells with paste-*Ag*-based metal electrodes (comparable to group $1I_{Ag}$ samples, five samples per group). IPL processing is conducted on the front whereas the rear is thermally annealed before.

Process	V_{OC} (mV)	FF (%)	pFF (%)	R_s ($\Omega \cdot \text{cm}^2$)	η (%)
<i>IPL-all</i>	736.8 ± 1.2	81.1 ± 0.3	84.5 ± 0.4	0.7 ± 0.0	22.7 ± 0.1
<i>IPL-opt</i>	738.4 ± 0.7	81.5 ± 0.1	85.0 ± 0.1	0.7 ± 0.0	22.9 ± 0.0

7.1.4 Entirely intense-pulsed-light-processed solar cells

After successful integration of *IPL-all* into the front metallization sequence of SHJ solar cells, in this section, a drying step before IPL annealing is checked for requirement and the potential of replacing thermal drying. In Figure 7-10, η , FF , V_{OC} , and the series resistance R_s of cells that passed varying drying and annealing processes are presented (see corresponding process flow in Figure 7-2 (b)). j_{SC} does not vary significantly between the groups. Its overall mean value is $37.9 \pm 0.1 \text{ mA/cm}^2$.

7 Metallization of solar cells with passivating contacts

Cells that are not dried before IPL annealing (group 6) exhibit the lowest values of FF and, therefore, the lowest η as well. The mean R_s is significantly increased by $0.3 \Omega \cdot \text{cm}^2$ compared to the entirely thermally annealed reference group (group 5). Obviously, one cannot omit a drying step.

Standard drying is performed thermally. Cells that pass such a drying step at 200°C for 1 min in an oven before IPL annealing (group 7) achieve $0.4\%_{\text{abs}}$ higher mean η values and $0.3 \Omega \cdot \text{cm}^2$ lower mean R_s than cells which are not dried before (group 6). Their efficiencies exceed also these of the entirely thermally processed reference cells by $0.1\%_{\text{abs}}$ (group 5). The reason is that SHJ cells benefit from IPL treatments in terms of FF and V_{OC} due to LS (see explanation in section 6.3.3).

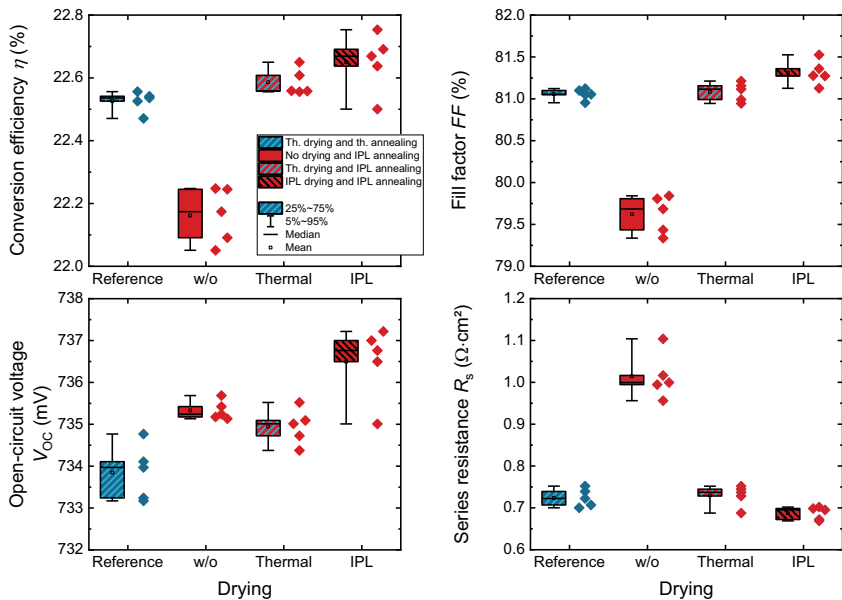


Figure 7-10 Conversion efficiency η , fill factor FF , series resistance R_s , and open-circuit voltage V_{OC} of four groups of busbarless SHJ cells that received varying drying processes (or abandon a drying step) before IPL annealing using the setting *IPL-all*. The fourth group is an entirely thermally processed reference group. The short-circuit current density j_{SC} does not vary significantly between the groups. Its overall mean value is $37.9 \pm 0.1 \text{ mA/cm}^2$. This graph is adapted from Ref. [120].

7.1 Intense pulsed light processing of silicon heterojunction solar cells

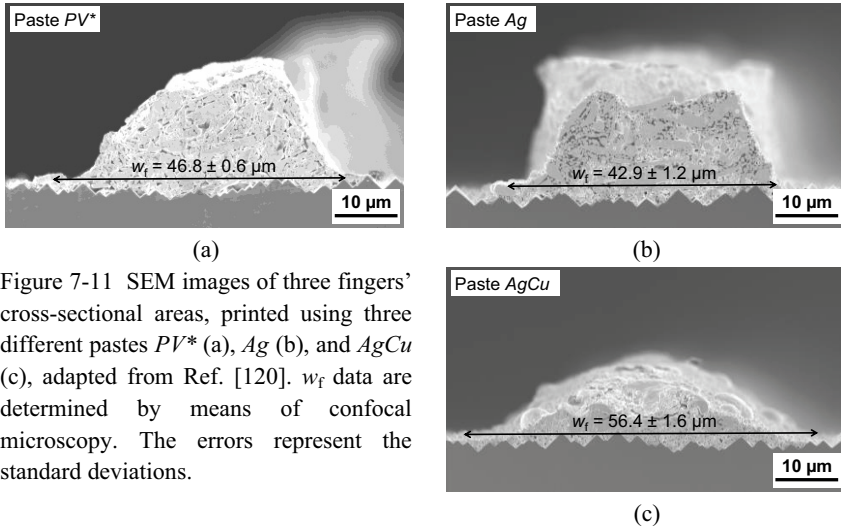


Figure 7-11 SEM images of three fingers' cross-sectional areas, printed using three different pastes PV^* (a), Ag (b), and $AgCu$ (c), adapted from Ref. [120]. w_f data are determined by means of confocal microscopy. The errors represent the standard deviations.

Even higher FF ($0.2\%_{\text{abs}}$) and V_{OC} (1.6 mV) values are reached if thermal drying is replaced by IPL drying (group 8). Therefore, η reaches the highest mean value of $22.7 \pm 0.1\%$ in this part of the experiment. These results confirm that IPL is capable of entirely replacing thermal treatments within back end processing of SHJ solar cells, whereas η is improved by $0.2\%_{\text{abs}}$ on average.

After the demonstration that (IPL) drying is beneficial before IPL processing, optimized both-sides IPL annealing ($IPL\text{-opt}$ with $f_{\text{pulse}} = 0.2$ Hz instead of $IPL\text{-all}$ with $f_{\text{pulse}} = 0.1$ Hz) and also IPL drying is applied to full-size SHJ solar cells metallized using different screen printing pastes.

First, the thermally annealed groups 9 and 10 are compared to each other. The corresponding cells differ regarding the printed pastes and, consequently, in terms of finger geometry (see Figure 7-11) and j_{SC} (see Figure 7-12). No significant difference of the finger geometry is detected comparing fingers of the same paste, which are annealed (thermally or by means of IPL) using varying processes (not shown here). Figure 7-11 presents cross-sectional views of three fingers printed using three different pastes. Additionally, the mean shading finger width w_f corresponding to each paste is presented. Both silver fingers appear narrow and high at the same time. Paste PV^* achieves

7 Metallization of solar cells with passivating contacts

$w_f = 46.8 \pm 0.6 \mu\text{m}$ and Ag even $w_f = 42.9 \pm 1.2 \mu\text{m}$. Therefore, the cells exhibit similar mean j_{SC} values of $38.0 \pm 0.1 \text{ mA/cm}^2$ and 38.1 mA/cm^2 , respectively. The fingers printed by means of paste $AgCu$ are significantly flatter and wider ($w_f = 56.4 \pm 1.6 \mu\text{m}$), which results in a slightly reduced mean j_{SC} of 37.8 mA/cm^2 .

Then, the thermally annealed group *10* is compared to the IPL-processed group *11*. From Figure 7-12 it is obvious that both FF and V_{OC} are significantly higher after IPL annealing. Besides from healing of sputter-induced damage, these cells additionally benefit from IPL processing due to LS effects (see discussion in section 6.3.3). The mean R_s reduction of 0.2 and $0.1 \Omega \cdot \text{cm}^2$ for paste $AgCu$ and Ag , respectively, from group *10* to *11* further indicates that resistive losses are decreased. As a result, the mean conversion efficiency in group 11_{Ag} and 11_{AgCu}

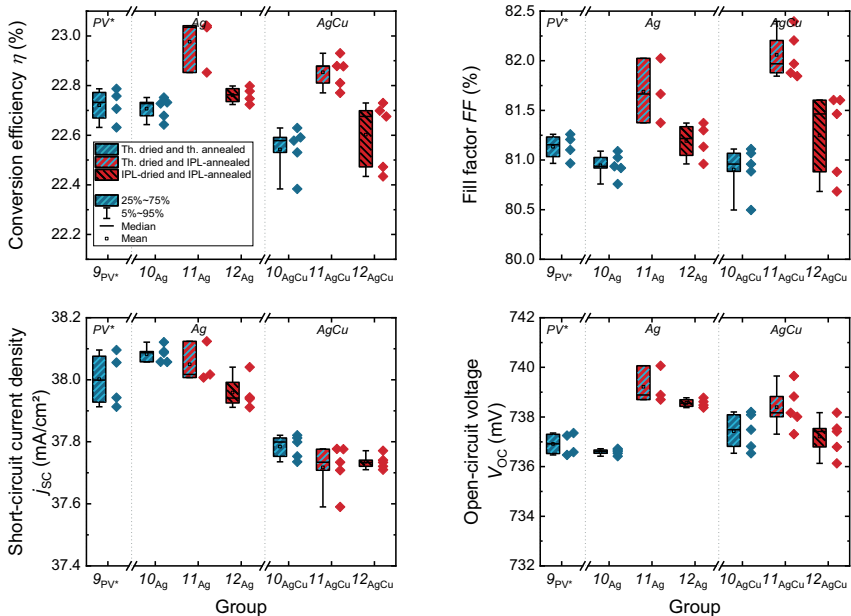


Figure 7-12 IV -related data of SHJ cells after thermal drying and thermal annealing (group 9 and 10), thermal drying and IPL annealing (group 11), IPL drying and IPL annealing (group 12). IPL drying is performed with reduced radiant exposure compared to the experiment leading to the results displayed in Figure 7-10. This adaption is required to ensure process stability due to the $20 \mu\text{m}$ thinner samples.

7.1 Intense pulsed light processing of silicon heterojunction solar cells

is 0.3%_{abs} and 0.4%_{abs} higher than in the corresponding thermal reference groups 10_{Ag} and 10_{AgCu} . Furthermore, the IPL-annealed group 11_{Ag} outperforms the overall reference group 9_{PV^*} by 0.3%_{abs}.

Please note that not only LS may lead to the increase of FF but also an annealing-induced sheet resistance reduction of the ITO layer. Considering thermal processing, this is studied in detail in Ref. [183]. It has also been observed as an effect of IPL processing as described in Ref. [156].

In this experiment, the highest efficiency of 23.0% is achieved by an IPL-annealed cell of group 11_{Ag} . The IV -related data are independently confirmed by Fraunhofer ISE CalLab (see Table 7-2).

Table 7-2 IV -related data of the cell with the highest η in this experiment, confirmed by Fraunhofer ISE CalLab (STC, black/non-reflecting chuck).

j_{sc} (mA/cm ²)	V_{oc} (mV)	FF (%)	η (%)
38.1	741.0	81.6	23.0

Replacing thermal drying by IPL drying in a next step still leads to slightly higher mean η values for both pastes Ag and $AgCu$ compared to their corresponding thermal reference groups. In fact, from the results provided in Figure 7-10 higher η values would be expected than achieved in this experiment here. Moreover, the lower FF in group 12 compared to group 11 (0.5%_{abs} and 0.9%_{abs} in the case of Ag and $AgCu$, respectively) due to higher series resistance losses is conspicuous. This and the mentioned contradiction to the results in Figure 7-10 actually originate from a reduced radiant energy of IPL drying compared to the IPL drying process used above (see Figure 7-10). Since the wafers used in this part of the experiment are 20 μm thinner, they tend to crack at too high drying energy. It is further conspicuous that this happens less in the case of non-metallized samples. Therefore, it is assumed that solvents in the freshly screen-printed contact fingers are rapidly outgassed during IPL processing causing mechanical stress on the thin wafers. Moreover, metal contacts exhibit a significantly higher thermal expansion than silicon wafers. In consequence, the

thermomechanical stress on wafers increases when sufficient mechanical adhesion between metal contacts and substrate is provided. The combination of both effects results in an increased breakage of metallized (thin) wafers using this drying process featuring higher E_{rad} . To ensure sufficient process stability, t_{pulse} is reduced by 10% at the price of higher series resistance losses. It is to be investigated in the future, whether the t_{pulse} reduction can be compensated by higher U_{lamp} or by the application using higher n_{pulse} . However, the present results of this experiment demonstrate that entire both-sides IPL processing of SHJ cells is possible, whereby conversion efficiencies are exceeding these of thermally processed cells.

7.1.5 Intense pulsed light processing of advanced metallization

Certainly, an even increased resource saving potential in SHJ back end processing would result from the combination of IPL with inkjet or FlexTrail printing, as developed in chapter 5. In order to demonstrate its feasibility, full-size SHJ solar cells exhibiting inkjet- or FlexTrail-printed front grids are manufactured and annealed using the *IPL-opt* process (applied to the front).¹⁶ Corresponding *IV*-related data is provided in Figure 7-13. Please note the assessed overestimation of *FF* and η of 1.3%_{abs} and 0.4%_{abs}, respectively, due to the specific configuration of the PCB^{TOUCH} setup. For more details about the *FF* and η overestimation, the reader is kindly referred to section 5.4.

Thermally annealed inkjet-printed SHJ cells exhibit a mean conversion efficiency of $23.0 \pm 0.1\%$. As in the case of the screen-printed cells (see section 7.1.4), the IPL-processed cells exhibit a higher mean η , namely $23.2 \pm 0.2\%$. Furthermore, these cells benefit from LS during IPL processing, which is reflected in a mean V_{OC} that is increased by 1.5 mV and in a 0.1%_{abs} higher mean *FF* compared to thermal annealing. Moreover, the mean j_{SC} of the IPL-processed cells is

¹⁶ In a preliminary study, it has been investigated whether an IPL drying step performed directly after inkjet or FlexTrail printing and before *IPL-opt* would have a beneficial impact on cell performance. Since no significant effect could be identified, IPL drying of inkjet- and FlexTrail-printed grids is discarded in the following.

7.1 Intense pulsed light processing of silicon heterojunction solar cells

0.1 mA/cm² higher. However, the latter is not induced by IPL processing but rather by slight variations of the inkjet-printed finger width w_f .

The FlexTrail-printed front grids exhibit a mean w_f reduced from $84.3 \pm 1.3 \mu\text{m}$ (inkjet) down to $20.9 \pm 1.9 \mu\text{m}$ (FlexTrail). The strong w_f reduction is reflected in a mean j_{SC} increased by 0.5 mA/cm² to $38.8 \pm 0.0 \text{ mA/cm}^2$, mainly contributing to an increased η . Both after thermal and IPL annealing, the FlexTrail-printed SHJ cells exhibit a mean η of $23.5 \pm 0.1\%$. Their mean V_{OC} slightly increases by 1.2 mV.

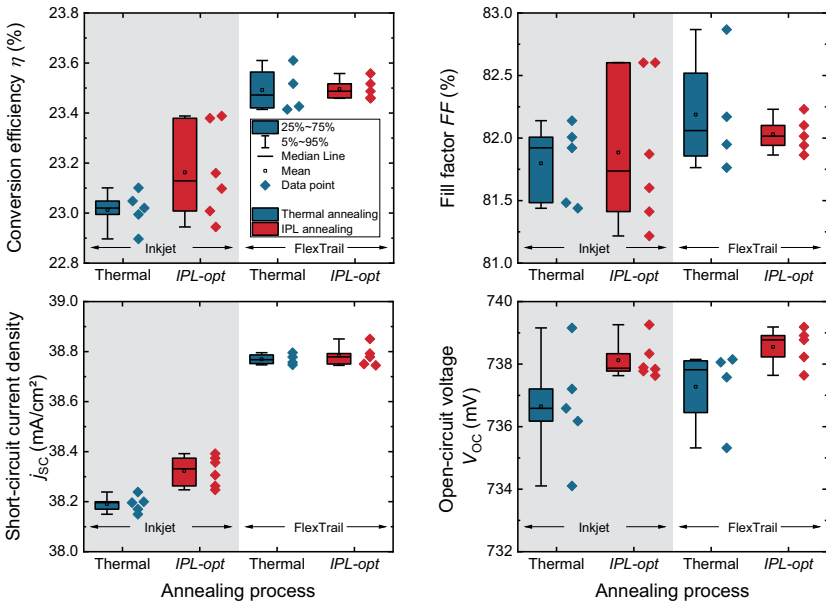


Figure 7-13 IV -related data of full-size busbarless SHJ solar cells exhibiting front grids fabricated by means of inkjet (grey background) or FlexTrail (white background) printing. For both inkjet and FlexTrail printing the same ink *Nano-Ag* is employed. Annealing is performed either thermally (200°C, 30 min) or by means of *IPL-opt* applied to the cells' front sides. Inkjet printing is performed using a heated sample table (60°C). In the case of FlexTrail, the sample table exhibits room temperature. No explicit drying step is performed. FF and η are assumed to be overestimated by 1.3%_{abs} and 0.4%_{abs}, respectively, due to the specific configuration of the PCB^{TOUCH} setup. The presented data shows the values as-measured without correction.

However, the influence of LS is not reflected in a significant manner in the mean FF of FlexTrail-printed cells (group 16) compared to group 15 in Figure 7-13. This might be caused by the comparatively wide-spread data points. Nevertheless, the results demonstrate that FlexTrail can achieve superior results compared to inkjet and screen printing (also compare previous section 7.1.4) leading to a mean conversion efficiency of 23.5%. Moreover, IPL-processed and inkjet-printed cells outperform their thermally treated counterparts on average by up to 0.2%_{abs}. In the case of FlexTrail, IPL-processed SHJ cells exhibit a similar mean η as thermally treated ones. Thereby, annealing time is reduced from 30 min down to several milliseconds per light pulse.

In order to further increase cell performance, the finger number of the FlexTrail-printed front grids is varied from 80 to 100. Corresponding cell results are presented in Table 7-3.

Table 7-3 IV -related data corresponding to SHJ solar cells (five samples per group) with FlexTrail-printed front grids exhibiting 80, 90, or 100 fingers. All cells are annealed using *IPL-opt*. The values are as-measured without corrections due to the PCB^{TOUCH} setup.

Cell parameter	Front finger number		
	80 fingers	90 fingers	100 fingers
V_{OC} (mV)	738.5 ± 0.6	738.6 ± 1.3	738.0 ± 1.0
FF (%)	82.0 ± 0.1	82.5 ± 0.2	82.5 ± 0.5
j_{SC} (mA/cm ²)	38.8 ± 0.0	38.7 ± 0.1	38.7 ± 0.0
η (%)	23.5 ± 0.0	23.6 ± 0.1	23.5 ± 0.1

Whereas V_{OC} and j_{SC} remain almost unaffected by the variation of the finger number, the mean FF is increased by 0.5%_{abs} (reduction of R_s -related losses) in the case that the front grid exhibits 90 or 100 fingers. This results in a slight mean efficiency gain of 0.1%_{abs}. The cell with the highest conversion efficiency

achieved in this experiment, and overall in the entire work, exhibits a front grid with 90 fingers and $\eta = 23.7\%$ (as-measured).

7.2 Post-metallization annealing of cells with polysilicon-based contacts

7.2.1 Motivation

The great potential of IPL integrated into SHJ back end processing is demonstrated on cell level in section 7.1. However, certain IPL annealing processes exist that offer an even greater potential for printed metal contacts in terms of their electrical performance but are restricted due to temperature constraints of the sensitive *a*-Si:H layers. Such a process is introduced as *IPL-PV* in section 6.3.4.

This is valid not only for IPL but also for thermal annealing. It is demonstrated in section 6.1 that low-temperature metallization electrically performs comparably to fired contacts after mid-temperature annealing operated at temperatures between 250 and 350°C. As in the case of *IPL-PV*, substrate temperatures are achieved which exceed the critical temperature for *a*-Si:H layers. Consequently, in order to make use of such printed metal contacts' full electrical potential on passivating contacts, the *a*-Si:H layers can be replaced by more temperature-tolerant ones such as *poly*-Si-based layers. This section presents such cells exhibiting both-sides TOPCon contacts.

In order to combine TOPCon with thermally or IPL-annealed screen-printed low-temperature metallization, they are coated with ITO layers. Similar to SHJ cells, the TCO acts both as anti-reflection coating and lateral transport layer for charge carriers. On the one hand, such structures require careful consideration of thermal budget owing to interactions at the *poly*-SiC_x/SiO_x/ITO contact [63]. On the other hand, the annealing has to be intense enough in order to cure sputter-induced damage in the TOPCon layer system. This study addresses this trade-off, e.g., by means of fast and precisely tailored IPL annealing, which is developed in section 6.3.6.

7.2.2 Sample preparation and characterization

In order to investigate thermal mid-temperature annealing and IPL processing on cell level, 2 cm x 2 cm-sized solar cells with TOPCon layers on both sides are realized. Each seven of them are fabricated on a four-inch wafer (see Figure 7-14 (a)). These are 250 μm thick *p*-type float-zone wafers that exhibit an alkaline texture on the front. The corresponding layer stack is depicted in Figure 7-14 (b). Both sides of the wafers are provided with 1.2 nm thin SiO_x layers. Additionally, the rear exhibits a 40 nm thick *poly*- $\text{SiC}_x(\text{p})$ layer and the front a 15 nm thick *poly*- $\text{SiC}_x(\text{n})$ layer. More details about the fabrication of such layers can be found in section 2.2.2. The ITO layers on the cells' front sides are deposited by means of DC magnetron sputtering. Here, the low-invasive ITO dual layer sputter process developed for the application on ultra-thin *poly*- SiC_x -based passivating contacts is utilized [63]. The cells are equipped with a full-area tin/palladium/silver (Ti/Pd/Ag) rear contact, which is temperature-tolerant towards subsequent annealing at the prize of decreased rear side reflection compared to an entirely silver-based rear.

The front grids are screen-printed using paste *PV* (for more details see appendix B) and dried using a conveyor furnace (200°C, 1 min). Thereby, $w_{\text{f,set}}$ is chosen to be 40 μm . The grid exhibits 14 fingers with a busbar in the middle exhibiting a set width of 0.8 mm. After screen printing, one group of cells is thermally

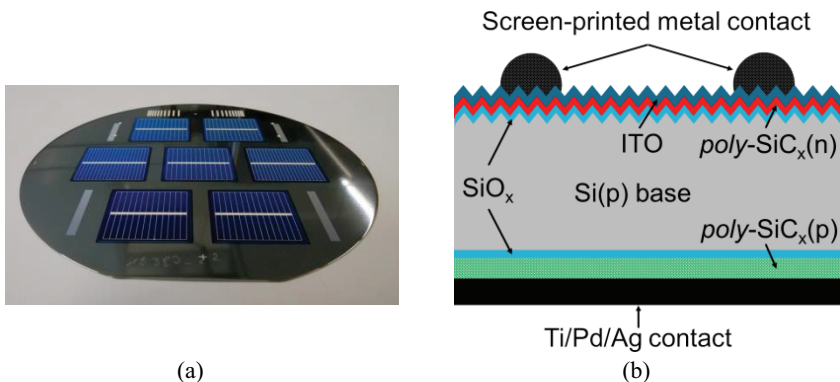


Figure 7-14 Seven both-sides TOPCon solar cells fabricated on a four-inch float-zone wafer (a) and schematic drawing of a monofacial solar cell's architecture exhibiting TOPCon layers on both sides (b). The latter is redrawn from Ref. [120].

7.2 Post-metallization annealing of cells with polysilicon-based contacts

annealed at 350°C for 3 min on a hotplate. A second group is annealed by means of *IPL-TOP2* (for more details about this process see Table 6-2). Then, *IV*-measurements at standard testing conditions on a black chuck and $Suns-V_{OC}$ measurements are performed. The thermally annealed solar cells are annealed at 350°C for additional 7 min and *IV*- and $Suns-V_{OC}$ -measured again. Selected cells are measured in terms of their quantum efficiencies. Moreover, confocal microscopy and SEM are performed in order to extract w_f .

7.2.3 Thermal and intense pulsed light annealing of solar cells

Based on the work conducted in sections 6.1 and 6.3, thermal annealing at 350°C for 3 and 10 min and also the IPL process *IPL-TOP2* are selected to be integrated into the fabrication of 2 cm x 2 cm-sized both-sides TOPCon solar cells. In Table 7-4, corresponding *IV*-related data are provided. The mean V_{OC} values of the thermally annealed groups of cells do not differ significantly from the IPL-annealed group. This holds for the R_s and *FF* data as well. As expected from Figure 6-31 (b), there is a slight tendency towards higher R_s after annealing at 350°C for 10 min due to higher values of $\rho_{c,stack}$ compared to the other groups.

Table 7-4 *IV*-related data corresponding to 2 cm x 2 cm-sized both-sides TOPCon solar cells (10 cells per group).

Cell parameter	Annealing process		
	350°C, 3 min	350°C, 10 min	<i>IPL-TOP2</i>
V_{OC} (mV)	706.1 ± 1.3	707.8 ± 1.9	705.7 ± 2.2
R_s ($\Omega \cdot cm^2$)	1.1 ± 0.1	1.2 ± 0.3	1.2 ± 0.2
<i>FF</i> (%)	76.6 ± 0.8	77.7 ± 1.1	77.2 ± 1.7
j_{SC} (mA/cm ²)	36.3 ± 0.1	36.5 ± 0.2	36.2 ± 0.2
η (%)	19.6 ± 0.2	20.1 ± 0.3	19.8 ± 0.5

7 Metallization of solar cells with passivating contacts

To better assess the V_{OC} and FF data achieved with thermal annealing and IPL processing, it is contrasted with the data of a cell that is measured directly after the post-screen-printing drying process performed at 200°C for 1 min (without subsequent annealing). This cell's V_{OC} and FF is 693.3 mV and 60.6%, respectively. From that, V_{OC} is increased by up to 14.5 mV as a consequence of post-metallization annealing (compare Table 7-4). This indicates the potential in passivation quality released by the developed IPL and thermal annealing processes. The FF increase of up to 17.1%_{abs} achieved by such annealing reflects the increase in passivation quality, too, and also indicates the high electrical performance of the (IPL-)annealed screen-printed low-temperature metal electrodes.

The mean j_{SC} values of 36.1 to 36.5 mA/cm² of all three groups of cells are low both because of shading-related losses caused by the front busbar covering 4% of the entire cell area and also by optical losses due to the Ti/Pd/Ag rear contact. According to quantum efficiency (QE) measurements presented in Figure 7-15, a j_{SC} gain of 4 mA/cm² can be expected from an improved front grid layout and an evaporated-silver-based rear electrode instead of a Ti/Pd/Ag-based rear contact. The QE data indicates that especially the rear metallization requires

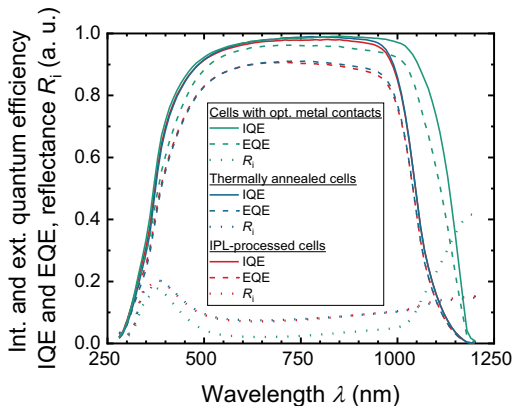


Figure 7-15 Internal quantum efficiency (IQE), external quantum efficiency (EQE) and reflectance R_i of two cells built-up as sketched in Figure 7-14 (b). They are thermally annealed and IPL-treated after screen printing of the front metal electrodes. For comparison reasons, a similar cell with evaporated Ag front (no busbar) and rear contacts is measured. One cell per measurement is used.

7.2 Post-metallization annealing of cells with polysilicon-based contacts

optimization in order to achieve higher j_{SC} values. A solar cell with optimized evaporated silver contacts on the front (without a busbar) and also on the rear side serves as the reference for the QE measurements (green lines in Figure 7-15). Actually, the mean w_f of the screen-printed paste-*PV*-based contacts of $42.5 \pm 1.4 \mu\text{m}$ leaves only little room for improvement compared to the evaporated front contacts, which are only $5 \mu\text{m}$ thinner on average. Figure 7-16 depicts a cross-sectional view of such a screen-printed metal electrode applied on the front side of a TOPCon solar cell. The w_f data is obtained by means of confocal microscopy. However, the busbar width of the screen-printed grids could be significantly reduced. Moreover, a tapered busbar or even a busbarless layout would enable a further j_{SC} gain.

From a j_{SC} gain of 4 mA/cm^2 a V_{OC} increase of 3 mV can be expected for these cells according to the well-known one-diode equation (see equation (2-21)). Such a j_{SC} and V_{OC} gain together would lead to about $0.8\%_{\text{abs}}$ higher η values than the measured ones listed in Table 7-4. With regard to conversion efficiency, thermal annealing at 350°C for 10 min reaches the highest mean value of $\eta = 20.1 \pm 0.3\%$. Thermal annealing at 350°C for 3 min and *IPL-TOP2* achieve similar values, namely $\eta = 19.6 \pm 0.2\%$ and $\eta = 19.8 \pm 0.5\%$, respectively. The top cell in this experiment regarding η is an IPL-annealed cell exhibiting $\eta = 20.8\%$. According to the discussion of the QE data, a conversion efficiency

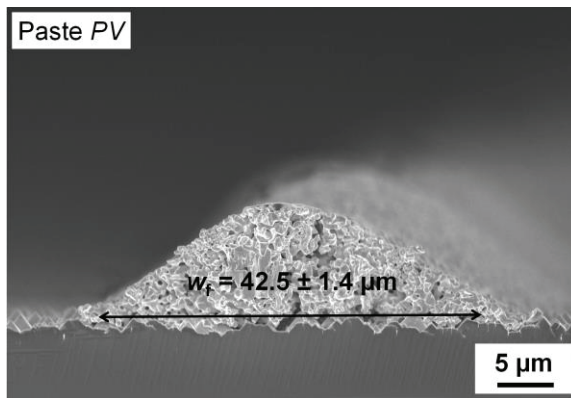


Figure 7-16 SEM image of a screen-printed and thermally annealed (350°C , 10 min) metal electrode printed on the front side of a TOPCon solar cell.

potential of $\eta = 21.6\%$ is identified. The best thermally annealed cell achieves a conversion efficiency potential of 21.2%.

These results demonstrate both the feasibility of thermal mid-temperature annealing and IPL processing as contact formation techniques for TOPCon solar cells featuring screen-printed metal electrodes. Certainly, cells with an optimized screen-printed front grid (in particular in terms of optical performance) and an improved rear contact would allow for exploitation of the full performance potential of TOPCon.

7.3 Chapter summary

Section 7.1 addresses challenges arising in IPL processing of full-size SHJ solar cells. Using the *IPL-AgCu* process, it is shown that its integration into back end processing without adaptations of the IPL setup is accompanied by degradation of such cells. This is caused by forming of a bow of the samples leading to heating of the specimens above the *a*-Si:H-specific critical temperature during *IPL-AgCu*. This issue is technologically solved by using a sample table featuring a vacuum suction. However, the process *IPL-all* is integrated into SHJ back end processing without any adaptations and straightaway achieves a SHJ solar cell mean η gain of 0.2%_{abs} compared to the thermal reference process.

Moreover, it is demonstrated that IPL processing can entirely replace thermal treatments within back end processing of SHJ solar cells. This includes both IPL drying and annealing. Due to a pulse time of milliseconds in the case of IPL, a great potential of drastically reduced process time and costs exists. According to cost of ownership calculations, a substitution of thermal annealing by IPL would cause a cost reduction of 6%_{rel} today. Furthermore, full-size IPL-processed, busbarless SHJ cells are fabricated with an independently certified efficiency of up to 23.0%. Metallization is performed by means of state-of-the-art screen printing using both silver- and silver-coated-copper-based pastes. Entirely IPL-processed cells outperform thermally treated ones by 0.3-0.4%_{abs}. In contrast to solely thermally annealed cells, IPL-processed cells are assumed to benefit, besides from curing of sputtering damage, from light soaking effects, and sheet

resistance reduction in the ITO layers, which additionally increase V_{OC} , FF , and, therefore, η as well.

The advantages of IPL over thermal annealing are used for inkjet- and Flex-Trail-printed SHJ cells as well. In fact, the resource and cost saving potential of both of these innovative metallization techniques and IPL processing can be combined. Thereby, IPL-processed cells outperform the thermally treated ones by up to 0.2%_{abs} on average. The use of FlexTrail printing offers an additional increase in η of 0.5%_{abs}. The cell with the highest η achieves 23.7% (as-measured). The low silver consumption of inkjet and FlexTrail printing as well as the high throughput potential of IPL is certainly of high interest for industrial back end processing of Si solar cells with passivating contacts.

In section 7.2, IPL and thermal mid-temperature annealing are successfully applied to the front of screen-printed 2 cm x 2 cm-sized, both-sides TOPCon solar cells. V_{OC} values of significantly above 705 mV are achieved both by means of thermal annealing and IPL, respectively. The high V_{OC} values indicate that the TOPCon layers' passivation quality is not harmed by the metallization, e.g., due to penetration by metal. Moreover, the trade-off between curing of sputter-induced damages, contact formation, and contact resistivity of the TOPCon/ITO interfaces is well balanced. By means of IPL, cells with a conversion efficiency potential of up to 21.6% are fabricated. This demonstrates both the potential of screen-printed low-temperature metallization annealed at temperatures significantly above 200°C and IPL processing of such TOPCon solar cells.

8 Summary

Solar cells with passivating contacts based on amorphous or polycrystalline silicon layers currently undergo a transition from lab to mass production. In fact, they are expected to be the successors of state-of-the-art solar cells, such as PERC, due to a higher efficiency potential and the prospective to further reduce the levelized cost of electricity. However, back end processing of these next-generation cells is a major challenge. Metallization needs to be resource-efficient, fast, reliable, and low-invasive while at the same time it has to maintain passivating contacts' high efficiency potential. The present work tackles this trade-off both by novel printing approaches, such as screen printing of silver-coated-copper-based pastes, inkjet printing, and FlexTrail printing, and innovative contact formation processing, such as intense pulsed light and thermal annealing combined with plasma or ultrasonic pretreatments. These developments are based on an in-depth understanding of contact formation.

The first part of this work focusses on **novel printing approaches with significant silver reduction** compared to the state of the art, i.e., 100 mg/cell by means of screen printing of busbarless Si heterojunction (SHJ) cells. The straightforward approach is to use conventional screen printing but to replace expensive silver pastes by silver-coated-copper-based ones. With regard to weight, they offer a silver reduction potential of up to 40%_{wt}. Thereby, SHJ solar cells exhibiting a silver-coated copper grid achieve comparable conversion efficiencies to those with silver-based contacts. A higher silver saving potential of up to 90% is achieved by replacing screen printing by advanced printing techniques such as inkjet of nanosilver-based inks (silver consumption below 10 mg/cell). Silver saving is even exceeded by **FlexTrail printing**. This new technique is co-invented by the present author in order to obtain a high reliability and throughput potential in printing of nanosilver inks at the same time. By taking the example of full-size busbarless SHJ solar cells, FlexTrail printing demonstrates a potential silver reduction of down to below 5 mg per cell. Using the same ink as for inkjet printing, SHJ solar cell efficiency is increased from

8 Summary

23.2% (inkjet, as-measured) up to 23.7% (FlexTrail, as-measured). This gain is caused by an outstanding finger width reduction down to 15 μm on average.

Table 8-1 *IV*-related data of busbarless silicon heterojunction solar cells that achieve the highest conversion efficiencies in this work. Corrected values are presented in brackets.

Printing technique, medium, section	Annealing	j_{sc} (mA/cm²)	V_{oc} (mV)	FF (%)	η (%)
Screen printing, paste <i>Ag</i> , section 7.1.4	Thermal	38.1	736.7	81.1	22.8
Screen printing, paste <i>Ag</i> , section 7.1.4	IPL	38.1	741.0	81.6	23.0
Screen printing, paste <i>AgCu</i> , section 7.1.4	Thermal	37.8	738.1	81.1	22.6
Screen printing, paste <i>AgCu</i> , section 7.1.4	IPL	37.7	738.0	82.4	22.9
Inkjet, ink <i>NanoAg</i> , section 5.5	Thermal	38.7	736.7	81.5 (79.9)	23.2 (22.7)
Inkjet, ink <i>NanoAg</i> , section 7.1.5	IPL	38.4	737.8	82.6 (81.0)	23.4 (22.9)
FlexTrail, ink <i>NanoAg</i> , section 5.5	Thermal	39.2	737.4	82.1 (80.5)	23.7 (23.2)
FlexTrail, ink <i>NanoAg</i> , section 7.1.5	IPL	38.8	739.5	82.5 (81.0)	23.7 (23.3)

Second, the focus is set on **contact formation processing** conducted on solar cells with passivating contacts. Typical thermal annealing of SHJ cells is performed at temperatures of about 200°C and an annealing time of more than 10 min. Thus, it is a significant cost driver. Furthermore, the resistivity of low-temperature-annealed metal electrodes is high (5.5-10.0 $\mu\Omega\cdot\text{cm}$) and, hence, reduces cell performance. It is a finding of this work that this is caused by non-optimal densification and sintering of metal particles in the electrodes and the presence of organic, non-conductive binders. Further, it is demonstrated that the

use of thermal annealing operating at up to 350°C enables an electrical conductivity of low-temperature metallization down to 2.4-3.5 $\mu\Omega\cdot\text{cm}$. This can be correlated with a very compact microstructure and the burning of binders in the metal contacts based on detailed analyses. However, surface-tension-driven effects have to be taken into account when operating with such high temperatures harming the electrical metal/TCO contact. A **contact formation model** is introduced stating that the higher the discrepancy of the metal's and the TCO layer's surface energy, the higher the contact resistivity at the metal/TCO interface due to the presence of voids. In order to achieve high conductivity and low metal/TCO contact resistivity simultaneously, the surface-energy-driven processes have to be balanced. For this purpose, an atmospheric pressure air plasma pretreatment of the solar cell surface is used. It temporarily increases the TCO layer's surface energy and leads to a reduction in contact resistivity in the range of 30%. Thermal annealing operating at up to 350°C is integrated into the fabrication of solar cells featuring tunnel oxide passivating contacts (TOPCon) on both sides and screen-printed front grids. The feasibility of such a metallization scheme is demonstrated and potential cell efficiencies of up to 21.2% are obtained and high open-circuit voltages of up to 709.4 mV are reached.

Yet, thermal annealing continues to be a time-consuming process. In order to achieve an annealing time reduction down to milliseconds, thermal post-metallization annealing is replaced by **intense pulsed light (IPL)** processing. The sample temperature during an IPL flash in the millisecond range can be detected time-resolved using a high-speed pyrometer in combination with a sophisticated measurement setup. The correlation of sample temperature and passivation quality reveals that SHJ structures can withstand temperatures significantly higher than 200°C, if, simultaneously, annealing time is reduced tremendously. The samples temporarily reach temperatures of greater than 300°C for milliseconds. Thereby, the implied open-circuit voltage is increased by 5.5 mV compared to thermal annealing. Based on these findings, high-performance IPL drying and annealing processes designed for SHJ solar cells are developed.

It is found by means of optical and electrical investigations that IPL is directly absorbed by printed metal electrodes, which significantly increases their

electrical conductivity. The electrical metal/ITO contact, in contrast, is mainly formed by transferred heat during IPL. It is generated both by absorption of photons in the metallization and in the substrate. The deep understanding of IPL processing of SHJ structures provided in this work is utilized in order to fabricate screen-printed busbarless **SHJ solar cells** with a maximum efficiency of 23.0%. This is independently confirmed by Fraunhofer ISE CaLab. Such cells outperform their thermally treated counterparts by up to 0.4%_{abs} due to improved FF and V_{OC} , caused by healing of sputter damage, sheet resistance reductions in the ITO, and by light soaking effects. SHJ cells exclusively benefit from these effects together during one IPL process step. Moreover, the extremely fast IPL process allows for a great throughput potential and, therefore, cost of ownership reduction of 6%_{rel} today. It is demonstrated that IPL can be combined with state-of-the-art screen printing of both silver- and silver-copper-based pastes allowing low costs and simple integration into industrial mass production.

Additionally, **IPL is transferred from SHJ to both-sides TOPCon solar cells** with screen-printed metal contacts. This step is motivated by the higher temperature tolerance of such passivating contacts allowing more intense and, therefore, effective IPL processing. As a consequence of higher radiant flux density, the sample temperature is increased resulting in an electrical performance gain of the metal electrodes. In fact, the best TOPCon solar cell annealed at 350°C is outperformed by an IPL-treated one by 0.4%_{abs}. It exhibits a conversion efficiency potential of 21.6%.

Finally, **IPL processing is combined with inkjet- and FlexTrail-printed SHJ solar cells**. Thereby, key findings in terms of metallization and contact formation are brought together resulting in the highest conversion efficiency achieved in this work of 23.7% (as-measured).

Selected IV -related results of significant silicon heterojunction solar cells representing the outcome of this thesis are summarized in Table 8-1. Moreover, the presented technological and scientific achievements of this work have the potential to lead to further cost reduction in solar cell manufacturing in the near future. It is desirable that they, hence, contribute to a limitation of global warming according to the *Paris agreement*.

9 Outlook

As pointed out before, it is very likely that silicon solar cells with passivating contacts will replace PERC in the near future. In a long-term perspective, tandem cells consisting of different sub-cells, for example, SHJ as bottom cell and perovskite as top cell, will be even more temperature-sensitive as the solar cells with passivating contacts investigated in this work. Thereby, industry-related high-performance metallization at low temperatures will remain an important topic and the developments presented in this work may be useful also for future solar cell generations.

In terms of printing technique, FlexTrail printing is expected to grow into this field in the near future because it offers many advantages: printing of very narrow structures, resource saving, reliability, high throughput potential, and great flexibility. However, there is room for improvement of FlexTrail-printed metal electrodes with regard to aspect ratio. One possible optimization route is to increase the ink's metal content. In contrast to inkjet, FlexTrail allows for such a modification of the printed medium due to its high flexibility towards the ink's viscosity. Moreover, the flexible printing of extremely thin (conductive) lines, which FlexTrail exclusively offers, may be attractive for other fields apart from PV production as well. Some examples are printed electronics, display manufacturing, and circuit board fabrication. Therefore, future development of FlexTrail also addresses parallelization and automatization.

The present work demonstrates the great potential of IPL in back end processing of silicon solar cells with passivating contacts. It is further demonstrated that, used as a substitute for thermal post-metallization drying and annealing, it can be easily combined with state-of-the-art PV manufacturing tools. Certainly, this aspect as well as the availability of inline tools will attract PV production to IPL. The processes developed in this work offer a good basis for IPL integration into mass production. The newly developed in-situ temperature measurement further enables a fast and high-quality process control instrument for the first time.

10 Appendix

A Calibration and correction of in-situ temperature measurements

The custom calibration of the pyrometer integrated in the setup used for high-speed temperature measurements during IPL is conducted by means of a hot-air treatment and a type k thermocouple. For this purpose, the setup as described in section 4.5 is located outside the IPL device. A non-metallized SHJ precursor (see section 2.2.1 and 6.3.2) is heated with a hot air gun from the front side (α -Si:H(n) side). The SHJ sample is placed on top of quartz glass rings without changing the optical path of the thermal radiation detected by the pyrometer. Its temperature progression is recorded by means of a thermocouple mounted at the rear of the sample (rear side, α -Si:H(p) side) and by the pyrometer (front side, α -Si:H(n) side), simultaneously. Both measurements are taken in the middle of the sample directly one above the other: the thermocouple is mounted at the sample's rear by means of a conductive adhesive (thermal coupling) and the pyrometer measurement spot is directed to the sample's front side.

The sample temperature propagates from about 20 to 220°C due to the hot air treatment. The emissivity ε is adjusted in the pyrometer software in order to

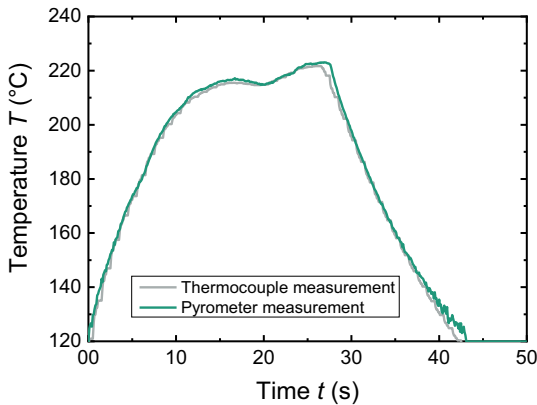


Figure 10-1 Progression of the temperature T in time t of a non-metallized SHJ precursor heated by a hot air gun. T is simultaneously measured by means of a thermocouple and a calibrated pyrometer.

achieve a sufficient agreement of pyrometer and thermocouple measurements. Both measured temperature profiles are displayed in Figure 10-1. The fact that the profiles coincide indicates a sufficient calibration.

As explained in section 4.5, a stack of two band pass filters of the type *FGS900S* from *Thorlabs* is mounted blocking thermal radiation of the Xenon flash lamp but transmitting the Xenon flash (see sketch of the measurement setup depicted in Figure 4-9). Without such a filter stack, the thermal radiation of the flash lamp would artificially superimpose the radiation from the sample and distort the determination of the sample temperature. Since in usual IPL processing (without temperature measurement) no filters are utilized and the transmission of the Xenon flash through the filters stack is less than 100%, the recorded data need to be corrected. The corresponding procedure is explained in the following paragraphs.

The transmission T_i of the filter stack is measured by means of an ultraviolet-visible-near-infrared spectrometer (*PerkinElmer Lambda 900*). T_i is displayed in Figure 10-2. Moreover, the normalized spectral flux density Φ_λ of an unfiltered IPL flash is displayed. In order to obtain the normalized spectral flux density of

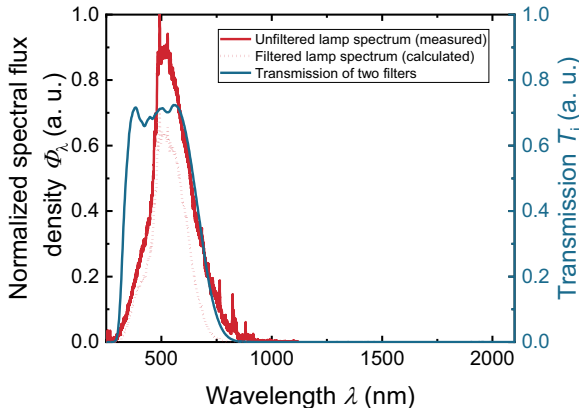


Figure 10-2. Normalized spectral flux density Φ_λ of an unfiltered light pulse (setting *IPL-all*, $n_{\text{pulse}} = 1$, for more details see Table 6-3) measured from 250 to 1100 nm and calculated spectral flux density (from 250 to 1100 nm) of a filtered light pulse (filter stack existing of two band pass filters). The transmission T_i of the filter stack is presented in addition, measured from 250 to 2100 nm.

an IPL flash including the impact of the band pass filters, the unfiltered Φ_λ is multiplied by the transmission of the filter stack. The resulting calculated spectral flux density of the IPL flash is additionally plotted in Figure 10-2. Both spectral flux densities are integrated over the wavelength λ from 250 to 1000 nm. The ratio of the areas below the curves indicates the amount of radiant energy blocked by the filter stack, i.e., 39% in the case of two *FGS900S* band pass filters. Please note that in this case a potential heating of SHJ samples due to the lamp's emitted thermal radiation, which is not blocked in usual IPL processing, is not taken into account.

Moreover, the radiant exposure E_{rad} of the pulse without the presence of a filter stack needs to be measured by means of a bolometer. The difference of E_{rad} in the filtered and unfiltered case ΔE_{rad} is $0.39 \cdot E_{\text{rad}}$. Hence, the offset of the peak temperature ΔT_{peak} can be calculated using the equation

$$\Delta T_{\text{peak}} = \frac{\Delta E_{\text{rad}}}{c_{\text{Si}} \cdot m_{\text{sample}}}, \quad (10-1)$$

with the specific heat capacity of silicon c_{Si} and m_{sample} , which is the mass of the sample underneath the sample area irradiated by E_{rad} . The linear correlation in equation (10-1) is motivated by the linear progression of the measured and non-

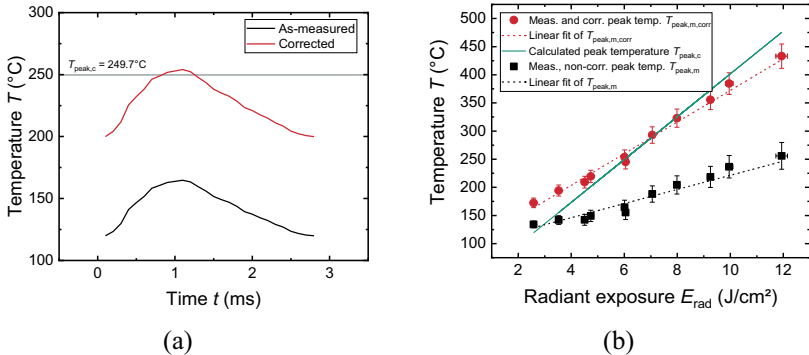


Figure 10-3 Exemplary temperature profiles, as measured and corrected, depicted in (a). The process *IPL-all* is utilized (see Table 6-3). In (b), the measured and corrected peak temperature $T_{\text{peak,m,corr}}$ as well as the measured and non-corrected temperature $T_{\text{peak,m}}$ is plotted as a function of the measured radiant exposure. Additionally, the calculated peak temperature is plotted. It is calculated as described in section 6.3.3.

corrected peak temperature $T_{\text{peak,m}}$ displayed in Figure 10-3 (b). Furthermore, it is assumed that c_{sample} is constant. Especially in the case of IPL operating with long pulses of high intensity, it is expected that this linear correlation is not valid any more due to cooling effects (see following paragraph and section 6.3.3). Moreover, it is assumed in equation (10-1) that the sample absorbs 100% of the impinging Xenon flash. Using ΔT_{peak} , the measured peak temperature $T_{\text{peak,m}}$ can be corrected to $T_{\text{peak,m,corr}}$ using

$$T_{\text{peak,m,corr}} = T_{\text{peak,m}} + \Delta T_{\text{peak}}. \quad (10-2)$$

In order to correct the measured temperature profile, it is assumed that $T_{\text{peak,m,corr}}$ is proportional to $T_{\text{peak,m}}$ (also motivated by Figure 10-3 (b)). The constant of proportionality χ is obtained by

$$\chi = \frac{T_{\text{peak,m,corr}}}{T_{\text{peak,m}}}. \quad (10-3)$$

Accordingly, the measured temperature profile is corrected by multiplication with χ . Figure 10-3 (a) shows an exemplary temperature measurement as-measured and corrected as described in the present section.

Figure 10-3 (b) shows $T_{\text{peak,m,corr}}$ as a function of E_{rad} . It is compared to the calculated peak temperature $T_{\text{peak,c}}$, which is calculated as described in section 6.3.3. Calculated and measured and corrected peak temperatures match for $4 \text{ J/cm}^2 < E_{\text{rad}} < 9 \text{ J/cm}^2$, which is the relevant E_{rad} range in this work. For $E_{\text{rad}} \leq 4 \text{ J/cm}^2$, $T_{\text{peak,m,corr}}$ is overestimated by the measurement. This could be caused by the fact that the lower edge of the pyrometer's measurement range is reached in this case. For $E_{\text{rad}} \geq 9 \text{ J/cm}^2$ $T_{\text{peak,m,corr}}$ remains below $T_{\text{peak,c}}$, presumably due to cooling effects and/or absorption of latent heat. This is discussed in detail in section 6.3.3.

The error of the temperature measurement is estimated to be 5%. Reasons are the calibration procedure, which is performed separately, where the surroundings could have an artificial influence, the use of a band pass filter stack between flash lamp and sample, which has an impact on IPL flashes' spectral

composition (i.e., blocking of (near-)infrared radiation), and the assumptions made for correcting of each measurement.

B Overview of printing media and annealing and drying processes utilized in this work

Seven different commercially available printing media are considered in this work. Their key properties according to the corresponding data sheets are listed in Table 10-1. Please note that paste *PV* (or paste *PV**, which is a further development of paste *PV*) serves as reference in every experiment of this work.

Table 10-1 Overview of key properties of printing media utilized in this work according to corresponding data sheets.

Printing medium	Application	Material, part. shape	Metal(s) (%wt)	Solvent(s) (%wt)	Binder(s) (%wt)
Paste <i>PV</i> (reference)	PV	Ag, spherical	70-90	5-15	< 2
Paste <i>PV*</i> (reference)	PV	Ag, spherical, flakes	80-95	<15	<1
Paste <i>Ag</i>	PV	Ag, spherical, flakes	> 85	< 10	< 5
Paste <i>PE</i>	Printed electronics	Ag, flakes	85	15-35	Unknown
Paste <i>NP</i>	Printed electronics	Ag, spherical	56-62	1-30	Unknown
Paste <i>AgCu</i>	PV	Ag and Cu, spherical	Ag 58-62, Cu 25-35	5-15	Unknown
Ink <i>Nano-Ag</i>	PV, printed electronics	Ag, spherical	50	50	Unknown

In terms of annealing, the reference process in every experiment presented in this work is thermal annealing performed at 200°C for 30 min either by means of a hotplate (in the case of test samples) or a conveyor furnace (in the case of full-size solar cells). Moreover, thermal annealing is performed at 180°C and 220°C for 30 min (low-temperature annealing) and 250°C, 300°C, and 350°C for 15 min (mid-temperature annealing). Thermal drying is either performed at 100°C for 10 min (hotplate) or 200°C for 1 min (conveyor furnace) corresponding to the requirements defined by the design of experiment.

Table 10-2 Overview of IPL processes developed in this work. The values of E_{rad} correspond to the application of one pulse.

IPL process	Description	U_{lamp} (V)	t_{pulse} (ms)	n_{pulse}	f_{pulse} (Hz)	E_{rad} (J/cm²)
Drying	Standard SHJ drying	400	4	2	0.1	7.1
<i>IPL-all</i>	Standard SHJ annealing	550	1	3	0.1	6.0
<i>IPL-opt</i>	Optimum SHJ annealing	550	1	3	0.2	6.0
<i>IPL-PE</i>	Developed for paste <i>PE</i>	500	1	3	0.1	4.7
<i>IPL-AgCu/-NanoAg</i>	Developed for paste <i>AgCu/ink Nano-Ag</i>	450	4	3	0.1	9.3
<i>IPL-PV</i>	Developed for paste <i>PV</i>	550	2	3	0.1	10.0
<i>IPL-TOP1</i>	Developed for TOPCon	550	2	3	0.5	10.0
<i>IPL-TOP2</i>	Developed for TOPCon	550	2	6	0.5	10.0

An overview of the developed intense pulsed light processes utilized in this work is provided in Table 10-2.

Bibliography

- [1] Intergovernmental Panel on Climate Change, *Special Report: Global Warming of 1.5 °C*. 2018.
- [2] Q. Schiermeier, J. Tollefson, T. Scully, A. Witze, and O. Morton, “Energy alternatives: Electricity without carbon,” *Nature*, vol. 454, no. 7206, pp. 816–823, 2008, doi: 10.1038/454816a.
- [3] IW Group, *International Technology Roadmap for Photovoltaic (ITRV): 2018 Results*. Berlin, 2019.
- [4] T. G. Allen, J. Bullock, X. Yang, A. Javey, and S. de Wolf, “Passivating contacts for crystalline silicon solar cells,” *Nat. Energy*, vol. 3, no. 14, p. 1184, 2019, doi: 10.1038/s41560-019-0463-6.
- [5] A. Richter, M. Hermle, and S. W. Glunz, “Reassessment of the limiting efficiency for crystalline silicon solar cells,” *IEEE J. Photovoltaics*, vol. 3, no. 4, pp. 1184–1191, 2013, doi: 10.1109/JPHOTOV.2013.2270351.
- [6] A. W. Blakers, A. Wang, A. M. Milne, J. Zhao, and M. A. Green, “22.8% efficient silicon solar cell,” *Appl. Phys. Lett.*, vol. 55, no. 13, pp. 1363–1365, 1989, doi: 10.1063/1.101596.
- [7] M. Despeisse, C. Ballif, A. Faes, and A. Lachowicz, “Metallization and interconnection for silicon heterojunction solar cells and modules,” *Photovoltaics International*, vol. 30, 2015.
- [8] H. E. Çiftçinar, M. K. Stodolny, Y. Wu, G. J.M. Janssen, J. Löffler, J. Schmitz, M. Lenes, J.-M. Luchies, and L. J. Geerligs, “Study of screen printed metallization for polysilicon based passivating contacts,” *Energy Procedia*, vol. 124, pp. 851–861, 2017, doi: 10.1016/j.egypro.2017.09.242.
- [9] P. Würfel, *Physics of Solar Cells: From Principles to New Concepts*. Weinheim: Wiley-VCH, 2005.
- [10] A. Götzberger, B. Voß, and J. Knobloch, *Sonnenenergie: Photovoltaik: Physik und Technologie der Solarzelle*. Stuttgart: Teubner, 1997.
- [11] S. M. Sze, *Physics of Semiconductor Devices*. New York: Wiley, 1981.
- [12] C. Kittel, J. M. Gress, Lessard, and Jochen Matthias, *Einführung in die Festkörperphysik*. München: Oldenbourg, 1969.

- [13] W. Shockley and W. T. Read, “Statistics of the recombinations of holes and electrons,” *Phys. Rev.*, vol. 87, no. 5, pp. 835–842, 1952, doi: 10.1103/PhysRev.87.835.
- [14] M. A. Green, “Solar cells - operating principles, technology and system applications,” *Solar Energy*, vol. 28, no. 5, p. 447, 1982, doi: 10.1016/0038-092x(82)90265-1.
- [15] R. A. Sinton and A. Cuevas, “A quasi-steady-state open-circuit voltage method for solar cell characterization,” in *16th European Photovoltaic Solar Energy Conference and Exhibition*, Glasgow, Great Britain, 2000.
- [16] A. G. Aberle, “Surface passivation of crystalline silicon solar cells: A review,” *Prog Photovolt Res Appl*, vol. 8, no. 5, pp. 473–487, 2000, doi: 10.1002/1099-159X(200009/10)8:5<473::AID-PIP337>3.0.CO;2-D.
- [17] B. Min, M. Müller, H. Wagner, G. Fischer, R. Brendel, P. P. Altermatt, and H. Neuhaus, “A roadmap toward 24% efficient PERC solar cells in industrial mass production,” *IEEE J. Photovoltaics*, vol. 7, no. 6, pp. 1541–1550, 2017, doi: 10.1109/JPHOTOV.2017.2749007.
- [18] F. Feldmann, “Carrier-selective contacts for high-efficiency Si solar cells,” Ph.D. dissertation, Albert-Ludwigs-Universität, Freiburg, 2015.
- [19] M. Tanaka, M. Taguchi, T. Matsuyama, T. Sawada, S. Tsuda, S. Nakano, H. Hanafusa, and Y. Kuwano, “Development of new a-Si/c-Si heterojunction solar cells: ACJ-HIT (artificially constructed junction-heterojunction with intrinsic thin-layer),” *Jpn. J. Appl. Phys.*, vol. 31, Part 1, No. 11, pp. 3518–3522, 1992, doi: 10.1143/JJAP.31.3518.
- [20] S. de Wolf, A. Descoedres, Z. C. Holman, and C. Ballif, “High-efficiency silicon heterojunction solar cells: A review,” *green*, vol. 2, no. 1, 2012, doi: 10.1515/green-2011-0018.
- [21] J. Haschke, O. Dupré, M. Boccard, and C. Ballif, “Silicon heterojunction solar cells: Recent technological development and practical aspects - from lab to industry,” *Solar Energy Materials and Solar Cells*, vol. 187, pp. 140–153, 2018, doi: 10.1016/j.solmat.2018.07.018.
- [22] M. Bivour, “Silicon heterojunction solar cells analysis and basic understanding,” Ph.D. dissertation, Albert-Ludwigs-Universität, Freiburg, 2015.
- [23] A. Descoedres, Z. C. Holman, L. Barraud, S. Morel, S. de Wolf, and C. Ballif, “>21% efficient silicon heterojunction solar cells on n- and p-type

-
- wafers compared,” *IEEE J. Photovoltaics*, vol. 3, no. 1, pp. 83–89, 2013, doi: 10.1109/JPHOTOV.2012.2209407.
- [24] A. Descoedres, L. Barraud, S. de Wolf, B. Strahm, D. Lachenal, C. Guérin, Z. C. Holman, F. Zicarelli, B. Demaurex, J. Seif, J. Holovsky, and C. Ballif, “Improved amorphous/crystalline silicon interface passivation by hydrogen plasma treatment,” *Appl. Phys. Lett.*, vol. 99, no. 12, p. 123506, 2011, doi: 10.1063/1.3641899.
- [25] S. de Wolf and M. Kondo, “Nature of doped a-Si:H/c-Si interface recombination,” *J. Appl. Phys.*, vol. 105, no. 10, p. 103707, 2009, doi: 10.1063/1.3129578.
- [26] B. Demaurex, S. de Wolf, A. Descoedres, Z. Charles Holman, and C. Ballif, “Damage at hydrogenated amorphous/crystalline silicon interfaces by indium tin oxide overlayer sputtering,” *Appl. Phys. Lett.*, vol. 101, no. 17, p. 171604, 2012, doi: 10.1063/1.4764529.
- [27] T. F. Schulze, L. Korte, E. Conrad, M. Schmidt, and B. Rech, “Electrical transport mechanisms in a-Si:H/c-Si heterojunction solar cells,” *J. Appl. Phys.*, vol. 107, no. 2, p. 23711, 2010, doi: 10.1063/1.3267316.
- [28] K. Ellmer, “Past achievements and future challenges in the development of optically transparent electrodes,” *Nature Photon.*, vol. 6, no. 12, pp. 809–817, 2012, doi: 10.1038/NPHOTON.2012.282.
- [29] M. Bivour, S. Schröer, and M. Hermle, “Numerical analysis of electrical TCO/a-Si:H(p) contact properties for silicon heterojunction solar cells,” *Energy Procedia*, vol. 38, pp. 658–669, 2013, doi: 10.1016/j.egypro.2013.07.330.
- [30] A. Kanevce and W. K. Metzger, “The role of amorphous silicon and tunneling in heterojunction with intrinsic thin layer (HIT) solar cells,” *J. Appl. Phys.*, vol. 105, no. 9, p. 94507, 2009, doi: 10.1063/1.3106642.
- [31] M. Bivour, H. Steinkemper, J. Jeurink, S. Schröer, and M. Hermle, “Rear emitter silicon heterojunction solar cells: Fewer restrictions on the optoelectrical properties of front side TCOs,” *Energy Procedia*, vol. 55, pp. 229–234, 2014, doi: 10.1016/j.egypro.2014.08.035.
- [32] M. Bivour, C. Reichel, M. Hermle, and S. W. Glunz, “Improving the a-Si:H(p) rear emitter contact of n-type silicon solar cells,” *Solar Energy*

- Materials and Solar Cells*, vol. 106, pp. 11–16, 2012, doi: 10.1016/j.solmat.2012.06.036.
- [33] D. Adachi, J. L. Hernández, and K. Yamamoto, “Impact of carrier recombination on fill factor for large area heterojunction crystalline silicon solar cell with 25.1% efficiency,” *Appl. Phys. Lett.*, vol. 107, no. 23, p. 233506, 2015, doi: 10.1063/1.4937224.
- [34] Z. C. Holman, A. Descoedres, L. Barraud, F. Z. Fernandez, J. P. Seif, S. de Wolf, and C. Ballif, “Current losses at the front of silicon heterojunction solar cells,” *IEEE J. Photovoltaics*, vol. 2, no. 1, pp. 7–15, 2012, doi: 10.1109/JPHOTOV.2011.2174967.
- [35] K. Yoshikawa, H. Kawasaki, W. Yoshida, T. Irie, K. Konishi, K. Nakano, T. Uto, D. Adachi, M. Kanematsu, H. Uzu, and K. Yamamoto, “Silicon heterojunction solar cell with interdigitated back contacts for a photoconversion efficiency over 26%,” *Nat. Energy*, vol. 2, no. 5, p. 17032, 2017, doi: 10.1038/nenergy.2017.32.
- [36] J. Peter Seif, A. Descoedres, M. Filipič, F. Smole, M. Topič, Z. Charles Holman, S. de Wolf, and C. Ballif, “Amorphous silicon oxide window layers for high-efficiency silicon heterojunction solar cells,” *J. Appl. Phys.*, vol. 115, no. 2, p. 24502, 2014, doi: 10.1063/1.4861404.
- [37] M. Boccard and Z. C. Holman, “Amorphous silicon carbide passivating layers for crystalline-silicon-based heterojunction solar cells,” *J. Appl. Phys.*, vol. 118, no. 6, p. 65704, 2015, doi: 10.1063/1.4928203.
- [38] G. Nogay, J. P. Seif, Y. Riesen, A. Tomasi, Q. Jeangros, N. Wyrsh, F.-J. Haug, S. de Wolf, and C. Ballif, “Nanocrystalline silicon carrier collectors for silicon heterojunction solar cells and impact on low-temperature device characteristics,” *IEEE J. Photovoltaics*, vol. 6, no. 6, pp. 1654–1662, 2016, doi: 10.1109/JPHOTOV.2016.2604574.
- [39] M. Morales-Masis, E. Rucavado, R. Monnard, L. Barraud, J. Holovsky, M. Despeisse, M. Boccard, and C. Ballif, “Highly conductive and broadband transparent Zr-doped In_2O_3 as front electrode for solar cells,” *IEEE J. Photovoltaics*, vol. 8, no. 5, pp. 1202–1207, 2018, doi: 10.1109/jphotov.2018.2851306.
- [40] INES, 24.63% - New Heterojunction Solar Cell Efficiency Record Certified. Online available: <https://www.ines-solaire.org/actu/!/news/2463->

new-heterojunction-solar-cell-efficiency-record-certified/. Accessed on: February 15th, 2019.

- [41] S. W. Glunz and F. Feldmann, “SiO₂ surface passivation layers - a key technology for silicon solar cells,” *Solar Energy Materials and Solar Cells*, vol. 185, pp. 260–269, 2018, doi: 10.1016/j.solmat.2018.04.029.
- [42] J. Schmidt, R. Peibst, and R. Brendel, “Surface passivation of crystalline silicon solar cells: Present and future,” *Solar Energy Materials and Solar Cells*, vol. 187, pp. 39–54, 2018, doi: 10.1016/j.solmat.2018.06.047.
- [43] I.R.C. Post, P. Ashburn, and G. R. Wolstenholme, “Polysilicon emitters for bipolar transistors: A review and re-evaluation of theory and experiment,” *IEEE Trans. Electron Devices*, vol. 39, no. 7, pp. 1717–1731, 1992, doi: 10.1109/16.141239.
- [44] F. Feldmann, M. Bivour, C. Reichel, M. Hermle, and S. W. Glunz, “Passivated rear contacts for high-efficiency n-type Si solar cells providing high interface passivation quality and excellent transport characteristics,” *Solar Energy Materials and Solar Cells*, vol. 120, pp. 270–274, 2014, doi: 10.1016/j.solmat.2013.09.017.
- [45] M. A. Green, E. D. Dunlop, J. Hohl - Ebinger, M. Yoshita, N. Kopidakis, and A. W.Y. Ho - Baillie, “Solar cell efficiency tables (version 55),” *Prog Photovolt Res Appl*, vol. 28, no. 1, pp. 3–15, 2020, doi: 10.1002/pip.3228.
- [46] A. Richter, J. Benick, F. Feldmann, A. Fell, M. Hermle, and S. W. Glunz, “n-Type Si solar cells with passivating electron contact: Identifying sources for efficiency limitations by wafer thickness and resistivity variation,” *Solar Energy Materials and Solar Cells*, vol. 173, pp. 96–105, 2017, doi: 10.1016/j.solmat.2017.05.042.
- [47] F. Haase, C. Hollemann, S. Schäfer, A. Merkle, M. Rienäcker, J. Krügener, R. Brendel, and R. Peibst, “Laser contact openings for local poly-Si-metal contacts enabling 26.1%-efficient POLO-IBC solar cells,” *Solar Energy Materials and Solar Cells*, vol. 186, pp. 184–193, 2018, doi: 10.1016/j.solmat.2018.06.020.
- [48] F. Feldmann, M. Simon, M. Bivour, C. Reichel, M. Hermle, and S. W. Glunz, “Carrier-selective contacts for Si solar cells,” *Appl. Phys. Lett.*, vol. 104, no. 18, p. 181105, 2014, doi: 10.1063/1.4875904.

- [49] G. Nogay, A. Ingenito, E. Rucavado, Q. Jeangros, J. Stuckelberger, P. Wyss, M. Morales-Masis, F.-J. Haug, P. Loper, and C. Ballif, “Crystalline silicon solar cells with coannealed electron- and hole-selective SiC_x passivating contacts,” *IEEE J. Photovoltaics*, pp. 1–8, 2018, doi: 10.1109/jphotov.2018.2866189.
- [50] R. Peibst, C. Kruse, S. Schäfer, V. Mertens, T. Dullweber, and Brendel R., “Efficiency potential of the 'Both polarities poly-Si front side structured' (Boss) cell and its elegant realization by LPCVD,” in *36th European Photovoltaic Solar Energy Conference and Exhibition*, Marseille, France, 2019.
- [51] S. Mack, J. Schube, T. Fellmeth, F. Feldmann, M. Lenes, and J.-M. Luchies, “Metallisation of boron-doped polysilicon layers by screen printed silver pastes,” *Phys. Status Solidi RRL*, vol. 11, no. 12, p. 1700334, 2017, doi: 10.1002/pssr.201700334.
- [52] H. Steinkemper, F. Feldmann, M. Bivour, and M. Hermle, “Numerical simulation of carrier-selective electron contacts featuring tunnel oxides,” *IEEE J. Photovoltaics*, vol. 5, no. 5, pp. 1348–1356, 2015, doi: 10.1109/JPHOTOV.2015.2455346.
- [53] M. Bivour, M. Reusch, S. Schroer, F. Feldmann, J. Temmler, H. Steinkemper, and M. Hermle, “Doped layer optimization for silicon heterojunctions by injection-level-dependent open-circuit voltage measurements,” *IEEE J. Photovoltaics*, vol. 4, no. 2, pp. 566–574, 2014, doi: 10.1109/JPHOTOV.2013.2294757.
- [54] F. Feldmann, M. Simon, M. Bivour, C. Reichel, M. Hermle, and S. W. Glunz, “Efficient carrier-selective p- and n-contacts for Si solar cells,” *Solar Energy Materials and Solar Cells*, vol. 131, pp. 100–104, 2014, doi: 10.1016/j.solmat.2014.05.039.
- [55] A. Moldovan, F. Feldmann, K. Kaufmann, S. Richter, M. Werner, C. Hagendorf, M. Zimmer, J. Rentsch, and M. Hermle, “Tunnel oxide passivated carrier-selective contacts based on ultra-thin SiO₂ layers grown by photo-oxidation or wet-chemical oxidation in ozonized water,” in *2015 IEEE 42nd Photovoltaic Specialist Conference*, New Orleans, LA, 2015, pp. 1–6.

-
- [56] Y. H. Kwark and R. M. Swanson, “n-type SIPOS and poly-silicon emitters,” *Solid-State Electronics*, vol. 30, no. 11, pp. 1121–1125, 1987, doi: 10.1016/0038-1101(87)90076-1.
- [57] H. C. de Graaff and J. G. de Groot, “The SIS tunnel emitter: A theory for emitters with thin interface layers,” *IEEE Trans. Electron Devices*, vol. 26, no. 11, pp. 1771–1776, 1979, doi: 10.1109/T-ED.1979.19684.
- [58] F. Feldmann, G. Nogay, P. Löper, D. L. Young, B. G. Lee, P. Stradins, M. Hermle, and S. W. Glunz, “Charge carrier transport mechanisms of passivating contacts studied by temperature-dependent J-V measurements,” *Solar Energy Materials and Solar Cells*, vol. 178, pp. 15–19, 2018, doi: 10.1016/j.solmat.2018.01.008.
- [59] J. Y. Gan and R. M. Swanson, “Polysilicon emitters for silicon concentrator solar cells,” in *1990 IEEE 21st Photovoltaic Specialist Conference*, Kissimmee, USA, 1990, pp. 245–250.
- [60] R. Peibst, U. Romer, K. R. Hofmann, B. Lim, T. F. Wietler, J. Krugener, N.-P. Harder, and R. Brendel, “A simple model describing the symmetric I-V characteristics of p polycrystalline Si/n monocrystalline Si, and n polycrystalline Si/p monocrystalline Si,” *IEEE J. Photovoltaics*, vol. 4, no. 3, pp. 841–850, 2014, doi: 10.1109/JPHOTOV.2014.2310740.
- [61] M. K. Stodolny, M. Lenes, Y. Wu, G.J.M. Janssen, I. G. Romijn, J.R.M. Luchies, and L. J. Geerligts, “n-type polysilicon passivating contact for industrial bifacial n-type solar cells,” *Solar Energy Materials and Solar Cells*, vol. 158, pp. 24–28, 2016, doi: 10.1016/j.solmat.2016.06.034.
- [62] M. K. Stodolny, J. Anker, B. L.J. Geerligts, G. J.M. Janssen, B. W.H. van de Loo, J. Melskens, R. Santbergen, O. Isabella, J. Schmitz, M. Lenes, J.-M. Luchies, W. M.M. Kessels, and I. Romijn, “Material properties of LPCVD processed n-type polysilicon passivating contacts and its application in PERPoly industrial bifacial solar cells,” *Energy Procedia*, vol. 124, pp. 635–642, 2017, doi: 10.1016/j.egypro.2017.09.250.
- [63] L. Tutsch, F. Feldmann, J. Polzin, C. Luderer, M. Bivour, A. Moldovan, J. Rentsch, and M. Hermle, “Implementing transparent conducting oxides by DC sputtering on ultrathin SiO_x/poly-Si passivating contacts,” *Solar Energy Materials and Solar Cells*, vol. 200, p. 109960, 2019, doi: 10.1016/j.solmat.2019.109960.

- [64] L. Tutsch, F. Feldmann, M. Bivour, W. Wolke, M. Hermle, and J. Rentsch, "Integrating transparent conductive oxides to improve the infra-red response of silicon solar cells with passivating rear contacts," in *SiliconPV 2018*, Lausanne, Switzerland, 2018.
- [65] P. Peng, A. Hu, A. P. Gerlich, G. Zou, L. Liu, and Y. N. Zhou, "Joining of silver nanomaterials at low temperatures: Processes, properties, and applications," *ACS applied materials & interfaces*, vol. 7, no. 23, pp. 12597–12618, 2015, doi: 10.1021/acsami.5b02134.
- [66] F. Cardarelli, *Materials Handbook: A Concise Desktop Reference*. London: Springer-Verlag, op. 2008.
- [67] P. Buffat and J.-P. Borel, "Size effect on the melting temperature of gold particles," *Phys. Rev. A*, vol. 13, no. 6, pp. 2287–2298, 1976, doi: 10.1103/PhysRevA.13.2287.
- [68] J. Perelaer, P. J. Smith, D. Mager, D. Soltman, S. K. Volkman, V. Subramanian, J. G. Korvink, and U. S. Schubert, "Printed electronics: The challenges involved in printing devices, interconnects, and contacts based on inorganic materials," *J. Mater. Chem.*, vol. 20, no. 39, p. 8446, 2010, doi: 10.1039/c0jm00264j.
- [69] A. Gautrein, C. Schmiga, M. Glatthaar, W. Tremel, and S. W. Glunz, "Nanometallic silver inks for metallization of ITO-coated silicon solar cells: Influence of organic components," in *29th European Photovoltaic Solar Energy Conference and Exhibition*, Amsterdam, The Netherlands, 2014, doi: 10.4229/EUPVSEC20142014-2CV.4.2.
- [70] H. E. Exner and E. Arzt, "Sintering processes," in *Physical Metallurgy*. Amsterdam: Elsevier, 1996, pp. 2627–2662.
- [71] J. R. Greer and R. A. Street, "Thermal cure effects on electrical performance of nanoparticle silver inks," *Acta Materialia*, vol. 55, no. 18, pp. 6345–6349, 2007, doi: 10.1016/j.actamat.2007.07.040.
- [72] D. Chen, L. Zhao, H. Diao, W. Zhang, G. Wang, and W. Wang, "Low-temperature sintering properties of the screen-printed silver paste for a-Si:H/c-Si heterojunction solar cells," *J Mater Sci: Mater Electron*, vol. 25, no. 6, pp. 2657–2664, 2014, doi: 10.1007/s10854-014-1925-z.

-
- [73] F. Braun, “Ueber die Stromleitung durch Schwefelmetalle,” *Ann. Phys. Chem.*, vol. 229, no. 12, pp. 556–563, 1875, doi: 10.1002/andp.18752291207.
- [74] W. Schottky, “Halbleitertheorie der Sperrschicht,” *Naturwissenschaften*, vol. 26, no. 52, p. 843, 1938, doi: 10.1007/bf01774216.
- [75] W. Schottky, “Zur Halbleitertheorie der Sperrschicht- und Spitzengleichrichter,” *Z. Physik*, vol. 113, 5-6, pp. 367–414, 1939, doi: 10.1007/bf01340116.
- [76] J. Bardeen, “Surface states and rectification at a metal semiconductor contact,” *Phys. Rev.*, vol. 71, no. 10, pp. 717–727, 1947, doi: 10.1103/PhysRev.71.717.
- [77] A. M. Cowley and S. M. Sze, “Surface states and barrier height of metal-semiconductor systems,” *Phys. Rev.*, vol. 36, no. 10, pp. 3212–3220, 1965, doi: 10.1063/1.1702952.
- [78] E. H. Rhoderick, “Metal-semiconductor contacts,” *IEEE Proc. I Solid State Electron. Devices UK*, vol. 129, no. 1, p. 1, 1982, doi: 10.1049/ip-i-1.1982.0001.
- [79] D. K. Schroder and D. L. Meier, “Solar cell contact resistance - a review,” *IEEE Trans. Electron Devices*, vol. 31, no. 5, pp. 637–647, 1984, doi: 10.1109/t-ed.1984.21583.
- [80] D. L. Meier and D. K. Schroder, “Contact resistance: Its measurement and relative importance to power loss in a solar cell,” *IEEE Trans. Electron Devices*, vol. 31, no. 5, pp. 647–653, 1984, doi: 10.1109/T-ED.1984.21584.
- [81] S. Werner, E. Lohmüller, A. Wolf, and F. Clement, “Extending the limits of screen-printed metallization of phosphorus- and boron-doped surfaces,” *Solar Energy Materials and Solar Cells*, vol. 158, pp. 37–42, 2016, doi: 10.1016/j.solmat.2016.05.064.
- [82] E. Lohmüller, S. Werner, R. Hoenig, J. Greulich, and F. Clement, “Impact of boron doping profiles on the specific contact resistance of screen printed Ag-Al contacts on silicon,” *Solar Energy Materials and Solar Cells*, vol. 142, pp. 2–11, 2015, doi: 10.1016/j.solmat.2015.04.039.

- [83] T. Söderström, P. Papet, and J. Ufheil, “Smart wire connection technology,” in *28th European Photovoltaic Solar Energy Conference and Exhibition*, Paris, France, 2013, doi: 10.4229/28thEUPVSEC2013-1CV.2.17.
- [84] A. Faes, M. Despeisse, J. Levrat, J. Champliand, N. Badel, M. Kiaee, T. Söderström, Y. Yao, R. Grischke, M. Gragert, J. Ufheil, P. Papet, B. Strahm, B. Cattaneo, J. Cattin, Y. Baumgartner, A. Hessler-Wyser, and C. Ballif, “SmartWire solar cell interconnection technology,” in *29th European Photovoltaic Solar Energy Conference and Exhibition*, Amsterdam, The Netherlands, 2014, doi: 10.4229/EUPVSEC20142014-5DO.16.3.
- [85] H. Kipphan, *Handbook of Print Media: Technologies and Production Methods*. Berlin: Springer electronic media, 2001.
- [86] A. Mette, “New concepts for front side metallization of industrial silicon solar cells,” Ph.D. dissertation, Albert-Ludwigs-Universität, Freiburg, 2007.
- [87] A. Dabirian, A. Lachowicz, J.-W. Schüttauf, B. Paviet-Salomon, M. Morales-Masis, A. Hessler-Wyser, M. Despeisse, and C. Ballif, “Metallization of Si heterojunction solar cells by nanosecond laser ablation and Ni-Cu plating,” *Solar Energy Materials and Solar Cells*, vol. 159, pp. 243–250, 2017, doi: 10.1016/j.solmat.2016.09.021.
- [88] D. Adachi, T. Terashita, T. Uto, J. L. Hernández, and K. Yamamoto, “Effects of SiO_x barrier layer prepared by plasma-enhanced chemical vapor deposition on improvement of long-term reliability and production cost for Cu-plated amorphous Si/crystalline Si heterojunction solar cells,” *Solar Energy Materials and Solar Cells*, vol. 163, pp. 204–209, 2017, doi: 10.1016/j.solmat.2016.12.029.
- [89] T. Hatt, S. Kluska, M. Yamin, J. Bartsch, and M. Glatthaar, “Native oxide barrier layer for selective electroplated metallization of silicon heterojunction solar cells,” *Sol. RRL*, vol. 3, no. 6, p. 1900006, 2019, doi: 10.1002/solr.201900006.
- [90] A. Lorenz, A. Münzer, M. Lehner, R. Greutmann, H. Brocker, H. Reinecke, and F. Clement, “High-throughput front and rear side metallization of silicon solar cells using rotary screen printing,” *Energy Procedia*, vol. 124, pp. 680–690, 2017, doi: 10.1016/j.egypro.2017.09.343.

-
- [91] A. Lorenz, M. Linse, H. Frintrup, M. Jeitler, A. Mette, M. Lehner, R. Greutmann, H. Brocker, M. König, d. Erath, and F. Clement, “Screen printed thick film metallization of silicon solar cells - recent developments and future perspectives,” in *35th European Photovoltaic Solar Energy Conference and Exhibition*, Brussels, Belgium, 2018, doi: 10.4229/35THEUPVSEC20182018-2DV.3.65.
- [92] M. Pospischil, T. Riebe, A. Jimenez, M. Kuchler, S. Tepner, T. Geipel, D. Ourinson, T. Fellmeth, M. Breitenbücher, T. Buck, M. Dhamrin, and F. Clement, “Applications of parallel dispensing in PV metallization,” in *8th Workshop on Metallization and Interconnection*, Konstanz, Germany, 2019.
- [93] D. Stüwe, D. Mager, D. Biro, and J. G. Korvink, “Inkjet technology for crystalline silicon photovoltaics,” *Advanced materials (Deerfield Beach, Fla.)*, vol. 27, no. 4, pp. 599–626, 2015, doi: 10.1002/adma.201403631.
- [94] J. Schube, T. Fellmeth, M. Jahn, R. Keding, and S. W. Glunz, “Inkjet- and FlexTrail- printing with low silver consumption for silicon heterojunction solar cells,” *Phys. Status Solidi RRL*, vol. 3, p. 1900186, 2019, doi: 10.1002/pssr.201900186.
- [95] J. Schube, T. Fellmeth, M. Jahn, R. Keding, and S. W. Glunz, “Advanced metallization with low silver consumption for silicon heterojunction solar cells,” in *8th Workshop on Metallization and Interconnection*, Konstanz, Germany, 2019.
- [96] L. Ney, S. Tepner, N. Wengenmeyr, M. Linse, A. Lorenz, S. Bechmann, R. Weber, M. Pospischil, and F. Clement, “Optimization of fine line screen printing using in-depth screen mesh analysis,” in *8th Workshop on Metallization and Interconnection*, Konstanz, Germany, 2019.
- [97] S. Tepner, L. Ney, M. Linse, A. Lorenz, M. Pospischil, and F. Clement, “Studying knotless screen patterns for fine-line screen printing of Si-solar cells,” *IEEE J. Photovoltaics*, vol. 10, no. 2, pp. 319–325, 2020, doi: 10.1109/JPHOTOV.2019.2959939.
- [98] S. Tepner, N. Wengenmeyr, L. Ney, M. Linse, M. Pospischil, and F. Clement, “Improving wall slip behavior of silver pastes on screen emulsions for fine line screen printing,” *Solar Energy Materials and Solar Cells*, vol. 200, p. 109969, 2019, doi: 10.1016/j.solmat.2019.109969.

- [99] F. Roca, G. Sinno, G. Di Francia, P. Proisini, G. Fameli, P. Grillo, A. Citarella, F. Pascarella, and D. Della Sala, "Process development of amorphous silicon/crystalline silicon solar cells," *Solar Energy Materials and Solar Cells*, vol. 48, 1-4, pp. 15–24, 1997, doi: 10.1016/S0927-0248(97)00063-9.
- [100] R. Faddoul, N. Reverdy-Bruas, and A. Blayo, "Formulation and screen printing of water based conductive flake silver pastes onto green ceramic tapes for electronic applications," *Materials Science and Engineering: B*, vol. 177, no. 13, pp. 1053–1066, 2012, doi: 10.1016/j.mseb.2012.05.015.
- [101] S. LaPlante and S. Sylla, "Investigating different polymeric systems for heterojunction screen printing technology," in *36th European Photovoltaic Solar Energy Conference and Exhibition*, Marseille, France, 2019.
- [102] A. Descoedres, C. Allebé, N. Badel, L. Barraud, J. Champliaud, G. Christmann, F. Debrot, A. Faes, J. Geissbühler, J. Horzel, A. Lachowicz, J. Levrat, S. Martin de Nicolas, S. Nicolay, B. Paviet-Salomon, L.-L. Senaud, C. Ballif, and M. Despeisse, "Low-temperature processes for passivation and metallization of high-efficiency crystalline silicon solar cells," *Solar Energy*, 2018, doi: 10.1016/j.solener.2018.01.074.
- [103] S. Tepner, L. Ney, M. Linse, A. Lorenz, M. Pospischil, K. Masuri, and F. Clement, "Screen pattern simulation for an improved front-side Ag-electrode metallization of Si-solar cells," *Progress in Photovoltaics: Research and Applications*, 2020, doi: <https://doi.org/10.1002/pip.3313>.
- [104] J. Hermans, P. Papet, K. Pacheco, Y. Yao, W. J M Brok, and B. Strahm, "Inkjet printing of Ag nanoparticle inks for heterojunction solar cell metallization," in *SNEC PV Power Expo.*, Shanghai, China, 2015.
- [105] G. Cummins and M. P.Y. Desmulliez, "Inkjet printing of conductive materials: A review," *Circuit World*, vol. 38, no. 4, pp. 193–213, 2012, doi: 10.1108/03056121211280413.
- [106] G. C. Che, R. P. Mertens, R. van Overstraeten, and L. Frisson, "Thick-film metallization for solar cell applications," *IEEE Trans. Electron Devices*, vol. 31, no. 5, pp. 602–609, 1984, doi: 10.1109/T-ED.1984.21575.
- [107] D. Ourinson, G. Emanuel, A. Csordás, G. Dammaß, H. Müller, C. Sternkiker, F. Clement, and S. W. Glunz, "In-situ wafer temperature measurement during firing process via inline infrared thermography," in

8th Workshop on Metallization and Interconnection, Konstanz, Germany, 2019.

- [108] J. Wodara and H. Herold, *Ultraschallfügen und -trennen*. Düsseldorf: DVS-Verl., 2004.
- [109] S. Krüger, G. Wagner, and D. Eifler, “Ultrasonic welding of metal/composite joints,” *Adv. Eng. Mater.*, vol. 6, no. 3, pp. 157–159, 2004, doi: 10.1002/adem.200300539.
- [110] K. L. Kelly, E. Coronado, L. L. Zhao, and G. C. Schatz, “The optical properties of metal nanoparticles: The influence of size, shape, and dielectric environment,” *J. Phys. Chem. B*, vol. 107, no. 3, pp. 668–677, 2003, doi: 10.1021/jp026731y.
- [111] J. West, M. Carter, S. Smith, and J. Sears, “Photonic sintering of silver nanoparticles: Comparison of experiment and theory,” in *Sintering - Methods and Products*, V. Shatokha, Ed.: InTech, 2012.
- [112] D. K. Schroder, *Semiconductor material and device characterization*. New Jersey: IEEE Press Wiley-Interscience, 2006.
- [113] M. Hösel and F. C. Krebs, “Large-scale roll-to-roll photonic sintering of flexo printed silver nanoparticle electrodes,” *J. Mater. Chem.*, vol. 22, no. 31, p. 15683, 2012, doi: 10.1039/C2JM32977H.
- [114] S. Wünscher, R. Abbel, J. Perelaer, and U. S. Schubert, “Progress of alternative sintering approaches of inkjet-printed metal inks and their application for manufacturing of flexible electronic devices,” *J. Mater. Chem. C*, vol. 2, no. 48, pp. 10232–10261, 2014, doi: 10.1039/c4tc01820f.
- [115] S.-H. Park and H.-S. Kim, “Flash light sintering of nickel nanoparticles for printed electronics,” *Thin Solid Films*, vol. 550, pp. 575–581, 2014, doi: 10.1016/j.tsf.2013.11.075.
- [116] K. A. Schroder, “Mechanisms of photonic curingTM: processing high temperature films on low temperature substrates,” *Nanotechnology*, vol. 2, pp. 220–223, 2011.
- [117] T. Druffel, R. Dharmadasa, B. W. Lavery, and K. Ankireddy, “Intense pulsed light processing for photovoltaic manufacturing,” *Solar Energy Materials and Solar Cells*, vol. 174, pp. 359–369, 2018, doi: 10.1016/j.solmat.2017.09.010.

- [118] H.-J. Hwang, D.-J. Kim, Y.-R. Jang, Y.-T. Hwang, I.-H. Jung, and H.-S. Kim, “Multi-pulsed flash light sintering of copper nanoparticle pastes on silicon wafer for highly-conductive copper electrodes in crystalline silicon solar cells,” *Applied Surface Science*, vol. 462, pp. 378–386, 2018, doi: 10.1016/j.apsusc.2018.08.098.
- [119] H. Kim and J. Kim, “Heterojunction solar cell and manufacturing method thereof,” US20190198693A1, US 16/289 310, 2019.
- [120] J. Schube, L. Tutsch, T. Fellmeth, F. Feldmann, M. Weil, A. Harter, J.-I. Polzin, M. Bivour, R. Keding, and S. W. Glunz, “Intense pulsed light processing of silicon solar cells with passivating contacts,” *Solar Energy Materials and Solar Cells*, vol. 216, p. 110711, 2020, doi: <https://doi.org/10.1016/j.solmat.2020.110711>.
- [121] A. Cuevas and D. Macdonald, “Measuring and interpreting the lifetime of silicon wafers,” *Solar Energy*, vol. 76, 1-3, pp. 255–262, 2004, doi: 10.1016/j.solener.2003.07.033.
- [122] H. Nagel, C. Berge, and A. G. Aberle, “Generalized analysis of quasi-steady-state and quasi-transient measurements of carrier lifetimes in semiconductors,” *J. Appl. Phys.*, vol. 86, no. 11, pp. 6218–6221, 1999, doi: 10.1063/1.371633.
- [123] R. A. Sinton and A. Cuevas, “Contactless determination of current-voltage characteristics and minority-carrier lifetimes in semiconductors from quasi-steady-state photoconductance data,” *Appl. Phys. Lett.*, vol. 69, no. 17, pp. 2510–2512, 1996, doi: 10.1063/1.117723.
- [124] D. Verma and A. Fahr, “Confocal laser scanning microscopy,” in *Percutaneous Penetration Enhancers*, E. Smith and H. Maibach, Eds. Boca Raton: CRC Press, 2005, pp. 335–357.
- [125] A. A. Brand, F. Meyer, J.-F. Nekarda, and R. Preu, “Reduction of picosecond laser ablation threshold and damage via nanosecond pre-pulse for removal of dielectric layers on silicon solar cells,” *Appl. Phys. A*, vol. 117, no. 1, pp. 237–241, 2014, doi: 10.1007/s00339-014-8444-x.
- [126] T. Strauch, M. Demant, A. Lorenz, J. Haunschild, and S. Rein, “Two image processing tools to analyse alkaline texture and contact finger geometry in microscope images,” in *29th European Photovoltaic Solar Ener-*

-
- gy Conference and Exhibition, Amsterdam, The Netherlands, 2014, doi: 10.4229/EUPVSEC20142014-2BV.8.12.
- [127] J. I. Goldstein, *Scanning Electron Microscopy and X-Ray Microanalysis*. New York: Springer, 2009.
- [128] H. Takahashi, A. Sato, M. Takakura, N. Mori, J. Boerder, W. Knoll, and J. Critchell, "A new method of surface preparation for high spatial resolution EPMA/SEM with an argon ion beam," *Microchim Acta*, vol. 155, 1-2, pp. 295–300, 2006, doi: 10.1007/s00604-006-0559-0.
- [129] H. Berger, "Contact resistance on diffused resistors," in *1969 IEEE International Solid-State Circuits Conference. Digest of Technical Papers*, Philadelphia, USA, 1969, pp. 160–161.
- [130] H. Murrmann and D. Widmann, "Messung des Übergangswiderstandes zwischen Metall und Diffusionsschicht in Si-Planarelementen," *Solid-State Electronics*, vol. 12, no. 11, pp. 879–886, 1969, doi: 10.1016/0038-1101(69)90045-8.
- [131] W. Shockley, A. Götzberger, and R. M. Scarlett, *Theory and Experiments on Current Transfer from Alloyed Contact to Diffused Layer*. Appendix B of "Research and investigation of inverse epitaxial UHF power transistors," Shockley Res. Lab., Palo Alto, USA, 1964.
- [132] H. El Omari, J. P. Boyeaux, and A. Laugier, "TLM extension for the study of screen printing contacts on multicrystalline silicon," *Eur. Phys. J. AP*, vol. 2, no. 1, pp. 87–92, 1998, doi: 10.1051/epjap:1998160.
- [133] S. Eidelloth and R. Brendel, "Analytical theory for extracting specific contact resistances of thick samples from the transmission line method," *IEEE Electron Device Lett.*, vol. 35, no. 1, pp. 9–11, 2014, doi: 10.1109/led.2013.2290602.
- [134] M. Hörteis, "Fine-line printed contacts on crystalline silicon solar cells," Ph.D. dissertation, Universität Konstanz, Konstanz, 2009.
- [135] H. Murrmann and D. Widmann, "Current crowding on metal contacts to planar devices," *IEEE Trans. Electron Devices*, vol. 16, no. 12, pp. 1022–1024, 1969, doi: 10.1109/T-ED.1969.16904.
- [136] A. Fell, "A free and fast three-dimensional/two-dimensional solar cell simulator featuring conductive boundary and quasi-neutrality approxima-

- tions,” *IEEE Trans. Electron Devices*, vol. 60, no. 2, pp. 733–738, 2013, doi: 10.1109/TED.2012.2231415.
- [137] P. R. i. Cabarrocas, “Deposition of intrinsic, phosphorus-doped, and boron-doped hydrogenated amorphous silicon films at 50°C,” *Appl. Phys. Lett.*, vol. 65, no. 13, pp. 1674–1676, 1994, doi: 10.1063/1.112882.
- [138] S.-H. Park, W.-H. Chung, and H.-S. Kim, “Temperature changes of copper nanoparticle ink during flash light sintering,” *Journal of Materials Processing Technology*, vol. 214, no. 11, pp. 2730–2738, 2014, doi: 10.1016/j.jmatprotec.2014.06.007.
- [139] O. Breitenstein, W. Warta, and M. Langenkamp, *Lock-in Thermography*. Berlin, Heidelberg: Springer, 2010.
- [140] A. Cezairliyan and F. Righini, “Issues in high-speed pyrometry,” *Metrologia*, vol. 33, no. 4, pp. 299–306, 1996, doi: 10.1088/0026-1394/33/4/3.
- [141] G. Gaussorgues, M.-H. Carpentier, and B. L. Smith, *Infrared Thermography*. Dordrecht: Springer Netherlands, 1994.
- [142] D. Reinwand, B. King, J. Schube, F. Madon, R. Einhaus, and D. Kray, “Lab-scale manufacturing of medium-sized N.I.C.E.TM modules with high-efficiency bifacial silicon heterojunction solar cells,” in *8th Workshop on Metallization and Interconnection*, Konstanz, Germany, 2019.
- [143] A. Faes, A. Lachowicz, A. Bettinelli, P.-J. Ribeyron, J.-F. Lerat, D. Munoz, J. Geissbühler, H.-Y. Li, C. Ballif, and M. Despeisse, “Metallization and interconnection for high-efficiency bifacial silicon heterojunction solar cells and modules,” *Photovoltaics Bulletin*, no. 41, pp. 1–5, 2018.
- [144] K. Nakamura, K. Muramatsu, A. Tanaka, and Y. Ohshita, “Newly developed Ag coated Cu paste for Si hetero-junction solar cell,” in *35th European Photovoltaic Solar Energy Conference and Exhibition*, Brussels, Belgium, 2018, doi: 10.4229/35thEUPVSEC20182018-2AV.3.37.
- [145] T. Fellmeth, F. Clement, and D. Biro, “Analytical modeling of industrial-related silicon solar cells,” *IEEE J. Photovoltaics*, vol. 4, no. 1, pp. 504–513, 2014, doi: 10.1109/JPHOTOV.2013.2281105.
- [146] A. Wolf, D. Biro, J. Nekarda, S. Stumpp, A. Kimmerle, S. Mack, and R. Preu, “Comprehensive analytical model for locally contacted rear surface passivated solar cells,” *J. Appl. Phys.*, vol. 108, no. 12, p. 124510, 2010, doi: 10.1063/1.3506706.

-
- [147] *IEC 60904-3:2019: Photovoltaic Devices - Part 3: Measurement Principles for Terrestrial Photovoltaic (PV) Solar Devices with Reference Spectral Irradiance Data.*
- [148] N. Bassi, C. Clerc, Y. Pelet, J. Hiller, V. Fakhfour, C. Droz, M. Despeisse, J. Levrat, A. Faes, D. Bätzner, and P. Papet, "GridTOUCH: Innovative solution for accurate IV measurement of busbarless cells in production and laboratory environments," in *29th European Photovoltaic Solar Energy Conference and Exhibition*, Amsterdam, The Netherlands, 2014, 2014, doi: 10.4229/EUPVSEC20142014-2BV.8.24.
- [149] M. Rauer, K. Kordelos, A. Krieg, and J. Hohl-Ebinger, "Accurate measurements of busbarless silicon solar cells," in *8th Workshop on Metallization and Interconnection*, Konstanz, Germany, 2019.
- [150] E. Saint-Sernin, R. Einhaus, K. Bamberg, and P. Panno, "Industrialisation of Apollon Solar's NICE module technology," in *23rd European Photovoltaic Solar Energy Conference and Exhibition*, Valencia, Spain, 2008, doi: 10.4229/23rdEUPVSEC2008-4AV.3.15.
- [151] D. Reinwand, D. Pysch, N. Bay, J. Burschik, H. H. Kuehnlein, F. Madon, R. Einhaus, A. Brand, V. Arya, B. Smith, D. Richter, and D. Kray, "All copper NICE modules," in *2018 IEEE 7th World Conference on Photovoltaic Energy Conversion*, Waikoloa, USA, 2018, pp. 628–631.
- [152] *IEC 61215-1-1:2016: Terrestrial Photovoltaic (PV) Modules - Design Qualification and Type Approval - Part 1-1: Special Requirements for Testing of Crystalline Silicon Photovoltaic (PV) Modules.*
- [153] F. Clement, "Die Metal-wrap-through-Solarzelle. Entwicklung und Charakterisierung," Ph.D. dissertation, Albert-Ludwigs-Universität, Freiburg, 2009.
- [154] A. Faes, L. Curvat, H. Li, J. Levrat, J. Champiaud, K. Thomas, J. Escarre, N. Badel, B. Paviet-Salomon, J. Geissbuhler, C. Allebe, L. Barraud, F. Debrot, A. Descoeurdes, A. Lachowicz, J. Horzel, L.-L. Senaud, L.-E. Perret-Aebi, C. Ballif, and M. Despeisse, "Direct contact to TCO with SmartWire connection technology," in *2018 IEEE 7th World Conference on Photovoltaic Energy Conversion*, Waikoloa, USA, 2018.
- [155] J. Schube, L. Tutsch, T. Fellmeth, F. Bivour, F. Feldmann, T. Hatt, F. Maier, R. Keding, F. Clement, and S. W. Glunz, "Low-resistivity screen-

- printed contacts on indium tin oxide layers for silicon solar cells with passivating contacts,” *IEEE J. Photovoltaics*, vol. 8, no. 5, pp. 1208-1214, 2018.
- [156] J. Schube, M. Weil, T. Fellmeth, R. Keding, and S. W. Glunz, “Intense pulsed light meets the metallization of silicon heterojunction solar cells,” in *2019 IEEE 46th Photovoltaic Specialists Conference*, Chicago, USA, 2019, pp. 3231–3237.
- [157] M. Weil, “Entwicklung eines photonischen Sinterprozesses zur Kontaktierung von Silicium Heterojunction Solarzellen,” Master thesis, Hochschule Offenburg, Offenburg, 2019.
- [158] A. Harter, “TOPCon: Development of polysilicon passivated contacts using slow furnace anneal and fast firing oven anneal,” Master thesis, Albert-Ludwigs-Universität, Freiburg, 2020.
- [159] J. Geissbühler, A. Faes, A. Lachowicz, C. Ballif, and M. Despeisse, “Metallization techniques and interconnection schemes for high-efficiency silicon heterojunction photovoltaics,” *Phot. International*, no. 37, 2017.
- [160] R.C.G. Naber, M. Lenes, A.H.G. Vlooswijk, J.R.M. Luchies, J. Wang, F. Zheng, J. Lin, and Z. Zhang, “n-PERT solar cells with passivated contact technology based on LPCVD polysilicon and fire-through contact metallization,” in *32nd European Photovoltaic Solar Energy Conference and Exhibition*, Munich, Germany, 2016, doi: 10.4229/EUPVSEC20162016-2CO.3.2.
- [161] G. W. H. Höhne, W. F. Hemminger, and H.-J. Flammersheim, *Differential Scanning Calorimetry*. Berlin, Heidelberg: Springer, 2003.
- [162] J. van Humbeeck, “Simultaneous thermal analysis,” in *Handbook of Thermal Analysis and Calorimetry, Principles and Practice*. Amsterdam: Elsevier, 1998, pp. 497–508.
- [163] L. J. van der PAUW, “A method of measuring specific resistivity and Hall effect of discs of arbitrary shape,” in *Semiconductor Devices: Pioneering Papers*, S. M. Sze, Ed. Singapore: World Scientific, 1991, pp. 174–182.
- [164] D. Erath, M. Pospischil, R. Keding, M. Jahn, I. Lacmago Lontchi, A. Lorenz, and F. Clement, “Comparison of innovative metallization approaches for silicon heterojunction solar cells,” *Energy Procedia*, vol. 124, pp. 869–874, 2017, doi: 10.1016/j.egypro.2017.09.245.

-
- [165] L. Vitos, A. V. Ruban, H. L. Skriver, and J. Kollár, “The surface energy of metals,” *Surface Science*, vol. 411, 1-2, pp. 186–202, 1998, doi: 10.1016/s0039-6028(98)00363-x.
- [166] H. L. Skriver and N. M. Rosengaard, “Surface energy and work function of elemental metals,” *Phys. Rev. B*, vol. 46, no. 11, pp. 7157–7168, 1992, doi: 10.1103/PhysRevB.46.7157.
- [167] J. S. Kim, R. H. Friend, and F. Cacialli, “Surface energy and polarity of treated indium-tin-oxide anodes for polymer light-emitting diodes studied by contact-angle measurements,” *J. Appl. Phys.*, vol. 86, no. 5, pp. 2774–2778, 1999, doi: 10.1063/1.371124.
- [168] Z. Zhong, S. Yin, C. Liu, Y. Zhong, W. Zhang, D. Shi, and C.’a. Wang, “Surface energy for electroluminescent polymers and indium-tin-oxide,” *Applied Surface Science*, vol. 207, 1-4, pp. 183–189, 2003, doi: 10.1016/S0169-4332(02)01328-4.
- [169] O. V. Penkov, M. Khadem, W.-S. Lim, and D.-E. Kim, “A review of recent applications of atmospheric pressure plasma jets for materials processing,” *J. Coat. Technol. Res.*, vol. 12, no. 2, pp. 225–235, 2015, doi: 10.1007/s11998-014-9638-z.
- [170] E. S. Lee, J. H. Choi, and H. K. Baik, “Surface cleaning of indium tin oxide by atmospheric air plasma treatment with the steady-state airflow for organic light emitting diodes,” *Surface and Coatings Technology*, vol. 201, 9-11, pp. 4973–4978, 2007, doi: 10.1016/j.surfcoat.2006.07.202.
- [171] T. Homola, J. Matoušek, V. Medvecká, A. Zahoranová, M. Kormunda, D. Kováčik, and M. Černák, “Atmospheric pressure diffuse plasma in ambient air for ITO surface cleaning,” *Applied Surface Science*, vol. 258, no. 18, pp. 7135–7139, 2012, doi: 10.1016/j.apsusc.2012.03.188.
- [172] T. Trupke, R. A. Bardos, M. C. Schubert, and W. Warta, “Photoluminescence imaging of silicon wafers,” *Appl. Phys. Lett.*, vol. 89, no. 4, p. 44107, 2006, doi: 10.1063/1.2234747.
- [173] A. D. MacCalman, H. Vieira, and T. Lucas, “Second-order nearly orthogonal Latin hypercubes for exploring stochastic simulations,” *Journal of Simulation*, vol. 11, no. 2, pp. 137–150, 2017, doi: 10.1057/jos.2016.8.
- [174] S. Wasmer, A. A. Brand, and J. M. Greulich, “Metamodeling of numerical device simulations to rapidly create efficiency optimization roadmaps of

- monocrystalline silicon PERC cells,” *Energy Procedia*, vol. 124, pp. 207–214, 2017, doi: 10.1016/j.egypro.2017.09.312.
- [175] E. Kobayashi, S. de Wolf, J. Levrat, G. Christmann, A. Descoedres, S. Nicolay, M. Despeisse, Y. Watabe, and C. Ballif, “Light-induced performance increase of silicon heterojunction solar cells,” *Appl. Phys. Lett.*, vol. 109, no. 15, p. 153503, 2016, doi: 10.1063/1.4964835.
- [176] E. Kobayashi, S. de Wolf, J. Levrat, A. Descoedres, M. Despeisse, F.-J. Haug, and C. Ballif, “Increasing the efficiency of silicon heterojunction solar cells and modules by light soaking,” *Solar Energy Materials and Solar Cells*, vol. 173, pp. 43–49, 2017, doi: 10.1016/j.solmat.2017.06.023.
- [177] D. L. Staebler and C. R. Wronski, “Reversible conductivity changes in discharge-produced amorphous Si,” *Journal of Non-Crystalline Solids*, vol. 31, no. 4, pp. 292–294, 1977, doi: 10.1063/1.89674.
- [178] S. de Wolf and M. Kondo, “Boron-doped a-Si:H/c-Si interface passivation: Degradation mechanism,” *Appl. Phys. Lett.*, vol. 91, no. 11, p. 112109, 2007, doi: 10.1063/1.2783972.
- [179] A. W. Blakers, “Shading losses of solar-cell metal grids,” *J. Appl. Phys.*, vol. 71, no. 10, pp. 5237–5241, 1992, doi: 10.1063/1.350580.
- [180] M. Wimmer, M. Bär, D. Gerlach, R. G. Wilks, S. Scherf, C. Lupulescu, F. Ruske, R. Félix, J. Hüpkens, G. Gavrila, M. Gorgoi, K. Lips, W. Eberhardt, and B. Rech, “Hard x-ray photoelectron spectroscopy study of the buried Si/ZnO thin-film solar cell interface: Direct evidence for the formation of Si–O at the expense of Zn–O bonds,” *Appl. Phys. Lett.*, vol. 99, no. 15, p. 152104, 2011, doi: 10.1063/1.3644084.
- [181] S. Nold, “Techno-ökonomische Bewertung neuer Produktionstechnologien entlang der Photovoltaik-Wertschöpfungskette,” Ph.D. dissertation, Albert-Ludwigs-Universität, Freiburg, 2018.
- [182] Fujifilm, *UVSCALE*. Online Available: <https://www.fujifilm.com>. Accessed on: June 24th, 2020.
- [183] J. Haschke, R. Lemerle, B. Aissa, A. Abdallah, M. Kivambe, M. Boccard, and C. Ballif, “Annealing of silicon heterojunction solar cells: Interplay of solar cell and indium tin oxide properties,” *IEEE J. Photovoltaics*, vol. 9, no. 5, pp. 1202–1207, 2019, doi: 10.1109/JPHOTOV.2019.2924389.

List of symbols

Symbol	Description	Unit
a	Distance between finger and sample edge	mm
A^*	Richardson constant	
A_f	Finger cross-sectional area	μm^2
AR	Aspect ratio	
A_{ultra}	Ultrasound displacement amplitude	μm
c	Velocity of light	$\text{m}\cdot\text{s}^{-1}$
c_{Si}	Specific heat capacity of silicon	$\text{J}\cdot\text{kg}^{-1}\cdot\text{K}^{-1}$
$D(E)$	Energy-dependent density of charge carrier states	cm^{-3}
D_n, D_p	Diffusion parameters for electrons and holes	$\text{cm}^{-2}\cdot\text{s}^{-1}$
d_{wafer}	Thickness of semiconductor material/wafer	μm
E	Energy	J
E_{00}	Characteristic energy for metal semiconductor interface	eV
E_c, E_v	Conduction and valence band edge	eV
E_F	Fermi energy	eV
$E_{F,c}, E_{F,v}$	Fermi level for electrons and holes	eV
$E_{F,l}, E_{F,r}$	Fermi energy at the left and right terminal	eV

List of symbols

Symbol	Description	Unit
E_g	Band gap	eV
E_{rad}	Radiant exposure	$\text{J}\cdot\text{cm}^{-2}$
$E_{\text{surface,Ag}}$ $E_{\text{surface,ITO}}$	Surface energy of silver and ITO	$\text{J}\cdot\text{m}^{-2}$
E_{ultra}	Energy applied by means of ultrasound	J
$f(E)$	Probability distribution	
f_{abs}	Absorption fraction	
FF	Fill factor	%
FF_0	Ideal fill factor	%
f_{pulse}	Intense pulsed light pulse frequency	Hz
f_{ultra}	Ultrasonic frequency	kHz
G	Generation rate	$\text{cm}^{-3}\cdot\text{s}^{-1}$
g	Geometry factor	
h	Planck constant	$\text{J}\cdot\text{s}$
h_f	Finger height	μm
I_0	Applied current	mA
I_{SC}	Short-circuit current	mA
iV_{OC}	Implied open-circuit voltage	mV
$iV_{\text{OC,after}}$	Implied open-circuit voltage after process	mV

Symbol	Description	Unit
$iV_{OC, \text{before}}$	Implied open-circuit voltage before process	mV
j	Electrical current density	$\text{mA} \cdot \text{cm}^{-2}$
j_0	Dark saturation current density	$\text{mA} \cdot \text{cm}^{-2}$
j_{01}, j_{02}	Dark saturation current density of diode one and two	$\text{mA} \cdot \text{cm}^{-2}$
j_{mpp}	Current density at maximum power point	$\text{mA} \cdot \text{cm}^{-2}$
j_n, j_p	Electron and hole current density	$\text{mA} \cdot \text{cm}^{-2}$
j_{ph}	Photo-generated current density	$\text{mA} \cdot \text{cm}^{-2}$
j_{SC}	Short-circuit current density	$\text{mA} \cdot \text{cm}^{-2}$
k	Wave vector	cm^{-1}
k_B	Boltzmann constant	$\text{J} \cdot \text{K}^{-1}$
L	Width of test structure	mm
l_f	Finger length	μm
L_T	Transfer length	μm
m_0	Electron rest mass	g
m_n^*, m_p^*	Effective mass of electrons and holes	g
m_{sample}	Sample mass	g
M_λ	Specific irradiation of a black body	$\text{W} \cdot \text{cm}^{-3}$
n	Density of electrons	cm^{-3}

List of symbols

Symbol	Description	Unit
n_1, n_2	Ideality factors of diode one and two	
N_c, N_v	Effective density of states in the conduction and valence band	cm^{-3}
N_D	Doping concentration	cm^{-3}
n_D, n_A	Density of donors and acceptors	cm^{-3}
N_e	Charge carrier density	cm^{-3}
n_i	Intrinsic density	cm^{-3}
n_{pass}	Number of passes in inkjet printing	
n_{pulse}	Number or applied Intense Pulsed Light pulses	
N_{ph}	Incident flux of photons	$\text{cm}^{-2}\text{s}^{-1}$
n_x	Ideality factor	
p	Density of holes	cm^{-3}
p_c	Power density	$\text{mW}\cdot\text{cm}^{-2}$
pFF	Pseudo fill factor	%
p_{mpp}	Power density at maximum power point	$\text{mW}\cdot\text{cm}^{-2}$
P_{mpp}	Maximum power point	W
$P_{\text{out}}, P_{\text{in}}$	Output and input power	W
p_{TLM}	Contact distance in TLM pattern	mm
P_{ultra}	Ultrasonic power	W

Symbol	Description	Unit
q	Elementary charge	C
\mathbf{r}	Position vector	cm
R	Recombination rate	$\text{cm}^{-3} \cdot \text{s}^{-1}$
$R_{1,2}$	Resistance between contact pad one and two	Ω
R_c	Contact resistance	Ω
R_e	End resistance	Ω
R_f	Absolute finger resistance	Ω
r_f	Normalized finger resistance	$\Omega \cdot \text{cm}^{-1}$
$r_{f,\text{eff}}$	Effective normalized finger resistance	$\Omega \cdot \text{cm}^{-1}$
R_i	Reflectance	%
R_{ITO}	Resistance of ITO layer	Ω
R_{layer}	Resistance of layer (system)	Ω
R_p	Shunt resistance	$\Omega \cdot \text{cm}^2$
R_s	Series resistance	$\Omega \cdot \text{cm}^2$
R_{SH}	Sheet resistance	Ω/sq
$R_{\text{SH,IO:Zr}}$	Sheet resistance of zirconium-doped indium oxide layer	Ω/sq
$R_{\text{SH,ITO}}$	Sheet resistance of indium tin oxide layer	Ω/sq
$R_{\text{SH,metal}}$	Sheet resistance of metal finger	Ω/sq

List of symbols

Symbol	Description	Unit
$R_{\text{SH,TCO}}$	Sheet resistance of transparent conductive oxide	Ω/sq
R_{sk}	Sheet resistance underneath metal electrode	Ω/sq
R_{TLM}	Resistance between two fingers of a TLM pattern	Ω
S_{eff}	Effective surface recombination velocity	$\text{cm}\cdot\text{s}^{-1}$
t	Time	s
T	Temperature	$^{\circ}\text{C}$
$t_{\text{annealing}}$	Annealing time	min
$T_{\text{annealing}}$	Annealing temperature	$^{\circ}\text{C}$
t_{flash}	Duration of the flash used in lifetime measurements	ms
T_i	Transmission	%
$T_{\text{m,corr}}$	Measured and corrected temperature	$^{\circ}\text{C}$
$T_{\text{peak,c}}$	Calculated peak temperature	$^{\circ}\text{C}$
$T_{\text{peak,m}}$	Measured peak temperature	$^{\circ}\text{C}$
$T_{\text{peak,m,corr}}$	Measured and corrected peak temperature	$^{\circ}\text{C}$
t_{pulse}	Intense pulsed light pulse time	ms
T_{room}	Room temperature	$^{\circ}\text{C}$
T_{sample}	Sample temperature	$^{\circ}\text{C}$

Symbol	Description	Unit
t_{ultra}	Duration of ultrasound application	s
U	Measurement voltage	mV
$u(\mathbf{r})$	Periodic function	$\text{cm}^{-3/2}$
U_{lamp}	Intense pulsed light lamp voltage	V
V	Voltage of a solar cell	mV
v_0	Normalized voltage	mV
V_{mpp}	Voltage at maximum power point	mV
V_{OC}	Open-circuit voltage	mV
w_{f}	Finger width	μm
$w_{\text{f,set}}$	Set finger width	μm
$\eta_{\text{n}}, \eta_{\text{p}}$	Electrochemical potentials for electrons and holes	eV
$\psi(\mathbf{r})$	Electron wave function	$\text{cm}^{-3/2}$
ΔE_{rad}	Offset in radiant exposure	$\text{J}\cdot\text{cm}^{-2}$
ΔiV_{OC}	Change in implied open-circuit voltage	mV
Δn	Excess electron density	cm^{-3}
Δp	Excess hole density	cm^{-3}
ΔT_{peak}	Offset in peak temperature	$^{\circ}\text{C}$
$\Delta \eta_{\text{sim}}$	Simulated change in conversion efficiency	%

List of symbols

Symbol	Description	Unit
Φ	Radiant flux density	$\text{kW}\cdot\text{cm}^{-2}$
Φ_λ	Spectral flux density	$\text{kW}\cdot\text{cm}^{-2}\cdot\text{nm}^{-1}$
\mathcal{I}_{PL}	Photoluminescence intensity	
Ψ_s	Electron affinity	eV
α	Absorption probability	
χ	Constant of proportionality	
ε	Emissivity	
ϕ_B	Schottky barrier	eV
ϕ_m	Metal work function	eV
γ	Angle under which thermal radiation is transmitted	$^\circ$
η	Conversion efficiency	%
φ	Electrical potential	eV
λ	Wavelength	nm
μ_n, μ_p	Electron and hole mobility	$\text{m}^2\cdot\text{V}^{-1}\cdot\text{s}^{-1}$
ν	Frequency	Hz
$\rho_{\text{a-Si(p)}}$	Electrical resistivity of <i>p</i> -type amorphous silicon	$\Omega\cdot\text{cm}$
ρ_{base}	Base resistivity	$\Omega\cdot\text{cm}$

Symbol	Description	Unit
ρ_c	Contact resistivity	$\text{m}\Omega \cdot \text{cm}^2$
$\rho_{c,\text{stack}}$	Total contact resistivity of the <i>c</i> -Si/SiO _x /poly-SiC _x /ITO/silver stack	$\text{m}\Omega \cdot \text{cm}^2$
ρ_f	Electrical finger resistivity	$\mu\Omega \cdot \text{cm}$
σ	Electrical conductivity	$(\mu\Omega \cdot \text{cm})^{-1}$
τ_{Auger}	Auger charge carrier lifetime	s
$\tau_{b,\text{SRH}}$	Shockley-Read-Hall charge carrier lifetime	s
τ_{eff}	Effective lifetime	s
τ_{rad}	Radiative charge carrier lifetime	s
ξ	Work function	eV

List of abbreviations

Abbreviation	Meaning
Ag	Silver
Al	Aluminum
Al-BSF	Aluminum Back Surface Field
AlO _x	Aluminum oxide
ARC	Anti reflection coating
As	Arsenic
<i>a</i> -Si, <i>a</i> -Si:H	Amorphous and hydrogenated amorphous silicon
B	Boron
BSC	Both-sides-contacted
CAPEX	Capital expenditure
CB	Conduction band
CLSM	Confocal laser scanning microscopy
COO	Cost of ownership
<i>c</i> -Si	Crystalline silicon
CTM	Cell-to-module
Cu	Copper
EDX	Energy dispersive X-ray spectroscopy

List of abbreviations

Abbreviation	Meaning
EQE	External quantum efficiency
EVA	Ethylene-vinyl acetate
FE	Field emission
IBC	Interdigitated back contact
In	Indium
InGaAs	Indium gallium arsenide
IO:Zr	Zirconium-doped indium oxide
IPCC	Intergovernmental Panel on Climate Change
IPL	Intense pulsed light
IQE	Internal quantum efficiency
ITO	Indium tin oxide
LPCVD	Low-pressure chemical vapor deposition
LS	Light soaking
NICE	New Industrial Solar Cell Encapsulation
P	Phosphorus
Pd	Palladium
PECVD	Plasma-enhanced chemical vapor deposition
PERC	Passivated Emitter and Rear Cell
PL	Photoluminescence

Abbreviation	Meaning
<i>poly</i> -Si	Polycrystalline silicon
<i>poly</i> -SiC _x	Polycrystalline silicon carbide
PV	Photovoltaics
QE	Quantum efficiency
SEM	Scanning electron microscopy
SHJ	Silicon heterojunction
Si	Silicon
SiN _x	Silicon nitride
SiO _x	Silicon oxide
SRH	Shockley Read Hall
STC	Standard testing conditions
SWCT	Smart Wire Interconnection Technology
TCO	Transparent conductive oxide
TE	Thermionic emission
TFE	Thermionic field emission
TG-DSC	Thermogravimetric-differential scanning calorimetry
Ti	Tin
TLM	Transfer length method
TOPCon	Tunnel oxide passivating contact

List of abbreviations

Abbreviation	Meaning
TPO	Thermoplastic polyolefin
UV	Ultraviolet
VB	Valence band

Publications

Journal contributions

First author

J. Schube, L. Tutsch, T. Fellmeth, M. Bivour, F. Feldmann, T. Hatt, F. Maier, R. Keding, F. Clement, and S. W. Glunz, “Low-resistivity screen-printed contacts on indium tin oxide layers for silicon solar cells with passivating contacts,” *IEEE Journal of Photovoltaics*, vol. 8, no. 5, pp. 1208-1214, 2018.

J. Schube, T. Fellmeth, M. Jahn, R. Keding, and S. W. Glunz, “Inkjet- and FlexTrail-printing with low silver consumption for silicon heterojunction solar cells,” *physica status solidi Rapid Research Letters*, 2019.

J. Schube, L. Tutsch, T. Fellmeth, F. Feldmann, M. Weil, A. Harter, J.-I. Polzin, M. Bivour, R. Keding, and S. W. Glunz, “Intense pulsed light in back end processing of solar cells with passivating contacts based on amorphous or polycrystalline silicon layers,” *Solar Energy Materials and Solar Cells*, vol. 216, p. 110711, 2020.

Co-author

S. Mack, J. Schube, T. Fellmeth, F. Feldmann, M. Lenes, and J. M. Luchies, “Metallisation of boron-doped polysilicon layers by screen printed silver pastes,” *physica status solidi Rapid Research Letters*, 2017.

Conference contributions

Oral presentations

J. Schube, L. Tutsch, T. Fellmeth, M. Bivour, F. Feldmann, T. Hatt, F. Maier, R. Keding, F. Clement, and S. W. Glunz, “Low-resistivity screen-printed contacts on indium tin oxide layers for silicon solar cells with passivating contacts,” in *7th World Conference on Photovoltaic Energy Conversion*, Waikoloa, USA, 2018.

J. Schube, T. Fellmeth, F. Maier, R. Keding, and S. W. Glunz, “Printed metal contacts for silicon heterojunction solar cells,” in *SiliconFOREST*, Falkau, Germany, 2019.

J. Schube, M. Weil, T. Fellmeth, R. Keding, and S. W. Glunz, “Intense pulsed light meets the metallization of silicon heterojunction solar cells,” in *46th IEEE Photovoltaic Specialists Conference*, Chicago, USA, 2019.

J. Schube, T. Fellmeth, M. Weil, S. Nold, R. Keding, and S. W. Glunz, “Intense pulsed light in back end processing of silicon heterojunction solar cells,” in *47th IEEE Photovoltaic Specialists Conference*, Calgary, Canada, 2020.

Visuals

J. Schube, T. Fellmeth, F. Maier, R. Keding, F. Clement, and S. W. Glunz, “Applicability of photonic sintering and autoclaving as alternative contact formation methods for silicon solar cells with passivating contacts,” in *7th SiliconPV*, Lausanne, Switzerland, 2017.

J. Schube, T. Fellmeth, M. Jahn, R. Keding, and S. W. Glunz, “Advanced metallization with low silver consumption for silicon heterojunction solar cells,” in *8th Workshop on Metallization and Interconnection for Crystalline Silicon Solar Cells*, Konstanz, Germany, 2019.

Co-author

S. Mack, T. Fellmeth, J. Schube, F. Feldmann, M. Lenes, and J. M. Luchies, “Screen-printed metallization for p-type poly-Si passivated contacts formed by LPCVD,” in *33rd European Photovoltaic Solar Energy Conference and Exhibition*, Amsterdam, The Netherlands, 2017.

M. Bivour et al., “SHJ/passivating contact activities and research possibilities at Fraunhofer ISE,” in *1st International Workshop on SHJ Solar Cells*, Shanghai, China, 2018.

D. Reinwand, B. King, J. Schube, F. Madon, R. Einhaus, and D. Kray, “Lab-scale manufacturing of medium-sized NICE™ modules with high-efficiency bifacial silicon heterojunction solar cells,” in *8th Workshop on Metallization and Interconnection for Crystalline Silicon Solar Cells*, Konstanz, Germany, 2019.

R. Keding, A. Lorenz, J. Schube, M. Pospischil, T. Hatt, Y. Franzl, D. Erath, and F. Clement, “Metallization processes for HJT technology,” in *AMPERE School*, Catania, Italy, 2019.

S. Pingel, D. Erath, T. Wenzel, D. Eberlein, A. De Rose, S. Tepner, J. Schube, S. Nold, A. Moldovan, A. Lorenz, and F. Clement, “Low temperature Ag-paste screening for silicon hetero junction solar cells and modules,” in *37th European Photovoltaic Solar Energy Conference and Exhibition*, Lisbon, Portugal, 2020.

Acknowledgment

I am very thankful for the intense and formative experience of my doctoral studies. Besides the research, this time thrived especially from the great people that accompanied me and, thereby, contributed to my work.

First of all, I would like to thank Prof. Dr. Stefan W. Glunz and Prof. Dr. Frank Balle for the scientific supervision and guidance throughout my work. Both gave me the time and freedom to develop as a researcher. I always enjoyed the atmosphere of our highly motivating meetings and I really appreciate their interest in my research and the fruitful discussions we had.

My sincere thanks go to Dr. Florian Clement and Dr. Roman Keding, too. They are a great source of motivation and, hence, always supported my work. It is great to be part of the department “Production Technology – Structuring and Metallization” and the group “Process Integration” in particular.

I was lucky enough that Dr. Tobias Fellmeth supervised my work. He was always there and supported me with his great physical and technical knowledge and his particular perspective on scientific issues, whenever I had to ask for help. Moreover, his constructive criticism significantly formed and influenced my scientific writing.

Mike Jahn and I always had a great time in (and outside) the lab. I am very thankful for his introduction into inkjet printing and related topics, especially in the first weeks of my doctoral studies. Later, we developed FlexTrail together, which is an ongoing and unique experience. However, this work has also benefitted from long nights with (fractal) discussions in various pubs!

It was a pleasure for me to supervise Maximilian Weil during his master thesis. With his great work and total commitment in the lab and during discussions, he really contributed to the results of this work. This holds for Florian Maier as well, who I supervised during an internship and during the time of his bachelor thesis.

Acknowledgment

Sincere thanks are dedicated to all other co-workers at Fraunhofer ISE who contributed to this work in many different ways: Dr. Martin Bivour, Santiago Franco Corredor, Denis Erath, Dr. Frank Feldmann, Christian Harmel, Fiona Hatzelmann, Alexander Krieg, Dr. Andreas Lorenz, Marc Retzlaff, Milad Sailimi Sabet, Leonard Tutsch, Timo Wenzel, and Diana Witt.

I would also like to thank Puzant Baliozian, Denis Erath, Dr. Frank Feldmann, Dr. Tobias Fellmeth, Mike Jahn, Dr. Roman Keding, and Mascha Wieland for detailed proofreading of this work. Moreover, I'd like to thank Jonas Huyeng for persistent sparring to prepare for the defense.

Special thanks go to Puzant Baliozian for musical outbursts on guitar (“Contact, contact formation...”) and Daniel Ourinson for support with snacks (nuts) on *The Island*. I would further like to thank Christian Bischoff, Raphael Effinger, Mariana Garcia Prince, Katharina Gensowski, Thibaud Hatt, Jonas Huyeng, Markus Klawitter, Dr. Sebastian Nold, Sebastian Tepner, Svetlana Weit, and Dr. Nico Wöhrle for the great time and discussions we had in (and outside) the office.

Special thanks are dedicated to my parents Helga and Werner Schube for their warm and loving support during my entire period of education.

Warmest thanks go to Mascha Wieland for her love, encouragement, and patience with her boyfriend, who was often a little absent-minded during his doctoral studies.

Last but not least, thanks a lot to the Reiner Lemoine Foundation for the doctoral scholarship.

